

“Dynamics of excitons, polaritons and collective excitations in semiconductors and semiconductor microcavities”

Resumen:

El objetivo final de este trabajo es mostrar una imagen transversal, a través de diferentes condiciones de confinamiento (desde tres a dos dimensiones), de las propiedades de muchos cuerpos de las excitaciones ópticas en semiconductores de gap directo. En concreto, la dinámica de tales excitaciones será estudiada a través de técnicas de fotoluminiscencia resuelta en tiempo.

Se ha estudiado la dinámica de fotoluminiscencia resuelta en tiempo de GaAs volúmico, y se ha encontrado una transición de Mott inducida óptimamente entre las fases excitónicas y de plasma. En pozos cuánticos, se ha propuesto una técnica novedosa que permite la modificación de las distribuciones de los portadores en las bandas. Finalmente, en microcavidades, se ha estudiado la dinámica de polaritones y fluidos de polaritones, obteniéndose resultados compatibles con la observación de superfluidez en estos sistemas.

Summary

The aim of this work is to provide a wide picture, using different confinement conditions (from bulk to two-dimensional) of the many-body properties of the optical excitations in direct gap semiconductors. In particular, the dynamics of such excitations will be studied by means of time-resolved photoluminescence. In this technique, the system is excited with an optical pulse with energy above the band gap and the emitted light dynamics is recorded and analyzed.

We have studied the polarization resolved photoluminescence dynamics of bulk GaAs photoexcited carriers finding an optically induced Mott transition between an exciton and plasma phases. In quantum wells a novel experimental technique has been introduced to tailor the distribution of carriers in the bands. Finally, in microcavities, the dynamics of polaritons and polariton fluids was studied, finding results compatible with the observation of superfluidity in these systems.

Dynamics of excitons, polaritons and collective excitations in semiconductors and semiconductor microcavities

Alberto Amo

Departamento de Física de Materiales
Universidad Autónoma de Madrid

Dissertation submitted for the degree of Doctor of Philosophy at
Universidad Autónoma de Madrid

Thesis Supervisor: Luis Viña

Madrid, February 2008

Acknowledgments

I would like to express my gratitude to the people who helped me in the work presented in these thesis, and who enriched my academic and research formation during these past years. A grateful acknowledge to Luis Viña who wisely introduced and guided me through the world semiconductor research, and to the members of the ultrafast spectroscopy group: Lola, Dario, Lukasz and Daniele.

The experiments would have not been possible without the help of Elías, Manolo (always with fresh Helium), Valentín Guadaño and Andrés Buendía.

Many people helped me to understand many physical effects and experimental techniques: Dipankar, Sne, Eva, Fran, Hermann, Nacho, Elena and Fabrice; and the Randall team: Bo, Qiong, Katherine, Xiaodong, Erik and Yanwen. A special thanks to Herko van der Meulen, Pepe Calleja and, in particular, to Carlos Tejedor. I would like to acknowledge Paolo Lugli, who introduced me in Munich to the world of Monte-Carlo. And I am in debt with Duncan Steel, who taught me so much about quantum physics and the insights of experimental research, and who warmly received me in Ann Arbor.

The people who visited the lab brought fresh ideas and inspirations: Adalberto Brunetti, Ivan Shelykh, Paulina Plotchocka and Elena Kozhemyakina.

I must acknowledge Konstantin Zhuravlev, Maurice Skolnick and Jacqueline Bloch, who grew and provided the samples used for these experiments.

List of publications

Optically-induced ultrafast quenching of the semiconductor quantum well luminescence

by A. Amo, D. Ballarini, D. Sanvitto, E. Kozhemyakina, L. Viña, A. Lematre, D. Bajoni, J. Bloch, in Appl. Phys. Lett. (accepted)

Exciton warming in III-V microcavities: probe for polariton relaxation processes

by A. Amo, D. Ballarini, D. Sanvitto, E. Kozhemyakina, L. Viña, M. S. Skolnick, J. S. Roberts, in Superlattices and Microstructures (accepted)

Ultrafast tailoring of the exciton distribution in quantum wells

by A. Amo, D. Ballarini, E. Kozhemyakina, D. Sanvitto, L. Klotkowski, L. Viña, D. Bajoni, J. Bloch, M. S. Skolnick, J. S. Roberts, in Phys. Status Solidi (c), (accepted)

Coexistence of weak- and strong-coupled modes in semiconductor microcavities

by D. Ballarini, A. Amo, D. Sanvitto, L. Viña, M. Skolnick, and J. S. Roberts, in Physica E, (in press)

Polariton and spin dynamics in semiconductor microcavities under non-resonant excitation

by M. D. Martín, G. Aichmayr, A. Amo, D. Ballarini, L. Klotkowski, L. Viña, in Journal of Physics: Condensed Matter, **19**, 295204 (2007)

Photoluminescence Dynamics in GaAs along an Optically Induced Mott Transition

by A. Amo, M. D. Martín, L. Viña, A. I. Toropov, K. S. Zhuravlev, in J. of Appl. Phys. **101**, 081717 (2007)

Transition from the strong- to the weak-coupling regime in semiconductor microcavities: polarization dependence

by D. Ballarini, A. Amo, L. Viña, D. Sanvitto, M. S. Skolnick, J. S. Roberts, in Appl. Phys. Lett. **90**, 201905 (2007)

Pauli blockade of the electron spin flip in bulk GaAs

by A. Amo, L. Viña, P. Lugli, A. I. Toropov, K. S. Zhuravlev, in Phys. Rev. B **75**, 085202 (2007)

Spin-dependent coexistence of weak- and strong-coupled modes in semiconductor microcavities

by D. Ballarini, A. Amo, M. D. Martín, L. Viña, D. Sanvitto, M. S. Skolnick, J. S. Roberts, in Superlattices and Microstructures **41**, 321 (2007)

Dynamics of polaritons resonantly created at the upper polariton branch

by M. D. Martín, D. Ballarini, A. Amo, L. Viña, R. André, in Superlattices and Microstructures **41**, 328 (2007)

Photoluminescence of "dark" excitons in CdMnTe quantum well, embedded in a microcavity

by A. Brunetti, M. Vladimirova, D. Scalbert, R. André, D. Ballarini, A. Amo, M. D. Martín, L. Viña, in Superlattices and Microstructures **41**, 386 (2007)

Optical anisotropy and pinning of the linear polarization of light in semiconductor microcavities

by L. Klopotoski, M. D. Martín, A. Amo, L. Viña, I. A. Shelykh, M. M. Glazov, G. Malpuech, A. V. Kavokin, R. André, in Semicond. Sci. Technol. **139**, 511 (2006)

Interplay of the exciton and electron-hole plasma recombination on the photoluminescence dynamics in bulk GaAs

by A. Amo, M. D. Martín, L. Viña, A. I. Toropov, K. S. Zhuravlev, in Phys. Rev. B **73**, 035205 (2006)

Influence of Trapping on the Exciton Dynamics of $Al_xGa_{1-x}As$ Films

by A. Amo, M. D. Martín, L. Klotowski, L. Viña, A. I. Toropov, K. S. Zhuravlev, in Appl. Phys. Lett. **86**, 111906 (2005)

Polarization dynamics of microcavity polaritons: Three excitation regimes

by L. Klotowski, A. Amo, M. D. Martín, L. Viña, R. André, in Phys. Status Solidi (a) **202**, 357 (2005)

Angular switching of the linear polarization of the emission in InGaAs microcavities

by A. Amo, M. D. Martín, D. Ballarini, L. Viña, D. Sanvitto, M. S. Skolnick, J. S. Roberts, in Phys. Status Solidi (c) **2**, 3868 (2005)

Striking dynamics of II-VI microcavity polaritons after linearly polarized excitation

by M. D. Martín, D. Ballarini, A. Amo, L. Klotowski, L. Viña, A. V. Kavokin, R. André, in Phys. Status Solidi (c) **2**, 3880 (2005)

Dynamics of polariton emission in the linear regime

by L. Klotowski, R. Santos, A. Amo, M. D. Martín, L. Viña, R. André, in Acta Physica Polonica A **106**, 443 (2004)

List of symbols

- a_B : Bohr radius
 $A^0 - X$: Acceptor bound exciton
 BAP: Bir-Aronov-Pikus spin-flip mechanism
 BX : Bound exciton
 c : Speed of sound
 $C_{k_{\parallel}}$: Cavity Hopfield coefficient; its square denotes the photon component of the polariton
 CW: Continuous wave (laser light)
 $D^0 - X$: Donor bound exciton
 DBR: Distributed Bragg Reflector
 δ : Exciton-photon detuning
 δE_{so} : Splitting between the $J = 3/2$ and $J = 1/2$ valence bands
 Δ : Spatial size of the wavepacket
 DOS : Denity of states
 DP: Dyakonov-Perel spin-flip mechanism
 e : electron; electron charge
 $e - A^0$: Electron acceptor transition
 ϵ_i : Energy of a quantum state
 E_b : Exciton binding energy
 E_{gap} : Energy of the fundamental gap in the consider semiconductor
 E_{gap}^* : Renormalized band-gap energy
 E_k : Kinetic energy
 E_{LPB} : Energy of the lower polariton branch mode (at $k = 0$ if not stated otherwise)
 E_{UPB} : Energy of the upper polariton branch mode (at $k = 0$ if not stated otherwise)
 EY: Elliot-Yaffet spin-flip mechanism
 ϵ_0 : Vacuum permitivity
 f_{BE} : Bose-Einstein distribution function
 f_e : Fermi-Dirac distribution function of the electron population
 f_{FD} : Fermi-Dirac distribution function
 f_{hh} : Fermi-Dirac distribution function of the heavy-hole population
 f_{hl} : Fermi-Dirac distribution function of the light-hole population
 f_{MB} : Maxwell-Boltzmann distribution function
 \mathbf{F} : Electric field
 F_P : Amplitue of the electric field of the pump
 FX : Free exciton

- g : Exciton-exciton repulsive interaction
- $g(E)$: Density of states in energy space
- $g(\mathbf{k})$: Density of states in momentum space
- hh : heavy-hole
- \hbar : Planck's constant over 2π
- GRINSCH: Graded index separate confinement heterostructure laser
- $\gamma_{x(c)}$: Homogeneous broadening of the exciton (cavity photon) mode
- hh : Heavy-hole
- $\hbar\omega_{x(c)}(\mathbf{k})$: In-plane energy dispersion of the excitons (cavity photons)
- J : Total angular momentum of a band [labeled by the value of J in the eigenvalue of \hat{J}^2 : $\hbar J(J+1)$]
- J^z : Third component of the angular momentum
- J_X^z : Third component of the exciton angular momentum
- \mathbf{k} : electron momentum
- k_B : Boltzmann's constant
- k_{\parallel} : in-plane momentum of the electrons or excitons
- K : center of mass momentum of the excitons
- L_c : Length of the cavity spacer
- L_{DBR} : Penetration depth of the electromagnetic field in the DBR
- LED: Light emitting diode
- L_{eff} : Cavity effective length
- lh : light-hole
- LO: Longitudinal-optical (referred to phonons)
- LPB: Lower polariton branch
- λ_T : De Broglie thermal wavelength
- m_0 : Free electron mass
- m_e^* : Electron effective mass
- m_h^* : Hole effective mass
- m_{nuc} : Mass of the nucleus
- m_p : Lower branch polariton mass
- m_{ph} : Photon mass in a cavity
- μ : Chemical potential
- μ_{eh} : Electron-hole reduced effective mass
- μ_{e-hh} : Electron—heavy-hole reduced effective mass
- μ_{e-lh} : Electron—light-hole reduced effective mass
- μ_X : Exciton mass
- N : Number of particles

n :	Particle density
n_c :	Critical excitation density
n_{cav} :	Refraction index of the cavity
n_i^r :	Refraction index
n_{x-x} :	Density for the onset of strong exciton exciton interaction
OPA:	Optical Parametric Amplifier
OPO:	Optical Parametric Amplifier
ω :	Angular frequency of the light field
Ω_R :	Rabi frequency
\wp :	Degree of polarization
PL:	Photoluminescence
Q :	Cavity quality factor
QW:	Quantum well
\mathbf{r} :	Position vector
$\rho_1(\mathbf{r}, \mathbf{r}')$:	Density matrix
$\boldsymbol{\sigma}$:	Spin Pauli matrices
σ^+ :	Right handed circularly polarized light
σ^- :	Left handed circularly polarized light
T :	Carrier temperature
τ_B :	Exciton localization time
τ_{e-h} :	Electron-hole scattering time
τ_k :	Momentum relaxation time
τ_p :	Electron momentum relaxation time
τ_\wp :	Decay time of the polarization
τ_r :	Free exciton recombination time
τ_{rB} :	Bound exciton recombination time
τ_{sf} :	Spin-flip time
T_c :	Critical temperature
TE:	Transverse electric (linear polarization)
T_L :	Lattice temperature
TM:	Transverse magnetic (linear polarization)
t_{max} :	Time for the PL to reach its maximum intensity after the arrival of the excitation pulse.
TOPO:	Triggered optical parametric oscillator
UPB:	Upper polariton branch
VCSEL:	Vertical Cavity Surface Emitting Lasers
v_g :	Polariton group velocity

v_s : Polariton sound velocity

$V_{x(c)}(\boldsymbol{x})$: Spatial fluctuations of the exciton (photon) confining potential

$X_{\boldsymbol{k}_{\parallel}}$: Exciton Hopfield coefficient; its square denotes the exciton component of the polariton

Contents

Contents	xi
List of Figures	1
1 Introduction	13
2 Introduction to zinc-blende type bulk semiconductors	21
2.1 Electronic structure in III-V bulk semiconductors: the bands	21
2.1.1 Crystalline structure	22
2.1.2 Band structure	25
2.1.3 Valence band mixing	33
2.1.4 Parabolic band approximation	34
2.1.5 Density of States	37
2.2 Band excitations: electrons, holes and excitons	38
2.2.1 Excitons	39
2.2.2 Many body effects	43
2.3 Optical transitions	44
2.3.1 Electron-hole pair transitions	44
2.3.2 Exciton emission	49
3 Reducing the dimensionality: QWs and semiconductor microcavities	51
3.1 Exciton confinement: semiconductor Quantum Wells	51
3.1.1 Electron and hole subbands	51
3.1.2 2D excitons	54
3.1.3 Optical properties	57
3.1.4 Effect of interface fluctuations and defects on the exciton linewidth . .	58
3.2 Light confinement and polaritons: semiconductor microcavities	59
3.2.1 Distributed Bragg Reflectors and the optical cavity	60
3.2.2 Semiconductor microcavity with an embedded quantum well: exciton- photon normal mode coupling	63
3.2.3 Finite cavity and exciton lifetimes	69

4	Samples and description of the experimental set-ups	73
4.1	Samples description	73
4.1.1	Bulk GaAs and AlGaAs	73
4.1.2	InGaAs/GaAs/AlGaAs/AlAs microcavity	74
4.1.3	GaAs/AlGaAs/AlAs microcavity	74
4.1.4	Single QW sample	75
4.2	Experimental set-ups	75
4.2.1	General time-resolved PL set-up	77
4.2.2	Non-resonant time-resolved PL from microcavities	77
4.2.3	The TOPO experiment	77
5	Carrier dynamics of photoexcited bulk GaAs	82
5.1	Introduction: photocreation of carrier populations	82
5.1.1	Coherent and incoherent emission	82
5.1.2	Exciton formation	84
5.1.3	Summary	87
5.2	Bulk GaAs photoluminescence under non-resonant excitation	87
5.2.1	The origin of the $1s$ exciton luminescence	87
5.2.2	Time evolution of the PL rise	89
5.2.3	GaAs	90
5.3	Low power regime: exciton dynamics	92
5.3.1	Spectral and time evolution characteristics	92
5.3.2	The effect of trapping on t_{max} : rate equations model	95
5.4	Medium and high power regime: towards the Mott transition	100
5.4.1	Introduction: Mott transition in photoexcited semiconductors	100
5.4.2	Spectral characteristics	102
5.4.3	Rise time characteristics	107
5.4.4	Phase diagram for t_{max}	116
5.4.5	Summary	118
6	Electron spin dynamics in the plasma regime	119
6.1	Phenomenological introduction	119
6.2	Optical orientation	121
6.3	Experimental results	123
6.4	Monte-Carlo simulation and discussion of the experimental results	128
6.4.1	Spin relaxation mechanisms	128
6.4.2	Monte-Carlo simulations: phase-space filling effects	131
6.4.3	Scaling relation	135
6.5	Summary	138
7	Tailoring the carrier distributions in QWs: two pulses experiments:	140
7.1	Introduction	140
7.2	Photoluminescence under two pulses excitation	141
7.3	Origin of the dip: thermodynamical model	142
7.4	Summary	150

8	Introduction to the many-body properties of microcavity polaritons	151
8.1	Bose-Einstein condensation of polaritons	151
8.2	Microcavity polaritons phase diagram	156
8.3	Spontaneous BEC of polaritons	158
8.4	The polariton system under resonant excitation of the LPB	162
8.5	Superfluidity of polaritons	166
8.6	Final remarks	171
9	Dynamics of microcavity polaritons under non-resonant excitation	172
9.1	Introduction: CW characterization	172
9.2	Power dependent dynamics	173
9.3	Polariton relaxation from the UPB in the strong coupling regime	180
9.4	Polarization dynamics in the weak coupling regime	184
9.5	Summary	193
10	Polariton quantum hydrodynamics	194
10.1	Introduction	194
10.2	Making polaritons flow	195
10.3	Polariton flow in the absence of defects	201
10.3.1	Polariton flow	201
10.3.2	Polariton diffusion	206
10.3.3	The pump and signal polariton quantum fluids	209
10.4	Interaction of the polariton fluids with localized defects	210
10.4.1	Scattering with a small point-like defect	210
10.4.2	Scattering with a large defect	214
10.4.3	Reflexion on a line defect	214
10.5	Summary and future perspectives	218
11	General conclusions	221

List of Figures

2.1	(a) Unit cell of a binary zinc-blende semiconductor. (b) Primitive lattice vectors conforming the Bravais lattice. (c) Reciprocal lattice. In grey are shown the first Brillouin zones of two neighboring unit cells. The high symmetry directions and points are indicated. From Ref. [301].	23
2.2	(a) Free electron dispersion in one dimension. (b) Dispersion relations separated by a reciprocal lattice wavevector (\mathbf{K}), the first step in the construction of the band diagram of electrons in a weak periodic potential. (c) Same as (b) including the reflection effects at the edge of the Bragg plane. (d) Portions of (c) that belong to the original parabola centered at $k = 0$. (e) Effect of all Bragg planes at integer multiples of the reciprocal lattice wavevectors. (f) Levels of (e) in a reduced-zone scheme. (g) Levels of (e) in a repeated-zone scheme. From Ref. [11].	27
2.3	Energy bands of Si (a) and GaAs (b) calculated with the pseudopotential method. The red lines depict the highest occupied bands at <i>zero</i> temperature. From Ref. [301].	29
2.4	(a) Conduction and valence band dispersions of GaAs in the effective mass spherical approximation. (b) <i>Warping</i> of the heavy- and light-hole bands shown on two constant energy surfaces in the (010-100) plane; from Ref. [301].	36
2.5	Carrier density in the conduction (black), light-hole (blue) and heavy-hole (red) bands in GaAs at which an occupation of 0.5 at $E = 0$ is attained following $f_{MB}^n(E)$	39
2.6	(a) Polarization and relative intensity of the matrix elements associated to the electric dipole allowed transitions from the valence to the conduction band. (b) Same as (a) for the resonant creation and recombination of heavy- and light-hole excitons.	47
3.1	(a) Γ point band structure of the layers of a semiconductor QW. The z -direction is taken as the growth or confinement direction. In dotted lines the confined $k = 0$ electron and hole levels corresponding to the $n' = 1$ subband are depicted. (b) Typical dispersion relations of the $n' = 1$ subbands in the QW layer of a GaAs/AlGaAs heterostructure in the effective mass approximation. The dashed lines depict the highest valence bands in the absence of mixing.	52

3.2	Calculated $1s$ heavy- and light-hole exciton binding energies (a, Ref. [96]) and oscillator strengths (b, Ref [9]) as a function of well width in symmetric GaAs/ $\text{Al}_x\text{Ga}_{1-x}\text{As}$ heterostructures.	56
3.3	(a) Polarization and relative intensity of the matrix elements associated to the electric dipole allowed transitions from the heavy- and light-hole subbands to the conduction subband with same n' . (b) Same as (a) for the resonant creation and recombination of heavy- and light-hole excitons.	58
3.4	(a) Normal incidence reflectivity ($R = r(\omega) ^2$) of a 20 pair DBR with $n_{out} = n_{sub} = 1$ and $n_1 = 3.0$, $n_2 = 3.6$, <i>vs</i> normalized frequency (ω/ω_m). (b) Corresponding phase ϕ_r of the complex reflection coefficient. Both magnitudes are calculated using a transfer matrix approach.[237]	60
3.5	(a) Reflectivity spectrum of a typical microcavity. (b) Black line, right scale: profile of the index of refraction of a $\lambda/2$ microcavity. In this case three QWs have been embedded at its center. The surface is on the left side. The growth direction is given by the horizontal axis. Blue line, right scale: electric field of the bare cavity mode. Inset: close up of the cavity spacer region. The electric field is maximum at the position of the QWs. This is the configuration in which exciton-photon strong coupling is observed, as detailed in Sec. 3.2.2. (c) Scanning electron microscope image of the cross section of an actual cavity, where both DBRs and cavity spacer are clearly seen. The black region on the left side has a size of ~ 225 nm. Courtesy of M. D. Martín.	64
3.6	Left panels: calculated bare exciton and cavity mode dispersions (dashed lines) as well as the polariton dispersions (solid lines) for different exciton-cavity detunings δ in a microcavity with a Rabi splitting $2\hbar\Omega_R = 6.6$ meV. Right panels: corresponding Hopfield coefficients obtained from Eqs. 3.29-3.30. Detunings: (a)-(b) $+2\hbar\Omega_R$, (c)-(d) <i>zero</i> , (e)-(f) $-2\hbar\Omega_R$	68
3.7	(a) Energy difference between the UPB/LPB and the cavity mode at $k_{\parallel} = 0$ as a function of reflectivity for a fixed bare QW γ_X for $\delta = 0$. The dashed line depicts the minimum reflectivity for the onset of strong coupling ($R \approx 0.85$). (b) Broadening of the cavity mode γ_c and modified γ_X inside the cavity ($R < 0.85$), and polariton modes width ($R > 0.85$), as a function of reflectivity. From Ref. [237].	71
4.1	Principles of operation of a synchroscan streak camera. See text for details.	76
4.2	General experimental set-up for time-resolved PL under non-resonant excitation. The polarization optics and the translation stage are used only when needed.	78
4.3	Experimental set-up for time-resolved PL under non-resonant excitation with selection of angle of emission via a pinhole. In the particular depicted configuration, the pinhole selects the $k_{\parallel} = 0$ luminescence. Polarization optics (not shown) and translation stage are used only when needed.	79
4.4	Set-up for the experiment in the TOPO configuration, in which real- and momentum-space 2D films can be recorded.	80

- 5.1 (a) Directionally and temporally resolved emission intensity (logarithmic grey scale) of a 35, 15, and 8 nm GaAs single quantum well at 5 K and low excitation intensity (exciton density of $\sim 2 \times 10^8 \text{ cm}^{-2}$). Γ_{inh} indicates the disorder induced inhomogeneous broadening of the exciton transition (from Ref. [166]). (b) Build-up of the emission at 10 K in a GaAs/AlGaAs multiple quantum well after resonant photoexcitation of the heavy-hole exciton line with a 150 fs-long pulse for different excitation densities. The rise changes from quadratic at low densities (originated from disorder induced dephasing) to linear at high densities (originated from incoherent exciton photoluminescence). (From Ref. [101]). 84
- 5.2 Bimolecular exciton formation coefficient as a function of the carrier temperature and for a lattice temperature of 10 K. At low carrier temperatures, electron and holes mainly populate the low energy states in the bands, and exciton formation occurs mainly via acoustic-phonon interaction. At high temperatures, carriers start to populate states with energy $\hbar\omega_{LO} - E_{bin}$ and the more efficient LO-phonon mediated process is activated (from Ref. [204]). 86
- 5.3 Calculated $1s$ -exciton distributions in a quantum well as a function of the center of mass momentum (in units of the exciton Bohr radius (a_0) at different times following a pulsed photoexcitation (1.5 ps long) at the energy of the $1s$ resonance, at a delay of (1) 2 ps, (2) 9 ps and (3) 25 ps. The low momentum optically active states are depopulated due to spontaneous emission (from Ref. [150]). 86
- 5.4 *Exciton populations or correlated electron-hole pairs as the source of excitonic photoluminescence?* The left column shows calculated luminescence spectra for an InGaAs/GaAs quantum well on a linear (top) and a logarithmic (bottom) scale, assuming just a quasi-equilibrium electron-hole population at a temperature of 20 K without any excitonic population. The corresponding panels in the right column present the results for the same situation, but where 10% excitons in a thermal distribution have been added. The black and red curves show the situation for two different carrier densities ($\times 10^9$ and 10^{10} cm^{-2}). The linear spectra are normalized, whereas the spectra on the logarithmic scale are in absolute units relative to the peak of the $1s$ peak of the black curve in the lower left frame (from Ref. [150, 44]). 88
- 5.5 Schematic diagram of the $1s$ -exciton dispersion showing the most significant processes contributing to the rise dynamics of the PL at the $1s$ -exciton energy (2) after a pulse photoexcitation above the bandgap (1): [A] thermalization and cooling of the electron-hole plasma, [B] geminate exciton formation with $K \approx 0$, [C] bimolecular exciton formation, [D] exciton relaxation within its own band, [E] free exciton trapping into bound states, which also radiatively recombine (4). (3) indicates the free electron-hole pair recombination. 91

- 5.6 (a) Low temperature (5 K) PL spectra of the GaAs (black line) and $x = 0.03$ (grey line) samples recorded at a delay of 1 ns after excitation (excitation density $0.18 \times 10^{15} \text{ cm}^{-3}$; excitation energy 1.630 eV). (b) GaAs spectra at 5 K at different excitation densities. The numbers on the right indicate the excitation density in units of 10^{15} cm^{-3} . Each spectrum has been normalized to the FX intensity and rigidly offset. 94
- 5.7 (a) Time evolution of the FX (solid dots) and the BX ($A^0 - X$; open dots) for the GaAs sample (excitation density $1.8 \times 10^{14} \text{ cm}^{-3}$; $T = 5 \text{ K}$). (b) same as (a) for the $\text{Al}_x\text{Ga}_{1-x}\text{As}$ $x = 0.03$ sample. t_{max} is indicated by horizontal bars. The solid lines are fits to the model described in the text ($\tau_k = 464 \text{ ps}$, $\tau_B = 1240 \text{ ps}$ and $\tau_r = \tau_{rB} = 565 \text{ ps}$ for GaAs). The inset shows the level scheme and the transitions considered in the model. 96
- 5.8 (a) Time for the free exciton to reach its maximum intensity, t_{max} , as a function of excitation density in the four investigated $\text{Al}_x\text{Ga}_{1-x}\text{As}$ epilayers at a lattice temperature of 5 K. The Aluminum content is indicated in each curve. (b) t_{max} as a function of excitation density for the GaAs sample at different lattice temperatures, up to 45 K. 98
- 5.9 Simulated FX PL time evolution for different values of τ_B for fixed τ_r , τ_{rB} and τ_k [those corresponding to the fits shown in Fig. 5.7(a)]. $\uparrow [\downarrow]$ indicate t_{max} for $\tau_B = \infty$ [430 ps, the value from the fit in Fig. 5.7(a)]. 100
- 5.10 PL spectra recorded 1.8 ns after an initial pulsed excitation density of $n = 0.75 \times 10^{15} \text{ cm}^{-3}$ for different lattice temperatures, specified on the side. Arrows indicate the energy position of the band gap at each temperature using the parameters of Ref. [81]. The shadowed regions show the electron-hole pair luminescence. The inset depicts the 30 K spectrum (open symbols) and the fit to a Lorentzian plus band-to-band recombination (green solid line) as described in the text; the dashed lines show these two contributions. . . . 103
- 5.11 (a) Energy of the spectral maximum extracted from the curves of Fig. 5.10 (solid points) and that obtained from the Lorentzian contribution of the spectra fitted to Eq. 5.6 (open diamonds), and energy position of the band gap for each lattice temperature (open red circles; obtained from Ref. [81]). (b) Full width at half maximum (FWHM) of the whole luminescence band (solid points) and that of the Lorentzian contribution of the fit (open diamonds) for each temperature; the lines are a guide to the eye. 105
- 5.12 (a) PL spectra at $T_L = 30 \text{ K}$, 60 ps after the pulse arrival, for different carrier densities (shown on the right in units of 10^{15} cm^{-3}). The straight lines are a guide to the eye. (b) Energies and (c) FWHM of the PL peak as a function of carrier density at a delay of 60 ps (solid points) and 2000 ps (green diamonds). The vertical dashed line marks the boundary between the insulating and metallic phase. The arrows emphasize the peak energy shift and FWHM jump at the boundary. 106
- 5.13 Time evolution traces at the spectral maximum for $T_L = 20 \text{ K}$ (a) and $T_L = 80 \text{ K}$ (b). The numbers on the right side of each panel show the excitation density for each trace in units of 10^{15} cm^{-3} 108

- 5.14 Time evolution traces at the spectral maximum of the luminescence for different lattice temperatures at an excitation density of $0.75 \times 10^{15} \text{cm}^{-3}$. The circle encloses the *fast component* of the onset of the PL for $T_L = 20 \text{ K}$ 109
- 5.15 (a) Initial carrier temperature $\langle T \rangle$, (averaged over the first 25 ps), as a function of excitation density for $T_L = 80 \text{ K}$; the solid line is a guide to the eye. (b) Simulated photoluminescence 0.5 meV above the band gap and (c) carrier temperature in the plasma regime. In order to simulate the curves in (b) and (c), Boltzmann distributions of electrons and holes were assumed with a carrier decay time of 3.5 ns. For the large (small) photoinjected n —solid line (red dotted line)—a cooling (warming) time of 40 ps and an initial temperature of 100 K (64 K) were employed. The inset of (a) depicts the electron occupation in the conduction band for carrier temperatures of 100 K (black line), 80 K (blue line) and 64 K (red dotted line). 112
- 5.16 t_{max} as a function of excitation density for different lattice temperatures. Solid symbols correspond to the excitonic/insulating phase; open symbols correspond to the electron-hole/metallic phase. The solid grey line is a guide to the eye. 114
- 5.17 t_{max} versus lattice temperature for each set of excitation densities (note that excitation densities are in units of 10^{15}cm^{-3}). The inset shows the temperature range 42 K-105 K in greater detail for excitation densities $0.3 \times 10^{15} \text{cm}^{-3}$ (squares), $30 \times 10^{15} \text{cm}^{-3}$ (solid triangles) and $300 \times 10^{15} \text{cm}^{-3}$ (open triangles). 115
- 5.18 Color map of the t_{max} as a function of temperature and carrier density (in units of 10^{15}cm^{-3}). The z -scale in picoseconds is indicated on the right-hand side bar. 117
- 6.1 GaAs PL spectra (σ^+ —closed points—, σ^- —open points—; left scales) and degree of circular polarization (right scales) for different excitation densities and delays after the σ^+ pulse arrival: (a) very low excitation density, $1.5 \times 10^{15} \text{cm}^{-3}$ at 300 ps; (b) $130 \times 10^{15} \text{cm}^{-3}$ at 150 ps; (c) $390 \times 10^{15} \text{cm}^{-3}$ at 150 ps; (d) $390 \times 10^{15} \text{cm}^{-3}$ at 515 ps. The thick solid lines are fits to the PL as explained in the text. The dashed vertical lines in (c)-(d) depict the selected energies at which the time evolution of the PL is depicted in Fig. 6.2. 124
- 6.2 PL intensity (upper panels) of the σ^+ (black line) and σ^- (grey line) components, after σ^+ excitation, for the highest excitation density ($390 \times 10^{15} \text{cm}^{-3}$), at two emission energies [denoted by vertical lines in Figs. 6.1(c) and 6.1(d)]: (a) 1.514 eV ($E_{k-e} = 5 \text{ meV}$); (b) 1.544 eV ($E_{k-e} = 33 \text{ meV}$). The lower panels show the corresponding degree of circular polarization. The lines are fits to a exponential decay function, with polarization decay times of 4.2 ns in (a) and 0.72 ns in (b). Note the different vertical scales in (a) and (b). . . . 127

- 6.3 (a) Measured spin-flip time as a function of the electron kinetic energy for initial excitation densities of $390 \times 10^{15} \text{ cm}^{-3}$ (circles), $240 \times 10^{15} \text{ cm}^{-3}$ (triangles) and $130 \times 10^{15} \text{ cm}^{-3}$ (squares). Solid lines depict the fitted spin-flip time as discussed in the text. The dashed line corresponds to the non-degenerate case ($\tau_{sf}^{non-deg}$, Eq. 6.9) with a hole density of $143 \times 10^{15} \text{ cm}^{-3}$, which corresponds to the hole density at 150 ps for the highest excitation case ($n = 390 \times 10^{15} \text{ cm}^{-3}$). The black dashed line is then to be compared with the solid black line. (b) Occupation of the electron states with spin-down and -up (dashed lines), as well as the total electron-hole scattering rate (solid dark line) for the excitation and time delay shown in Fig. 6.1(c). The solid light green line depicts the scattering rate for the conditions of Fig. 6.1(b). The inset presents a zoom of the electron occupations in order to clearly show the electron spin imbalance in the 20-42 meV electron kinetic energy range. The non-linear upper scale in (a) corresponds to the momentum of the electrons. . 129
- 6.4 Electron-hole scattering event with spin exchange (momentum, J^z). Note that momentum and spin are conserved in the process as $\mathbf{k} + \mathbf{k}' = \mathbf{k}'' + \mathbf{k}'''$. 131
- 6.5 Computed electron-hole scattering rate for an injected carrier density of $390 \times 10^{15} \text{ cm}^{-3}$ at different delays after the arrival of the pulse (solid lines). Black: 150 ps, red: 265 ps, blue: 515 ps. The dashed line depicts the averaged scattering rate. 134
- 6.6 (a) Figure 5 of Ref. [53]: calculated electron-electron scattering rate as a function of density for electrons with a distribution 20 meV wide in energy, centered at an excess energy of 60 meV. Triangles: static screening approximation without exchange (τ_{direct}); diamonds: static screening approximation with exchange (τ_{total}); squares: dynamic screening with exchange; circles: electron—LO-phonon scattering. (b) τ_{exc} vs τ_{direct} obtained from the points enclosed in a circle in (a). Note that both scales are logarithmic. The dashed line is a linear fit to the data. 136
- 7.1 Streak camera images of the single QW hh -PL under one pulse excitation (left panel) and under two consecutive pulses excitation with a delay between pulses of 400 ps (right panel). The color scales are normalized in each panel. The white arrow indicates the arrival of P_{II} and the subsequent formation of a dip in the hh -exciton PL emission. The black (red) arrow mark the emission from hh (lh) excitons. 142
- 7.2 (a) Photoluminescence dynamics of the single QW hh -exciton under one pulse excitation (grey dashed lines) and under two consecutive pulses excitation (black solid line; conditions of Fig. 7.1). In red dotted line the emission of the lh excitons (enhanced by a factor of 4) is presented under two pulses excitation. (b) Measured electron-hole temperature for a single (open points) and double (solid points) pulse experiment. (c) Exciton occupation right before (black line) and right after (orange line) the arrival of P_{II} ; the black (red) arrow indicates the energy of the $K = 0$ heavy (light)-hole exciton. . . . 143
- 7.3 Schematic time evolution of the electron distributions in a two pulses experiment (holes are not shown for simplicity). See text for details. 145

- 7.4 Spectra taken at different delays for the conditions of Fig. 7.2 for the single, wide QW. The spectra have been rigidly offset. The thick solid lines are fits to the free electron-hole pair recombination following a Maxwell-Boltzmann distribution, from which the temperature of the carriers can be extracted. Recall that the second pulse reaches the sample at a delay of 400 ps. 148
- 7.5 Temperature ratio (just before the second pulse/just after the pulse) in the single GaAs/AlAs QW sample as a function of (a) *delay* between pulses for a fixed power for both pulses (70 μ W), and (b) *power* of P_{II} for a fixed delay between pulses of 400 ps and fixed power of P_I (70 μ W). The solid (open) dots quantify the temperature ratio as directly measured from the PL (predicted from the model). The dashed lines are guides to the eye. The inset of (a) shows the corresponding relative dip depths (r). (c) Same as (b) for the multiple narrow QW sample with delay between pulses of 300 ps; the solid line computes the model (see text). 149
- 8.1 Occupation of particles following Bose-Einstein statistics at a temperature of 10 K and increasing density in the system (μ increases with density). 152
- 8.2 Phase diagrams for microcavities based on (a) GaAs, (b) CdTe, (c) GaN and (d) ZnO. The vertical and horizontal dashed lines show the limits of the strong coupling regime imposed by the exciton thermal broadening and screening, respectively. The solid lines show n_c vs temperature relation at the BKT phase transition. The dotted and dashed lines show the n_c for the case of quasi-condensation in finite size systems (lateral dimension of 100 μ m and 1 m, respectively). Taken from Ref. [181]. 157
- 8.3 Microcavity dispersion in the strong coupling showing the trap in momentum space and the polariton formation and relaxation channels. 158
- 8.4 (a) Far field emission (k_x and k_y momentum space) from the LPB of a CdTe based microcavity under non-resonant excitation at 5 K at different polariton densities, in the experiment of Kasprzak *et al.* where a BEC of polaritons was observed. (b) Same as (a) for $k_y = 0$ and energy resolution. Extracted from Ref. [133]. 161
- 8.5 (a) PL spectra of a resonantly excited GaAs-based microcavity at the magic angle and at a CW power above the threshold for stimulated OPO operation. The inset shows the dispersion, where the pair scattering process is indicated by arrows. From Ref. [231]. (b) Power dependence of the PL spectra under similar conditions of excitation as (a), in the range 0.5–500 W/cm². The laser intensity saturates the detector. The onset of the stimulated OPO regime occurs at 150 W/cm² (marked with an arrow). From Ref. [263]. 163

- 8.6 (a) Spectrum of excitations of the pump polariton state, i.e., the eigenenergies of Eq. 8.19, (b) intensity (arb. units) of the photonic resonant Rayleigh scattering signal $|\delta\phi_c(\mathbf{k})|^2$, and (c) near field image of the photonic scattered signal (Fourier transform of $|\delta\phi_c(\mathbf{k})|^2$), for $k_P = 0.7 \mu\text{m}^{-1}$, $\hbar\omega_P = \hbar\omega_{LP}(k_P) + 0.599 \text{ meV}$, and $\hbar g |\Psi_x^{ss}|^2 = 1 \text{ meV}$. Note that $\hbar\omega_{LP}(k_P)$ is that of the lower polariton state with k_P in the low density linear regime (no exciton-exciton interaction). This situation corresponds to the Čerenkov regime, in which a Bogoliubov linear excitations dispersion is present near the pump state but the relative velocity of the defect [placed in the center of (c)] is higher than v_s , producing scattering in a Čerenkov pattern. 169
- 8.7 Same as Fig. 8.6, for $k_P = 0.4 \mu\text{m}^{-1}$, $\hbar\omega_P = \hbar\omega_{LP}(k_P) + 0.467 \text{ meV}$, and $\hbar g |\Psi_x^{ss}|^2 = 1 \text{ meV}$. This situation corresponds to the superfluid regime, in which a Bogoliubov linear dispersion of the excitations is present with a singularity at the pump state, which additionally lies at the bottom of the excitations branch. In this situation the polariton state cannot scatter to any other state as long as the relative velocity of the defect is below v_s , and the Rayleigh signal has collapsed. 170
- 9.1 (a) Color map of the $k = 0$ emission from the InGaAs/GaAs/AlAs microcavity under non-resonant CW excitation at 5 K. The horizontal axis indicates the position in millimeters along a straight line parallel to the cavity wedge on the sample. The UPB peaks are indicated by a white solid line; its position in the map is evidenced in a z -logarithmic scale. The dashed lines depict the energy of the exciton and cavity modes. (b) Energy of the UPB and LPB peaks extracted from (a); the open points depict the emission from uncoupled excitons, visible at slightly negative detunings. (c) Detuning as a function of position on the sample calculated from Eq. 9.1. The minimum energy difference takes place at the position of $\delta = 0$ 174
- 9.2 (a) Streak camera image of the $k = 0$ microcavity emission for a detuning of $+7 \text{ meV}$. (b) Time evolution traces of the upper and lower polariton branches, extracted from (a). 175
- 9.3 (a) Carrier relaxation in a microcavity in the strong-coupling regime: [A] polariton formation from the photocreated plasma of electrons and holes, [B] polariton relaxation and thermalization within the *reservoir* states, [B*] polariton relaxation from the bottom of the UPB to the *reservoir* states, [C] polariton relaxation from the bottleneck to the bottom of the LPB. The grey line indicates the light cone: polaritons with k_{\parallel} greater than that of the line cannot escape from the cavity due to total internal reflection. (b) Carrier relaxation and light emission in the weak-coupling regime above the threshold for photon lasing (VCSEL regime). The numbers indicate the leveling of the 4-level lasing system. 176

- 9.4 Microcavity luminescence at $k = 0$ at 5 K after pulsed non-resonant excitation above the first minimum of the stop band at different powers: (a) 1 mW, (b) 6 mW, (c) 10 mW, (d) 15 mW, (e) 20 mW, (f) 25 mW, (g) 30 mW, (h) 35 mW, (i) 45 mW. The dotted lines in (a) depict the energy of the $k = 0$ states of the LPB (1.4507 eV), cavity mode (1.4542 eV) and UPB (1.4574 eV). 179
- 9.5 Energy of the $k = 0$ emission of the UPB (green dots), LPB (black dots) and cavity mode (blue open triangles) —left scales—, and total integrated emission (red dots) —right scales— as a function of non-resonant pulse power for several values of δ : (a) +8.3 meV, (b) +5.1 meV, (c) +0.8 meV, (d) -4.1 meV, (e) -8.1 meV. The blue area shows the transition from the strong to the weak coupling regimes. The dotted lines indicate the energy of the bare cavity and exciton modes. 181
- 9.6 (a) PL dynamics of the $k = 0$ lower branch polaritons in the microcavity under one pulse excitation (grey dashed lines) and under two consecutive pulses excitation (black solid line; delay between pulses: 450 ps; power of both pulses: 0.1 mW). (b) Same as (a) for the PL dynamics of the bare QW excitons in an identical microcavity without top mirror. In this case the delay between pulses is 400 ps and the power of each pulse is 0.3 mW. 182
- 9.7 Upper panels: polariton dispersion (solid lines) at $\delta = -5.6$ meV (a), $\delta = 0$ (b), $\delta = +11$ meV (c). The blue dashed lines depict the dispersion of the uncoupled excitons and cavity photons. The short red line indicates the energy of the electron-hole continuum in the QWs. The yellow circles indicate the excitation energy and momentum. The red arrows in (c) indicate the upper polariton scattering into *reservoir* states. Lower panels: PL emission at $k = 0$ in the LPB under one pulse excitation (black lines) and under two consecutive pulses excitation (red lines) at the detunings indicated in the upper panels. In each case the power of both pulses is equal. The first pulse is linearly polarized, while the second one is σ^+ circularly polarized; only the σ^- component of the emission is detected (see text for details). 185
- 9.8 Excitation of TE and TM polarization modes. The sample surface is parallel to the quantum well and cavity spacer, and the plane of incidence is that defined by the incoming beam and the normal to the surface. The green arrow indicates the direction of linear polarization *perpendicular* to the plane of incidence. The red arrow represents the linear polarization *parallel* to the plane of incidence. In this case there is always a component of the electric field *parallel* to the propagation direction in the cavity (orange arrow). 187
- 9.9 Degree of circular polarization (left scales, blue lines) and PL intensity for each circularly polarized component at $k = 0$ (right scales) under σ^+ excitation in the low power (a) —2 mW, strong coupling, LPB— and high power (b) —45.5 mW, photon lasing— regimes. (c) and (d), same as (a) and (b) for linearly polarized (TM) excitation. The black (red) lines denote emission co-(cross-)polarized to the excitation. Note the logarithmic scale for the PL intensity in the lower panels. The position on the sample corresponds to a detuning of -4.1 meV 188

-
- 9.10 (a) Time- and energy- integrated degree of circular polarization (open triangles) and total PL intensity (red dots) as a function of the photoexcitation power of σ^+ pulses. (b) Same as (a) for the degree of linear polarization under TM-polarized excitation. The dotted line depicts the onset of non-linear emission. 190
- 9.11 (a) Angle dependence of the energy- and time-integrated linear polarization of the cavity mode emission at high power (42 mW, weak-coupling regime) for TM (blue solid dots) and TE (red triangles) polarized excitation at $\delta = -4.1$ meV. The open dots depict the emission energy. (b) Same as (a) for $\delta = +5.3$ meV at high power (43 mW, solid blue dots; weak coupling, cavity mode emission) and low power (14 mW, open dots; strong coupling, LPB emission). 191
- 10.1 (a) Far field PL emission from the investigated microcavity under non-resonant excitation at $\delta = 0$. In the LPB, a sketch of the TOPO configuration is presented. The CW pump and pulsed idler arrive at the sample with angles of 10° and 16° respectively, giving rise to a signal state expected at 4° from the growth direction (normal to the surface). (b) Far field PL emission under resonant pump and idler excitation in the OPA configuration (same configuration as the TOPO with both pump and idler beams being CW). The laser scattered-light from the CW pump and idler (indicated by the yellow dots) has been blocked in order to avoid the bleaching of the detection CCD. The signal state is visible at $k_x - 0.5 \mu\text{m}^{-1}$. (c) Sketch of the pump and idler laser spots on the sample. 197
- 10.2 Time evolution of the TOPO signal at $k = 0$ after the arrival of the pulsed idler for pump and idler energies and momenta such that the phase matching conditions result in a signal at $k = 0$ (pump incidence angle: 12°). (a) Streak-camera image. (b) Time profile, showing a signal decay-time of 1.1 ns. 200
- 10.3 Spectrally selected observation at the TOPO signal energy of a coherent polariton gas moving at $v_g = 1.7 \mu\text{m}/\text{ps}$. The images are real space shots taken at different times after the probe pulse arrival ($t = 0$). (b) Reciprocal (momentum) space frames recorded at the same time delays and energy as (a). The inset displays a 3D view which evidence the narrowness of the k distribution. The diffusion-less motion and the invariance of the k -vector are a clear signature that polaritons are in a regime showing quantum coherence. The CW pump power is 20 mW (10°), while the pulsed probe power is $110 \mu\text{W}$ (16°). 202

- 10.4 (a) PL intensity as a function of energy and momentum of the emission for $k_y = 0$, at short time (12 ps) after the arrival of the pulsed laser in the TOPO configuration. Note that the image is obtained by recording the emission of the TOPO (CW-pump plus pulsed-idler) and subtracting the emission caused by the CW pump only. In this way only the polaritons populated by parametric processes triggered by the pulsed idler are recorded. The white lines are a linear and parabolic fit as in (b). (b) Black dots: PL-peak positions extracted from (a). Open points: dispersion under just CW-pump excitation (no idler pulse). Red dots: LPB dispersion obtained under low-power, non-resonant excitation in the same spot as that depicted by the black dots. The orange arrow indicates the energy of the CW-pump, while the green arrow depicts the position of the signal state. The blue line is a linear fit to the black dots with $k_x < -0.45 \mu\text{m}^{-1}$, while the grey line is a parabolic fit to the emission at $k_x > -0.45 \mu\text{m}^{-1}$ 204
- 10.5 Solid dots: Gaussian width of the polariton packet in the y -direction extracted from the real space images of Fig. 10.3(a). Solid red line: calculated wavepacket diffusion for a parabolic dispersion [Eq. 10.3]. Blue dashed line: expected wavepacket diffusion in a linear dispersion. 207
- 10.6 Real-space (a) and momentum-space (b) images, of an incoherent polariton fluid, at a detection energy above the bottom of the LPB at different times. The color scales vary from panel to panel. The images are obtained at low pump power (7 mW, 10°). The idler is set at 16° at $130 \mu\text{W}$. In real space the fluid slowly moves diagonally to the right and upwards. The white circle at 43 ps depicts the position of the fluid at $t = 14$ ps. A $t \gtrsim 45$ ps the fluid gets localized in a shallow potential. 208
- 10.7 (a) Signal polariton movement in real space at different times in the presence of a small defect (marked with a white dot in the first panel). The observed Čerenkov waves reflect the local change in density of the pump polaritons, which are traveling at a supersonic velocity (see text and Fig. 10.8). (b) Corresponding momentum space images. The color scales vary from panel to panel. The pump (idler) power is 54 mW ($315 \mu\text{W}$) and the angle of incidence is $10^\circ(16^\circ)$ 211
- 10.8 Sketch of the TOPO in real space. The observation of the signal polariton-fluid is represented by the circles running from left to right on the black background. We are able to detect this motion thanks to the continuous feeding from the pump polaritons which are represented by the gray plane. The supersonic regime of the pump polaritons is evidenced by the presence of Čerenkov waves around the defect. The change in density of the pump polaritons is projected into the signal polaritons which, instead, move through the defect. The red point shows the position of the defect. 212

10.9	Images of a signal polariton quantum-fluid at different times facing a defect of size comparable with its own dimension. Under these conditions the polariton fluid is forced to “feel” the defect which is now breaking the polariton trajectory in real space (a) and showing the appearance of two independent polariton states with different k -vectors (b). The pump (idler) power is 39 mW (70 μ W) and the angle of incidence is 10° (16°).	215
10.10	Real-space images at the energy of the signal polaritons at different times. The polariton fluid encounters a line defect in its path, sketched in (a) as a white line. The initial momentum points in the $(x, y) = (1, 1)$ direction. When the polariton fluid encounters the line defect its partially reflected and partially transmitted as indicated by the purple arrows in (a). In this case TOPO is configured with a pulsed idler angle of incidence of 15° (80 μ W), a pump angle of 10° (100 mW), giving rise to a signal at 10° . The white lines depict the line defect.	216
10.11	Simulation of the time evolution of an atomic Na BEC with a lentil shape colliding against a tunnel barrier at a velocity of 6.3 mm/s^{-1} in the x direction. The figure shows real space snapshots at $t = 3 \text{ ms}$ (a), 4 ms (c), 5 ms (d), 6 ms (e), 7 ms (f). The tunnel barrier is created by the optical field of a laser. From Ref. [184].	218

Chapter 1

Introduction

Semiconductor materials offer a privileged workbench for the study of many fundamental aspects of the light-matter interaction and the collective excitations in solids. Due to the vast richness of their physical properties, they have been the subject of intense study in the past five decades. Still, the advent of new semiconductor species, the never-ending improvement of the growth techniques, and the continuous development of the experimental methods make this field more active than ever.

One of the fundamental factors in the development of the field of optical properties of semiconductors has been the appearance of epitaxial growth techniques. They have enabled the fabrication of high quality artificial semiconductor heterostructures in which the excitations can be confined from three to two dimensions (quantum wells), one dimension (quantum wires) and *zero* dimensions (quantum dots).

Regardless the dimensionality, electrons, holes and excitons are the fundamental excitations of direct gap semiconductors, and dominate their optical properties. These quasi-particles can be both created and probed through the absorption and emission of photons in these materials. When a small number N of excitations are created in a semiconductor, the behavior and properties of the system can be considered the same as those for just one excitation. At most, the amplitude of the considered effect (for instance, the number of emitted photons) must be scaled with N . When many of such excitations are created, the physics of the system changes significantly, giving rise to very rich phenomena.

The aim of this work is to provide a wide picture, using different confinement conditions (from bulk to two-dimensional) of the many-body properties of the optical excitations in direct gap semiconductors. In particular, the dynamics of such excitations will be studied

by means of time-resolved photoluminescence. In this technique, the system is excited with an optical pulse with energy above the band gap and the emitted light dynamics is recorded and analyzed.

Chapter 2 presents a brief introduction to the energy levels (bands), symmetries and optical properties of the excitations of bulk zinc-blende type semiconductors. GaAs and its ternary relatives InGaAs and AlGaAs are semiconductors of this type, and will be the constituent materials of the heterostructures investigated here. Particular attention will be paid to the description of the excitonic resonances, as excitons dominate many of the optical properties and will be the subject of intense experimental study in later chapters.

In Chapter 3 we describe the effect of reducing the material dimensionality on the optical excitations. Namely, we will address the properties of quantum wells. In the final part of this chapter we will introduce a novel heterostructure with very exotic and rich properties: the semiconductor microcavity. In this heterostructure not only the material excitations (quantum well excitons) but also the interacting light-field modes are confined to two dimension. This is achieved by the epitaxial growth of one or several quantum wells inside a planar cavity sandwiched between two high-reflectivity dielectric mirrors. The cavity and the mirrors conform a micro-Fabry-Perot resonator, in which the electromagnetic field is confined. The continuum of available electromagnetic modes in vacuum is reduced to a discrete number of modes inside the cavity, with increased energy density. Light-matter interactions in such an environment are expected to be strongly modified. Indeed, under particular circumstances that are detailed in Chapter 3, the excitations in this system are no longer cavity photons or excitons, but a quantum mixture called *polariton*.

In those two chapters (2 and 3), the fundamentals of the optical excitations subject of study in this work are introduced. The next chapter (4) describes the samples and employed experimental techniques. The remaining of this work is then devoted to experimental results and their analysis.

Chapters 5 and 6 discuss experimental results in bulk GaAs. In Chapter 5 the microscopic origin of the emission at the exciton resonance is investigated. Koch and coworkers recently proposed that the emission at the $1s$ exciton energy might not exclusively arise from the radiative recombination of excitons: Coulomb correlated electron-hole pairs can also participate in the emission at that energy.[145, 44] This proposal is very different to the traditional conception of the optical properties of direct-gap semiconductors, and has opened a very active debate.[270, 44, 150, 18] In this framework, in this chapter we show

that attending to the photoluminescence dynamics in bulk GaAs, a precise phase diagram of the microscopic origin of the luminescence (either from excitons or electron-hole pairs) can be obtained. Depending on the sample temperature and excitation density conditions, the emission arises from the radiative recombination of excitons or from unbound electron-hole pairs. The many-body interactions in the system rule which type of excitation is responsible for the luminescence characteristics.

In the next chapter (6) we explore the spin dynamics of photoexcited electrons in GaAs. The study of the electron spin in semiconductors has been very active since the early seventies, with the pioneering works of the soviet community.[187] However, not much attention has been paid to the many-body effects on the electron spin dynamics, which will be the subject of this chapter.

In the roadmap we are following in the study of the many body physics of photoexcited semiconductors under different light/matter confinements, the next step is the investigation of quantum well (2D) excitations. In Chapter 7 we report an experimental configuration that allows for the tailoring of the electron and hole distributions in the quantum well bands by means of laser pulses.

The last three Chapters (8, 9 and 10) are devoted to the physics of microcavities, in which light and matter excitations are simultaneously confined in an environment of strong interaction, giving rise to polaritons. The first one of them (Chapter 8) offers a detailed introduction to the many-body effects in these systems. Chapter 9 presents a detailed experimental map of the microcavity light-emission dynamics under non-resonant excitation, paying special attention to the conditions that lead to the destruction of polaritons, driving the microcavity system into VCSEL operation.¹

The most important many-body effects in microcavities are related to the bosonic nature of polaritons. Polaritons are composite bosons with a very small mass (10^{-5} times the electron mass) due to their partially photonic nature, and the quantum phenomena associated to their bosonic character can be observed in optical experiments. Recently, Bose-Einstein condensation of polaritons has been observed,[133] revealing properties such as the spontaneous appearance of long-range order.[161] Other important bosonic effects, like the observation of superfluidity of polaritons, are expected in these systems. In Chapter 10

¹VCSEL is the acronym for a Vertical Cavity Surface Emitting Laser, a device with a material structure very similar to that of a microcavity. However, in this system, the conditions of strong light matter coupling leading to the observation of polaritons are not fulfilled. In a VCSEL the quantum well is the active medium and the cavity conforms the optical resonator.

we present experimental results on the interaction of polariton fluids with native defects on the samples. In order to create and observe the polariton fluids, a novel experimental space- and time-resolved imaging system is presented. The fluids interact in very particular ways with the defects showing, for the first time in a polariton system, behavior compatible with manifestations of superfluidity.

Introducción

Los semiconductores ofrecen un privilegiado banco de pruebas para el estudio de muchos de los aspectos fundamentales de la interacción luz-materia y las excitaciones colectivas en los sólidos. Debido a la gran riqueza de sus propiedades físicas, los semiconductores han sido objeto de intenso estudio en las pasadas cinco décadas. Aun así, la síntesis de nuevos materiales semiconductores, interminable mejora de las técnicas de crecimiento y el constante desarrollo de las técnicas experimentales hacen que este campo se encuentre más activo que nunca.

Uno de los factores fundamentales en el desarrollo del campo de las propiedades ópticas de semiconductores ha sido la aparición de las técnicas de crecimiento epitaxial. Éstas han posibilitado la fabricación de heteroestructuras artificiales de alta calidad, en las que las excitaciones propias del material pueden ser confinadas desde tres a dos dimensiones (pozos cuánticos), una dimensión (hilos cuánticos) y *cero* dimensiones (puntos cuánticos).

Cualquiera que sea la dimensionalidad, las excitaciones fundamentales de los semiconductores de gap directo son los electrones, huecos y excitones, y determinan sus propiedades ópticas. Estas cuasipartículas pueden ser tanto creadas como estudiadas a través de la absorción y emisión de fotones. Cuando un número pequeño N de excitaciones es creado en un semiconductor, su comportamiento y propiedades pueden ser consideradas equivalentes a las obtenidas para una única excitación. Como mucho, la amplitud del efecto considerado (por ejemplo, el número de fotones emitidos) debe escalar con N . Cuando son muchas las excitaciones creadas, la física del sistema cambia de forma importante, dando lugar a nuevos y ricos fenómenos.

El objetivo final de este trabajo es mostrar una imagen transversal, a través de diferentes condiciones de confinamiento (desde tres a dos dimensiones), de las propiedades de muchos cuerpos de las excitaciones ópticas en semiconductores de gap directo. En concreto, la dinámica de tales excitaciones será estudiada a través de técnicas de fotoluminiscencia resuelta en tiempo. En esta técnica, el sistema es excitado con un pulso óptico de energía superior a la de la banda prohibida, y la dinámica de emisión es medida y analizada.

El capítulo 2 presenta una pequeña introducción a los niveles de energía (bandas), simetrías, propiedades ópticas de semiconductores volúmicos de tipo zinc-blenda. GaAs y los compuestos ternarios relacionados InGaAs y AlGaAs son semiconductores de este tipo, y

serán los materiales constituyentes de las heteroestructuras investigadas aquí. Se prestará especial atención a la descripción de las resonancias excitónicas, dado que los excitones dominan la mayoría de las propiedades ópticas de estos sistemas y serán objeto de intenso estudio en capítulos posteriores.

En el capítulo 3 se describe el efecto de la reducción de la dimensionalidad del material en las excitaciones ópticas. En concreto nos centraremos en las propiedades de los pozos cuánticos. En la parte final de este capítulo introduciremos una heteroestructura novedosa con propiedades muy exóticas y diversas: la micocavidad semiconductor. En esta heteroestructura no sólo las excitaciones materiales (excitones de pozo cuántico) sino también los modos del campo de luz interactuante están confinadas a dos dimensiones. Esto se consigue mediante el crecimiento epitaxial de uno o varios pozos cuánticos dentro de una cavidad plana emparedada entre dos espejos dieléctricos de alta reflectividad. La cavidad y los espejos conforman un micro-resonador de Fabry-Perot, en el que el campo electromagnético se encuentra confinado. El continuo de modos electromagnéticos disponibles en el vacío se reduce a un número discreto de modos dentro de la cavidad, con una mayor densidad energética. La interacción luz-materia en un entorno como éste se ve fuertemente modificada. De hecho, bajo determinadas circunstancias detalladas en el capítulo 3, las excitaciones en este sistema dejan de estar bien descritas por fotones o excitones y pasan a componerse de una mezcla cuántica de ambos, los *polaritones*.

En esos dos capítulos (2 y 3) se hará una introducción a los fundamentos básicos de las excitaciones ópticas objeto de estudio en este trabajo. El siguiente capítulo (4) describe las muestras y técnicas experimentales empleadas. El resto de este trabajo está dedicado a la descripción de resultados experimentales y a su análisis.

Los capítulos 5 y 6 muestran resultados experimentales en GaAs volúmico. En el capítulo 5 se investiga el origen microscópico de la emisión a la energía de la resonancia excitónica. Koch y sus colaboradores han propuesto recientemente que la emisión a la energía del exciton $1s$ puede no ser debida exclusivamente a la recombinación radiativa de excitones: pares de electrones y huecos correlacionados por interacción Coulombiana también pueden participar en la emisión a esa energía.[145, 44] Esta propuesta es muy diferente de la concepción tradicional de las propiedades ópticas de los semiconductores de gap directo, y ha provocado un debate muy activo.[270, 44, 150, 18] En este contexto, en este capítulo se demuestra que, atendiendo a la dinámica de fotoluminiscencia en GaAs volúmico, se puede obtener un diagrama de fases detallado del origen microscópico de la luminiscencia

(con origen en excitones o en pares electrón-hueco). Dependiendo de la temperatura de la muestra y de las condiciones de excitación, la emisión procede de la recombinación radiativa de excitones o de pares no ligados de electrones y huecos. Las interacciones de muchos cuerpos en este sistema determinan qué tipo de excitación es responsable de las propiedades de la luminiscencia.

En el siguiente capítulo (6) se exploran la dinámica de espín de electrones fotoexcitados en GaAs. El estudio del espín de los electrones ha sido un campo muy activo desde principios de los años setenta, con los trabajos pioneros de la comunidad soviética.[187] Sin embargo, no se ha prestado mucha atención a los efectos de muchos cuerpos en la dinámica de espín, este será el contenido de este capítulo.

En esta ruta que estamos siguiendo en el estudio de la física de muchos cuerpos en semiconductores fotoexcitados bajo distintos confinamientos de luz y materia, el siguiente paso es la investigación de las excitaciones de los pozos cuánticos (2D). En el capítulo 7 se muestra una configuración experimental que permite la manipulación de las distribuciones de electrones y huecos en las bandas del pozo cuántico por medio de pulsos láser.

Los tres últimos capítulos (8, 9 and 10) se dedican a la física de microcavidades, en las que las excitaciones de luz y materia están simultáneamente confinadas, en un entorno de fuerte interacción, dando lugar a los polaritones. El primero de ellos (capítulo 8) ofrece una introducción a los efectos de muchos cuerpos en estos sistemas. El capítulo 9, muestra un detallado mapa experimental de la dinámica de emisión de luz bajo excitación no-resonante, prestando especial atención a las condiciones que conducen a la destrucción de polaritones, llevando el sistema al régimen de operación VCSEL.²

Los efectos de muchos cuerpos más importante en microcavidades están relacionados con la naturaleza bosónica de los polaritones. Los polaritones son bosones compuestos con una masa muy pequeña (10^{-5} veces la masa del electrón), debido a su naturaleza parcialmente fotónica, y los fenómenos cuánticos asociados a su carácter bosónico pueden ser observados en experimentos ópticos. Recientemente, la condensación de Bose-Einstein de polaritones ha sido observada,[133] revelando propiedades tales como la aparición espontánea de orden de largo alcance.[161] Otros importantes efectos bosónicos, como la superfluidez,

²VCSEL son las sigla en inglés de láser de emisión superficial de cavidad vertical (Vertical Cavity Surface Emitting Laser). Se trata de un dispositivo con una estructura material muy similar al de una microcavidad. Sin embargo en este sistema no se dan las condiciones de acoplamiento fuerte luz-materia que conducen a la aparición de polaritones. En un VCSELs los pozos cuánticos actúan como medio activo y la cavidad conforma el resonador óptico.

deberían ser, en principio, observables. En el capítulo 10 se presentan resultados experimentales sobre la interacción de fluidos de polaritones con defectos nativos en las muestras. Para crear y observar los fluidos de polaritones, hemos diseñado un experimento novedoso de formación de imágenes espaciales con resolución temporal. Los fluidos interactúan de un modo muy especial con los defectos mostrando, por primera vez en un sistema polaritónico, comportamientos compatibles con manifestaciones de superfluidez.

Chapter 2

Introduction to zinc-blende type bulk semiconductors

2.1 Electronic structure in III-V bulk semiconductors: the bands

In this thesis we will deal with crystalline semiconductors, which are ordered structures with a high atom density (on the order of 10^{23} per cm^3). The formal way of finding the eigenstates of such systems consist on solving the Schrödinger equation with the Hamiltonian that describes *all* the interactions and particles in the system. However, the large number of particles demands the use of several approximations to make the problem tractable. One usually starts by taking the Born-Oppenheimer approximation that assumes that electrons respond almost instantaneously to the movement of the nuclei, due to the very large difference in the mass of the two types of particles [$m_0/m_{nuc} \sim 10^{-4}$, where m_0 is the free electron (nuclear) mass]. Accordingly, one can separate the Hamiltonian into three contributions:

$$\mathcal{H} = \mathcal{H}_{ions} + \mathcal{H}_{e-ions} + \mathcal{H}_e. \quad (2.1)$$

\mathcal{H}_{ions} is the Hamiltonian that describes the interaction between the atomic nuclei and the core electrons, i.e., those electrons lying in the filled atomic orbitals, with high binding energies. The eigenstate of \mathcal{H}_{ions} , accounts for the crystalline structure of the material, characterized by the different spatial positions of the ions. \mathcal{H}_{e-ions} describes the interaction

between the valence electrons and the ions when they suffer small displacements from their equilibrium positions. The valence electrons are those occupying the outer incomplete shells of the atoms conforming the crystal. They are loosely bound to the nucleus and propitious to interact with charges of surrounding nuclei. For example, in the case of Ga the incomplete shell is $4s^2 4p^1$ and in As $4s^2 4p^3$ and so the valence electrons in GaAs will have p -character in their ground state. \mathcal{H}_{e-ions} is also known as the electron-phonon interaction Hamiltonian and is responsible for some of the energy relaxation mechanisms of excited electrons. In this section we will neglect this term as its contribution to \mathcal{H} is much smaller than the others. Finally, \mathcal{H}_e is Hamiltonian describing the valence electrons with the ions fixed in their equilibrium positions, and can be written in the following way (cgs units):

$$\mathcal{H}_e = \sum_i \frac{p_i^2}{2 \cdot m_0} + \frac{1}{2} \sum_{i \neq j} \frac{e^2}{4\pi\epsilon_0 |\mathbf{r}_i - \mathbf{r}_j|^2} - \sum_{i,j} \frac{Q_j \cdot e^2}{4\pi\epsilon_0 |\mathbf{r}_i - \mathbf{R}_j|^2}, \quad (2.2)$$

where p_i is the electron momentum, e is the electron charge, ϵ_0 is the vacuum permittivity, m_0 the free electron mass, Q_j is the absolute ion valence, and $r_i(R_j)$ is the electron (ion) position.

2.1.1 Crystalline structure

As we introduced earlier, the eigenstate of \mathcal{H}_{ions} defines the crystalline structure of the considered material. Many III-V (GaAs, AlP, AlAs, GaP, GaSb, InP, InAs, InSb, as well as their ternary compounds) and II-VI (ZnS, ZnSe, ZnTe, CdTe) semiconductors present the well known zinc-blende structure. This structure, which is also present in diamond, is characterized by two face center cubic (fcc) lattices shifted one from the other by a distance $a/4$ along the main diagonal of the unit cell depicted in Fig. 2.1, where a is the length of the sides of the cell. In diamond (or elemental semiconductors such as Si, Ge, α -Sn), all the atomic sites are occupied by C atoms, in a tetrahedral covalent bonding configuration in which the outer shell orbitals present sp^3 hybridization. In the case of the binary compounds, each type of atom (A and B) occupies one of the fcc lattices. In this configuration each A atom is bound to four B atoms. Due to the slightly different electronic affinities of A and B , the chemical bond is partly ionic.

The highly symmetrical structure of the crystal reduces the number of possible solutions of Eq. 2.2. In order to find them it is convenient to define the crystallographic unit cell of the binary zinc-blende structure, indicated by the primitive lattice vectors \mathbf{a}_1 ,

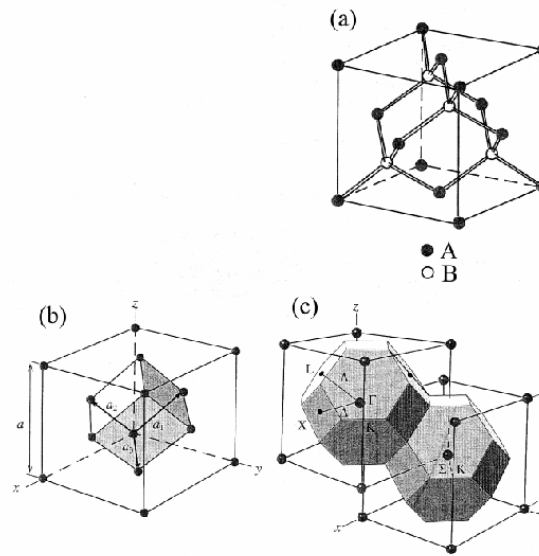


Figure 2.1: (a) Unit cell of a binary zinc-blende semiconductor. (b) Primitive lattice vectors conforming the Bravais lattice. (c) Reciprocal lattice. In grey are shown the first Brillouin zones of two neighboring unit cells. The high symmetry directions and points are indicated. From Ref. [301].

\mathbf{a}_2 and \mathbf{a}_3 , as shown in Fig. 2.1(b). By translating this unit cell by integer multiples of the primitive lattice vectors, the whole crystal structure can be composed, in what is called a Bravais lattice. It is also useful to define a reciprocal lattice, whose primitive vectors \mathbf{b}_i are given by the expression:

$$\mathbf{a}_i \cdot \mathbf{b}_j = 2\pi \cdot \delta_{ij} \quad (2.3)$$

or, equivalently, by:

$$\mathbf{b}_i = 2\pi \frac{(\mathbf{a}_j \times \mathbf{a}_k)}{(\mathbf{a}_1 \times \mathbf{a}_2) \cdot \mathbf{a}_3}, \quad (2.4)$$

where i, j, k are permutations of the indexes 1, 2, 3. The reciprocal primitive cell for the case of zinc-blende crystal is shown in Fig. 2.1(c), and conforms a body centered cubic lattice. A first Brillouin zone can be defined in the reciprocal space as the volume determined by the bisectrix of the reciprocal primitive vectors. Two first Brillouin zones are indicated in shades in Fig. 2.1(c). The center of each one of them is labeled Γ , from which three high symmetry directions can be identified [labeled Λ ($\Gamma \rightarrow L$), Δ ($\Gamma \rightarrow X$) and Σ ($\Gamma \rightarrow K$)].

The symmetry properties of the direct lattice will simplify the solution of the real-space valence-electron Hamiltonian denoted by Eq. 2.2. The reciprocal space, characterized by the reciprocal lattice, represents the space of the momentum of the electrons in the crystal as it is defined following the same commutation relations as those of the position and momentum operators. The high symmetry of the reciprocal space, will determine many properties of the eigenstates (wavefunctions) and band structure (eigenvalues) of the valence electrons in the semiconductor. For instance, if two wavevectors in reciprocal space can be transformed one into each other by a unitary transformation (symmetry operation), the energies of the corresponding states should be the same. On the same ground, the wavefunctions describing those states should reflect the same symmetry operation properties. The symmetry of the wave functions can help to determine if any matrix element associated to a given operator is *zero*. In this way, selection rules for different processes (light absorption/emission, Raman scattering, spin properties) can be established without the need to know the exact form of the wavefunctions.

The zinc-blende crystalline structure presents 24 symmetry transformations, belonging to the point group T_d , in group theory terminology. Considering the unit cell vectors described in Fig. 2.1 the 24 transformations are six reflections (σ_d), six 90° rotations

plus reflection (S_4), three 180° rotations (C_2), eight 120° rotations (C_3), and the identity transformation (E). In reciprocal space the 24 symmetry transformations can only be performed for momentum states at the Γ point. Once we consider states with other momenta the symmetry of the wavefunctions is reduced and its calculations hardened, while along the directions of high symmetry and at the L, X and K points the wavefunctions retain invariance under many of those transformations. Let us also point out that the zinc-blende crystal does not possess inversion symmetry. This gives rise to the so called *bulk inversion asymmetry* effects.

2.1.2 Band structure

Once we have seen the symmetry properties of the direct and reciprocal lattice in zinc-blende type semiconductors, we can come back to the problem of finding the eigenstates of the Hamiltonian given by Eq. 2.2. In order to further simplify that Hamiltonian, we will consider a mean-field approximation, in which each valence electron feels an averaged interaction coming from the ions and the rest of the electrons. Therefore, all valence electrons can be described by the same Schrödinger equation, given by:

$$\mathcal{H}_{single-e} \cdot \psi_{n\mathbf{k}}(\mathbf{r}) = \left[\frac{p^2}{2 \cdot m_0} + V(\mathbf{r}) + \frac{\hbar}{4 \cdot m_e^2 \cdot c^2} (\boldsymbol{\sigma} \times \boldsymbol{\nabla} \cdot \mathbf{V}) \cdot \mathbf{p} \right] \cdot \psi_{n\mathbf{k}}(\mathbf{r}) = E_n(\mathbf{k}) \cdot \psi_{n\mathbf{k}}(\mathbf{r}), \quad (2.5)$$

where \hbar is Plank's constant over 2π , c is the speed of light, $\boldsymbol{\sigma}$ sigma are the spin Pauli matrices, $\psi_{n\mathbf{k}}(\mathbf{r})$ are the eigenfunctions with a given momentum \mathbf{k} and band index n state, and $E_n(\mathbf{k})$ the energy of the eigenstates. The first term corresponds to the kinetic energy of the considered electron, and $V(\mathbf{r})$ is the screened crystalline potential. The third term, \mathcal{H}_{so} depicts the spin-orbit coupling, which is a relativistic effect resultant from the coupling between the electron spin and its orbital angular momentum. This term scales with the atomic number of the atom, and can be significant in semiconductors with heavy atoms, like InSb or CdTe. We have just seen that the crystal potential $V(\mathbf{r})$ presents many symmetry properties. For instance, due to this characteristic, $\mathcal{H}_{single-e}$ commutes with integer translations along the primitive unit cell vectors. We can then use the Bloch theorem and expand the eigenfunctions ψ_n into free electron plane waves enveloped by a periodic function:

$$\psi_{n\mathbf{k}}(\mathbf{r}) = u_{n\mathbf{k}}(\mathbf{r}) \cdot e^{i\mathbf{k} \cdot \mathbf{r}} \quad (2.6)$$

where $u_{n\mathbf{k}}(\mathbf{r})$ is a function with the same periodicity as the crystal potential, and \mathbf{k} are the momenta of the free electron plane waves. If \mathbf{R} is a vector obtained from a linear combination of the primitive vectors ($\mathbf{R} = n_1\mathbf{a}_1 + n_2\mathbf{a}_2 + n_3\mathbf{a}_3$, where n_i are integer numbers) then as $\psi_{n\mathbf{k}}(\mathbf{r} + \mathbf{R}) = \psi_{n\mathbf{k}}(\mathbf{r})$ and $u_{n\mathbf{k}}(\mathbf{r} + \mathbf{R}) = u_{n\mathbf{k}}(\mathbf{r})$:

$$e^{i\mathbf{k} \cdot (\mathbf{r} + \mathbf{R})} = e^{i\mathbf{k} \cdot \mathbf{r}} \quad (2.7)$$

If the crystal has a characteristic lateral size L , and a lattice parameter d (i.e., $L = Nd$, where N is the total number of atoms along the lateral direction of the crystal), then Eq. 2.7 imposes conditions on the allowed values of k :

$$k_i = \frac{2\pi \cdot n_i}{L} = \frac{2\pi \cdot n_i}{Nd} \quad (2.8)$$

where and k_i are the electronic wavevectors along the three spatial directions (x, y, z). Condition 2.8 quantizes the allowed eigenstates in the system, as n_i can only take the values $-N/2, -(N-1)/2, \dots, +N/2$. The momentum space states just enumerated are restricted to the first Brillouin zone in which k spans from $-\pi/a$ to π/a . However, due to the periodicity of the reciprocal lattice there is also an expression of the Bloch theorem in k space analogous to Eq. 2.7: the wavefunctions $\psi_{n\mathbf{k}}(\mathbf{r})$ are invariant under transformations of the form $\mathbf{k} \rightarrow \mathbf{k} + \mathbf{Q}$, where $\mathbf{Q} \equiv n_1\mathbf{b}_1 + n_2\mathbf{b}_2 + n_3\mathbf{b}_3$ [see Fig. 2.2(b)]. Usually all allowed wavevectors are represented in a reduced zone scheme which covers just the first Brillouin zone, with wavevectors represented as "folded" states [see Fig. 2.2(f)]. [301, 11]

The k -states are discretized with a separation given by $\Delta k = 2\pi/L$, which in a crystal of macroscopic size amounts to about 1 cm^{-1} , so small that states can be assumed to conform a continuum in most experiments and theoretical treatments. Such quasi-continuum of states gives rise to the characteristic bands of crystalline solids. The number of allowed states in a volume Ω in k space is given by $\frac{\Omega}{(2\pi/L)^3}$, or equivalently, the density of states (DOS ; the number of states per unit volume) in k space is given by:

$$g(\mathbf{k}) = \frac{L^3}{8\pi^3} \quad (2.9)$$

One of the most important consequences of the periodicity of the reciprocal lattice is the appearance of energy gaps for wavevector states close to the edges and center of the Brillouin zone. Even if the periodic potential $V(\mathbf{r})$ is very weak and it can be considered as a perturbation, the electron states with wavevectors close to \mathbf{Q} are subject to the so-called

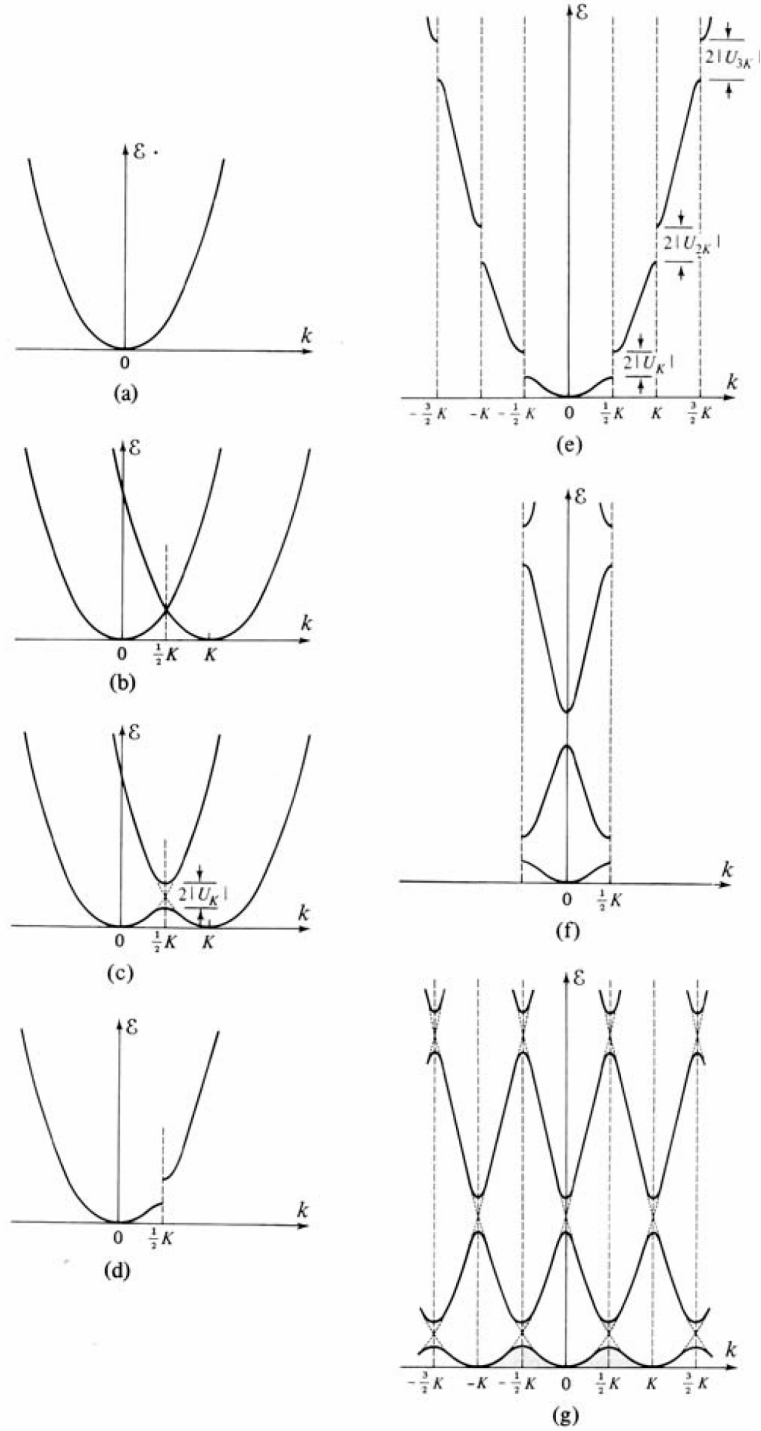


Figure 2.2: (a) Free electron dispersion in one dimension. (b) Dispersion relations separated by a reciprocal lattice wavevector (K), the first step in the construction of the band diagram of electrons in a weak periodic potential. (c) Same as (b) including the reflection effects at the edge of the Bragg plane. (d) Portions of (c) that belong to the original parabola centered at $k=0$. (e) Effect of all Bragg planes at integer multiples of the reciprocal lattice wavevectors. (f) Levels of (e) in a reduced-zone scheme. (g) Levels of (e) in a repeated-zone scheme. From Ref. [11].

Bragg reflections, as the momentum of these states cannot be unambiguously defined.[11] The direct consequence of this situation is the appearance of energy gaps in the quasi-free electron dispersion for such states, as depicted in Fig. 2.2(c)-(f). The magnitude of the gap in this approximation is given by the actual strength of the perturbation $V(\mathbf{r})$.

The simple arguments we have just described to find a first approximation to the solution of the electronic valence states in a crystal were just relying on the translation invariance of the system. Analogously to the use of these translational invariance, a careful account of the other above mentioned symmetry properties will constrain the actual shape of the possible wavefunctions and eigenenergies. However, the resolution of Eq. 2.5, even when considering these symmetry properties, requires a more profound approach and to take into account the precise shape of the periodic potential $V(\mathbf{r})$, which will eventually determine the band gaps and $u(\mathbf{r})$ in Eq. 2.6. For the case of zinc-blende type semiconductors, several theoretical approaches have been followed on this issue.[301] One of them is the pseudopotential method, that substitutes the real shape of $V(\mathbf{r})$, by a *pseudopotential* $V_{ps}(\mathbf{r})$ for each atom in the primitive cell. These *pseudopotentials* have strong oscillations near the ion cores and smooth variations in the outer shells, where the valence electrons lie, highly screened from the actual shape of the potential close to the cores. The pseudopotentials and the wavefunctions solution to Eq. 2.5 are expanded in series characterized by the so called *pseudopotential form factors*, which are determined in an iterative process by making use of empirical information or from first principles calculations accounting for many body effects.[301] Figure 2.3 shows the energy bands of Si and GaAs in the single electron approximation, which define the allowed energy states that are solution to Eq. 2.5 calculated by the pseudopotential method. Only the dispersions along the high symmetry directions Λ , Δ and Σ are shown. The actual shape of the bands calculated by the this method is qualitatively not far from the quasi-free electron situation depicted in Fig. 2.2. This is caused by the strong screening of the sea of valence electrons around the ions in the mean field approximation, which smooths and weakens the actual potential $V(\mathbf{r})$ felt by these electrons.

The valence electrons in semiconductors fill complete bands, thus conferring the insulating character to these materials at zero temperature. In Fig. 2.3 the highest occupied valence bands in Si and GaAs have been marked in red. The major difference between the two is that in the case of GaAs the momentum of the highest energy valence band states coincides (in the so-called *fundamental gap*) with that of the bottom of the first excited

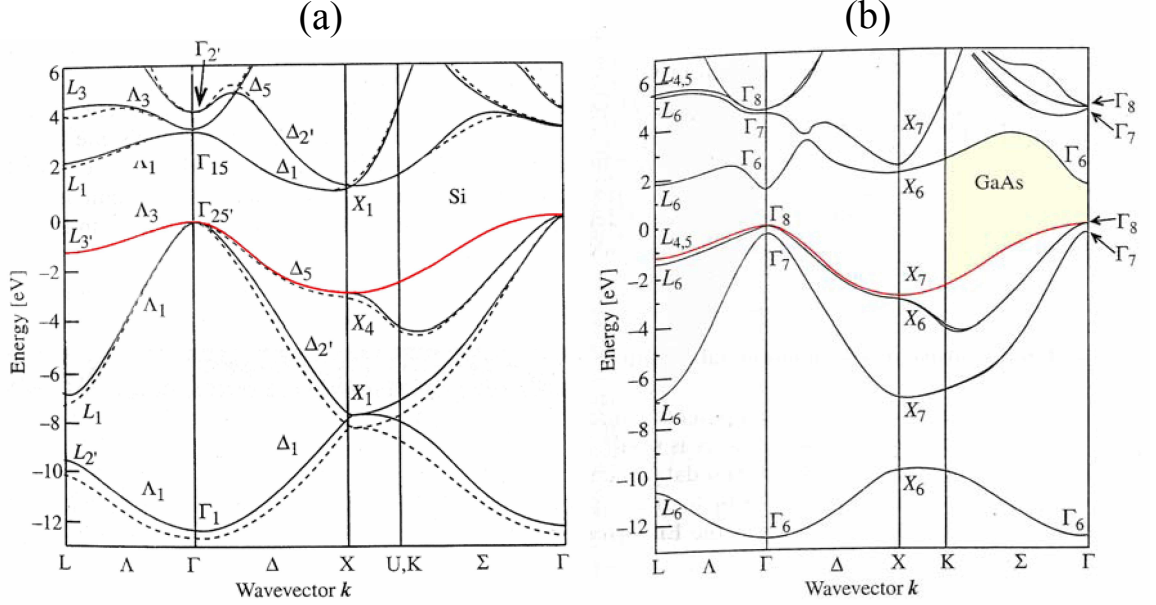


Figure 2.3: Energy bands of Si (a) and GaAs (b) calculated with the pseudopotential method. The red lines depict the highest occupied bands at *zero* temperature. From Ref. [301].

band, the so called *conduction band*, while in the case of Si these two points have different momenta. Attending to this property, GaAs is said to be a direct gap semiconductor, while Si is of the indirect type. This difference will have major implications in the light-matter coupling properties in these two materials, as exposed later.

Other methods to calculate the band structure in semiconductors are, for instance, the $\mathbf{k} \cdot \mathbf{p}$ method or the tight binding approach.[301] The first one makes direct use of the Bloch theorem (Eq. 2.6) and concentrates on finding the electron wavefunctions around the high symmetry points making use of perturbation theory. When Eq. 2.6 is substituted into Eq 2.5 we obtain an equation for the u_{nk} of the form (here we will not consider the \mathcal{H}_{so} term):

$$\left[\frac{p^2}{2 \cdot m_0} + \frac{\hbar \mathbf{k} \cdot \mathbf{p}}{m_0} + \frac{\hbar^2 k^2}{2 \cdot m_0} + V(\mathbf{r}) \right] \cdot u_{nk}(\mathbf{r}) = E_{nk} \cdot u_{nk}(\mathbf{r}), \quad (2.10)$$

which at $k = 0$ takes the form:

$$\left[\frac{p^2}{2 \cdot m_0} + V(\mathbf{r}) \right] \cdot u_{n0}(\mathbf{r}) = E_{n0} \cdot u_{n0}(\mathbf{r}). \quad (2.11)$$

The solutions to this equation are much easier to obtain than those to Eq. 2.5. Once the

eigenenergies and eigenfunctions at $k = 0$ have been obtained, the solutions to other k -states around the high symmetry points can be attained by standard perturbation theory. Assuming that E_{n0} lies at a band maximum or minimum, considering the k -terms in Eq. 2.10 as perturbations to the functions u_{n0} , a second order expansion in k gives:

$$u_{n\mathbf{k}} = u_{n\mathbf{0}} + \frac{\hbar}{m_0} \sum_{n' \neq n} \frac{\langle u_{n\mathbf{0}} | \mathbf{k} \cdot \mathbf{p} | u_{n'\mathbf{0}} \rangle}{E_{n\mathbf{0}} - E_{n'\mathbf{0}}} u_{n'\mathbf{0}}, \quad (2.12)$$

$$E_{n\mathbf{k}} = E_{n\mathbf{0}} + \frac{\hbar^2 k^2}{2 \cdot m_0} + \frac{\hbar^2}{m_0^2} \sum_{n' \neq n} \frac{|\langle u_{n\mathbf{0}} | \mathbf{k} \cdot \mathbf{p} | u_{n'\mathbf{0}} \rangle|^2}{E_{n\mathbf{0}} - E_{n'\mathbf{0}}}. \quad (2.13)$$

From Eq. 2.13 it is straightforward to define an effective mass m_n^* of the band n just by considering small values of k around $k = 0$:

$$E_{n\mathbf{k}} = E_{n\mathbf{0}} + \frac{\hbar^2 k^2}{2 \cdot m_n^*}, \quad (2.14)$$

where

$$\frac{1}{m_n^*} = \frac{1}{m_0} + \frac{2}{m_0^2 k^2} \sum_{n' \neq n} \frac{|\langle u_{n\mathbf{0}} | \mathbf{k} \cdot \mathbf{p} | u_{n'\mathbf{0}} \rangle|^2}{E_{n\mathbf{0}} - E_{n'\mathbf{0}}}. \quad (2.15)$$

The effective mass definition can be generalized, no matter the method for the band calculation, as:

$$\frac{1}{m_n^*} = \frac{1}{\hbar^2} \left(\frac{\partial^2 E}{\partial k^2} \right)^{-1}. \quad (2.16)$$

As the actual wavefunctions are obtained, the $\mathbf{k} \cdot \mathbf{p}$ method provides information on the matrix elements determining, for instance, optical phenomena. Thus, attending to the experimentally measured gaps and oscillator strengths of optical transitions, the wavefunctions around the high symmetry points can be accurately calculated and extended to the computation of the wavefunctions from over the entire Brillouin zone. An interesting characteristic of the $\mathbf{k} \cdot \mathbf{p}$ method is that it allows to follow how the momentum coupling between the states of different bands affects the curvature of those bands and the gaps between them, as can be directly observed in Eqs. 2.12 and 2.13.

The second mentioned method, the tight binding approach, is conceptually opposite to the $\mathbf{k} \cdot \mathbf{p}$. It starts by considering the atoms conforming the crystal as isolated (i.e., infinitely far apart). When the atoms are brought together the atomic orbitals start to

overlap and extended states are formed. In this approach the electronic states are described as linear combinations of the atomic orbitals, which have then to be diagonalized accounting for the interaction energy of the overlapping orbitals with neighboring atoms. In this way, the valence orbitals develop into bands, and the interactions open up energy gaps. Again, the coupling between different shells and orbitals influences the curvature of the bands.

From the band calculations, using the above mentioned methods, we can learn some qualitative features of the band structure. In particular, the $\mathbf{k} \cdot \mathbf{p}$ and tight binding methods provide very valuable information on the origin of the symmetry and angular momentum of the bands and their connection to the atomic valence orbitals. From now on we will restrict our analysis to the case of direct gap zinc-blender type semiconductors, like GaAs. In this case, the highest energy filled band [marked in red in Fig. 2.3(b)] originates from p -type atomic valence orbitals. This band, which we will refer to as the *valence band*, possesses a bonding character, with orbital angular momentum 1, inherited from its p -type origin. On the same grounds, the lowest energy empty band, which we will refer to as the *conduction band*, originates from s -type valence orbitals and has an antibonding character, with *zero* orbital angular momentum. The capital Greek letters and subindexes in Fig. 2.3 depict the symmetry characteristics of the wavefunctions, which are directly related to the angular momentum of the wavefunctions, with the notation of group theory.

So far we have not considered the spin of the electrons, except when we introduced the spin-orbit coupling term in Eq. 2.5. The effect of the spin of the electrons must be accounted in order to obtain the proper degeneracy of the bands as well as their total angular momentum, which will be of great importance when determining the selection rules for optical transitions. The conduction band near the fundamental gap (Γ point) has an orbital angular momentum of *zero*, with a wavefunction analogous to the $|s\rangle$ atomic wavefunction. Thus the composition of the *zero* orbital momentum with a spin $S = 1/2$ results in a band with total angular momentum $J_{cond} = 1/2$.¹ For the wavefunctions corresponding to these states \mathcal{H}_{so} is *zero* in first approximation and the only effect of the electron spin is to set the degeneracy (Kramers) of the band to two-fold, with the third component of the total angular momentum $J_{cond}^z = +1/2, -1/2$. We can thus label the conduction band wavefunctions at $k = 0$ as:

¹When we speak of total angular momentum we are referring to the operator \hat{J}^2 , with eigenvalues $\hbar J(J+1)$. From now on we will refer to the angular momentum operators by the value of J .

$$|u_{c,0}^{\uparrow}\rangle \equiv \left|\frac{1}{2}, \frac{1}{2}\right\rangle = |s, \uparrow\rangle, \quad (2.17)$$

$$|u_{c,0}^{\downarrow}\rangle \equiv \left|\frac{1}{2}, -\frac{1}{2}\right\rangle = |s, \downarrow\rangle \quad (2.18)$$

where \uparrow (\downarrow) indicates the magnitude of the third component of the spin S^z (which in this case coincides with J_{cond}^z).

The situation for the valence band in terms of the total angular momentum is much more complicated. Let us again initially restrict ourselves to the case of the *zero* linear-momentum states ($k = 0$) at the top of the valence band. Before introducing the electronic spin in the picture, let us recall that these states have a *p*-type origin with angular momentum $L = 1$. Thus, attending to orbital angular momentum this states are three-fold degenerate ($L^z = +1, 0, -1$) and their wavefunctions, by analogy with the *p*-shell atomic wavefunctions, can be labeled as $|x\rangle, |y\rangle, |z\rangle$. [52] With this nomenclature, the eigenstates of the orbital angular momentum L are ($|L, L^z\rangle$):

$$|1, 1\rangle = -\frac{1}{\sqrt{2}} (|x\rangle + i|y\rangle), \quad (2.19)$$

$$|1, 0\rangle = |z\rangle, \quad (2.20)$$

$$|1, -1\rangle = \frac{1}{\sqrt{2}} (|x\rangle - i|y\rangle). \quad (2.21)$$

We now introduce the spin of the electrons. The composition of the $L = 1$ orbital angular momentum with $S = 1/2$ results in states with total angular momenta $J = 3/2$ and $J = 1/2$. From the Clebsch-Gordan coefficients for the composition of angular momenta, the eigenstates of the total angular momentum \hat{J} can be written as ($|J, J^z\rangle$): [76]

$$|u_{hh,0}^{\uparrow}\rangle \equiv \left|\frac{3}{2}, \frac{3}{2}\right\rangle = -\frac{1}{\sqrt{2}} (|x, \uparrow\rangle + i|y, \uparrow\rangle) \quad (2.22)$$

$$|u_{lh,0}^{\uparrow}\rangle \equiv \left|\frac{3}{2}, \frac{1}{2}\right\rangle = -\frac{1}{\sqrt{6}} (|x, \downarrow\rangle + i|y, \downarrow\rangle) + \sqrt{\frac{2}{3}} |z, \uparrow\rangle \quad (2.23)$$

$$|u_{lh,0}^{\downarrow}\rangle \equiv \left|\frac{3}{2}, -\frac{1}{2}\right\rangle = \frac{1}{\sqrt{6}} (|x, \uparrow\rangle - i|y, \uparrow\rangle) + \sqrt{\frac{2}{3}} |z, \downarrow\rangle \quad (2.24)$$

$$|u_{hh,0}^\downarrow\rangle \equiv \left|\frac{3}{2}, -\frac{3}{2}\right\rangle = \frac{1}{\sqrt{2}} (|x, \downarrow\rangle - i|y, \downarrow\rangle) \quad (2.25)$$

$$|u_{so,0}^\uparrow\rangle \equiv \left|\frac{1}{2}, \frac{1}{2}\right\rangle = \frac{1}{\sqrt{3}} |z, \uparrow\rangle + \frac{1}{\sqrt{3}} (|x, \downarrow\rangle + i|y, \downarrow\rangle) \quad (2.26)$$

$$|u_{so,0}^\downarrow\rangle \equiv \left|\frac{1}{2}, -\frac{1}{2}\right\rangle = \frac{1}{\sqrt{3}} |z, \downarrow\rangle - \frac{1}{\sqrt{3}} (|x, \uparrow\rangle - i|y, \uparrow\rangle), \quad (2.27)$$

We have labeled the states according to the name of the valence bands to which they give rise when we consider the dispersions outside $k = 0$ (hh : heavy-hole band, lh : light-hole band, so : split-off band). We can extract two very important consequences from the description of the wavefunctions attending to the total angular momentum: (i) the total angular momentum of these states is a well defined quantity (i.e., a good quantum number),² and (ii) the $J = 3/2$ are four-fold degenerate and the $J = 1/2$ are two-fold. Note that \mathcal{H}_{so} in Eq. 2.5 splits the $J = 3/2$ from the $J = 1/2$ states by the so called spin-orbit splitting (δE_{so}). In Fig. 2.3(b), for GaAs the $J = 3/2$ valence band states are denoted by Γ_8 at the Γ point and the $J = 1/2$ by Γ_7 , and a splitting can be appreciated. In GaAs δE_{so} amounts to 0.34 eV at room temperature. As we mentioned earlier, this relativistic effect is stronger as the atomic number of the constituents atoms increases, values of δE_{so} for increasingly heavier binary compounds[301] are 0.75 eV for GaSb, 0.81 eV for InSb, and 0.93 eV for ZnTe. Lighter binary compounds like GaN or diamond show δE_{so} of 0.017 eV and 0.044 eV, respectively.

2.1.3 Valence band mixing

In the previous discussion we have seen that the valence band states with *zero* momentum at the Γ point present a well defined angular momentum (see footnote 2). When we consider states with $k \neq 0$, the $J^z = \pm 3/2$ states at $k = 0$ [Eqs. 2.22-2.25] give rise to the so called heavy-hole band, while the $J^z = \pm 1/2$ states [Eqs. 2.23-2.24] give rise to the so called light-hole bands (the origin of the names lies on the different curvatures of each band). However, as already mentioned, the $\mathbf{k} \cdot \mathbf{p}$ terms of the Hamiltonian 2.10 mix the wavefunctions of the different valence orbitals with well defined angular momentum when giving rise to the band states with $k \neq 0$. This can be clearly seen in the sum terms of

²In order to arrive to this conclusion, several approximations were made. If the full Hamiltonian is considered, it can be shown that even restricting our analysis to $k = 0$ the valence band states are not eigenstates of \hat{J}^z . The reason for this is that the zinc-blende crystal lacks inversion symmetry, as will be discussed in Sec. 2.1.3.

Eqs. 2.12 and 2.13. While the total angular momentum of the band states at $k = 0$ can be well defined, the $k \neq 0$ states do not present a well defined third component of the angular momentum J^z . The mixing effect is more important as the considered value of k increases and the considered band is closer to another band [Eq. 2.12]. Therefore this effect can be very important for the heavy- and light-hole bands, which actually lie very close together (they are degenerate at $k = 0$). In this work, we will restrict the experiments and analysis to states close enough to the $k = 0$, Γ point for the wavefunction valence-band mixing to be important, and therefore they can be neglected.

Let us mention that in reduced dimensionality systems, such as QWs, confinement induces the splitting of the valence band states, and the mixing effects, though still present, are greatly reduced at $k = 0$.

Another effect worth mentioning, which is not directly related to the valence-band mixing but affects the angular momentum properties of the system, is the aforementioned *bulk inversion asymmetry*. This effect arises from the lack of inversion symmetry in zinc-blende crystals and results in the appearance of spin-dependent terms in the Hamiltonian 2.10. The most important consequence is the momentum splitting of the conduction band,[40] i.e. electrons with the same wavevector but opposite spin have slightly different energies. However this effect is very small compared to the linewidths and scales considered here and will be neglected, except in Chapter 6, where we will see that it is relevant when considering the electron spin-flip mechanisms.

2.1.4 Parabolic band approximation

Although the precise shapes of the conduction and valence bands may be very complicated, in particular for large k values, many properties of semiconductors can be well characterized, and understood, considering only small momenta states around the fundamental gap (Γ point in GaAs). As seen in Fig. 2.3 the curvature of the bands at this point are pretty constant. Therefore it is convenient to approximate the band shapes as parabolic bands around the fundamental gap, as it was already introduced in Eqs. 2.14, 2.15 and 2.16 in the framework of the $\mathbf{k} \cdot \mathbf{p}$ method. Inherent to this approximation is the definition of effective masses for the bands. We can generalize Eqs. 2.14 by considering different curvatures along different momentum directions[11]:

$$E_{n\mathbf{k}} = E_{n\mathbf{0}} + \frac{\hbar^2}{2} \sum_{i,j} k_i \frac{1}{\mu_n^{ij}} k_j \quad (2.28)$$

where i, j denote the three spatial components of the considered \mathbf{k} -vector and μ_n^{ij} is an effective mass tensor. Fig. 2.4(a) shows the conduction band Γ_6 , the heavy-hole (hh) and light-hole (lh) Γ_8 bands as well as the Γ_7 split-off band in a given direction. We will restrict our analysis to these three bands as all our studies will concentrate on excitations with energy close to the fundamental gap. Despite the fact that the valence bands show negative curvature, which according to Eq. 2.16 would result in negative effective masses, we will always regard the valence band effective masses as positive, as we will consider the hole picture of excitations in this band (see Sec. 2.2). Let us note that in this picture the angular momentum (J) and spin of holes is also opposite to that in the electron picture.

Figure 2.4(b) depicts constant energy surfaces of the hh and lh bands in a zinc-blende type semiconductor calculated by the $\mathbf{k} \cdot \mathbf{p}$ method.[301] Considering that these isoenergy lines collapse into one point at the band maximum, it is easy to see that different band curvatures exist along different directions. In particular, dispersions along the (010) and (100) directions present a so-called *warped* structure, due to the cubic symmetry of zinc-blende crystals.

An additional and convenient approximation is to consider the band structure as having spherical symmetry. In this way the tensor μ_n^{ij} reduces to a mean effective energy mass m_n^* for each band n . This is the approximation we will consider from now on, unless stated otherwise. Table 2.1 summarizes some effective masses of interest and band gaps of some relevant semiconductors.

Even though the spherical band approximation is commonly accepted, let us point out that around the Γ point the real curvatures of the heavy and light conduction bands present strong anisotropies when considering different momentum directions. In particular along a given direction x [100] the heavy-hole band is certainly “heavy” (small curvature) and the light-hole band is “light” (large curvature) while along the perpendicular direction (within the yz plane) the heavy-hole band becomes “light” and the light-hole band becomes “heavy”. This effect is known as the *mass reversal effect* which is particularly well accounted when calculating the bands within the Luttinger Hamiltonian, and has been profusely studied in two dimensional systems.[24, 86, 129] In bulk systems, this effect indirectly appears in the band calculations along different high symmetry directions,[91, 102, 40] but it is rarely shown

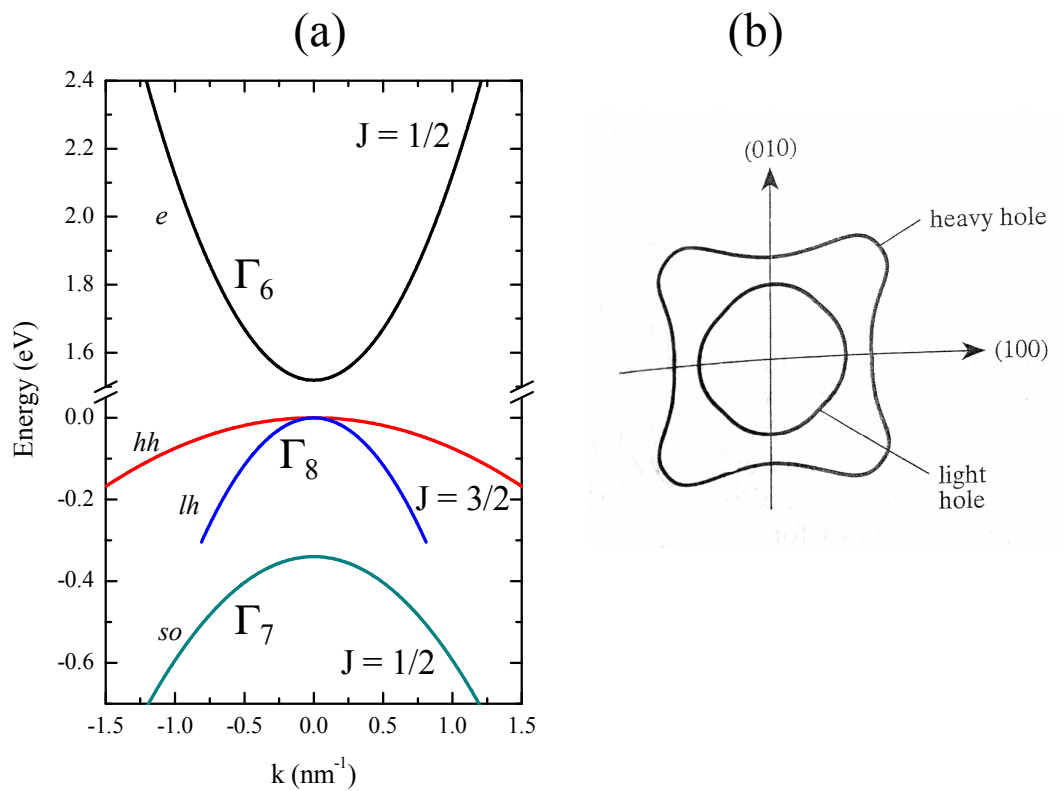


Figure 2.4: (a) Conduction and valence band dispersions of GaAs in the effective mass spherical approximation. (b) *Warping* of the heavy- and light-hole bands shown on two constant energy surfaces in the (010-100) plane; from Ref. [301].

	Fund. gap (eV)	δE_{so} (eV)	m_{cond}^*	m_{hh}^*	m_{lh}^*	m_{so}^*
Si	1.12	0.044	0.36	0.49	0.16	0.24
GaAs	1.519	0.34	0.063	0.51	0.082	0.15
CdTe	1.60	1.06*	0.096	1.38	-	-

Table 2.1: Fundamental gap energies, δE_{so} , and the effective masses (in units of the free electron mass) for Si at 300 K and GaAs [Ref. [122]] and CdTe [Ref. [104]] at 4 K along the Δ ($\Gamma \rightarrow X$, [100]) direction in reciprocal space. *Ref. [295].

explicitly when the valence band masses are calculated. In any case, when the bands are averaged in three dimensions it is found that the mean effective mass of the heavy and light bands is very similar.[8, 296] For this reason, we will consider just a mean hole effective mass m_h^* when treating excitons in bulk systems in Sec. 2.2.1, following the Baldereschi-Lipari theory in spherical approximation.[19, 20]

2.1.5 Density of States

Equation 2.9 evaluates the density of states in momentum space. It is sometimes convenient to express the density of states of a band in energy space (DOS), $g(E) d(E)$, defined as the number of one-electron levels in the energy range from E to $E + d(E)$. [11] If $f(\mathbf{k})$ determines the occupation distribution of a band, the total number of electrons in that band per unit volume would be:

$$N = \frac{1}{vol} \int g(\mathbf{k}) f(\mathbf{k}) d\mathbf{k} = \frac{1}{vol} \int_0^\infty 4\pi k^2 g(k) f(k) dk, \quad (2.29)$$

or:

$$N = \frac{1}{vol} \int_0^\infty g(E) f(\mathbf{k}(E)) dE, \quad (2.30)$$

where we have considered that the band presents no degeneracy, $g(\mathbf{k})$ is isotropic in momentum space and $f(\mathbf{k}) = f(k)$. Considering the DOS obtained in Eq. 2.9 and the effective mass approximation in spherical bands, by equating the right hand side of Eqs. 2.29 and 2.30 we obtain:

$$g(E) = \frac{(m_n^*)^{3/2}}{\sqrt{2}\hbar^3\pi^2} \sqrt{E} \quad (2.31)$$

A general expression for $g(E)$ can be obtained attending to the number of allowed states that fit within a given volume in k space. Attending to these basis, for a generic

energy dispersion function $E(\mathbf{k})$, $g(E)$ can be expressed as:

$$g(E) = \frac{1}{16\pi^3} \int \frac{dS_{\mathbf{k}}}{|\nabla E(\mathbf{k})|}, \quad (2.32)$$

where $S_{\mathbf{k}}$ is a constant energy surface. The *DOS* will be used to calculate the light absorption spectrum of direct gap semiconductors.

2.2 Band excitations: electrons, holes and excitons

In a semiconductor at *zero* temperature the valence bands are completely filled with electrons, while the conduction band is completely empty. This is the ground state of the system. The fundamental excitation consists on the promotion of an electron from the top of the valence band to the bottom of the conduction band. In this way all the valence band states except one remain occupied. It is convenient to picture this empty state as a positive charge in an empty valence band. This is the definition of *hole*, and its description as a positive charge enables us to consider the valence band masses as positive in all practical calculations, despite the fact that from the single electron picture they have negative curvature [See Fig. 2.4 and Eq. 2.16].

In intrinsic semiconductors (undoped), like those treated here, each electron excited in the conduction band leaves a hole in the valence band. We will only consider light excitations, in which each photon arriving at the sample with energy greater than the bandgap has a finite probability of creating an electron-hole pair, as we will treat later. However, other type of excitations are possible, like electrical injection of electron irradiation.

The excited electrons and holes in the bands conform an out of equilibrium system which will gradually tend to the ground state situation by radiative (in particular in direct gap semiconductors of high crystalline quality) and non-radiative processes. Nonetheless, as long as excited carriers populate the conduction and valence bands, electrons and holes tend to form thermalized distributions.[62, 225, 54] At low excitation densities, the low occupation of the band states allows to use Maxwell-Boltzmann statistics ($f_{MB}^n(E)$) to describe the carrier distributions in their respective bands, however, at high densities, Fermi-Dirac occupation functions ($f_{FD}^n(E)$) should instead be used:

$$f_{MB}^n(E) = \rho_n \left(\frac{2\pi\hbar^2}{m_n^* k_B T} \right)^{3/2} e^{-\frac{E}{k_B T}}, \quad (2.33)$$

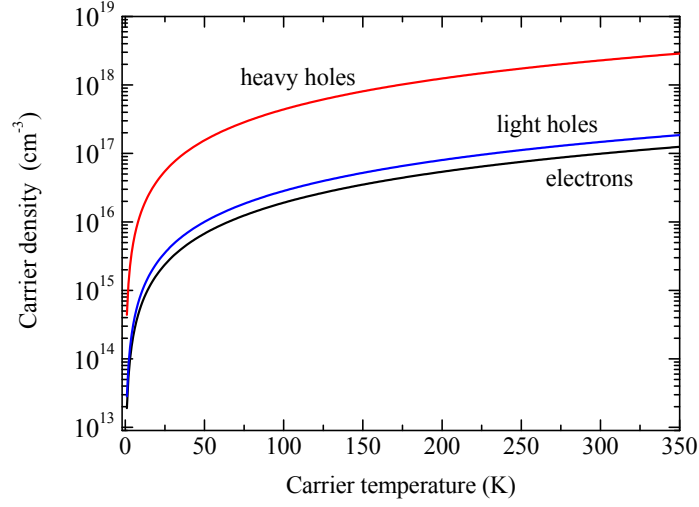


Figure 2.5: Carrier density in the conduction (black), light-hole (blue) and heavy-hole (red) bands in GaAs at which an occupation of 0.5 at $E = 0$ is attained following $f_{MB}^n(E)$.

$$f_{FD}^n(E) = \frac{1}{\left(e^{\frac{E}{k_B T} - \mu}\right) + 1}, \quad (2.34)$$

where ρ_n is the density of carriers in the n^{th} band, T is the temperature of the carriers, k_B is Boltzmann's constant, and μ is the chemical potential obtained in each case from the normalization condition $\rho_n = \int g_n(E) f_{FD}^n(E) dE$. At low densities $f_{MB}^n(E)$ presents the same shape as the truly fermionic distribution $f_{FD}^n(E)$, with the advantage of being much easier to manage in calculations. We can arbitrarily set a boundary in the use of Eqs. 2.33 and 2.34. At a given temperature, for densities up to an occupation of 0.5 at $E = 0$ we will keep using $f_{MB}^n(E)$, while for higher densities we will go back to $f_{FD}^n(E)$. Figure 2.5 shows the density at which an occupation of 0.5 is attained at $E = 0$, according to $f_{MB}^n(E)$, as a function of the carrier temperature for carriers in the conduction and valence bands in GaAs.

2.2.1 Excitons

Negatively charged electrons in the conduction band and positively charged holes in the valence band are subject to Coulomb attraction. This electron-hole interaction gives rise to bound states, called excitons. In semiconductors with the morphologies we are considering the electron-hole interaction is highly screened by the sea of non-excited electrons in the

valence band. In this case the net wavefunctions of the bound electron and hole are extended over several crystal unit cells, and the states are regarded as Wannier-Mott excitons. This situation is opposed to that found in ionic crystals, in which electrons and holes are strongly bound together and their wavefunctions localized in the same or nearest unit cell. In this case excitons are said to be of the Frenkel type.

To model the excitons within the effective mass approximation, let us just consider that we have in the crystal an excited electron with momentum \mathbf{k}_e and a hole with momentum \mathbf{k}_h . The time independent Schrödinger equation would be in this case:

$$\left(\frac{p_e^2}{2m_e^*} + \frac{p_h^2}{2m_h^*} + \frac{e^2}{\epsilon |\mathbf{r}_e - \mathbf{r}_h|} \right) \psi(\mathbf{r}_e, \mathbf{r}_h) = (E - E_{gap}) \psi(\mathbf{r}_e, \mathbf{r}_h) \quad (2.35)$$

where p_e (p_h) and $m_{e(h)}^*$ are, respectively, the momentum and effective mass of the electron (hole), \mathbf{r}_e and \mathbf{r}_h are the electron and hole positions, E_{gap} is the semiconductor fundamental gap, and ϵ is the dielectric function of the material. In the case of the mass of the hole, in Eq. 2.35 we have considered a mean hole mass m_h^* as discussed in Sec. 2.1.4 as a results of the spherical band approximation.

In the considered picture of a single electron-hole pair excitation, the effect of the rest of the valence electrons present in the crystal is accounted by the effective mass approximation and by the dielectric constant, that includes the background interaction with those electrons, and results in an effective screening of the electron-hole Coulomb interaction. Notice that Eq. 2.35 is analogous to that describing the hydrogen atom in atomic physics. As the Coulomb interaction depends only on the relative distance between the electron and the hole, it is convenient to define a new set of coordinates given by the position of the center of mass of the electron and hole (\mathbf{R}) and its relative distance (\mathbf{r}):

$$\mathbf{R} = \frac{m_e^* \mathbf{r}_e + m_h^* \mathbf{r}_h}{m_e^* + m_h^*}, \quad \mathbf{r} = \mathbf{r}_e - \mathbf{r}_h. \quad (2.36)$$

With that change of variables, Eq. 2.35 becomes:

$$\left(\frac{P^2}{2(m_e^* + m_h^*)} + \frac{p^2}{2\mu_{eh}} + \frac{e^2}{\epsilon r} \right) \psi(\mathbf{R}, \mathbf{r}) = (E - E_{gap}) \psi(\mathbf{R}, \mathbf{r}), \quad (2.37)$$

where $P = -i\hbar\nabla_{\mathbf{R}}$, $p = -i\hbar\nabla_{\mathbf{r}}$ and $\mu_{eh}^{-1} = (m_e^*)^{-1} + (m_h^*)^{-1}$ is the reduced mass of the electron-hole pair. The solutions to 2.37 can be factorized into $\psi(\mathbf{R}, \mathbf{r}) = \varphi(\mathbf{R}) \vartheta(\mathbf{r})$. The equation corresponding to $\varphi(\mathbf{R})$ corresponds to that of a free particle of mass $m_e^* + m_h^*$, while

that corresponding to $\vartheta(\mathbf{r})$ is the well known hydrogen atom equation whose solutions are the product of Laguerre polynomials $[L_{nl}(r)]$ and spherical harmonic functions $[Y_{lm}(\theta, \phi)]$ with the eigenenergies given by:

$$E_n^r = -\frac{E_b}{n^2}, \quad n = 1, 2, 3, \dots \quad E_b = \frac{\mu_{eh}e^2}{2\epsilon^2\hbar^2}. \quad (2.38)$$

Therefore, the total energy and eigenfunctions of the exciton are:

$$E_{nlm} = E_{gap} + \frac{\hbar^2 K^2}{2(m_e^* + m_h^*)} - \frac{E_b}{n^2}, \quad (2.39)$$

$$\psi_{nlm}(\mathbf{R}, \mathbf{r}) = e^{i\mathbf{K}\cdot\mathbf{R}} L_{nl}(r) Y_{lm}(\theta, \phi), \quad (2.40)$$

where n, l, m are the principal, angular and magnetic quantum numbers, respectively, \mathbf{K} is the exciton center of mass momentum and E_b is the binding energy. The exciton ground state at rest is given by the $n = 1, l = 0, m = 0$ wavefunction with $\mathbf{K} = 0$:

$$\psi_{100}(\mathbf{R}, \mathbf{r}) = \frac{2}{\sqrt{a_B^3}} e^{-r/a_B}, \quad (2.41)$$

where $a_B = \hbar^2\epsilon/\mu_{eh}e^2$ is the exciton Bohr radius and characterizes the spatial extension of the excitonic complex. In GaAs the heavy-hole exciton (formed from the binding of a conduction electron and a heavy-hole) has a Bohr radius at low temperature of 11.4 nm, while its binding energy is of 4.2 meV, four orders of magnitude smaller than the binding energy of an electron to a proton in the hydrogen atom. If the exciton is formed from the binding of an electron with a light-hole we will refer to it as a light-hole exciton. Note that so far we have considered just a mean hole mass for the excitons. This would mean that both heavy- and light-hole excitons have the same binding energy and Bohr radius. Nonetheless we can still distinguish and describe them independently because each hole-type wavefunction has different angular momenta. When we reduce the dimensionality of the system, the breakdown of the symmetry will result in the inhibition of the *mass reversal effect* and heavy- and light-hole excitons will present different reduced masses and binding energies (see Sec. 3.1.1).

Equations 2.39 and 2.40 tell us some important properties of the excitons. One of them is that excitons can move freely within the crystal. Nonetheless, interaction with the lattice excitations, with crystal defects and with carriers and other excitons will result

J^z	hh +3/2	hh -3/2	lh +1/2	lh -1/2
+1/2	$ +2\rangle$	$ -1\rangle$	$ +1\rangle$	$ 0\rangle$
-1/2	$ +1\rangle$	$ -2\rangle$	$ 0\rangle$	$ -1\rangle$

Table 2.2: Exciton spin state as a function of the third component of the total angular momentum of its constituent electron (left column) and hole (top row).

in dissipation. We can also see that the ground state energy of the exciton (before the constituent electron and hole pairs recombine) is located at an energy E_b below the band gap energy, and that the exciton possesses its own parabolic band. Therefore, the fundamental excitation in the system is not conformed by an electron and a hole at their band edges, but by the formation of a $1s$ exciton at rest.

So far we have not considered the spin of the excitons. As we have seen in the previous sections, the constituent particles of the exciton may have a well defined total angular momentum. For the sake of simplicity, given the complicated band mixing effects in the heavy and light hole bands far from the $k = 0$ states, let's restrict the analysis to excitons formed from electrons and holes with $k = 0$. In this case both particles have a well defined total (J) and third component (J^z) of the angular momentum, as depicted in Eqs. 2.22-2.25. The resulting exciton will also have a well defined total and third component of the angular momentum (J_X, J_X^z). From now on we will refer to J_X^z as the spin of the exciton. Table 2.2 presents all the possible spin states of excitons formed from the binding of an electron with a heavy or a light hole. Excitons with $J_X^z = 0, 1, 2$ can be formed, however, as we will describe later, only excitons with $J_X^z = 1, 0$ can couple to light due to momentum conservation rules.

Note also that though the exciton is conformed by two fermions, an electron and a hole, its total angular momentum is integer. For this reason, in the dilute limit regime, in which interexcitonic interaction and screening is not very important, excitons can be described as bosons. Particles of this kind, whose constituents are fermionic but follow bosonic statistics are referred to as “composite bosons”. Therefore, excitonic interactions are well described by bosonic operators, and such an approach is widely used when treating the photon-exciton interaction in the strong coupling regime (see Sec. 3.2.2). However, there have been some recent theoretical proposals which stress the importance of the fermionic composite nature of excitons even in the dilute regime.[60, 59, 58]

2.2.2 Many body effects

The description we have followed so far made use of the single electron picture, in which the system Hamiltonian 2.5 accounted for the average effect of the sea of valence electrons on a particular electron. Moreover, it assumed that all electrons were in the ground state of the system, i.e., fully occupying the valence band. Under these conditions the band diagrams depicted in Fig. 2.3 and the associated effective masses near the Γ point were calculated. If we create one excitation in the system, for instance, an exciton, the situation remains pretty much the same, with the same band gaps, effective masses and dielectric constants characterizing the material. However, when many electrons are promoted from the valence to the conduction band the situation starts to differ significantly from the one electron picture. Under these circumstances large populations of excited electrons and holes with spread momentum distributions can freely move and interact. If the densities are high enough so as to overcome the degeneration limit defined in Fig. 2.5, a first correction to the energy of the system with respect to the single electron picture would come from the antisymmetrization of the fermionic total electron and hole wavefunctions, in a Hartree-Fock approach. On the same grounds, Coulomb correlation effects, and the carrier screening associated to them, are very much affected by the wide spread in momentum of the carriers. These problems have been thoroughly treated theoretically in the literature.[105, 308, 280] One of the direct consequences of the many-body effects is the change of the band gaps. In particular, the increase in the screening of the system caused by the excited carriers results in the reduction of the fundamental gap. Also the effective masses are affected and even exotic spin-dependent phenomena has recently been predicted in this regime.[303] Interactions of the carrier ensembles are affected too, and the rate of exchange of energy between the excited electrons and holes and the lattice (carrier-phonon interaction) is altered.

As for the excitons, the increase in the carrier screening at high densities when both excitons and electron-hole plasma are present, results in a net change (an increase) of the dielectric constant ϵ that describes the surrounding excitonic media in Eqs. 2.39 and 2.40. Thus, the exciton binding energy gets progressively reduced with the increase of carrier density, and eventually excitons dissociate, as will be thoroughly discussed in Sec. 5.4.

An estimation of the density of these effects to be significant might be given by the degeneration threshold defined in Fig. 2.5.

2.3 Optical transitions

2.3.1 Electron-hole pair transitions

We have already mentioned that the promotion of electrons from the valence to the conduction band can be carried out by optical excitation. To analyze this process in some detail we will again consider the ground state of the system, in which the conduction band is completely filled with electrons. We will follow a quantum microscopic approach to the light absorption and emission. However, semiclassical approaches via the calculation of the dielectric functions near the optical transitions would yield analogous results.[301] The optical transitions in a semiconductor are directly determined by two very important momentum selection rules:

- Linear momentum in the absorption process³ must be conserved:

$$\mathbf{k}_\gamma = \mathbf{k}_i + \mathbf{k}_f \quad (2.42)$$

where \mathbf{k}_i and \mathbf{k}_f are the initial and final states of the considered excited electron (typically a state in the valence band and a state in the conduction band, respectively), and \mathbf{k}_γ is the momentum of the incident photon. As this momentum is very small compared to the typical carrier momenta in usual absorption experiments, Eq. 2.42 implies that only vertical transitions in the band diagram [Fig. 2.4(a)] are allowed. Therefore, the optically allowed transitions impose $\mathbf{k}_i \approx -\mathbf{k}_f$.

- Angular momentum in the absorption process must be conserved. This rule will impose polarization selection rules in the optical transitions as it will be analyzed below.

In order to include the light-matter interaction in the problem we should go back to the one electron Hamiltonian [Eq. 2.5] and substitute the momentum operator \mathbf{p} by $\mathbf{p} + \frac{e}{c}\mathbf{A}$, where \mathbf{A} is the vector potential of the incident beam:

$$\left[\frac{1}{2 \cdot m_0} \left(\mathbf{p} + \frac{e}{c}\mathbf{A} \right)^2 + V(\mathbf{r}) \right] \cdot \psi'_{n\mathbf{k}}(\mathbf{r}) = E_n(\mathbf{k}) \cdot \psi'_{n\mathbf{k}}(\mathbf{r}), \quad (2.43)$$

where we have neglected the spin-orbit coupling. To calculate the transition probabilities we do not need to solve the complete Hamiltonian 2.43. We can treat the applied optical field as

³Here we will make explicit reference to the absorption processes, but the same considerations apply to the emission.

a perturbation to the system. Keeping only the linear terms in the vector potential, selecting the appropriate gauge and considering the electric dipole approximation, the perturbation introduced by the light field can be introduced as an effective Hamiltonian $\mathcal{H}_{dip} = -e\mathbf{r} \cdot \mathbf{F}$, where \mathbf{F} is the amplitude and polarization of the excitation coherent electric field. Now we can apply Fermi's Golden rule to obtain the probability P_{vc} for the optically induced transition of an electron from the valence to the conduction band per unit time:

$$P_{cv} = \frac{2\pi}{\hbar} \sum_{\mathbf{k}} |\langle u_{c,\mathbf{k}} | \mathcal{H}_{dip} | u_{h,\mathbf{k}} \rangle|^2 \delta(E_c(\mathbf{k}) - E_v(\mathbf{k}) - \hbar\omega) \quad (2.44)$$

where $u_{c,\mathbf{k}}$ and $u_{h,\mathbf{k}}$ are the conduction and corresponding hole band wavefunctions as defined in 2.17, 2.18 and 2.22-2.25, and $\hbar\omega$ is the energy of the considered electromagnetic field (either excitation or emission field).

In order to calculate P_{cv} , we need to obtain the electric dipole matrix elements $\langle u_{c,\mathbf{k}} | \mathbf{r} \cdot \mathbf{F} | u_{h,\mathbf{k}} \rangle$. For this purpose it is convenient to expand the conduction and valence wavefunctions in terms of the $|s\rangle$, $|x\rangle$, $|y\rangle$, $|z\rangle$ wavefunctions as in Eqs. 2.17-2.25. Let us point out that given the symmetry properties of the wavefunctions and the position operator, the only matrix elements of the $\hat{\mathbf{r}}$ operator are:[52]

$$\langle s | r_x | x \rangle = \langle s | r_y | y \rangle = \langle s | r_z | z \rangle \equiv im_0\Pi, \quad (2.45)$$

where r_z can be chosen as the direction of propagation of light. Additionally, the spin part of the wavefunctions are not r dependent and keep the usual orthogonality properties. Recall that we are working in the electron-hole picture, in which the spin orthogonality is given by: $(\langle \uparrow_e | \downarrow_h \rangle = 1, \langle \uparrow_e | \uparrow_h \rangle = \langle \downarrow_e | \downarrow_h \rangle = 0)$, where e (h) indicates the electron (hole) spin. With these considerations, the allowed transitions and their relative strengths can be explicitly obtained.[186] If we restrict to the $k = 0$ states, the probability amplitudes for the transition from the heavy-hole to the conduction band are:

$$\langle u_{c,0}^\downarrow | \mathbf{r} \cdot \mathbf{F} | u_{hh,0}^\uparrow \rangle = \frac{-1}{\sqrt{2}} [\langle s, \downarrow | r_x F_x | x, \uparrow \rangle + i \langle s, \downarrow | r_y F_y | y, \uparrow \rangle] = \frac{-i}{\sqrt{2}} m_0 \Pi (F_x + i F_y) \quad (2.46)$$

$$\langle u_{c,0}^\uparrow | \mathbf{r} \cdot \mathbf{F} | u_{hh,0}^\uparrow \rangle = \frac{1}{\sqrt{2}} [-\langle s, \uparrow | r_x F_x | x, \uparrow \rangle + i \langle s, \uparrow | r_y F_y | y, \uparrow \rangle] = 0 \quad (2.47)$$

$$\left\langle u_{c,0}^\downarrow | \mathbf{r} \cdot \mathbf{F} | u_{hh,0}^\downarrow \right\rangle = \frac{1}{\sqrt{2}} [\langle s, \downarrow | r_x F_x | x, \downarrow \rangle - i \langle s, \downarrow | r_y F_y | y, \downarrow \rangle] = 0 \quad (2.48)$$

$$\left\langle u_{c,0}^\uparrow | \mathbf{r} \cdot \mathbf{F} | u_{hh,0}^\downarrow \right\rangle = \frac{1}{\sqrt{2}} [\langle s, \uparrow | r_x F_x | x, \downarrow \rangle - i \langle s, \uparrow | r_y F_y | y, \downarrow \rangle] = \frac{i}{\sqrt{2}} m_0 \Pi (F_x - i F_y) \quad (2.49)$$

and from light holes to the conduction band:

$$\begin{aligned} \left\langle u_{c,0}^\downarrow | \mathbf{r} \cdot \mathbf{F} | u_{lh,0}^\uparrow \right\rangle &= \frac{-1}{\sqrt{6}} [\langle s, \downarrow | r_x F_x | x, \downarrow \rangle + i \langle s, \downarrow | r_y F_y | y, \downarrow \rangle] + \sqrt{\frac{2}{3}} \langle s, \downarrow | r_z F_z | z, \uparrow \rangle = \\ &= \sqrt{\frac{2}{3}} i m_0 \Pi F_z \quad (2.50) \end{aligned}$$

$$\begin{aligned} \left\langle u_{c,0}^\uparrow | \mathbf{r} \cdot \mathbf{F} | u_{lh,0}^\uparrow \right\rangle &= \frac{-1}{\sqrt{6}} [\langle s, \uparrow | r_x F_x | x, \downarrow \rangle + i \langle s, \uparrow | r_y F_y | y, \downarrow \rangle] + \sqrt{\frac{2}{3}} \langle s, \uparrow | r_z F_z | z, \uparrow \rangle = \\ &= \frac{-1}{\sqrt{6}} i m_0 \Pi (F_x + i F_y) \quad (2.51) \end{aligned}$$

$$\begin{aligned} \left\langle u_{c,0}^\downarrow | \mathbf{r} \cdot \mathbf{F} | u_{lh,0}^\downarrow \right\rangle &= \frac{1}{\sqrt{6}} (\langle s, \downarrow | r_x F_x | x, \uparrow \rangle - i \langle s, \downarrow | r_y F_y | y, \uparrow \rangle) + \sqrt{\frac{2}{3}} \langle s, \downarrow | r_z F_z | z, \downarrow \rangle = \\ &= \frac{1}{\sqrt{6}} i m_0 \Pi (F_x - i F_y) \quad (2.52) \end{aligned}$$

$$\begin{aligned} \left\langle u_{c,0}^\uparrow | \mathbf{r} \cdot \mathbf{F} | u_{lh,0}^\downarrow \right\rangle &= \frac{1}{\sqrt{6}} (\langle s, \uparrow | r_x F_x | x, \uparrow \rangle - i \langle s, \uparrow | r_y F_y | y, \uparrow \rangle) + \sqrt{\frac{2}{3}} \langle s, \uparrow | r_z F_z | z, \downarrow \rangle = \\ &= \sqrt{\frac{2}{3}} i m_0 \Pi F_z \quad (2.53) \end{aligned}$$

Equations 2.46-2.53 show that two possible optical transitions are forbidden in the electric dipole approximation while the rest present very well defined polarization selection rules. Transitions from the $|u_{lh,0}^{\uparrow(\downarrow)}\rangle$ states to the $|u_{c,0}^{\downarrow(\uparrow)}\rangle$ are in principle allowed if the excitation field is linearly polarized along the propagation direction. This is not the case the excitation field is a plane wave, which is a very good approximation for the experimental

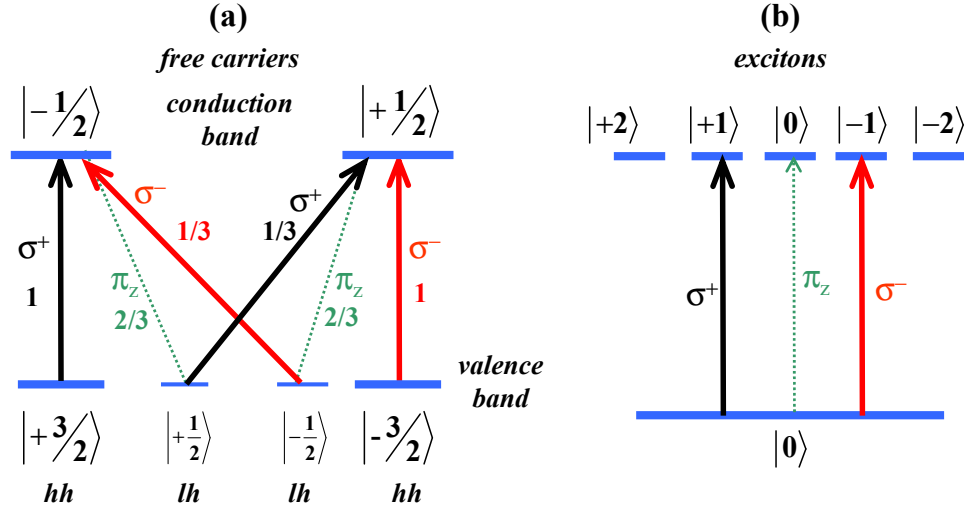


Figure 2.6: (a) Polarization and relative intensity of the matrix elements associated to the electric dipole allowed transitions from the valence to the conduction band. (b) Same as (a) for the resonant creation and recombination of heavy- and light-hole excitons.

excitation conditions treated in this work. Therefore, we will not consider this linearly polarized transitions here. The other allowed transitions are active under right and left circularly polarized light, as in the selected frame of reference these two polarizations (σ^+ and σ^-) are respectively defined as:

$$\mathbf{F}_+ = \frac{1}{\sqrt{2}} (\mathbf{F}_x + i\mathbf{F}_y), \quad (2.54)$$

$$\mathbf{F}_- = \frac{1}{\sqrt{2}} (\mathbf{F}_x - i\mathbf{F}_y). \quad (2.55)$$

Figure 2.6(a) sketches the relative value and associated polarization of the dipole matrix elements at the Γ point depicted in Eqs. 2.46-2.53. The allowed transitions depicted in Fig. 2.6(a) do not only account for the excitation of electrons to the conduction band but also for the recombination of an electron-hole pair and the emission of a photon of the proper polarization. For instance, a spin down electron from the conduction band is three times more likely to recombine with a spin up heavy-hole (emitting a σ^+ photon) than with a spin down light-hole (emitting a σ^- photon).

The previous analysis has focused on the conduction and band states at the band edge ($\mathbf{k}_e = \mathbf{k}_h = 0$). When we consider states with increasing wavevectors, valence band

mixing effects start to play an important role. As we have described above, the third component of the angular momentum is only well defined at the Γ point; at large wavevectors the polarization selection rules are not well defined and we can expect polarization forbidden transitions at $k \neq 0$ to become allowed. In this cases, a precise computation of the valence band wavefunctions is needed to calculate the amount of spin-up and spin-down electrons promoted from the valence to the conduction band by an excitation beam of well defined polarization. At $k = 0$ and $\hbar\omega$, a σ^+ excitation beam will promote three times more spin down electrons than spin up electrons to the conduction band. At large k states this electron spin imbalance generated by the excitation beam will be reduced due to the valence-band mixing effects.

In order to extract the actual absorption and emission spectra of an electron-hole pair transition, it is convenient to transform the sum in Eq. 2.44 into an integral involving a proper density of states. Within the parabolic band approximation, the energy difference between the electron and hole bands is well defined and given by $E_g + \hbar^2 k^2 / 2\mu_{eh}$, where μ_{eh} is the reduced effective mass of electrons and holes. In this sense we can define a *joint density of states* of the electron and hole bands, which will be the relevant density of states when considering transitions from the valence to the conduction bands:

$$g_{eh}(E) = \frac{(\mu_{eh}^*)^{3/2}}{\sqrt{2}\hbar^3\pi^2} \sqrt{E - E_{gap}} \quad (2.56)$$

In this way, Eq. 2.44 can be expressed as:

$$P_{cv}(E) dE = \frac{2\pi}{\hbar} |\langle u_{c,E_c} | \mathcal{H}_{dip} | u_{h,E_h} \rangle|^2 \frac{(\mu_{eh}^*)^{3/2}}{\sqrt{2}\hbar^3\pi^2} \sqrt{E - E_{gap}} dE \quad (2.57)$$

where now $P_{cv}(E)$ describes the probability per unit time that a valence to conduction transition (or viceversa) involving photons of energy between E and $E + dE$ takes place. The wavefunctions $|u_{c(h),E}\rangle$ can be labeled with the electron and hole kinetic energies in the parabolic and spherical approximation. As only vertical transitions are allowed, the kinetic energy of the electron (E_c) and hole (E_h) involved in the emission or absorption process are related by: $E_h = E - E_{gap} - E_c$, and their momenta is $k_e = k_h = \sqrt{\frac{2}{\hbar^2}\mu_{eh}(E - E_{gap})}$.

The emission (and absorption) due to electron hole pair recombination is proportional to $P_{cv}(E)$. If we only consider band to band transitions close to the Γ point, the matrix element $|\langle u_{c,E_c} | \mathcal{H}_{dip} | u_{h,E_h} \rangle|^2$ can be taken as constant and independent of the carrier kinetic energy. Nonetheless the polarization selection rules and transition relative

strengths detailed in Eqs. 2.46-2.52 must be taken into account. For instance, if we consider the recombination of conduction band electrons with heavy-holes, the total emission intensity will be given by:

$$I_{hh-c}(E) \propto \left[\left| \langle u_c^\downarrow | \mathcal{H}_{dip} | u_{hh}^\uparrow \rangle \right|^2 \cdot f(E)_{e\downarrow} f(E)_{hh\uparrow} + \right. \\ \left. + \left| \langle u_c^\uparrow | \mathcal{H}_{dip} | u_{hh}^\downarrow \rangle \right|^2 \cdot f(E)_{e\uparrow} f(E)_{hh\downarrow} \mu_{e-hh}^{3/2} \cdot (E - E_{gap})^{1/2} \right], \quad (2.58)$$

where $f(E)_{e\uparrow(\downarrow)}$ is the spin-up (spin-down) electron occupation function in the conduction band described by Eq. 2.34 [$f(E)_{hh\uparrow(\downarrow)}$: same for heavy holes in their valence band].

2.3.2 Exciton emission

Excitons can also couple to light. In fact, in high quality direct gap semiconductors at low temperature the photoluminescence spectrum is dominated by the exciton recombination. In this process, the excited electron and hole that conform the exciton relax to the ground state of the crystal by the emission of a photon. The same linear and angular momentum conservation rules aforementioned for unbound electrons and holes must be considered. For instance, linear momentum conservation implies that only excitons with center of mass momentum close to *zero* can couple to light, as $\mathbf{K}_X = \mathbf{k}_\gamma \approx 0$. This restricts the optically active excitons to a very narrow region in momentum space at the bottom of the exciton dispersion band. When non-radiative recombination effects are small, this narrow radiative region acts as a bottleneck for the exciton recombination (see Sec. 5.1.2 and Refs. [85, 203, 150]).

The total angular momentum conservation imposes again polarization-dependent selection rules. Given that the crystal ground state is the absence of an exciton ($J^z = 0$), the exciton absorption and emission selection rules is given by:

$$J_X^z + J_\gamma^z = 0 \quad (2.59)$$

where J_γ^z is the third component of the angular momentum of the incident photons, which in the case of a circularly polarized σ^+ (σ^-) incident beam is $+1$ (-1).

A precise calculation of the matrix elements corresponding to the transition from the *empty* state ($|0\rangle$) to the exciton state ($|X_{nlm}, J_X^z\rangle$) mediated by the electric dipole

interaction (\mathcal{H}_{dip}) is required to obtain the transition probabilities. It is easy to see that due to parity properties of the vector potential operator $\hat{\mathbf{A}}$ and the hydrogenic-like eigenfunctions of the exciton ($\psi_{nlm}(\mathbf{R}, \mathbf{r})$), the transition probabilities are proportional to $|\psi_{nlm}(\mathbf{R}, 0)|^2$ which is nonzero only for the $l = 0$ ($m = 0$) states.[301] Therefore, only the $1s, 2s, 3s, \dots$ can emit/absorb light in the recombination/emission of an exciton. The fact that the electric-dipole matrix element is proportional to $|\psi_{n00}(\mathbf{R}, 0)|^2$ indicates that the optical transition probability increases with the overlap of the electron and hole wavefunctions.

Attending to Eq. 2.59 and Table 2.2, where J_X^z of the $l = 0$ excitons is depicted, it is clear that heavy-hole excitons with spin ± 2 and light-hole excitons with spin 0 are optically inactive. For this reason they will be referred to as *dark states* from now on. Figure 2.6(b) shows the polarization of the allowed optical transitions for excitons.

The electron and hole wavefunctions that form an exciton overlap in a finite-size spatial extension around the exciton center of mass. In fact, most of the weight of their wavefunctions is concentrated within the Bohr radius, due to the Coulomb attraction between these particles. The enhanced overlap increases the optical transition rates associated to excitons as compared to the unbound electron-hole pair absorption and emission. It is useful then to define an oscillator strength for the exciton transition in the electric dipole approximation:

$$f_{osc}^X \equiv \frac{2\omega\mu_X}{\hbar} |\langle 0 | \mathbf{r} \cdot \mathbf{u}_F | \pm 1 \rangle|^2 \quad (2.60)$$

where \mathbf{u}_F is a unit vector indicating the direction polarization of the electric field, and the “ \pm ” signs refers to the optically active exciton states with $+1$ or -1 spin. The oscillator strength accounts for the total transition probability rate associated to the exciton optical transition (photon cross section).

Exciton radiative recombination is one of the sources of light emission at the exciton energy below the bandgap in semiconductors, but not the only one, as unbound Coulomb correlated electrons and holes can also radiatively recombine at that energy. Further discussion on the origin of this luminescence can be found in Sec. 5.2.1.

Chapter 3

Reducing the dimensionality: QWs and semiconductor microcavities

3.1 Exciton confinement: semiconductor Quantum Wells

3.1.1 Electron and hole subbands

Confinement of matter excitations (electrons, holes and excitons) can be easily attained in heterostructures composed of layers of different semiconductor materials. One dimensional confinement is typically created in Quantum Wells (QWs) by embedding a thin layer of a semiconductor crystal between two thick layers of a wider gap semiconductor, as depicted in Fig. 3.1(a). Matter excitations with low momentum that fall into the QW layer get trapped in a two-dimensional structure in which movement in the z -direction is inhibited. In these heterostructures quantum confinement effects start to be important when the extension of the excitation wavefunctions are greater or of the same size than the confinement dimension. A characteristic dimension in the systems we are interested in is given by the excitonic size. In GaAs based QWs, confinement sizes of the order of tens of nm or less are necessary to observe quantum confinement effects ($a_B = 11.4$ nm in GaAs). Lower dimensionality systems, such as Quantum Wires and Quantum Dots, will not be treated here.

Several approaches have been traditionally considered when calculating the eigenfunctions and eigenenergies in a two-dimensional heterostructure. The tight binding,[241, 242] pseudopotential[123] and $\mathbf{k} \cdot \mathbf{p}$ [264] methods, which have been widely used in bulk

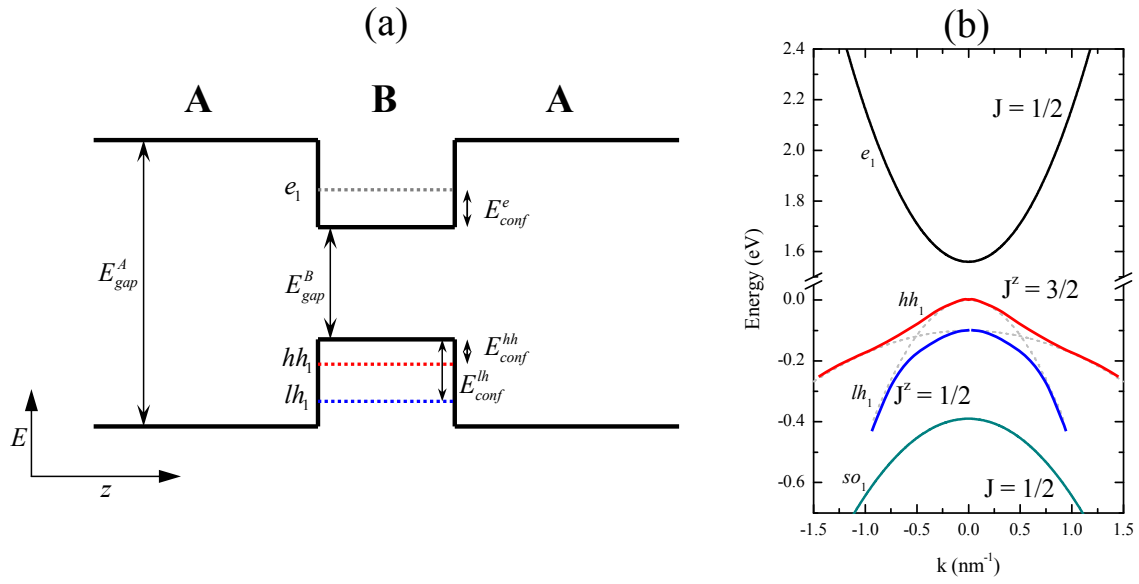


Figure 3.1: (a) Γ point band structure of the layers of a semiconductor QW. The z -direction is taken as the growth or confinement direction. In dotted lines the confined $k = 0$ electron and hole levels corresponding to the $n' = 1$ subband are depicted. (b) Typical dispersion relations of the $n' = 1$ subbands in the QW layer of a GaAs/AlGaAs heterostructure in the effective mass approximation. The dashed lines depict the highest valence bands in the absence of mixing.

semiconductors, and briefly described in Sec. 2.1.2 have also proved successful in the determination of the band structure in QWs. However, the most intuitive of them is the envelope wavefunction approach.[284, 10, 23]

Let us consider a symmetric QW in which the thin layer is composed by the semiconductor B and the barriers by the semiconductor A , whose three dimensional band wavefunctions are $u_{n,\mathbf{k}}^B(\mathbf{r})$ and $u_{n,\mathbf{k}}^A(\mathbf{r})$, respectively. In the heterostructure, in the envelope wavefunction method the eigenfunctions can be written as:

$$\Psi_{\mathbf{k}}(\mathbf{r}) = \sum_n f_n^A(\mathbf{r}) u_{n,\mathbf{k}}^A(\mathbf{r}), \quad (3.1)$$

if \mathbf{r} belongs to the barriers, and

$$\Psi_{\mathbf{k}}(\mathbf{r}) = \sum_n f_n^B(\mathbf{r}) u_{n,\mathbf{k}}^B(\mathbf{r}), \quad (3.2)$$

if \mathbf{r} belongs to the thin layer. Imposing the continuity of the wavefunctions and their effective mass weighted derivatives[23] at the material boundaries and accounting for the different band gap of the constituent materials in the effective mass approximation, the $\Psi_{\mathbf{k}}(\mathbf{r})$ can be determined.[23] Within this approximations this problem is analogous to the quantum mechanics textbook example of a particle in a two dimensional square QW.[52] The problem can then be solved for the conduction and valence bands considering the effective masses of each band. The direct consequence of the confinement is the splitting of each band in different confined states. The eigenenergies in the growth direction are quantized, while in the in-plane directions show parabolic dispersions:

$$E_{n'}(\mathbf{k}) = E_{n'}^z + \frac{\hbar k_{\parallel}^2}{2m^{*\parallel}} \quad (3.3)$$

where $m^{*\parallel}$ is the effective mass of the considered band *parallel* to the plane of the well (in-plane momentum). In the case of infinitely high barriers the $E_{n'}^z$ energies take the values:

$$E_{n'}^z = \frac{\pi^2 \hbar^2}{2m^{*\perp}} n'^2 \quad n' = 1, 2, 3, \dots \quad (3.4)$$

where $m^{*\perp}$ is the band effective mass along the growth direction (*perpendicular* to the QW plane). Both the conduction and the valence bands split in confined subbands, labeled by n' . From Eq. 3.4 it is clear that the heavy- and light-hole bands are not degenerate anymore as they have different effective masses $m^{*\perp}$. Nonetheless, it is important to consider in this

case the anisotropy related to the *mass reversal effect*. For instance, in AlGaAs based QWs grown in the [001] direction, the heavy-hole mass along the z -direction (growth direction) $m_{hh}^{*\perp}$ is greater than the light-hole mass along the same direction $m_{lh}^{*\perp}$. These are the relevant effective masses in order to calculate $E_{n'}^z$ in Eq. 3.4. The result is that for $n' = 1$ the confinement energy of heavy-hole band is smaller than that of the light-hole. However, in the QW plane $m_{hh}^{*\parallel} < m_{lh}^{*\parallel}$ and a crossing between the bands would be expected at large k as indicated by the dashed lines in Fig. 3.1(b), which shows the $n' = 1$ conduction, heavy and light hole subbands. Interaction between the bands analogous to that described in the $\mathbf{k} \cdot \mathbf{p}$ formalism in bulk [Eq. 2.13] induces the anticrossing of the bands (solid bands).[24]

Valence band mixing effects are, therefore, also important in QWs. The quantization axis now defines a direction to which set the angular momentum coordinates system. Then, we can associate the third component of the angular momentum (J^z) direction to the quantization axis. In this case, J^z for the heavy- and light-hole subbands is still well defined at $k = 0$. Actually, for momentum states around $k = 0$ the *purity* of J^z is enhanced respect to the 3D case, as the mixing bands (heavy and light) are split in energy. However, for large values of k , around the anticrossing positions valence band mixing is very important and J^z is no longer well defined in each subband. In any case, we will restrict the experiments and analysis to wavevectors close enough to $k = 0$ for which J^z is well defined.

Confinement of the wavefunctions also alters the density of states as compared to bulk systems. If movement is confined to a two-dimensional plane the density of states in momentum space changes to $g_{2D}(\mathbf{k}) = S/4\pi^2$ (where S is the surface of the QW), and the transformation into energy space, again assuming parabolic dispersion yields:

$$g_{2D}(E) = \frac{m^*}{\pi\hbar^2} \Theta(E - E_{n'}^z) \quad (3.5)$$

where $\Theta(x)$ is the Heaviside step function.

3.1.2 2D excitons

Analogously to the bulk case, electrons and holes from different subbands are subject to Coulomb interaction leading to the formation of excitons. The wavefunctions and energies of the exciton can be obtained by solving an equation analogous to Eq. 2.35 introducing the two-dimensionality of the system in the envelope wavefunction approach. The energy dispersion in this case takes the form:

$$E = E_{gap} + E_{n',e}^z + E_{m',h}^z - \frac{E_b^{2D}}{w^2} + \frac{\hbar^2 K_{\parallel}^2}{2(m_e^{*\parallel} + m_h^{*\parallel})}, \quad (3.6)$$

where $E_{n',e}^z$ and $E_{m',h}^z$ are the energies of the confinement energies of the electron and hole subbands that form the excitons, E_b^{2D} is the exciton binding energy, w is the exciton principal quantum number, and K_{\parallel} is the in-plane momentum of its center of mass.

The overlap of the electron and hole wavefunctions conforming the exciton is greatly enhanced due to the confinement. This is one of the major advantages of working with two-dimensional systems, as it has important consequences in the optical properties of these systems. For instance, the enhanced wavefunction overlap results in an increased oscillator strength of QW *vs* bulk excitons.

In the case of a purely two-dimensional situation the exciton Bohr radius would be half of the corresponding in bulk, while the binding energy would be as much as four times its bulk value (Eq. 2.38). By changing the width of the wells and the height of the barriers, both the electron and hole subbands and the exciton Bohr radius and binding energy can be modified. Figure 3.2(a) shows the calculated binding energy of the excitons formed from $n' = 1$ electrons and heavy- and light-holes,¹ for different well widths (L) and compositions of the barriers in a GaAs/Al_{*x*}Ga_{1-*x*}As heterostructure. In the infinite barrier case, the exciton binding energy increases when the well width is diminished as the electron and hole wavefunctions increase their overlap. In the case of finite barriers the wavefunctions penetration in the barriers and larger spatial extension results in a diminished overlap, resulting in overall lower values of E_b . Nonetheless, E_b still increases with decreasing width, except when the well width gets very small [below 40 Å in the case of $x = 0.15$ in Fig. 3.2(a)], when the confined electron and hole levels reach energies close to the barrier. The same behavior is found in the case of finite barriers. Let us mention that the band gap of Al_{*x*}Ga_{1-*x*}As increases as the Al content in the alloy is increased (for $x \lesssim 0.4$ to consider only direct band-gap alloys). Therefore, by changing x , the potential energy height of the barriers can be adjusted.

¹The exciton states formed from the $n' = 1$ electron and hole subbands are the lowest lying exciton levels, and will dominate most of the optical properties of the system. We will thus restrict our discussion to these subbands' excitons.

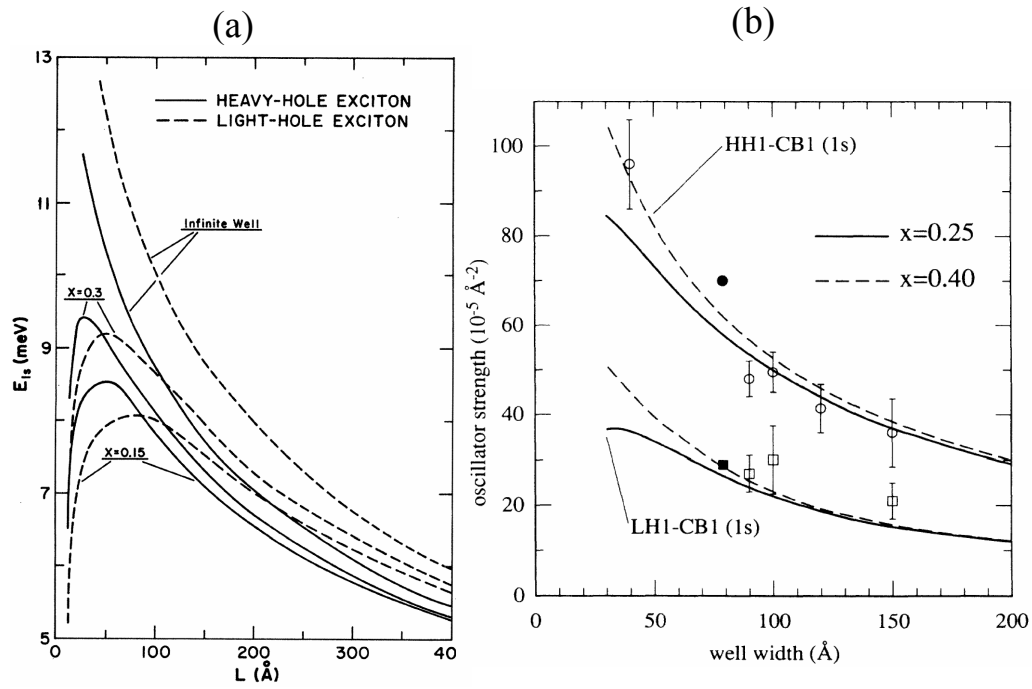


Figure 3.2: Calculated $1s$ heavy- and light-hole exciton binding energies (a, Ref. [96]) and oscillator strengths (b, Ref [9]) as a function of well width in symmetric GaAs/ $\text{Al}_x\text{Ga}_{1-x}\text{As}$ heterostructures.

3.1.3 Optical properties

The reduction of the symmetry in a two-dimensional system imposes a well defined quantization axis along the direction perpendicular to the QW plane (growth direction). In bulk systems (Sec. 2.3.1) the relevant axis, when attending for instance to polarization properties of the absorbed and emitted light, was the propagation axis of the incoming beam. In two-dimensional systems, it is convenient instead to use the quantization axis as the main axis of the system, defining the light polarizations.

The optical selection rules for transitions between heavy/light-hole and electron subbands are the same as those reported in bulk (see Fig. 3.3), with the following particularities:

- In-plane momentum of the absorbed/emitted photon must match the total in-plane momentum of the generated/destroyed electron-hole pair.
- Due to the parity of the confined wavefunctions in each subband, only transitions between subbands that satisfy $n'_e + m'_h = \text{even}$ are allowed in single photon processes. However, transitions within the subbands with the same index n' are the strongest (and the only ones allowed in an infinitely deep well) due to the enhanced overlap of their wavefunctions.
- When extending Fig. 2.6 to the QW case, for a given set of subbands n' , the heavy- and light-hole levels should be split, as indicated in Fig. 3.3(a).
- J^z is now defined along the quantization axis, the circularly polarized transitions in Fig. 3.3(a) refer to the coupling with light modes with in-plane angular momenta. Heavy-holes only couple to this kind of modes, while light-holes can also couple with light modes linearly polarized with propagation direction in the plane of the well [π transitions in Fig. 3.3(a)].

Analogously, the optical properties of QW excitons can be extended from those in bulk, attending to the same particularities related to the heavy-/light-hole exciton splittings, as indicated in Fig. 3.3(b). In this case the total in-plane momentum of the exciton should match that of the emitted/absorbed photon, restricting again the properties that can be investigated by spectroscopic techniques to the exciton states with $\mathbf{K}_{\parallel} \approx 0$.

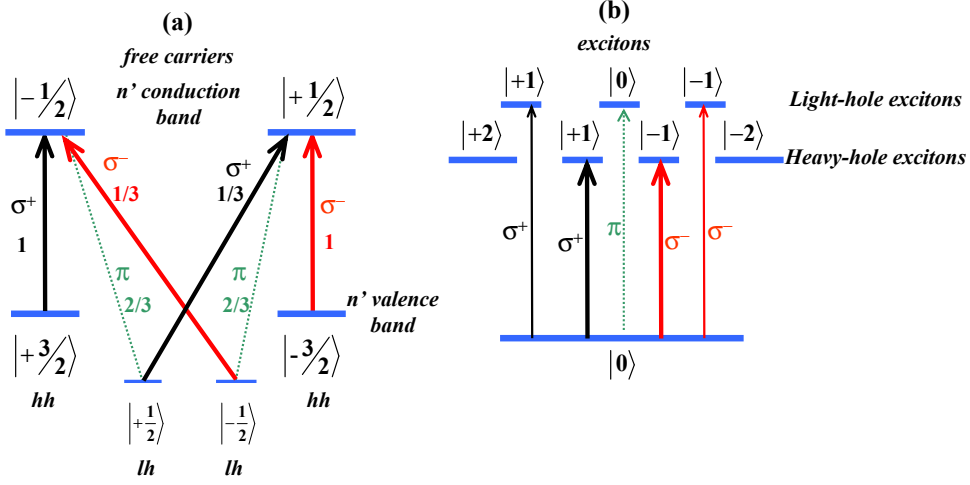


Figure 3.3: (a) Polarization and relative intensity of the matrix elements associated to the electric dipole allowed transitions from the heavy- and light-hole subbands to the conduction subband with same n' . (b) Same as (a) for the resonant creation and recombination of heavy- and light-hole excitons.

One of the most interesting consequences of the two-dimensional confinement is the enhanced oscillator strength of excitons in these systems. This results from the reduction in the Bohr radius caused by the increased overlap of the electron and hole wavefunctions [see Fig. 3.2(b)]. The transition probability $|\langle 0 | \mathbf{r} \cdot \mathbf{u}_F | \pm 1 \rangle|^2$ in the oscillator strength defined in Eq. 2.60 is proportional to $1/a_B^3$. Therefore, the oscillator strength of excitons is $(a_B^{3D}/a_B^{2D})^3$ times greater in QWs than in bulk. Thus, light emitting devices made of several QW stacks placed together present much better luminescence properties than bulk based devices.

3.1.4 Effect of interface fluctuations and defects on the exciton linewidth

Let us finally make some comments on the exciton lineshapes observable in luminescence measurements. In QW structures with no defects the exciton resonances would be characterized by a homogeneous lineshape of width γ_{hom} , whose magnitude is dominated by dephasing. Despite the high quality of the heterostructures grown by current epitaxial techniques, interface and composition fluctuations are present in the QWs.[236] Thus, excitons are subject to an irregular environment in which local fluctuations contribute to the inhomogeneous broadening (γ_{inh}) of the the exciton lineshape, and to Stokes shifts between the absorption and emission peak energies. In principle, the inhomogeneously broadened exciton should show a rather symmetric (Gaussian) lineshape. However, the specific distri-

bution in size of interface defects in the well, as well as the distributed oscillator strength of the different exciton sublevels result, in rather asymmetrical shapes.[136, 236]

Interface and composition fluctuation are particularly important in CdTe based heterostructures, as their quality is still quite far from the GaAs based systems. In applications in which narrow exciton lines are required, a way to overcome these problems is by growing wider QWs.² In this situation the weight of the exciton wavefunction is lowered at the QW interfaces, which is where roughness and defects are mostly located, resulting in more symmetrical lineshapes and smaller widths. The price to pay by doing this is the decrease of the oscillator strength as the confinement is reduced.

3.2 Light confinement and polaritons: semiconductor microcavities

In this section we will present a brief and qualitative introduction to optical confinement and exciton-photon coupling in semiconductor microcavities. Only an overview of the most relevant theoretical results will be presented here. Several works can be found in the literature that address many specific points of the theoretical basis in this field.[214, 237, 235, 47, 126, 127] The number of published articles is significant when it comes to the area of dynamics and luminescence properties of microcavity polaritons,[26, 214, 238, 237, 135, 73] which are light-matter species with very rich physical phenomena associated to them. For instance, the microcavity polariton system shows very exotic non-linear optical characteristics, the capability to form Bose-Einstein condensates, or superfluid behavior. A more detail introduction to the many-body properties of polaritons is presented in Sec. 8.

A semiconductor microcavity is a high finesse Fabry-Perot resonator with a QW, or a series of QWs, embedded inside the cavity spacer. In the next two sections we will present each of the ingredients that conform these systems. To do so, we will make use of a linear semiclassical approach.[126, 127, 237]

²This is the case of the exciton transitions in microcavities working in the strong coupling regime. As it will be discussed in Sec. 3.2, the conditions for an optimal exciton-photon coupling in these systems, require a narrow exciton linewidth, with a sharp distribution of oscillator strengths around the transition's peak.

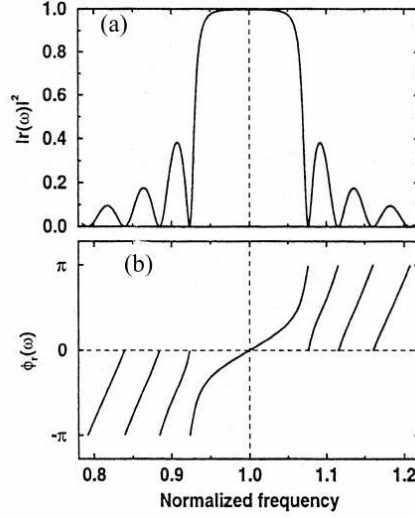


Figure 3.4: (a) Normal incidence reflectivity ($R = |r(\omega)|^2$) of a 20 pair DBR with $n_{out} = n_{sub} = 1$ and $n_1 = 3.0$, $n_2 = 3.6$, vs normalized frequency (ω/ω_m). (b) Corresponding phase ϕ_r of the complex reflection coefficient. Both magnitudes are calculated using a transfer matrix approach.[237]

3.2.1 Distributed Bragg Reflectors and the optical cavity

A Distributed Bragg Reflector (DBR) is a dielectric heterostructure composed of layers of two alternating materials of different index of refraction (n_i^r). Usually semiconductors with high indexes of refraction (~ 3.5) are employed. If the optical thickness of each material is $\lambda/4$, the heterostructure will present an enhanced reflectivity for an incoming light field of wavelength λ . At normal incidence and for a sufficiently high number N of dielectric layers (so that $1 - R \ll 1$), the reflectivity ($R = |r(\omega)|^2$) at wavelength $\lambda = \frac{2\pi c}{\omega}$ can be calculated using classical electromagnetic theory of continuum media:[36]

$$R \approx 1 - 4 \frac{n_{out}}{n_{sub}} \left(\frac{n_1}{n_2} \right)^{2N} \quad (3.7)$$

where $n_{out(sub)}$ is the index of refraction of the external medium (substrate on which the DBR is grown) and n_1 and n_2 are the refraction index of the two materials composing the DBR itself (we have assumed $n_1 < n_2$). As the number of layers is increased, both the reflectivity and the wavelength region around λ for which the reflectivity is enhanced, increase. The spectral region of enhanced reflectivity around λ is called *stop band*, and can be clearly observed in Fig. 3.4(a), where the reflectivity of a typical 20 pairs DBR is plotted.

The phase of the complex reflectivity $r(\omega)$ has an approximate linear dependence on ω (angular frequency of the light field) inside the stop band [Fig. 3.4(b)]:

$$\phi_r \approx \frac{n_{sub} L_{DBR}}{c} (\omega - \omega_m), \quad (3.8)$$

where ω_m is the frequency of the center of the stop band. L_{DBR} is the penetration depth of the electromagnetic field inside the mirror, and is given by:

$$L_{DBR} = \frac{\lambda}{2} \frac{n_1 n_2}{n_{sub} (n_2 - n_1)}. \quad (3.9)$$

An optical microcavity is formed by sandwiching a cavity spacer between two of such DBRs. The cavity spacer material is usually an additional semiconductor layer of width L_c . Such configuration conforms a Fabry-Perot, with a broad stop band in which high transmission peaks [minima of $R(\omega)$] open at the energy of the cavity modes [Fig. 3.5(a)]. In many cases, microcavities are designed so that the wavelength associated to the central frequency of the stop band (ω_m) is equal to the length of the spacer, L_c . In this case it is convenient to define an effective cavity length $L_{eff} = L_c + L_{DBR}$. The condition for constructive interference in a round trip is given by:

$$\left(\frac{\omega^2}{c^2} n_{cav}^2 - k_{\parallel}^2 \right)^{\frac{1}{2}} L_{eff} = M\pi, \quad (3.10)$$

where $M = 1, 2, 3, \dots$, and n_{cav} is the index of refraction of the cavity spacer. The parenthesis in Eq. 3.10 depicts the component of the photon wavevector normal to the plane of the mirrors. This direction is usually referred to as growth direction, and here we will label it as z . In other words:

$$k_z = \left(\frac{\omega^2}{c^2} n_{cav}^2 - k_{\parallel}^2 \right)^{\frac{1}{2}}. \quad (3.11)$$

k_{\parallel} is the photon wavevector parallel to the cavity plane, which can have any value, as the microcavity does not impose any confinement in such plane. At normal incidence, $k_{\parallel} = 0$, Eq. 3.10 imposes the appearance of cavity modes at wavelengths:

$$\lambda_M = \frac{2n_{cav} L_{eff}}{M}. \quad (3.12)$$

The lowest cavity mode corresponds to a wavelength equal to twice optical length of the effective cavity. Usually, microcavities are operated in one of the first modes. In this way,

the mode energy splitting is large enough to disregard any effect of other cavity modes in the optical properties. If we consider just one of the cavity modes M , the cavity mode presents a dispersion given by:

$$E(k_{\parallel}) = \frac{\hbar c}{n_{cav}} \sqrt{k_{\perp}^2 + k_{\parallel}^2}, \quad (3.13)$$

where $k_{\perp} = n_{cav} \frac{2\pi}{\lambda_M}$ is the confined momentum in the growth direction. k_{\parallel} is related to the angle of incidence θ of the photons outside the cavity by:

$$k_{\parallel} = k_{\perp} \tan \left[\arcsin \left(\frac{1}{n_{cav}} \sin \theta \right) \right], \quad (3.14)$$

$$k_{\parallel} = n_{cav} \frac{2\pi}{\lambda_M} \tan \left[\arcsin \left(\frac{1}{n_{cav}} \sin \theta \right) \right]. \quad (3.15)$$

The cavity mode dispersion of Eq. 3.13, allows the assignation of an effective mass for the cavity photons in the limit $k_{\parallel} \ll k_{\perp}$. A second order Taylor expansion around $k_{\parallel} = 0$ results in:

$$E(k_{\parallel}) \approx \frac{\hbar c}{n_{cav}} \left(k_{\perp} + \frac{1}{2k_{\perp}} k_{\parallel}^2 \right). \quad (3.16)$$

Applying Eq. 2.16 we obtain a photon effective mass of:

$$m_{ph} = \frac{2\pi\hbar}{c\lambda_M}, \quad (3.17)$$

which has a typical value of $3 \times 10^{-6} m_0$.

The linewidth of the cavity resonance is a very important factor of the microcavity. For the cavity modes at normal incidence and assuming symmetric DBRs with reflectivity R , the cavity homogeneous linewidth is:

$$\gamma_c = \frac{c}{2\pi n_{cav} L_{eff}} \frac{1 - R}{\sqrt{R}}. \quad (3.18)$$

It is convenient to use the cavity quality factor Q defined as $\frac{\lambda_M}{\Delta\lambda}$. Transforming the frequency width of Eq. 3.18 into $\Delta\lambda$, and considering just the $M = 1$ mode in Eq. 3.12 (the so called $\lambda/2$ cavity), the cavity quality factor is:

$$Q = \frac{\lambda}{\Delta\lambda} = \pi \frac{\sqrt{R}}{1 - R}. \quad (3.19)$$

The linewidth γ_c determines the lifetime of a photon in the cavity ($1/\gamma_c$) at the energy of the resonance before escaping. In the same sense, Q indicates the average number of round trips of a photon in the cavity before leaking out. Typical values of the cavity lifetime in real GaAs based semiconductor microcavities as those described in Sec. 4.1, are on the order of 4 ps ($R \approx 0.9982$). These values result in values of Q of about 1700 for a resonance centered at 810 nm.

Besides the Fabry-Perot characteristics of the microcavity, one of its most important features is the enhancement of the electromagnetic field inside the cavity spacer. Following the classical theory of fields employed so far,[237] the electric field strength in the center of a symmetric $\lambda/2$ cavity is given by:

$$|F(\omega)|^2 = F_0^2 \frac{1 - R(\omega)}{(1 - R(\omega))^2 + 4\sqrt{R(\omega)} \sin^2 \left[\frac{1}{2} (k_z L_c + \phi_r(\omega)) \right]}, \quad (3.20)$$

where the argument of the sine is the phase change in a round trip inside the cavity, and $\phi_r(\omega)$ is given by Eq. 3.8. F_0 is the amplitude of incoming electric field (i.e., the amplitude of the field in the absence of a cavity). For the case of a cavity lifetime of 4 ps, as in the example above, the strength of the electric field at the center of the cavity is increased by a factor of about 500.

The amplitude of the electric field for a $\lambda/2$ cavity with Bragg mirrors of 15 (left) and 21 (right) pair periods is shown in Fig. 3.5. Note that due to the boundary conditions imposed by the DBRs, the electromagnetic field inside the cavity is quasi-stationary.

3.2.2 Semiconductor microcavity with an embedded quantum well: exciton-photon normal mode coupling

For the sake of simplicity, let us consider a $\lambda/2$ photonic cavity. At the end of the previous section we described how the amplitude of the electric field in the center of the cavity at the energy of the photonic resonance is greatly enhanced as compared to the value of the field outside the cavity. If a material with an optical resonance close in energy to the cavity mode is placed at such position of enhanced electromagnetic field, an important light-matter interaction is expected. This is the basic idea behind a semiconductor optical microcavity. The usual configuration employs a QW with a $1s$ exciton energy close to the cavity mode. QW excitons are ideal structures to explore light-matter coupling in microcavities, as the 2D confinement enhances their oscillator strength while localizing them at the position of the

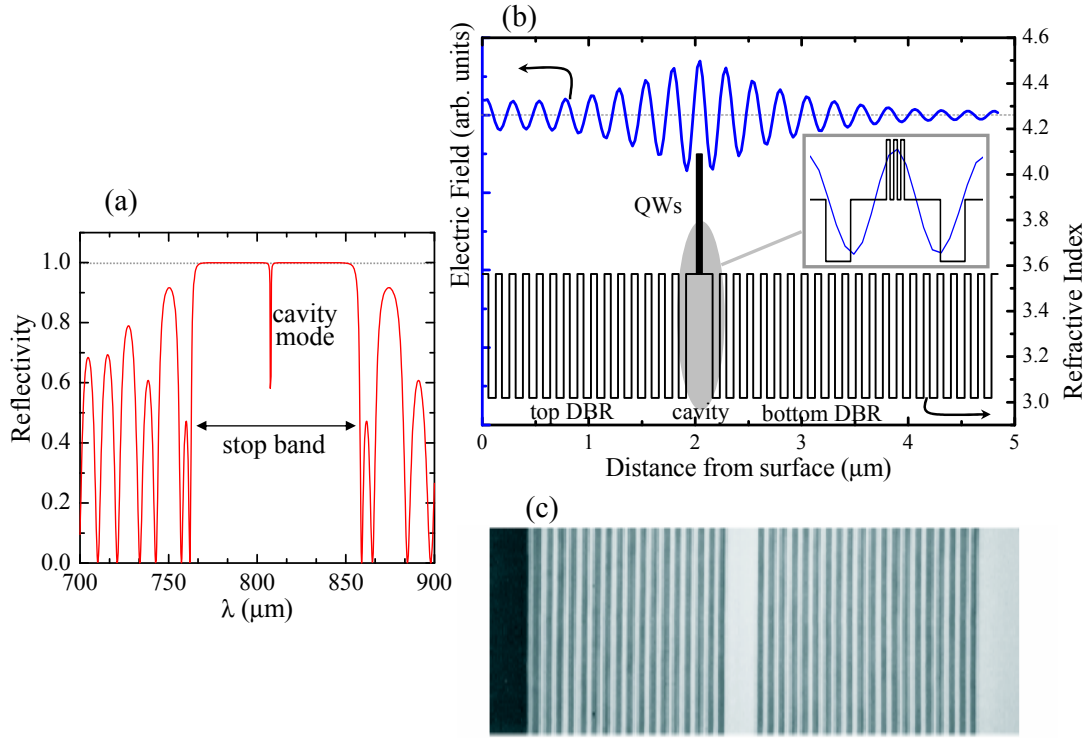


Figure 3.5: (a) Reflectivity spectrum of a typical microcavity. (b) Black line, right scale: profile of the index of refraction of a $\lambda/2$ microcavity. In this case three QWs have been embedded at its center. The surface is on the left side. The growth direction is given by the horizontal axis. Blue line, right scale: electric field of the bare cavity mode. Inset: close up of the cavity spacer region. The electric field is maximum at the position of the QWs. This is the configuration in which exciton-photon strong coupling is observed, as detailed in Sec. 3.2.2. (c) Scanning electron microscope image of the cross section of an actual cavity, where both DBRs and cavity spacer are clearly seen. The black region on the left side has a size of ~ 225 nm. Courtesy of M. D. Martín.

cavity where the electric field is maximum [see inset of Fig. 3.5(b)]. The excitons and the photons inside the cavity constitute a system of two bosonic oscillators, as both species can be treated as boson, coupled through light-matter interaction. As in any classical system of two coupled oscillators, renormalization of the eigenenergies of the system as compared to those of the independent oscillators is expected.

In order to understand the consequences of the strong exciton-photon interaction inside the cavity, we are going to follow a second quantization approach, which provides very intuitive results. Nonetheless, the physics behind this phenomena do not require the use of a quantum mechanical treatment; similar results can be obtained following classical linear approaches.[304, 126, 127, 237]

Within the framework of two coupled oscillators, the Hamiltonian describing the exciton-photon system inside the cavity can be written as:

$$\mathcal{H}_{pol} = \sum_{k_{\parallel}} \hbar\omega_c(k_{\parallel}) \hat{a}_{\mathbf{k}_{\parallel}}^{\dagger} \hat{a}_{\mathbf{k}_{\parallel}} + \sum_{k_{\parallel}} \hbar\omega_x(k_{\parallel}) \hat{B}_{\mathbf{k}_{\parallel}}^{\dagger} \hat{B}_{\mathbf{k}_{\parallel}} + \sum_{k_{\parallel}} \hbar\Omega_R \left(\hat{a}_{\mathbf{k}_{\parallel}}^{\dagger} \hat{B}_{\mathbf{k}_{\parallel}} + \hat{a}_{\mathbf{k}_{\parallel}} \hat{B}_{\mathbf{k}_{\parallel}}^{\dagger} \right), \quad (3.21)$$

where $\hat{B}_{\mathbf{k}_{\parallel}}$ ($\hat{a}_{\mathbf{k}_{\parallel}}$) is the exciton (photon) creation operator with in-plane wavevector \mathbf{k}_{\parallel} , $\hbar\omega_{x(c)}(k_{\parallel})$ is the in-plane energy dispersion of the excitons (cavity photons), and $\hbar\Omega_R$ is the exciton-photon dipole interaction. In the case of a single QW placed at one of the antinodes of the electromagnetic field inside the cavity, Ω_R is given by:[237]

$$\Omega_R^2 = \frac{(1 + \sqrt{R})^2}{2\sqrt{R}} \frac{c\Gamma_0}{n_{cav}L_{eff}}, \quad (3.22)$$

where Γ_0 is the exciton radiative lifetime in the absence of the cavity and accounts for the exciton oscillator strength. Note that $\hbar\Omega_R$ is independent of k_{\parallel} if $k_{\parallel} \ll k_{\perp}$, [238] as it is the case in the treatment we are following. If more QWs are placed in the antinodes of the cavity field, the total exciton oscillator strength of the system is multiplied by the number of QWs. In the case of N QWs, and assuming no polariton coupling between them, then $\Omega_{R,N} = \Omega_R\sqrt{N}$. [291, 115] The inset of Fig. 3.5(b) shows a situation of three QWs at the antinode of the electric field.

Within the exciton-photon³ basis $(\hat{a}_{\mathbf{k}_{\parallel}}, \hat{B}_{\mathbf{k}_{\parallel}})$ Hamiltonian 3.21 can be expressed in matrix form as:

³From now on we will use indistinctly the nomenclature: photon, photon mode, cavity mode, cavity resonance, cavity.

$$\mathcal{H}_{pol}(k_{\parallel}) = \begin{pmatrix} \hbar\omega_c(k_{\parallel}) & \hbar\Omega_R \\ \hbar\Omega_R & \hbar\omega_x(k_{\parallel}) \end{pmatrix}. \quad (3.23)$$

$\mathcal{H}_{pol}(k_{\parallel})$ can be diagonalized by the transformation into the basis given by the following creation operators, the polariton basis:

$$\hat{p}_{\mathbf{k}_{\parallel}} = X_{\mathbf{k}_{\parallel}} \hat{B}_{\mathbf{k}_{\parallel}} + C_{\mathbf{k}_{\parallel}} \hat{a}_{\mathbf{k}_{\parallel}}, \quad (3.24)$$

$$\hat{q}_{\mathbf{k}_{\parallel}} = -C_{\mathbf{k}_{\parallel}} \hat{B}_{\mathbf{k}_{\parallel}} + X_{\mathbf{k}_{\parallel}} \hat{a}_{\mathbf{k}_{\parallel}}. \quad (3.25)$$

\hat{p} and \hat{q} are the lower and upper polariton creation operators respectively, while $X_{\mathbf{k}_{\parallel}}$ and $C_{\mathbf{k}_{\parallel}}$ are the Hopfield coefficients with information on the exciton and photon component of each polariton type with a particular in-plane momentum \mathbf{k}_{\parallel} . In this basis, \mathcal{H}_{pol} is diagonal:

$$\mathcal{H}_{pol} = \sum_{k_{\parallel}} E_{LPB}(k_{\parallel}) \hat{p}_{\mathbf{k}_{\parallel}}^{\dagger} \hat{p}_{\mathbf{k}_{\parallel}} + \sum_{k_{\parallel}} E_{UPB}(k_{\parallel}) \hat{q}_{\mathbf{k}_{\parallel}}^{\dagger} \hat{q}_{\mathbf{k}_{\parallel}}, \quad (3.26)$$

with eigenenergies:

$$E_{UPB}(k_{\parallel}) = \frac{\hbar\omega_c(k_{\parallel}) + \hbar\omega_x(k_{\parallel})}{2} + \frac{1}{2} \sqrt{4\hbar^2\Omega_R^2 + [\hbar\omega_c(k_{\parallel}) - \hbar\omega_x(k_{\parallel})]^2}, \quad (3.27)$$

$$E_{LPB}(k_{\parallel}) = \frac{\hbar\omega_c(k_{\parallel}) + \hbar\omega_x(k_{\parallel})}{2} - \frac{1}{2} \sqrt{4\hbar^2\Omega_R^2 + [\hbar\omega_c(k_{\parallel}) - \hbar\omega_x(k_{\parallel})]^2}, \quad (3.28)$$

Note that the minimum energy separation between the UPB and the LPB take places at k_{\parallel} states where the exciton and cavity modes are resonant. This minimum energy separation is called *Rabi splitting* and amounts to $2\hbar\Omega_R$. Typically the Rabi splitting per QW in a GaAs based microcavity is on the order of 4 meV. The Hopfield coefficients[113] which weight the photonic and excitonic content of the upper and lower polaritons in Eqs. 3.24-3.25 are given by:

$$X_{\mathbf{k}_{\parallel}} = \frac{1}{\sqrt{2}} \left(1 + \frac{\hbar\omega_c(k_{\parallel}) - \hbar\omega_x(k_{\parallel})}{\sqrt{4\hbar^2\Omega_R^2 + [\hbar\omega_c(k_{\parallel}) - \hbar\omega_x(k_{\parallel})]^2}} \right)^{\frac{1}{2}} \quad (3.29)$$

$$C_{\mathbf{k}_{\parallel}} = \frac{1}{\sqrt{2}} \left(1 - \frac{\hbar\omega_c(k_{\parallel}) - \hbar\omega_x(k_{\parallel})}{\sqrt{4\hbar^2\Omega_R^2 + [\hbar\omega_c(k_{\parallel}) - \hbar\omega_x(k_{\parallel})]^2}} \right)^{\frac{1}{2}} \quad (3.30)$$

The coefficients satisfy the normalization condition $|X_{\mathbf{k}_{\parallel}}|^2 + |C_{\mathbf{k}_{\parallel}}|^2 = 1$. At k_{\parallel} points of the polariton dispersion in which the bare exciton and cavity energies are the same, both upper and lower polaritons have a 50% exciton and photon component. The polariton states, thus, conform quantum mixtures of the exciton and photon states. Figure 3.6 shows the polariton dispersions (Eqs. 3.27-3.28; left panels) and the corresponding Hopfield coefficients (Eqs. 3.29-3.30; right panels) for three different cavity-exciton detunings δ , which is defined as the energy difference at $k_{\parallel} = 0$ of the bare cavity and exciton modes. We can see that by choosing the appropriate detuning, the exciton-cavity content of polaritons at a given k_{\parallel} can be selected. Additionally, the polariton dispersions present very exotic features. The LPB conforms a trap for polaritons in momentum space. Polaritons “living” on such dispersion and subject to energy relaxation processes (by interacting with crystal phonons, for instance) will tend to occupy the energy states at the bottom of the trap. Most interesting is the inflexion point in the LPB, which will have important implications when exciting the system resonantly at that energy-momentum state, as detailed in Sec. 8.4.

The polarization properties of polaritons are determined by those of their constituents. Only optically active excitons couple to light, with $J^z = \pm 1$. These exciton states couple to light only via emission/absorption of circularly polarized photons. Thus, when the photonic part of the polariton leaks out of the cavity (destroying the polariton), it emits a circularly polarized photon. This is the situation at $k_{\parallel} = 0$, in which the system is symmetric about the growth axis. When $k_{\parallel} \neq 0$, the situation is slightly more complicated, as the cavity modes presents a small energy anisotropy between the modes linearly polarized along and perpendicularly to the direction of propagation inside the cavity.[27] More details about these issues will be found in Sec. 9.4.

In Fig. 3.6 the exciton dispersion is considered as flat, i.e., the exciton mass is considered as infinite. This approximation is valid for values of k_{\parallel} close to *zero*, as in this region the photon mass is much smaller than the exciton mass. Note that the upper and lower polariton branches (UPB and LPB, respectively) are approximately parabolic close to $k_{\parallel} = 0$. It is then possible to define a polariton effective mass for each branch. Expanding Eqs. 3.27-3.28 in a Taylor series up to second order, and using Eq. 2.16, the polariton

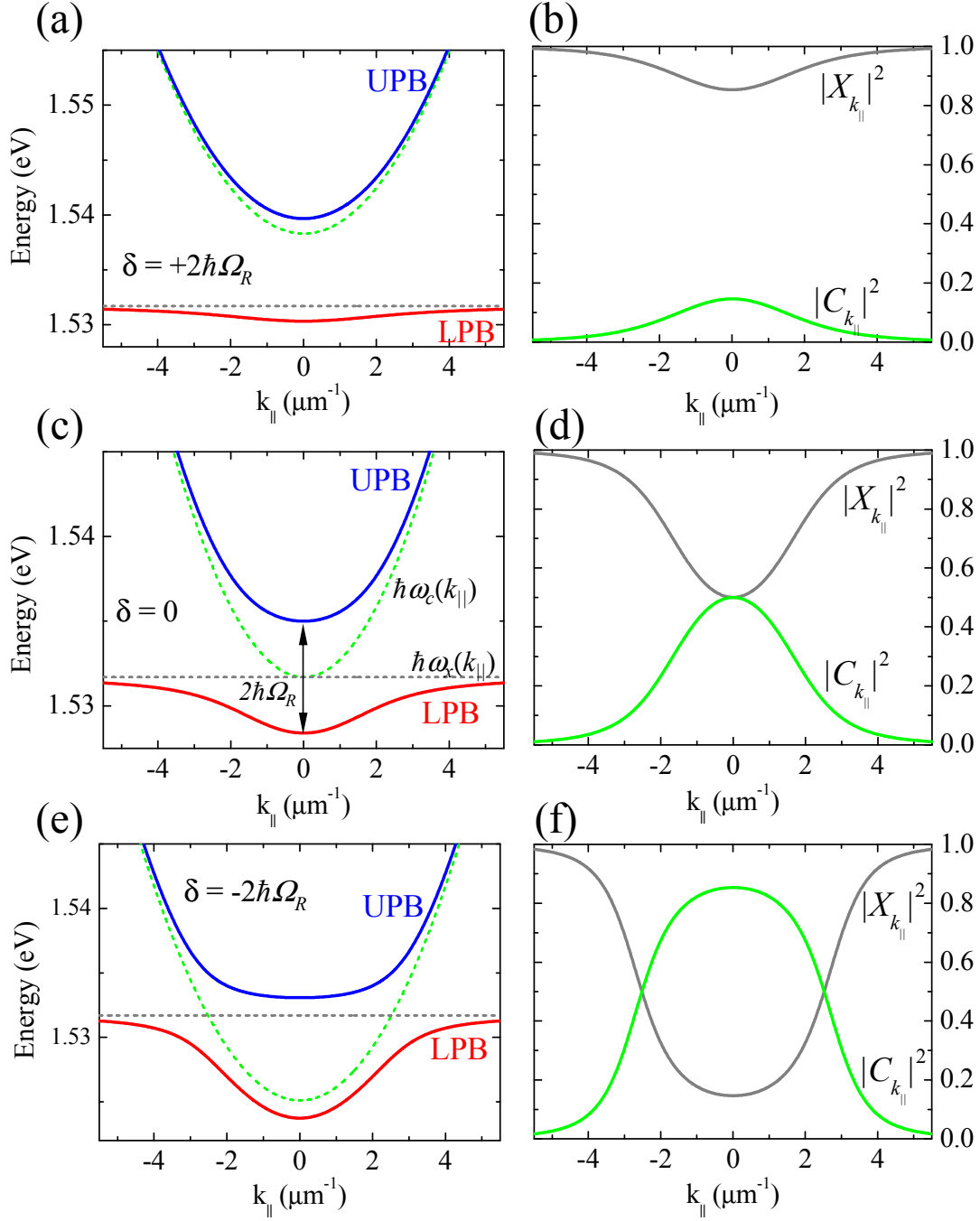


Figure 3.6: Left panels: calculated bare exciton and cavity mode dispersions (dashed lines) as well as the polariton dispersions (solid lines) for different exciton-cavity detunings δ in a microcavity with a Rabi splitting $2\hbar\Omega_R = 6.6$ meV. Right panels: corresponding Hopfield coefficients obtained from Eqs. 3.29-3.30. Detunings: (a)-(b) $+2\hbar\Omega_R$, (c)-(d) zero, (e)-(f) $-2\hbar\Omega_R$.

dispersion can be written as:

$$E_{UPB/LPB}(k_{\parallel}) \approx E_{UPB/LPB}(0) + \frac{\hbar^2 k_{\parallel}^2}{2m_{UPB/LPB}}, \quad (3.31)$$

where the polariton mass is again weighted by the Hopfield coefficients:

$$\frac{1}{m_{UPB}} = \frac{|X_{k_{\parallel}=0}|^2}{m_X^*} + \frac{|C_{k_{\parallel}=0}|^2}{m_{ph}}, \quad (3.32)$$

$$\frac{1}{m_{LPB}} = \frac{|C_{k_{\parallel}=0}|^2}{m_X^*} + \frac{|X_{k_{\parallel}=0}|^2}{m_{ph}}, \quad (3.33)$$

where m_X^* is the exciton effective in-plane mass ($m_e^{*\parallel} + m_h^{*\parallel}$). As $m_X^* \sim m_0 \ll m_{ph}$, at detunings close to *zero* the polariton masses are basically given by the mass of the cavity mode weighted by the exciton or photon content of polaritons at $k_{\parallel} = 0$, for each considered detuning. The polariton masses, thus, are on the order of the m_{ph} ($\sim 10^{-6} m_0$), resulting in a very small density of states inside the polariton trap [Eq. 3.5]. This property will also have important implications on the bosonic and condensation properties of cavity polaritons (Chapter 8).

3.2.3 Finite cavity and exciton lifetimes

In the preceding section, all results were derived assuming that the exciton and cavity modes have a vanishing homogeneous linewidth. Actually, it is the exciton decay rate and the cavity mode parameters (that eventually define its width) the elements that determine the Rabi splitting [Eq. 3.22]. The cavity parameters account for the enhancement of the electric field inside the cavity (Eq. 3.20) and the exciton decay rate reflects the strength of the interaction of excitons with the electromagnetic field. However, the finite cavity lifetime [homogeneous cavity linewidth γ_c , Eq. 3.18] and the exciton homogeneous linewidth (γ_X) modify the properties of polaritons. The most important consequence of the explicit inclusion of these two parameters, is the alteration of the Rabi splitting, which is now given by:

$$Rabi\ splitting = 2\sqrt{\hbar^2 \Omega_R^2 - \frac{\hbar^2}{4} (\gamma_c - \gamma_X)^2}. \quad (3.34)$$

If $2\Omega_R < (\gamma_c - \gamma_X)$ then the content of the square root is negative and solutions are purely imaginary, resulting in two modes with the same energy. This situation is called *weak coupling regime*, in which the exciton and cavity photon picture is still valid with small variations in their decay rate. In the opposite case ($2\Omega_R > (\gamma_c - \gamma_X)$, real valued Rabi splitting) the system must be fully described in the polariton picture, appearing a splitting between the two polariton modes.⁴ This splitting is analogous to the normal mode splitting observed in atoms inside cavities.[213, 304] This situation is called *strong coupling regime*, and reflects the fact that the exchange rate between the photon and exciton is much faster than their decoherence rate in order to conform a polariton (i. e., the quantum exciton-photon mixture that conforms the fundamental excitation of the system).

Figure 3.7(a) shows the Rabi splitting as a function of reflectivity of the microcavity, for a $\lambda/2$ microcavity system as calculated by Savona *et al.*[237] Figure 3.7(b) depicts the linewidth of each mode as a function of reflectivity. In general, the homogeneous linewidth for each particular polariton state is determined by its excitonic and photonic content:

$$\gamma_{UPB}(k_{\parallel}) = |X_{k_{\parallel}}|^2 \gamma_X + |C_{k_{\parallel}}|^2 \gamma_C, \quad (3.35)$$

$$\gamma_{LPB}(k_{\parallel}) = |C_{k_{\parallel}}|^2 \gamma_X + |X_{k_{\parallel}}|^2 \gamma_C. \quad (3.36)$$

For a situation of resonant exciton-cavity modes ($\delta = 0$; $|X_{k_{\parallel}}|^2 = |C_{k_{\parallel}}|^2 = 0.5$), as that depicted in Fig. 3.7, the linewidth of polaritons collapse into a single value, given by $\frac{1}{2}(\gamma_c + \gamma_X)$.

⁴Note that the maximum Rabi splitting is obtained when both oscillator linewidths are identical. However, in order to observe the Rabi splitting in spectroscopic experiments, both γ_c and γ_X must be smaller than Ω_R . [114]

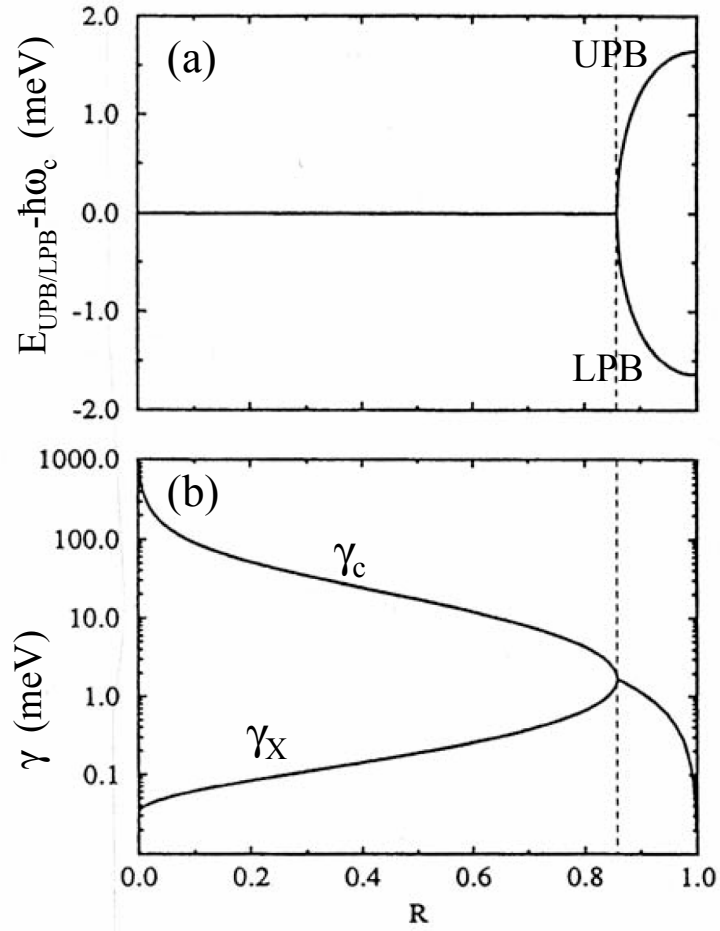


Figure 3.7: (a) Energy difference between the UPB/LPB and the cavity mode at $k_{\parallel} = 0$ as a function of reflectivity for a fixed bare QW γ_X for $\delta = 0$. The dashed line depicts the minimum reflectivity for the onset of strong coupling ($R \approx 0.85$). (b) Broadening of the cavity mode γ_c and modified γ_X inside the cavity ($R < 0.85$), and polariton modes width ($R > 0.85$), as a function of reflectivity. From Ref. [237].

Chapter 4

Samples and description of the experimental set-ups

4.1 Samples description

4.1.1 Bulk GaAs and AlGaAs

The bulk, high quality GaAs and AlGaAs samples of the experiments described in Chapters 5 and 6 were grown by molecular beam epitaxy by Konstantin Zhuravlev and co-workers at the *Institute of Semiconductor Physics* in Novosibirsk (Russia).

Different $\text{Al}_x\text{Ga}_{1-x}\text{As}$ epilayers were investigated, with Al concentrations of $x = 0, 0.015, 0.03$ and 0.05 . The active layer in each sample had a width of $2.5\ \mu\text{m}$, and was encapsulated between two thin ($25\ \text{nm}$) AlAs layers in order to decrease surface recombination. A GaAs buffer layer of $0.2\ \mu\text{m}$ was grown between the lower AlAs layer and the substrate, with an embedded superlattice of 20 pairs of $(\text{AlAs})_2(\text{GaAs})_5$.

Room temperature residual carrier measurements showed that all samples presented a p character, with hole concentrations ranging from $8 \times 10^{14}\ \text{cm}^{-3}$ in the GaAs layer to $(1 - 5) \times 10^{14}\ \text{cm}^{-3}$ in the $\text{Al}_x\text{Ga}_{1-x}\text{As}$ layers. Despite the presence of residual carriers, all the samples show a very narrow free-exciton linewidth at low temperature and excitation density, well below $1\ \text{meV}$ for $x < 0.1$, indicating their high crystalline quality.

4.1.2 InGaAs/GaAs/AlGaAs/AlAs microcavity

The microcavity employed in the non-resonant excitation experiments described in Chapter 9 was grown at the *University of Sheffield* by the group of Maurice S. Skolnick and John S. Roberts. The sample was grown by metal organic vapor-phase epitaxy. The top (bottom) Bragg reflector is composed of 17 (20) repeats of $\text{Al}_{0.13}\text{Ga}_{0.87}\text{As}/\text{AlAs}$ $\lambda/4$ layers (thickness of each $\text{Al}_{0.13}\text{Ga}_{0.87}\text{As}$ layer: 616 Å, AlAs layer: 699 Å). The GaAs cavity spacer has a $3\lambda/2$ configuration, with a nominal width of ~ 1500 Å. The cavity spacer presents a wedge across the sample that enables the tuning of the cavity-mode energy by excitation in different positions of the sample. The wedge is small enough to neglect any effect related to it, within the extension of the excitation spot. Two groups of three $\text{In}_{0.06}\text{Ga}_{0.94}\text{As}$ QWs (10 nm thick each) are embedded in the GaAs cavity at the antinodes of the electromagnetic field. Within each group, the QWs are separated by GaAs barriers of 100 Å.

The cavity and excitonic linewidths measured far from resonance (i.e., at very negative and very positive detuning, respectively) are, in both cases, ~ 1 meV. The cavity lifetime is on the order of ~ 4 ps. A Rabi splitting is 6.6 meV is obtained under non-resonant PL at low temperature and low power (see Fig. 9.1).

4.1.3 GaAs/AlGaAs/AlAs microcavity

The microcavity employed in the resonant excitation experiments described in Chapter 10 was grown at the *Laboratoire de Photonique et de Nanostructures* (CNRS, Paris, France) by the groups of Jacqueline Bloch and Aristide Lemaître, and it is very similar as that studied by Perrin *et al.*[201, 200] and Bajoni *et al.*[16]. The sample was grown by molecular beam epitaxy. The top (bottom) Bragg reflector is composed of 15.5 (24) repeats of $\text{Al}_{0.15}\text{Ga}_{0.85}\text{As}/\text{AlAs}$ $\lambda/4$ layers (thickness of each $\text{Al}_{0.15}\text{Ga}_{0.85}\text{As}$ layer: 572 Å, AlAs layer: 675 Å). The AlAs cavity spacer has a $\lambda/2$ configuration, with a nominal width of ~ 1200 Å. Analogously to the microcavity described in the previous section, the cavity spacer presents a wedge across the sample that enables the tuning of the cavity mode energy by excitation in different positions of the sample. The wedge is even smaller than in the microcavity described in the previous section. Therefore, wedge effects can be neglected within the extension of the excitation spot. One GaAs wide QW (20 nm thick) is embedded in at the center of the spacer, at the antinode of the electric field. This is the QW whose exciton resonances couple to the cavity mode.

One additional narrow QW (2.6 nm thick) is present at each side of the wide QW, separated by an AlAs layer of 10 nm. The exciton resonances of these QWs are much higher in energy than any of the polariton resonances of interest here, and do not affect the polariton physics investigated in Chapter 10.

The use of a single, wide QW results in very narrow exciton linewidths, as the effect of interface fluctuations and width distributions are greatly suppressed. In this case the heavy-hole QW exciton presents a low-temperature linewidth of about 0.3 meV, while the cavity-mode lifetime is still on the order of 4 ps. The Rabi splitting in the case of the heavy-hole exciton coupled to the cavity mode is 4.4 meV.

4.1.4 Single QW sample

A single GaAs/AlAs QW sample was employed for most of the experiments shown in Chapter 7. This QW sample was also grown at the *Laboratoire de Photonique et de Nanostructures*. The sample is actually identical to the microcavity described in the previous section, but a chemical etching was performed in order to remove the upper Bragg reflector. In this way the PL from the bare QW could be accessed. The presence of the lower DBR does not affect the PL dynamics from the QW. The amount of collected light might be increased by the reflection of the PL on that mirror.

4.2 Experimental set-ups

For the experiments presented in this work two different types of excitation sources were employed:

- A continuous wave (CW) Ti:Al₂O₃ (Spectra Physics) laser pumped by a CW Ar⁺ laser. The laser can be continuously tuned between 720 nm and 860 nm
- A pulsed Ti:Al₂O₃ (Spectra Physics Tsunami) laser pumped by a CW diode-laser (SP Millenia), with tunability between 680 nm and 950 nm. The laser was operated in the picosecond configuration, with a pulse width of ~ 1.5 ps and a repetition rate of 82.1 MHz.

For the detection, two devices were employed: a high resolution CCD and a synchroscan Hamamatsu streak camera. The principles of operation of such a streak camera

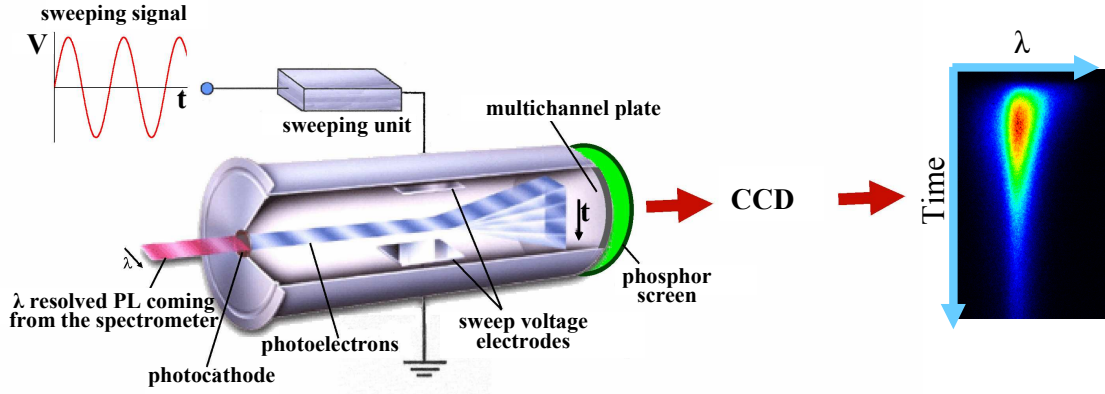


Figure 4.1: Principles of operation of a synchroscan streak camera. See text for details.

is depicted in Fig. 4.1. The light impinging upon the photocathode excites photoelectrons inside the streak tube. The photoelectrons are accelerated by an acceleration mesh (not shown). Then they travel inside the tube through a region in which there is an electric field whose strength varies in time (region between the electrodes). Early photons create photoelectrons that encounter a field that deviates them upwards. Photoelectrons created by later arriving photons suffer a field deflecting them in a different vertical direction (downwards). In this way, the vertical direction behind the electrodes acquires a meaning of time evolution.

After the electrodes a multichannel plate multiplies the number of electrons impinging upon it. Finally, the amplified photoelectrons hit a phosphor screen whose light is recorded by a CCD. In the CCD the vertical direction means time while the horizontal direction has the same meaning as the horizontal dimension of the light arriving at the photocathode, which can be wavelength or spatial dimension (real space or momentum space).

The sweeping voltage that deviates the photoelectrons has a sinusoidal shape, but only the linear part of the sinusoidal is employed. The sweeping-voltage frequency is synchronized with the repetition rate of the excitation laser via a fast photodiode. In this way, millions of identical measurements (one per excitation pulse) can be performed and signals can be obtained even in low-emission intensity conditions.

The largest time window of the streak camera has a size of 2100 ps with a resolution of about 30 ps. However the resolution can be improved below 10 ps by operating the camera in regimes with smaller time windows.

4.2.1 General time-resolved PL set-up

Figure 4.2 shows the time-resolved set-up employed for the experiments of Chapters 5, 6, and 7. The pulsed excitation beam arrives at the sample non-resonantly at small angle from the sample normal (growth direction). The sample is kept in a cold finger-cryostat where the temperature can be varied between 5 K and room temperature. The temperature sensor is placed very close to the sample holder, where the sample is attached with silver paint to ensure a good thermal contact.

The light is collected using the focusing lens, in a reflection geometry, and focused, with a second lens, on the entrance slit of a spectrometer. The spectrometer, which obtains the energy resolution in these experiments, is attached to a streak camera. For the experiments of Chapter 6 polarization optics (sets of quarter waveplates and linear polarizers) are added to the excitation and detection paths. For the experiments of Chapter 7 and Sec. 9.3 a delay stage is added to the pulsed-laser path so that excitation can be performed with two consecutive pulses on the same spot.

4.2.2 Non-resonant time-resolved PL from microcavities

The experiments described in Chapter 9 make use of a configuration very similar to that depicted in Fig. 4.2. In this case an addition is made in order to select the PL coming from different k -states of the microcavity, which consists on the inclusion of a pinhole in the detection arm, as depicted in Fig. 4.3. The pinhole is set-up so that it blocks all light except that corresponding to $k = 0$. Just by moving the pinhole perpendicularly to the optical axis, a given k -state is selected. Equation 3.15 relates the in-plane momentum of a polariton state with the angle of emission of that state. Additionally, polarization optics are employed (in the excitation and detection paths) in order to study the polarization emission dynamics.

4.2.3 The TOPO experiment

Here we will present a detailed description of the experimental set-up employed in the experiments shown in Chapter 10, where the sample is resonantly excited with CW and pulsed beams, and momentum and real space films are recorded.

As shown in Fig. 4.4, each excitation beam is directed towards the sample by an independent mirror. By positioning them at different distances from the optical axis (Δx)

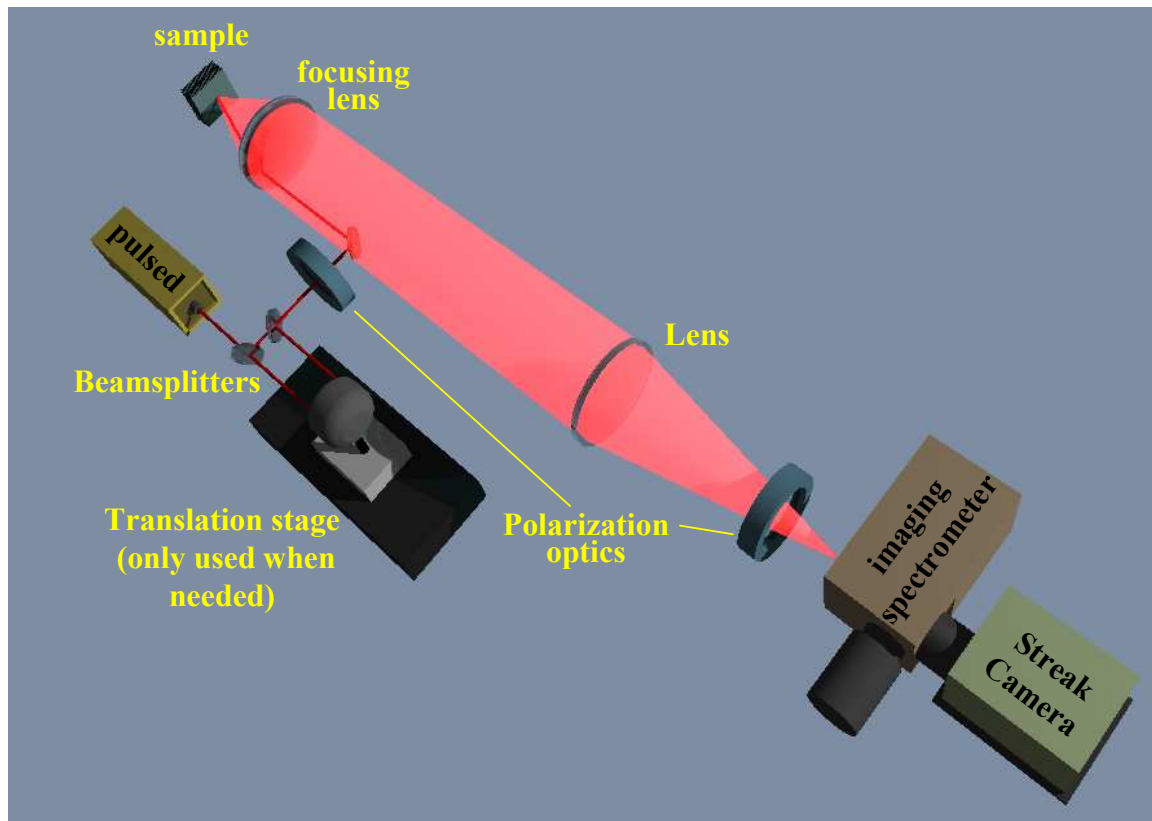


Figure 4.2: General experimental set-up for time-resolved PL under non-resonant excitation. The polarization optics and the translation stage are used only when needed.

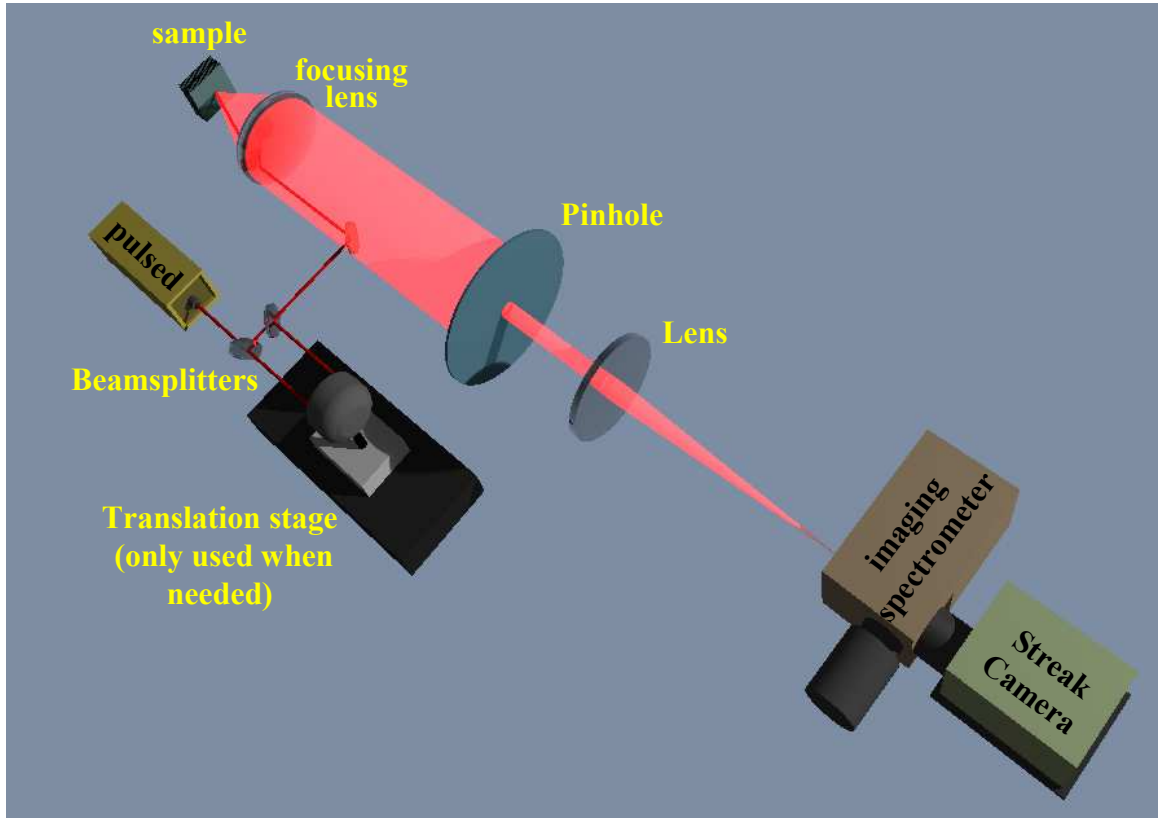


Figure 4.3: Experimental set-up for time-resolved PL under non-resonant excitation with selection of angle of emission via a pinhole. In the particular depicted configuration, the pinhole selects the $k_{\parallel} = 0$ luminescence. Polarization optics (not shown) and translation stage are used only when needed.

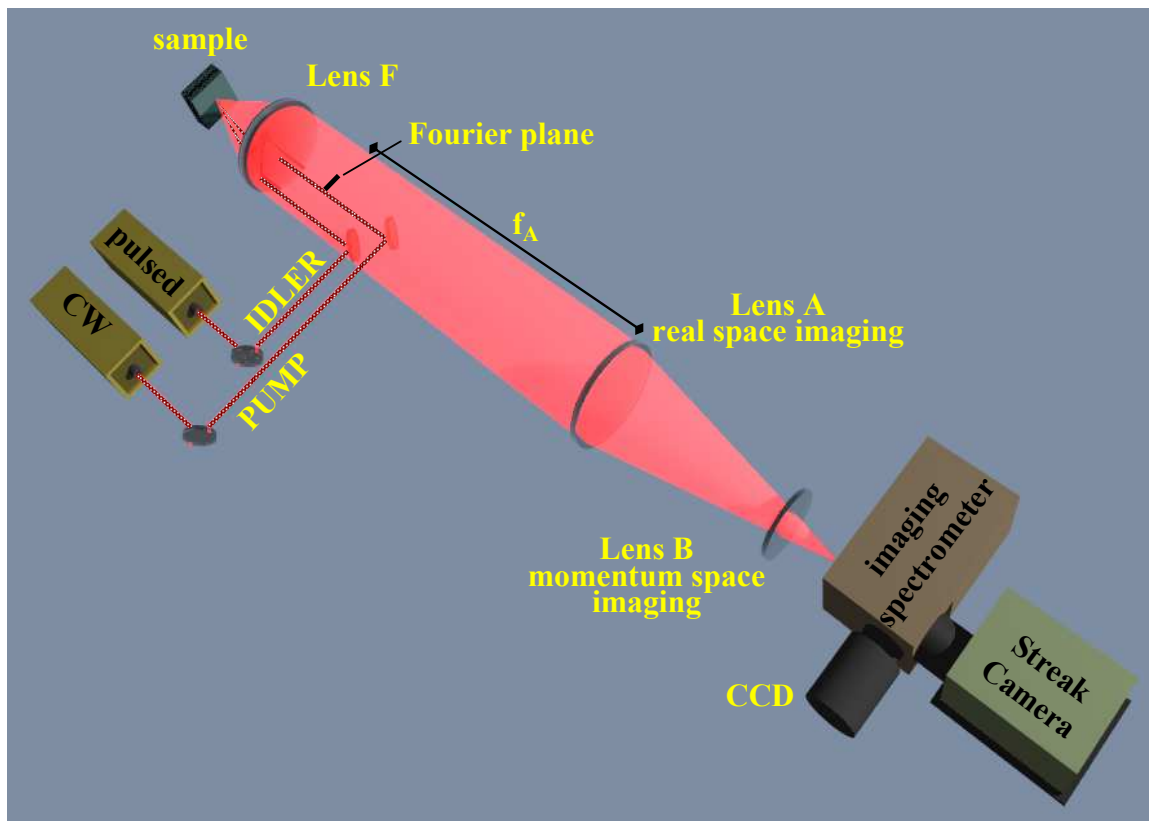


Figure 4.4: Set-up for the experiment in the TOPO configuration, in which real- and momentum-space 2D films can be recorded.

of the focusing lens F, the angle of incidence θ_{inc} of each beam can be selected ($\theta_{inc} = \arctan\left(\frac{\Delta x}{f_F}\right)$, where f_F is the focal distance of the focusing lens).

Two configurations can be used for detection. For real-space detection, lens B is removed from the set-up. Lens A forms an image of the real space of the sample's surface on the entrance slit of the spectrometer. Along the slit, a slice of the real-space image is selected and imaged either directly on the CCD or on the input slit of the streak camera. Additionally, the spectrometer disperses in energy the light arriving at the entrance slit. In this way, an image of the spectrometer entrance slit (y dimension) at a particular energy is imaged on the input slit of the streak camera. In this configuration a one dimension real space (y , the line selected by the input slit of the spectrometer) *vs* time image is obtained as an output of the system. In order to obtain 2D real-space images resolved in time, lens A is displaced sideways (x dimension, perpendicular to the optical axis), so that the x position of the image of the sample on the spectrometer entrance slit can be varied. By acquiring a number of one-dimensional y slices *vs* time at different x positions, 2D films can be composed.

If the momentum space is to be imaged, lens B is added to the set-up and lens A is moved from its previous position (at the focal distance f_A from the spectrometer entrance slit) to a distance f_A from the Fourier plane of the focusing lens F. In this way, the Fourier plane is imaged on the entrance slit of the spectrometer, and 2D films in momentum space can be recorded. The Fourier plane of the lens F is perpendicular to the optical axis and located at the focus point of this lens, symmetric to the sample (see Fig. 4.4). All rays coming out from the sample at a given angle (which correspond to a well defined in-plane momentum) form a point in the Fourier plane. The Fourier plane is therefore a map of the angular emission from the sample.

Note that switching from the real to the momentum space set-up, and viceversa, is straightforward taking just a few seconds, and the excitation conditions are not altered.

Chapter 5

Carrier dynamics of photoexcited bulk GaAs

5.1 Introduction: photocreation of carrier populations

5.1.1 Coherent and incoherent emission

Light encountering a medium with a non-vanishing susceptibility induces a macroscopic polarization which in turn creates an oscillatory electromagnetic field. The system in this situation is said to be in the coherent regime, and the polarizations can be described by the imaginary part of the solutions of the optical Bloch equations [178]. At energies close to a resonance the light matter-coupling is stronger and the induced polarization has a greater magnitude. The induced polarization in the medium is subject to dephasing processes, which limit the duration of the coherent regime, once the excitation source has been removed. Important sources of dephasing in direct gap semiconductors are the interaction (*scattering*) of the polarization fields with interface roughness and alloy fluctuations, [306, 236, 151, 101, 292] with lattice excitations (i.e., phonons), [143, 243, 277] and with carrier excitations, [143, 287, 188, 101] which limit the lifetime of the polarization field in two- and three-dimensional systems to a few picoseconds. Four-wave mixing [243, 244, 255, 289, 217], non-linear differential transmission [287] and resonant Rayleigh scattering [268, 166, 101, 167] are some of the phenomena associated to the creation (and destruction) of a polarization in the media and provide very valuable information about the specific light-scattering processes, and the dephasing mechanisms and times in a material.

The dephasing scattering processes described above lead to the decay of the polarization, which gives rise both to (i) coherent emission of light, and to (ii) the creation of populations in the semiconductor, i.e., excitons and unbound electrons and holes, which may decay. Process (i) includes both the purely coherent response of the material, which results in the emission in the reflected and transmitted directions of the excitation beam, and the coherent response arising from the decay of the polarization treated in the previous paragraph. In this case, the emission may occur in different spatial directions, as for example is the case of the *speckle* interference patterns, which retain part of the temporal phase coherence of the polarizations [see Fig. 5.1(a)].[166, 183]

As for process (ii), the populations and their subsequent radiative recombination do not retain any macroscopic phase coherence, and show no preferential direction of emission. From a conceptual point of view this situation can be regarded as the absorption mechanism of the light beam, taking place in timescales on the order of the dephasing time.

The experimental distinction between coherent emission and incoherent radiative recombination is not easy at short delays after the excitation, and not until relatively recent times a well defined picture of the observed initial light emitted by semiconductors has been obtained. For example, it has been theoretically predicted[307, 48] and experimentally observed[101] that coherent emission caused by static disorder should rise quadratically in time, while radiative recombination should do it linearly [see Fig. 5.1(b)]. When excitation densities are large, carrier-carrier and momentum relaxation enter into play and the emission is mainly dominated by the incoherent radiative recombination. [101, 288]

Unlike coherent polarizations, populations, which can be described by the real part of the solutions of the semiconductor optical Bloch equations,[178] can live very long compared to the dephasing time, as they are not affected by phase sensitive processes. For the case of optical excitation well above the band gap, the decay of the polarization gives rise to the formation of unbound electrons and holes. Due to the strong Coulomb interaction and LO-phonon scattering the formation of the electron-hole populations is very rapid (a few femtoseconds). Once the carrier populations have been created, effective carrier-carrier and carrier-phonon scattering leads to thermalized distributions of electrons and holes, i.e., distributions with a well defined temperature[225, 5] that can be well described by the Fermi-Dirac statistics.

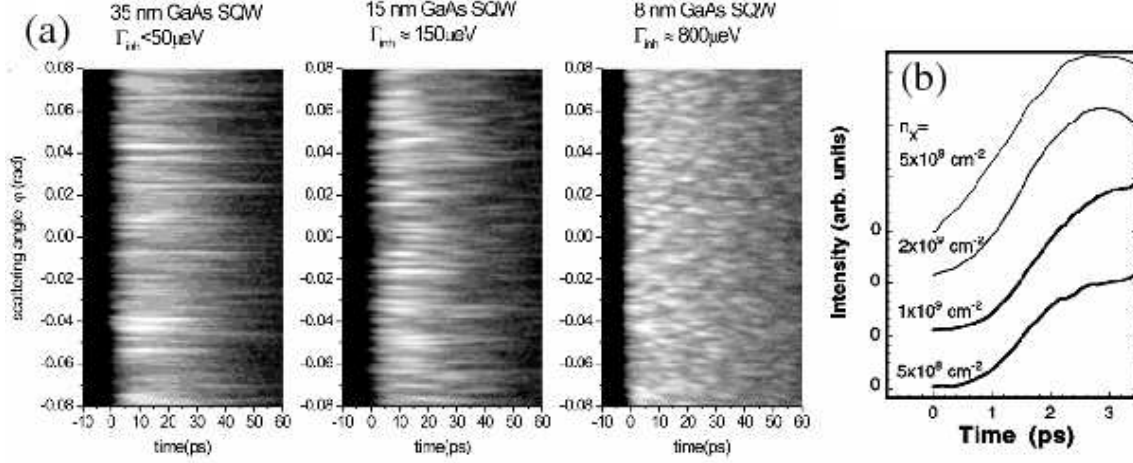


Figure 5.1: (a) Directionally and temporally resolved emission intensity (logarithmic grey scale) of a 35, 15, and 8 nm GaAs single quantum well at 5 K and low excitation intensity (exciton density of $\sim 2 \times 10^8 \text{ cm}^{-2}$). Γ_{inh} indicates the disorder induced inhomogeneous broadening of the exciton transition (from Ref. [166]). (b) Build-up of the emission at 10 K in a GaAs/AlGaAs multiple quantum well after resonant photoexcitation of the heavy-hole exciton line with a 150 fs-long pulse for different excitation densities. The rise changes from quadratic at low densities (originated from disorder induced dephasing) to linear at high densities (originated from incoherent exciton photoluminescence). (From Ref. [101]).

5.1.2 Exciton formation

Due to Coulomb interaction, the electron and hole populations in the semiconductor can give rise to the formation of excitons. Several mechanisms have been proposed for this process, the most important being geminate[204] and bimolecular[269, 250, 204, 99] formation. Geminate formation takes place directly from the correlated electron-hole pair created by the absorption of an above band-gap photon. The created correlated pair extend over the crystal with total momentum *zero*, and finally binds into an exciton via interaction with phonons. This process is dominated by optical phonon emission and, therefore, it has a threshold energy for the absorbed photons ($\hbar\omega$) given by the LO-optical phonon energy ($\hbar\omega > E_{gap} - E_b + \hbar\omega_{LO}$). As excitons may form from each generated pair, the geminate formation rate is linearly proportional to the excitation photon density. The geminate process takes place only during the time in which the correlation between the photocreated electron and hole survives. However, scattering with other carriers and phonons destroys this correlation very rapidly. Thus, the geminate formation mechanism is only possible during the time of the excitation pulse in time-resolved experiments.

In the bimolecular mechanism, excitons form from the thermalized distributions of electrons and holes. In this case a given electron interacts with all the available hole states, and the total momentum of the electron and the hole that end up conforming the excitons is not constrained. In this case the formation rate is given by the probability of interaction between electrons and holes:

$$\left(\frac{dX}{dt}\right)_{form\ bim} = C \cdot n_e \cdot n_h, \quad (5.1)$$

where X is the density of excitons formed by the bimolecular mechanism, $n_{e(h)}$ is the total thermalized unbound electron (hole) density, and C is the bimolecular formation coefficient which depends both on the carrier and on the lattice temperatures. After a pulse photoexcitation the density of carriers and their temperature changes with time, and so does C and the formation rate. In the calculation of C , LO-phonon mediated processes are the dominant contribution, also with an activation energy given by the LO-phonon energy. Acoustic phonon contributions only play a role for electrons and holes with low kinetic energies, close to the band edge [See Fig. 5.2]. Let us point out that the bimolecular formation rate is proportional the electron and hole densities, i.e. is quadratic on the excitation density (geminate is linear). Additionally, while the geminate processes only take place during the excitation pulse, the bimolecular mechanism is constantly depleting the carrier populations and forming excitons.

In the case of excitation resonant with the $1s$ -exciton transition, below the actual bandgap, the decay of the polarization can lead to the direct generation of cold incoherent exciton populations with center of mass momentum $K \approx 0$. [277, 107] Subsequent exciton-exciton and exciton-phonon interaction leads to a thermalized exciton population. [282, 288, 250] However, excitons are subject to decay processes. In particular, in high purity direct gap semiconductors the radiative decay is the most important of them. In this case, a thermal distribution of excitons cannot be truly achieved as the recombination process being selective in momentum space, is only allowed for excitons close to $K \approx 0$. Figure 5.3 shows an example of how the decay processes can affect the *thermal character* of a resonantly created exciton distribution. [203, 150]

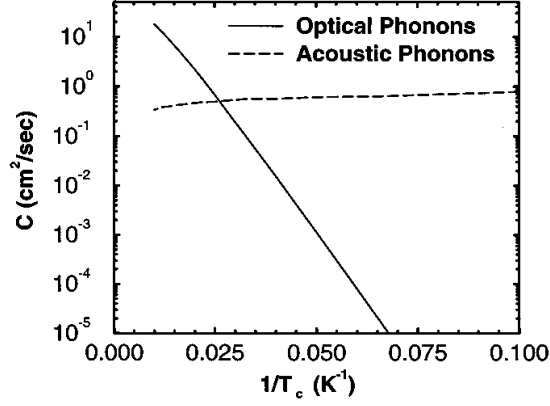


Figure 5.2: Bimolecular exciton formation coefficient as a function of the carrier temperature and for a lattice temperature of 10 K. At low carrier temperatures, electron and holes mainly populate the low energy states in the bands, and exciton formation occurs mainly via acoustic-phonon interaction. At high temperatures, carriers start to populate states with energy $\hbar\omega_{LO} - E_{bin}$ and the more efficient LO-phonon mediated process is activated (from Ref. [204]).

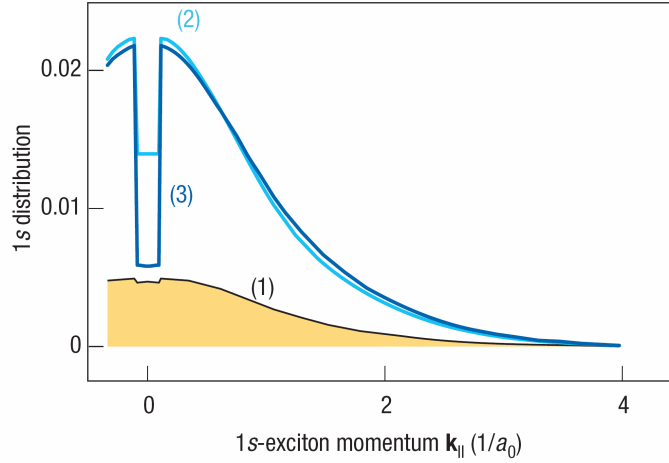


Figure 5.3: Calculated $1s$ -exciton distributions in a quantum well as a function of the center of mass momentum (in units of the exciton Bohr radius (a_0)) at different times following a pulsed photoexcitation (1.5 ps long) at the energy of the $1s$ resonance, at a delay of (1) 2 ps, (2) 9 ps and (3) 25 ps. The low momentum optically active states are depopulated due to spontaneous emission (from Ref. [150]).

5.1.3 Summary

We have just seen that the emission of light in a photoexcited direct gap semiconductor originates from (*i*) the radiative recombination of excitons, (*ii*) the pair recombination of electrons and holes, and (*iii*) emission associated to the decay of the polarization induced by the excitation source. In the first two cases the light emission is called photoluminescence (PL), and, though it is an incoherent response of the system (it has lost the excitation phase memory), it can provide valuable information about the carrier populations. In the next sections of this chapter we will concentrate on the study of the population dynamics *via* time- and energy-resolved photoluminescence. All the studies will be limited to photoexcitations at energies well above the detected signal. Therefore, coherent effects as those described in the previous paragraphs can be neglected.

5.2 Bulk GaAs photoluminescence under non-resonant excitation

5.2.1 The origin of the $1s$ exciton luminescence

The luminescence characteristics of direct gap semiconductors after photoexcitation at energies above the band-gap are dominated by the emission at the $1s$ exciton energy. Traditionally, the photoluminescence at this transition energy has been entirely attributed to the recombination of excitons with center of mass momentum $K \approx 0$. Despite the rather long history (over the last three decades) of optical studies in semiconductors, only recently a strong debate has arisen in the semiconductor community about the origin of this bright transition.

On one hand, there have been several attempts to calculate the exciton formation time by direct evaluation of the dynamics of the electron and hole ensembles, mainly in QWs.[250, 204, 99] These calculations rely on Monte-Carlo[250, 99] and Boltzmann equation approaches [204] that assume that the luminescence at the $1s$ exciton energy solely reflects exciton recombination. They have concentrated on the formation mechanisms and their effect on the time evolution of the exciton populations, but have not considered the origin of the spectral characteristics of the exciton-free carrier ensemble. On the other hand, using a quantum theory of the interaction between photons and an electron-hole population in GaAs QWs, Kira *et al.* have shown that a Coulomb-correlated unbound electron-hole

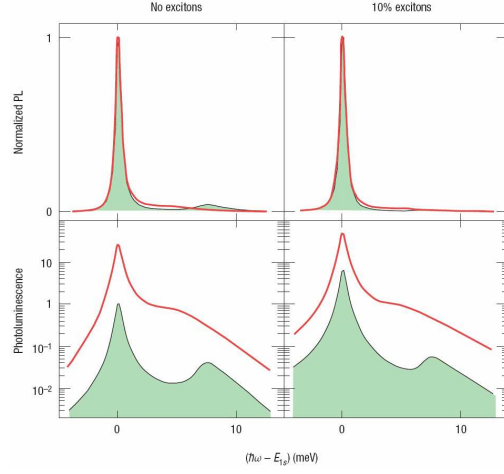


Figure 5.4: *Exciton populations or correlated electron-hole pairs as the source of excitonic photoluminescence?* The left column shows calculated luminescence spectra for an In-GaAs/GaAs quantum well on a linear (top) and a logarithmic (bottom) scale, assuming just a quasi-equilibrium electron-hole population at a temperature of 20 K without any excitonic population. The corresponding panels in the right column present the results for the same situation, but where 10% excitons in a thermal distribution have been added. The black and red curves show the situation for two different carrier densities ($\times 10^9$ and 10^{10} cm^{-2}). The linear spectra are normalized, whereas the spectra on the logarithmic scale are in absolute units relative to the peak of the $1s$ peak of the black curve in the lower left frame (from Ref. [150, 44]).

plasma can reproduce the PL features traditionally assigned to exciton recombination.[145] In particular, the work of the group of Stephan Koch has stressed that the emission at the $1s$ -exciton energy cannot be directly assigned only to the recombination of excitons, but Coulomb correlated electron-hole pairs can also participate in the emission at that energy (see Fig. 5.4).[150, 44] The debate, therefore, has recently been centered on the origin of the luminescence at the exciton energy.

The clarification of the situation by direct comparison between the theoretical predictions and actual experiments is not an easy task. Besides the need to determine the exciton and electron-hole pair recombination contributions to the PL, also the exciton formation times, exciton relaxation and thermalization and carrier cooling dynamics should be considered in the interpretation of the experimental results.[250, 62, 271, 116] A direct and simultaneous measure of the exciton and electron-hole densities as well as the exciton formation times would be desirable to clarify the situation. For instance, similar emission dynamics at the exciton and plasma energies would indicate that the emission at the $1s$ exciton line

originates from correlated electron-hole pairs.[116] Thus, time-resolved studies can provide a deep insight on this subject. Early time-resolved PL experiments already paid attention to the exciton formation dynamics.[62, 79, 222, 100, 300, 269] However these studies did not consider the unbound electron-hole contribution to the emission at the exciton energy. Only very recently, due to the availability of very high quality samples, PL experiments have addressed all these issues in detail by simultaneously considering the emission at the exciton energy and by a careful measurement of the electron-hole plasma temperature, from the recombination above the band-gap energy in high resolution experiments.[270, 271, 44, 116, 18]

New techniques like terahertz spectroscopy are worth mentioning in the investigation of these topics. Kaundl *et al.* have opened a promising path in the investigation of the thermodynamical balance between the exciton and electron-hole plasma populations.[128] By making use of a time-resolved pump and probe technique in which an infrared pump photoexcites a QW system, they can directly probe the $1s$ - $2p$ heavy-hole exciton transition with a terahertz pulse.[128] This experimental configuration enables the direct study of the exciton and plasma populations by analyzing the real and imaginary parts of the transmitted probe beams, which present very different features when the majority population of the system is conformed by excitons or by free electrons and holes.

In any case, all the above mentioned studies evidence that exciton formation is a very complex dynamical phenomenon, dependent upon many parameters.[117, 100, 250, 128, 300] These studies also show that at low temperatures and low/medium excitation densities, excitons constitute only a low percentage of the total number of excitations in the system;[250, 44, 300] however, due to the large radiative recombination rate of excitons as compared to that of band-to-band transitions, the exciton emission dominates the PL spectra. Indeed, the competition between the exciton and electron-hole pair contributions to the PL in direct gap semiconductors is still an open question, where time-resolved studies can help to clarify the situation.

5.2.2 Time evolution of the PL rise

The PL-rise dynamics at the energy of the $1s$ exciton after non-resonant excitation can be characterized by its rise time (t_r), defined as the time for the PL to reach its maximum intensity after a pulsed photoexcitation. In bulk and QW semiconductor structures, the PL rise dynamics contain very valuable information about the particular species (excitons or

electron-hole pairs) that originate the PL, the exciton formation and trapping dynamics, or the cooling/warming of the carriers after the excitation. All these ingredients are determined by the excitation conditions, lattice temperature and the particular structure and purity of the considered sample.[203] Thus, for conditions of exciton-dominated PL, the literature contains a wide spectrum of experimental data with t_r increasing[300, 100] or decreasing[62, 158, 192, 226, 79] when, for example, raising the excitation density.

If the carrier density or lattice temperature conditions are such that the PL primarily originates from electron-hole pair recombination (plasma regime), the rise-times dynamics get very short and have hardly been investigated. Most studies have concentrated on the thermalization[225, 5, 148] and cooling[285, 227, 175, 176] or warming[219] dynamics of the electron-hole gas. Figure 5.5 shows a schematic diagram of all the processes participating in the rise-time dynamics of the PL at the $1s$ -exciton energy, which will be main topic of study of the following sections in this chapter.

5.2.3 GaAs

The extraordinary luminescent characteristics of GaAs and its related compounds, like AlGaAs, along with the development of growth technologies resulting in the production of very high quality wafers, have converted these materials into the main constituents of many heterostructures like Vertical Cavity Surface Emitting Lasers (VCSELs), superlattices, microcavities, cavity Light Emitting Diodes (LEDs) or Graded Index Separate Confinement Heterostructures lasers (GRINSECHs). For this reason we are going to center the PL studies presented here in AlGaAs based heterostructures with a major emphasis in bulk GaAs. Due to particular historical scenarios,¹ while the luminescence and carrier dynamics of GaAs and AlGaAs low dimensional heterostructures have been intensely investigated,[290] little attention has been paid to the luminescence dynamics of their three-dimensional constituents. Therefore, historically there has been an important gap in the knowledge and understanding of many properties of this bulk material. Apart from its importance from a technological point of view, the use of bulk GaAs presents nice advantages over other systems in the study of many fundamental properties. GaAs samples are grown in much higher quality than any other semiconductor material, and can be easily doped. The interface roughness, typical of

¹The simultaneous availability of commercial pulsed lasers and of nanostructured semiconductors in the late 70s concentrated the attention of the optical studies on carrier dynamics on these heterostructures, diverting it from bulk III-V materials.

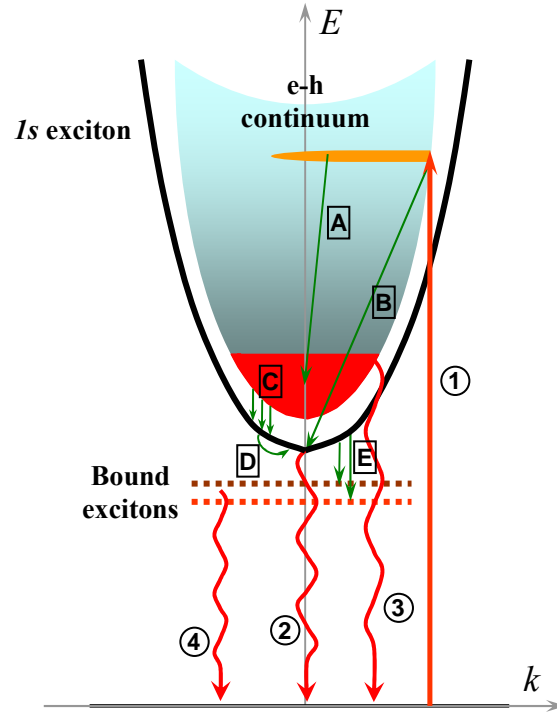


Figure 5.5: Schematic diagram of the $1s$ -exciton dispersion showing the most significant processes contributing to the rise dynamics of the PL at the $1s$ -exciton energy (2) after a pulse photoexcitation above the bandgap (1): [A] thermalization and cooling of the electron-hole plasma, [B] geminate exciton formation with $K \approx 0$, [C] bimolecular exciton formation, [D] exciton relaxation within its own band, [E] free exciton trapping into bound states, which also radiatively recombine (4). (3) indicates the free electron-hole pair recombination.

QW samples which leads to the appearance of quasi-localized states and to interface fluctuation trapping sites, is completely absent in bulk systems. Surface related defects can also be neglected, due to the large penetration depth ($0.7 \mu\text{m}$) of the light excitation. These two facts result in very narrow exciton lines with inappreciable Stokes shifts.

In the following sections of this chapter we will present novel experimental results on the photoluminescence dynamics of GaAs and AlGaAs bulk systems addressing some of the issues discussed in the preceding paragraphs. In particular we will concentrate on the effects of composition, excitation density and lattice temperature in the rise dynamics of the PL. We will see that the onset dynamics and rise times are strongly affected by the ratio of the populations of excitons and free carriers, which can be altered by changing the above mentioned parameters. The main result of this chapter is the determination and analysis of the phase diagram of the nature of the dominant contribution to the PL in the system (i.e., excitons or free carriers), in the phase space of lattice temperature and total carrier density. This phase diagram is obtained from the information contained in the PL rise dynamics. The transition from the exciton dominating phase to the plasma dominating phase can be regarded as a Mott transition, from an insulating to a conducting state.

5.3 Low power regime: exciton dynamics

As mentioned in the preceding section, little attention has been paid to the luminescence dynamics of bulk GaAs and AlGaAs. Only recently some works,[100, 262, 94] which complement but not complete older scattered studies,[273, 1, 31, 110] have investigated the emission dynamics just in GaAs. Yet, important issues in III-V alloys, such as the influence of defects or Aluminum content on the exciton dynamics, have not been addressed. In this section, results of the PL dynamics at the exciton energy at low excitation densities and low lattice temperatures will be presented.

5.3.1 Spectral and time evolution characteristics

The investigated samples were four high quality $\text{Al}_x\text{Ga}_{1-x}\text{As}$ epilayers of $2.5 \mu\text{m}$ thickness, with Al concentration $x = 0, 0.015, 0.03$ and 0.05 , grown by Molecular Beam Epitaxy.[305] All the samples, which were nominally undoped, showed p -type conductivity with hole concentrations in the range $1 - 8 \times 10^{14} \text{ cm}^{-3}$. The samples were mounted on a cold-finger cryostat, which enabled precise control of the lattice temperature. The time-

resolved photoluminescence excitation and detection configurations described in Sec. 4.2.1 were employed for this set of experiments, with a pulsed non-resonant excitation energy of 1.630 eV, and a laser excitation spot of 100 μm in diameter (FWHM). The excitation volume is defined by the FWHM of the laser spot and the penetration depth of the excitation in the material, which exponentially decays as it is absorbed with an absorption coefficient of $1.67 \mu\text{m}^{-1}$ (penetration depth of 0.6 μm). The area delimited by the FWHM of the laser spot concentrates 94% of the excited pairs, while the excitation volume concentrates 60% of the excited pairs. Thus the excitation is pretty well defined and concentrated within this volume.

Figure 5.6(a) shows the PL spectra at 5 K and low excitation density ($n = 1.8 \times 10^{14} \text{cm}^{-3}$) of the GaAs (black line) and $x = 0.03$ (grey line) samples 1 ns after the excitation. The PL is dominated by the emission from the free excitons (FX) and bound excitons (BX). In particular, attending to the emission energy,[31, 108] different types of bound exciton complexes can be identified —acceptor bound excitons ($A^0 - X$), donor bound excitons ($D^0 - X$)— as well as electron-acceptor ($e - A^0$) recombination peaks. An exciton localization energy in acceptor related sites, of about 2.7 meV, can be extracted from the peaks' position.² Despite the presence of localization centers, the narrowness of the excitonic lines (full width at half maximum below 1 meV) evidences the high quality of the samples.

At low excitation densities, the BX luminescence and $e - A^0$ recombination gets stronger than that of the FX as the Al fraction in the alloy is augmented, due to the increase in the number of defects. In Fig. 5.6(a) the ratio of the $e - A^0$ to FX luminescence intensity increases from 2.1 in the GaAs sample to 11.4 in the 3% Al one. However, at high excitation densities ($n = 7.5 \times 10^{15} \text{cm}^{-3}$) the PL is completely dominated by the FX emission in all samples, as depicted in Fig. 5.6(b). In the analysis of the time-resolved PL carried on in this section we will concentrate on the FX and $A^0 - X$ lines.

Figure 5.7 depicts the time evolution of the FX (solid points) and $A^0 - X$ (BX ; open points) emissions for the GaAs and the $x = 0.03$ samples under the same conditions of Fig. 5.6(a). We can characterize the emission rise dynamics by the time the free-exciton PL takes to reach its maximum, t_{max} . This rise time of the photoluminescence, which can be easily assigned as indicated in the figure by the horizontal bars, is considerably longer for the GaAs than for the $x = 0.03$ sample. We have observed that t_{max} is also longer for the BX

²The value of the localization energy will be important later as it sets the temperature (thermal energy) needed to ionize the bound excitons.

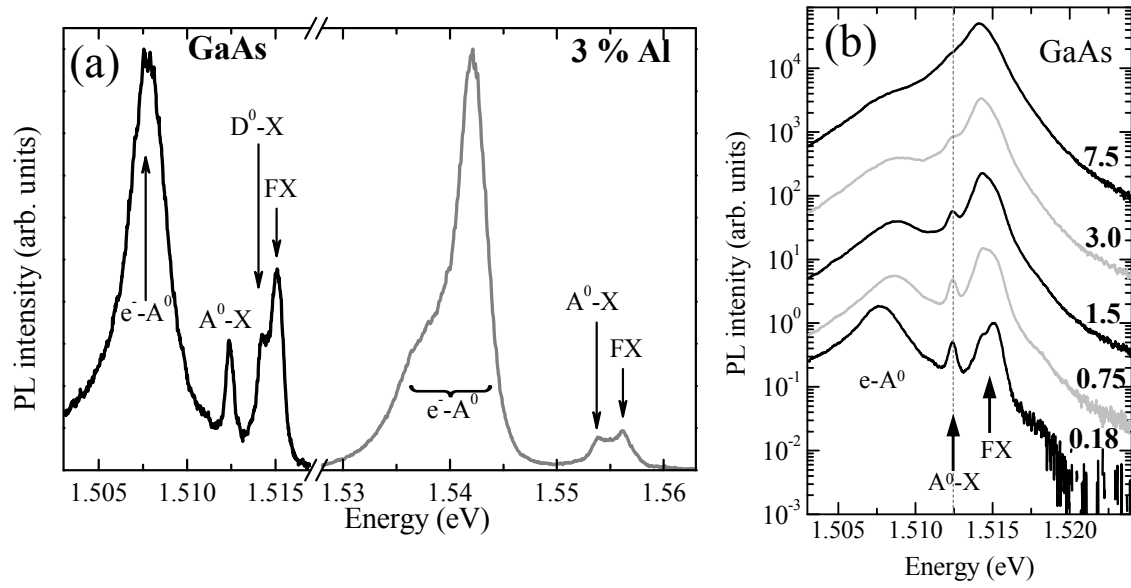


Figure 5.6: (a) Low temperature (5 K) PL spectra of the GaAs (black line) and $x = 0.03$ (grey line) samples recorded at a delay of 1 ns after excitation (excitation density $0.18 \times 10^{15} \text{ cm}^{-3}$; excitation energy 1.630 eV). (b) GaAs spectra at 5 K at different excitation densities. The numbers on the right indicate the excitation density in units of 10^{15} cm^{-3} . Each spectrum has been normalized to the FX intensity and rigidly offset.

than for the FX (Fig. 5.7) in all investigated samples, revealing longer energy-relaxation processes in the case of the BX . In addition, as can be clearly seen for GaAs in Fig. 5.7(a), the BX luminescence presents a concave time evolution at short times after the excitation, while that of the FX is convex. The concave curvature of the BX traces indicates that the build up of the BX population results from a multi-step relaxation process. Both facts, the shorter t_{max} for FX than for the BX and the concave curvature, evidence that the source of the BX luminescence is the trapping of FX with center of mass momentum $K \sim 0$, in a cascade process similar to that observed when carriers from the barrier are trapped in quantum dots.[262, 3]

5.3.2 The effect of trapping on t_{max} : rate equations model

In order to account for this cascade process we have considered a four-level rate-equation model as depicted in the inset of Fig. 5.7(b). The excitation pulse creates electron-hole pairs at high energies in the conduction and valence bands (level 3 in the inset). The free electrons and holes, which rapidly thermalize and spread over their bands,[225, 148] bind to form FX with a distributed momentum.[150] The FX relax their kinetic energy towards the radiative $K \sim 0$ states (level 2) via emission of acoustic phonons.[100] The characteristic relaxation time, τ_k , that describes the transition from level 3 to level 2, thus, reflects both the exciton formation and momentum relaxation times. Once they have reached the $K \sim 0$ states, FX can either radiatively recombine (τ_r) or get trapped in localization sites (τ_B) giving rise to a BX population (level 1), which can also radiatively recombine (τ_{rB}). The differential rate equations that describe the dynamics of such a four-level model, can be easily analytically integrated, are:

$$\frac{\partial n_3(t)}{\partial t} = -\frac{n_3(t)}{\tau_k}, \quad (5.2)$$

$$\frac{\partial n_2(t)}{\partial t} = \frac{n_3(t)}{\tau_k} - \frac{n_2(t)}{\tau_B} - \frac{n_2(t)}{\tau_r}, \quad (5.3)$$

$$\frac{\partial n_1(t)}{\partial t} = \frac{n_2(t)}{\tau_B} - \frac{n_1(t)}{\tau_{rB}}, \quad (5.4)$$

$$\frac{\partial n_0(t)}{\partial t} = \frac{n_2(t)}{\tau_{rB}} + \frac{n_1(t)}{\tau_r}, \quad (5.5)$$

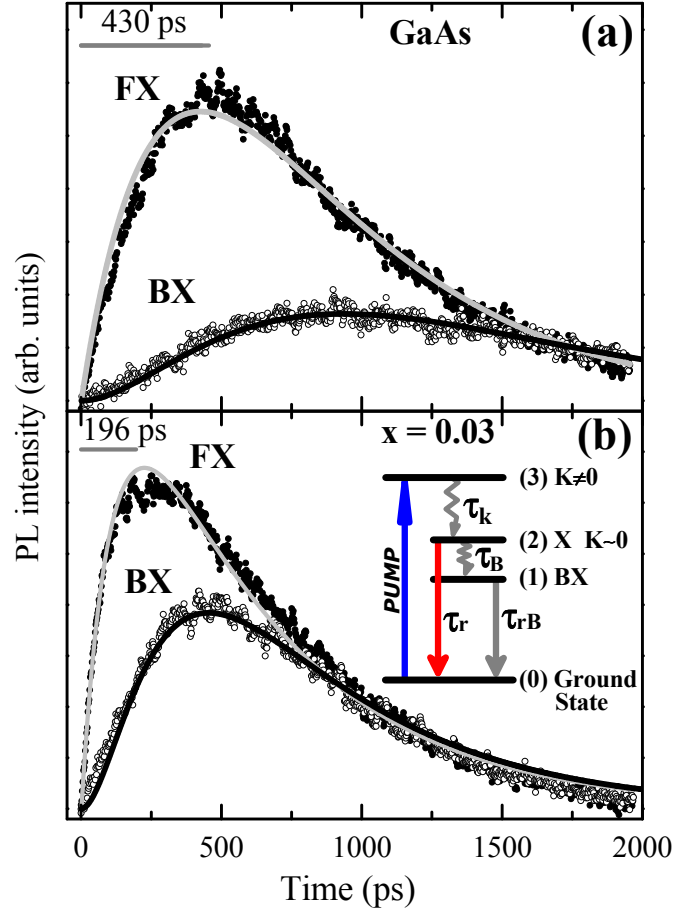


Figure 5.7: (a) Time evolution of the FX (solid dots) and the BX ($A^0 - X$; open dots) for the GaAs sample (excitation density $1.8 \times 10^{14} \text{cm}^{-3}$; $T = 5 \text{ K}$). (b) same as (a) for the $\text{Al}_x\text{Ga}_{1-x}\text{As}$ $x = 0.03$ sample. t_{max} is indicated by horizontal bars. The solid lines are fits to the model described in the text ($\tau_k = 464 \text{ ps}$, $\tau_B = 1240 \text{ ps}$ and $\tau_r = \tau_{rB} = 565 \text{ ps}$ for GaAs). The inset shows the level scheme and the transitions considered in the model.

where n_3, n_2, n_1 and n_0 are the populations of the 3, 2, 1 and 0 levels, respectively (inset of Fig. 5.7).

Figure 5.7 also shows the *simultaneous* least squares fits of the temporal traces extracted from the four-level model to the FX and BX data. For the sake of reducing the number of fitting parameters, the fits were performed assuming the same recombination times for FX and BX ($\tau_r = \tau_{rB}$). Good agreement is found between the experiments and the fits. From the fitting parameters we have found a trapping time τ_B four times shorter in the $x = 0.03$ epilayer than in the GaAs one, evidencing a density of traps about four times greater in the $x = 0.03$ sample ($\tau_B \propto [traps]^{-1}$).^[1]

Figure 5.8(a) shows the dependence of the FX - t_{max} on excitation density at 5 K for the four investigated epilayers. All the samples show a similar non-monotonic behavior,³ with a maximum t_{max} at a carrier density $n \sim 1.2 \times 10^{16} \text{ cm}^{-3} \equiv n_{x-x}$. This density corresponds to a mean distance between excitons of ~ 40 nm, which is of the same order of magnitude as the exciton Bohr radius in GaAs (11.2 nm). For $n > n_{x-x}$, exciton-exciton and carrier-exciton elastic scattering are important sources of scattering events and result in a fast relaxation of FX with large K toward the radiative states with $K \sim 0$, as previously reported in QWs.^[62, 226, 18] The higher the carrier density in the sample the more efficient these processes become, resulting in a decrease of t_{max} with increasing excitation density. For these densities, the free-carrier recombination contribution to the PL also results in a decrease of t_{max} , as will be discussed in section 5.4, in which the high density regime is treated in detail. The threshold density n_{x-x} only depends on a_B and thus is expected to be independent of the Al content for the low concentrations considered in our studies, as borne out by our experiments.

For $n < n_{x-x}$, FX - t_{max} increases with increasing excitation density. This behavior can be understood if trapping of FX in localized states is taken into account in the framework of the proposed four-level model. The PL spectra in all investigated samples are dominated by BX emission for densities below n_{x-x} . Therefore, at the lowest studied densities, there are two mechanisms for the depletion of excitons from the $K \sim 0$ FX level: (i) exciton radiative recombination, and (ii) trapping of FX with $K \sim 0$ into localized BX states. As the excitation density is increased, BX trapping states are gradually filled up to their saturation. When n is high enough, the number of available localization sites is small

³It should be mentioned that a similar non-monotonic behavior in the t_{max} dependence on n can be hinted in Fig. 4(a) of Ref. [100].

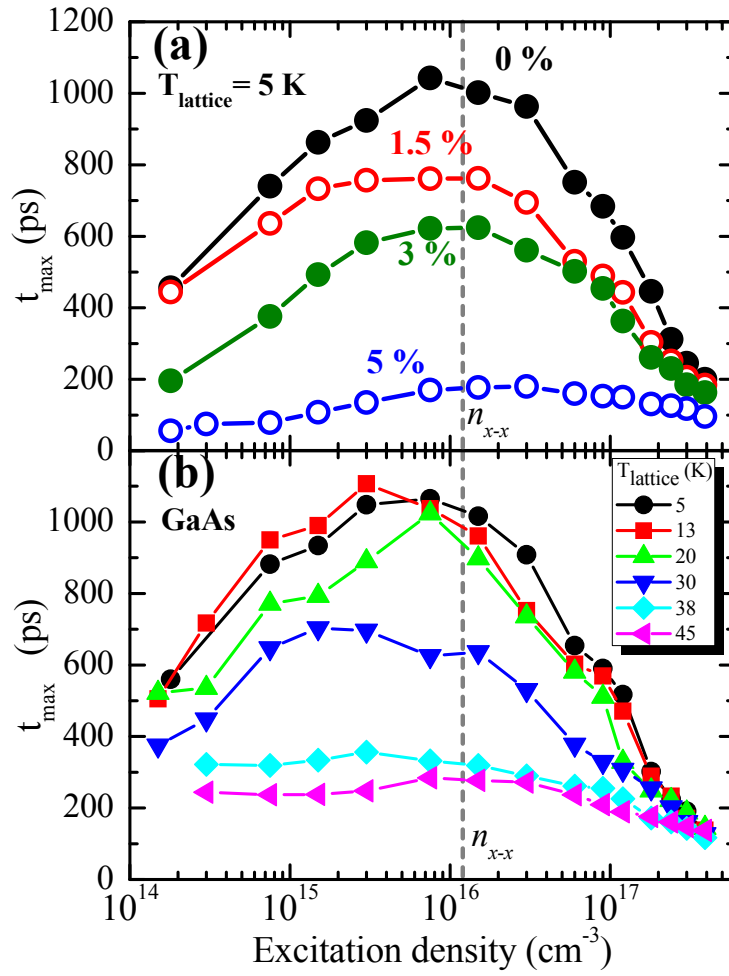


Figure 5.8: (a) Time for the free exciton to reach its maximum intensity, t_{\max} , as a function of excitation density in the four investigated $\text{Al}_x\text{Ga}_{1-x}\text{As}$ epilayers at a lattice temperature of 5 K. The Aluminum content is indicated in each curve. (b) t_{\max} as a function of excitation density for the GaAs sample at different lattice temperatures, up to 45 K.

compared to the FX population, and the trapping channel (ii) has very little effect on the dynamics of the FX population. The direct consequence of the saturation of trapping centers, and therefore, the closing of one of the depletion channels, is the increase of t_{max} .

This situation is reproduced by the model, as shown in detail in Fig. 5.9, where the time evolution of the FX -PL has been simulated according to the rate Eqs. 5.2-5.5 for different values of τ_B while fixing the values of τ_k and τ_r obtained from the fits of Fig. 5.7(a). As n increases, the number of available localization centers diminish and the trapping time increases.[1] The extreme case, when all localization centers are saturated, corresponds to the elimination of the BX level. Figure 5.9 shows that taking $\tau_B \rightarrow \infty$, the model would give a FX temporal trace with t_{max} considerably longer -512 ps- than that obtained in the presence of the localization channel -430 ps-. This is in qualitative agreement with the increase of t_{max} with carrier density shown in Fig. 5.8(a).

This simple phenomenological model can in partly account for the dispersion in t_{max} values found in the literature in GaAs epilayers, if the different densities of trapping centers inherent to all samples are considered. For instance, Shen et al. [262] find a value of t_{max} for the FX at 2 K of ~ 50 ps which is almost independent of the excitation density. This result can be well reproduced by our four level model if τ_B , is very short compared to τ_k . Indeed their PL spectra are dominated by the BX emission at all excitation powers, evidencing a high density of localization sites.

The increase of the Al content in the alloy results in two effects: (i) an acceleration of the dynamics due to the enhancement of alloy scattering, which results in the reduction of t_{max} for any n ; (ii) a larger number of alloy defect-related traps. As already mentioned above, a higher density of localization centers produces a reduction of the trapping time τ_B which, according to the four level model (see Fig. 5.9), results in an additional decrease of t_{max} for $n < n_{x-x}$, as observed in Fig. 5.8(a) when the Al content in the sample is increased. For a 5% content of Al the trapping time is reduced by a factor of ~ 20 .

In order to gain a deeper insight into the influence of trapping on the FX dynamics, time-resolved experiments have been performed at different lattice temperatures. The results for GaAs are shown in Fig. 5.8(b), which depicts t_{max} versus excitation density for temperatures (T) up to 45 K. For $T \leq 30$ K, the observed behavior follows the trends discussed above for low T (non-monotonous dependence of t_{max} on n). In contrast, if the lattice temperature is raised above the bound exciton localization energy (2.7 meV \leftrightarrow 31.3 K), the BX are ionized and trapping is hindered. In the absence of the trapping depletion

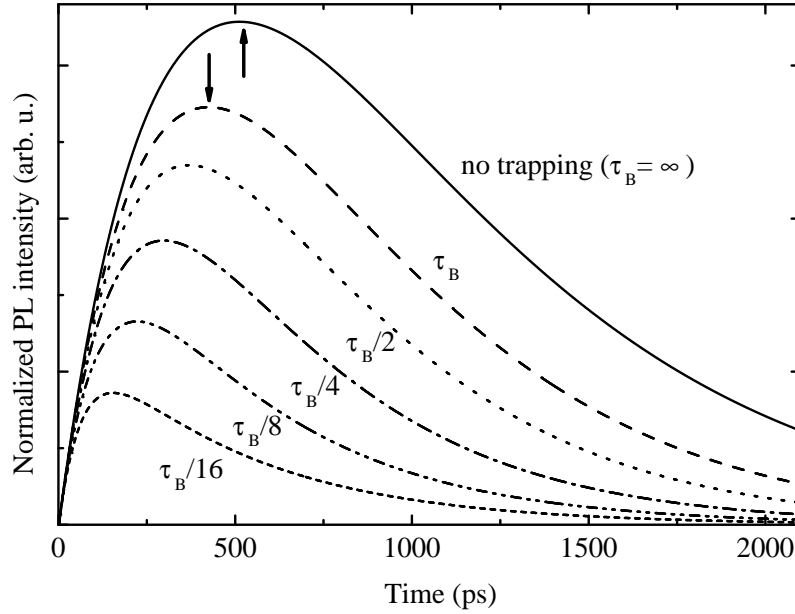


Figure 5.9: Simulated *FX* PL time evolution for different values of τ_B for fixed τ_r , τ_{rB} and τ_k [those corresponding to the fits shown in Fig. 5.7(a)]. \uparrow [\downarrow] indicate t_{max} for $\tau_B = \infty$ [430 ps, the value from the fit in Fig. 5.7(a)].

channel, according to the model, no dependence of t_{max} on excitation density for $n < n_{x-x}$ is expected, as found experimentally for $T = 38$ K and $T = 45$ K [Fig. 5.8(b)].

5.4 Medium and high power regime: towards the Mott transition

5.4.1 Introduction: Mott transition in photoexcited semiconductors

As we have just seen in the previous section, the GaAs luminescence at low power and low temperature is dominated by exciton emission, and t_{max} is greatly affected by trapping centers. In the opposite case, i.e., lattice temperature above the exciton binding energy and/or high excitation densities, the system is conformed by an electron-hole plasma and the PL is dominated by unbound electron-hole pair recombination. The carrier relaxation dynamics after a pulsed non-resonant excitation is pretty well understood in this plasma regime. Both bulk and QWs time-resolved studies have concentrated on the thermalization[225, 5, 148] and cooling[285, 175, 176, 257] mechanisms of the hot photocreated carriers but, for instance, little attention has been paid to the processes responsible

for the onset of the luminescence, characterized by t_{max} . Furthermore, the PL dynamics in the intermediate range, where a Mott transition[191] between the excitonic regime and the conducting electron-hole plasma phase should take place, has not been investigated in detail.

The concept of the Mott insulator was introduced after the studies of Mott on crystals with half-filled bands that showed no conductivity,[189] and his ideas on the transition from metallic to non-metallic states in crystals when the inter-atomic distance is varied.[190] In a metal, at large inter-atomic/valent-electron distances (or $U/W > 1$, where W is the intersite valent electron interaction and U is the intra-atomic binding Coulomb interaction) electrons are repelled from the neighboring sites and remain attached to their ions, conforming an insulator. As the density is increased (the ions in the crystal get closer together), the overlap of the valent electrons and the screening of the electron-ion binding Coulomb interactions reduces the ratio U/W to values smaller than 1, enabling the delocalization of electrons and giving rise to a metallic (conducting) phase.

In a semiconductor we can make an analogous picture to that of the metal-insulator transition. A system of dilute photocreated excitons is formed by electrons bound to holes due to Coulomb interaction. This situation would correspond to the insulating phase, in which electrons are tightly bound to holes conforming the neutral excitons. If the exciton density is increased, not only the inter-exciton distances but also the carrier screening is dramatically altered, eventually giving rise to a delocalized phase of conducting free electrons and holes, analogous to the metallic regime.

In direct gap semiconductors, the exciton and electron-hole populations can be, in principle, accessed via the energy- and time-resolved detection of their luminescence. Additionally, the density of carriers can be controlled by changing the excitation photon density in PL experiments. Thus, direct gap semiconductors, like GaAs, constitute an advantageous workbench for the study of the nature of this transition and the carrier correlations. The major complication, however, in such experiments is the difficulty in the identification of the precise exciton density present in the system at a given time, as already discussed in Sec. 5.2.

Many theoretical works have been devoted in semiconductors to the determination of the conditions of density and carrier and lattice temperature that define the Mott transition as defined in the previous paragraphs. Early studies concentrated on the calculations[279, 57, 216, 308] and experiments[256, 216] of the Mott transition phase dia-

gram in Si and Ge. However, the interest in this field has been renewed in the past four years, mainly from the theoretical point of view, concentrating in low-dimensional GaAs based systems and taking into consideration the modern perspectives on the formation, relaxation and relative contribution to the PL of excitons and electron-hole plasma.[28, 149]

In GaAs, experimental studies have been very scarce. We can quote a low-resolution time-resolved experiment performed in the early 80's in bulk GaAs[93] and two very recent studies in 2D (Refs. [131, 266]). These last two works can be included in the revival of this field that has taken place in the past 5 years. The works of Göbel *et al.*[93] and Kappei *et al.*[131] show that the Mott transition, as the density of photogenerated carriers is increased, is not abrupt. Let us also mention that recently, by means of time-resolved broadband THz spectroscopy, the group of Chemla has also addressed the issue of the exciton to electron-hole plasma transition in QWs by means of intraband differential absorption.[128, 118] Despite this experimental technique being very promising in the understanding of the phases and coexistence of the exciton/electron-hole system, this group has not reported further results on this topic.

In this section we will extend the study of the PL dynamics in bulk GaAs presented in Sec. 5.3 to a wider range of lattice temperatures (5-100 K) and excitation densities. By analyzing t_{max} and the luminescence onset dynamics we will study the interplay between the exciton and electron-hole pair recombination to the PL. As briefly discussed in Sec. 5.2 in the transition from the low temperature/low density to the high temperature/high density regimes, the origin of the major contribution to the PL shifts from excitonic to electron-hole pair recombination. Additionally, the *excitation-power dependence of the rise time* for different lattice temperatures presents a behavior typical of a metal-to-insulator transition, at a critical lattice temperature T_c . In a similar way, the *lattice-temperature dependence of the rise time* as the excitation density is increased, also undergoes a relatively abrupt change at a critical density n_c . In Sec. 5.4.4 we will present a detailed phase diagram of the Mott transition in bulk GaAs as obtained from the rise time characteristics.

5.4.2 Spectral characteristics

The first indication of the different contributions, either from excitons or electron-hole pairs, to the light emission can be obtained from the T dependence of the PL, as demonstrated in Fig. 5.10, which depicts spectra recorded 1.8 ns after the excitation at

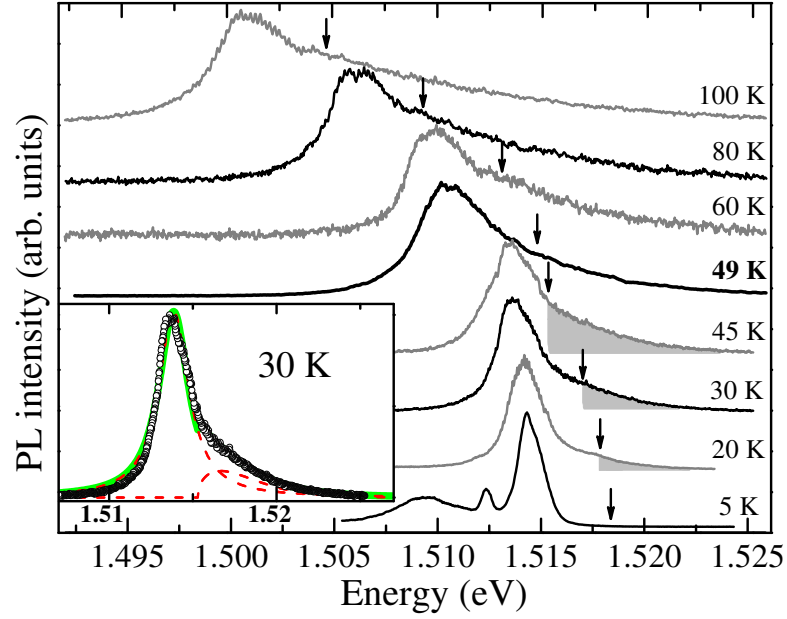


Figure 5.10: PL spectra recorded 1.8 ns after an initial pulsed excitation density of $n = 0.75 \times 10^{15} \text{ cm}^{-3}$ for different lattice temperatures, specified on the side. Arrows indicate the energy position of the band gap at each temperature using the parameters of Ref. [81]. The shadowed regions show the electron-hole pair luminescence. The inset depicts the 30 K spectrum (open symbols) and the fit to a Lorentzian plus band-to-band recombination (green solid line) as described in the text; the dashed lines show these two contributions.

different lattice temperatures for a low excitation density of $n = 0.75 \times 10^{15} \text{ cm}^{-3}$. For such a long delay, thermodynamical quasi-equilibrium between free carriers, excitons and the lattice has been reached.⁴

At 5 K the spectrum displays the characteristic excitonic emission (1.512-1.516 eV range) and electron-acceptor recombination structures discussed in Sec. 5.3. For temperatures up to a critical temperature, $T_c = 49 \text{ K}$, the spectra are dominated by the excitonic emission. In the range $5 \text{ K} \leq T < 49 \text{ K}$ the emission from electron-hole pairs becomes apparent (shaded regions) at the band gap energy (indicated by arrows), and its relative intensity increases. In this temperature range, the full width at half maximum (FWHM) of the PL band also increases with temperature (a factor of 2.2 from 5 to 45 K), as it is shown in Fig. 5.11(b). For $T_L \geq 49 \text{ K}$ the spectra present a much wider overall linewidth. Although these

⁴Thermal equilibrium between carriers and the lattice may not be reached at the lowest lattice temperatures ($T_L < 20 \text{ K}$) before all carriers have radiatively recombined, as found in QWs.[270, 176, 18] However, thermodynamic equilibrium between free carriers and excitons is present at all times (see Ref. [222]).

temperatures imply thermal energies that are above the exciton binding energy, Coulomb-correlation effects are responsible for the appearance of a wide PL peak at energies below the bandgap.[98] It is remarkable that the spectrum corresponding to $T_L \geq 49$ K undergoes an abrupt shift towards lower energies, as can be seen in Fig. 5.11(a), and it is significantly much wider than that at $T_L = 45$ K.

Let us note that the abrupt broadening that takes place at $T_L \approx 49$ K is observed not only in the overall emission band, but it also becomes apparent when we focus on each of the contributions to the PL that appear in the spectra shown in Fig. 5.10. For this purpose each spectrum shown in Fig. 5.10 is fit to a function of the form:

$$I_{PL}(E) = A \frac{w}{4(E - E_X)^2 + w^2} + B \sqrt{E - E_{gap}} \frac{1}{\exp\left(\frac{E - E_{gap} - \mu}{k_B T}\right) + 1} \quad (5.6)$$

In Eq. 5.6 the excitonic contribution to the PL is given by the first term, which is a Lorentzian of amplitude A and width w , centered at E_X . The second term corresponds to the band-to-band recombination, characterized by a 3D DOS and a Fermi-Dirac electron-hole distribution at temperature T and chemical potential μ . The inset of Fig. 5.10 depicts the PL (open symbols) together with the fit (solid line) for the case of $T_L = 30$ K, where A , B , w , E_X , T , and μ are the fitting parameters. Each of the contributions in Eq. 5.6 (excitonic/band-to-band) is plotted in dashed lines. The fits are only meaningful for T_L up to 49 K, as for higher temperatures the low energy Coulomb-correlated plasma requires a many-body treatment and cannot be described by a simple Lorentzian lineshape. The energy position and the FWHM of the Lorentzian contribution are plotted as open diamonds in Fig. 5.11. They present the same features as the overall PL (solid points), including the abrupt broadening at $T_L = 49$ K [a factor of 1.5 (1.7) from $T_L = 45$ K to $T_L = 49$ K in the excitonic (overall) PL band].

The abrupt shift and the broadening at T_c demonstrate that there are two kinds of spectra belonging to two different regimes, as we shall discuss below. Moreover, Fig. 5.11(a) shows that the exciton emission energy (diamonds) approaches the band gap (open dots) at T_c , indicating the disappearance of the exciton binding energy (exciton ionization) at this lattice temperature.

Similarly to the critical temperature just defined, we can also identify a critical density, n_c , that acts as a boundary between two very distinct behaviors if we focus on the

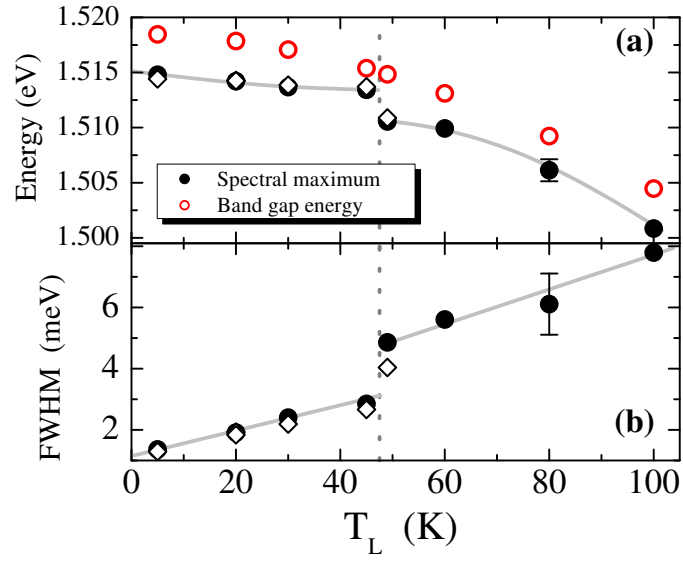


Figure 5.11: (a) Energy of the spectral maximum extracted from the curves of Fig. 5.10 (solid points) and that obtained from the Lorentzian contribution of the spectra fitted to Eq. 5.6 (open diamonds), and energy position of the band gap for each lattice temperature (open red circles; obtained from Ref. [81]). (b) Full width at half maximum (FWHM) of the whole luminescence band (solid points) and that of the Lorentzian contribution of the fit (open diamonds) for each temperature; the lines are a guide to the eye.

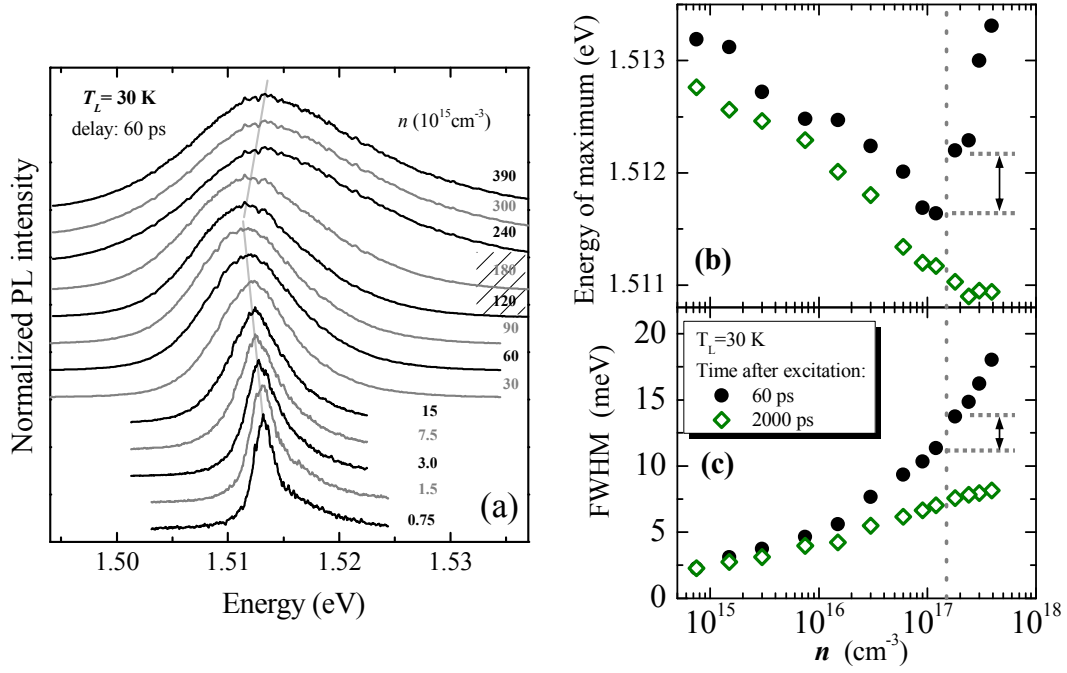


Figure 5.12: (a) PL spectra at $T_L = 30 \text{ K}$, 60 ps after the pulse arrival, for different carrier densities (shown on the right in units of 10^{15} cm^{-3}). The straight lines are a guide to the eye. (b) Energies and (c) FWHM of the PL peak as a function of carrier density at a delay of 60 ps (solid points) and 2000 ps (green diamonds). The vertical dashed line marks the boundary between the insulating and metallic phase. The arrows emphasize the peak energy shift and FWHM jump at the boundary.

spectral characteristics of the emission at a given T_L for different carrier densities. Figure 5.12(a) shows PL spectra at $T_L = 30$ K, obtained 60 ps after the arrival of the excitation pulse, for different carrier densities ranging from $0.75 \times 10^{15} \text{ cm}^{-3}$ to $390 \times 10^{15} \text{ cm}^{-3}$. Figure 5.12(a) is, then, analogous to Fig. 5.10, with n playing the role of T_L as the changing phase parameter in the observation of the spectral characteristics of the emission. The energy position of the peak of the emission shows a non-monotonous dependence on n : it red-shifts up to a density of $n_c = 120 - 150 \times 10^{15} \text{ cm}^{-3}$ and blue-shifts for larger densities, as compiled in Fig. 5.12(b) —solid dots—. Below n_c the shifts are due to many body effects, such as band-gap renormalization that red-shifts the emission. Above n_c the carriers start to fill the bands above the degeneration limit resulting in a displacement of the center of gravity of the emission towards higher energies. Finally, Fig. 5.12(c) —solid dots— shows the dependence of the FWHM on carrier density. A jump on the emitted FWHM is also apparent at n_c as marked by the arrow.

In the next sections we will see that n_c corresponds to the critical density for the transition from an exciton dominated PL ($n < n_c$) to an electron-hole plasma ($n > n_c$) dominated PL dynamics at short times. Figure 5.12(b) and (c) —green diamonds— shows that at very long times after the excitation the dependence on n of the spectral maximum and FWHM are monotonous and very similar to the situation at a delay of 60 ps for $n < n_c$, but in this case no jump is observable. This indicates that for the conditions of Fig. 5.12 ($T_L = 30$ K), at long times the system stays in the excitonic phase for all the densities used on our experiments.

In the remaining of this chapter we will concentrate on the carrier dynamics at short times after excitation, in particular we will pay attention to t_{max} . We will show experimental results on the behavior of t_{max} with T_L and n that will justify the definitions of critical lattice temperature and critical injected carrier density briefly introduced in the preceding paragraphs.

5.4.3 Rise time characteristics

Figure 5.13 depicts PL time-evolution traces at the energy of the spectral maximum for low [20 K; (a)] and high [80 K; (b)] T_L at different excitation densities, n . Let us start discussing the high excitation-density regime. The temporal traces at these densities ($n > 150 \times 10^{15} \text{ cm}^{-3}$) are qualitatively very similar for both lattice temperatures: for

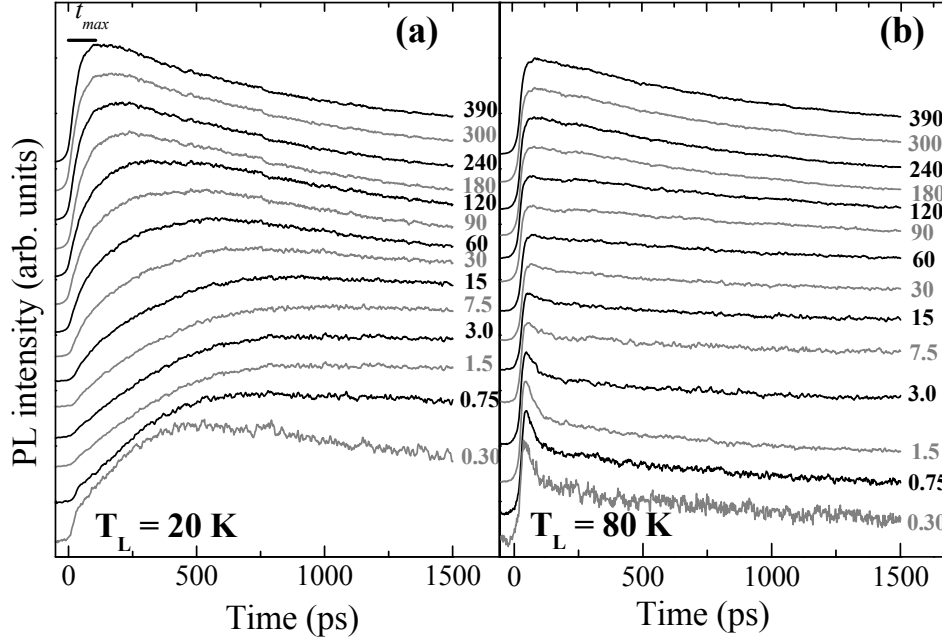


Figure 5.13: Time evolution traces at the spectral maximum for $T_L = 20$ K (a) and $T_L = 80$ K (b). The numbers on the right side of each panel show the excitation density for each trace in units of 10^{15} cm^{-3} .

such high densities the system behaves like an electron-hole plasma due to the effective carrier screening, and the initial carrier temperatures are much larger than T_L . A detailed analysis of the traces shows that for $T_L = 80$ K the rise times are slightly shorter due to the enhancement of the phonon-assisted relaxation of carriers in the bands, and to the opening of non-radiative recombination channels associated to carrier-phonon scattering at high lattice temperatures. On the other hand, at low excitation densities the PL time evolution presents very different features at $T_L = 20$ K and $T_L = 80$ K, as easily seen in Fig. 5.13.

The shape and characteristic times of the onset of the PL at low excitation densities, are strongly dependent on the lattice temperature. Figure 5.14 depicts temporal traces for an excitation of $0.75 \times 10^{15} \text{ cm}^{-3}$ at different T_L at the spectral maximum. For temperatures up to 45 K, the onset of the luminescence is characterized by two distinct features: (i) a *fast initial component* (enclosed by a circle in the trace of 20 K); and (ii) a subsequent *slower rise*. The interplay between the exciton and electron-hole pair emissions is responsible for the shape of the time evolution of the onset of the PL at the free-exciton energy. This interplay results in a competition between the *fast component* (related to electron-hole

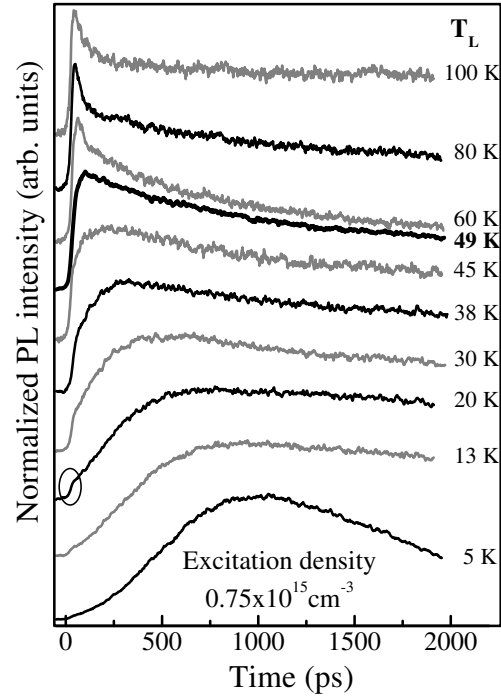


Figure 5.14: Time evolution traces at the spectral maximum of the luminescence for different lattice temperatures at an excitation density of $0.75 \times 10^{15} \text{ cm}^{-3}$. The circle encloses the *fast component* of the onset of the PL for $T_L = 20 \text{ K}$.

pair recombination) and the *slow component* (excitonic recombination) in the onset of the luminescence, as we will analyze in detail in the following paragraphs.

As we discussed in the preceding section, at low excitation densities, such as the one corresponding to Fig. 5.14, the *slow component* fully dominates the onset of the PL at the lowest T_L (5 K). Under these conditions the PL mostly arises from excitonic recombination.[270, 44] The long t_{max} reflects the slow phonon-assisted exciton relaxation from large momentum K to the radiatively active states at $K = 0$, [150] and the slow exciton formation time.[270, 18] The *fast component*, already seen at 13 K, has been previously observed in GaAs and tentatively attributed either to the emission of free electron-hole pairs[110] or to a rapid exciton formation mediated by LO-phonon interactions.[215] Our results discard the latter mechanism since the *fast component* is absent at the lowest temperature and LO-phonon emission is nearly temperature independent. Therefore, the *fast component* in the rise can be unambiguously attributed to the recombination of unbound electron-hole pairs. As T_L is increased, the *fast component* becomes more important, as can

be seen in Fig. 5.14, which implies that the fraction of excitons present in the system at short times is reduced when T_L is increased. This finding is in agreement with the computational results of Koch *et al.* presented in Ref. [149]. For $T_L > T_c = 49$ K, the *fast* initial *component* fully dominates the rise time. For those values of T_L excitons are ionized (as $k_B \cdot T_L > 4.2$ meV, the exciton binding energy, for $T_L > 49$ K) and the luminescence arises from the recombination of Coulomb-correlated electron-hole pairs. Such behavior is consistent with the observations depicted in Fig. 5.10, where the spectra above T_c is fully dominated by the electron-hole pair recombination.

We have just discussed the behavior of the *fast* rising *component* of the PL for a given low excitation density as a function of T_L . Let us now examine this dependence at a given T_L for different excitation powers. For a low T_L [i.e., 20 K; Fig. 5.13(a)], where exciton formation is not inhibited by thermal ionization, the fraction of electron-hole pairs that bind to form excitons increases with increasing excitation density.[270, 204, 250] As a result, the *fast component* in the PL rise (electron-hole recombination) is overcome by the *slow* excitonic *component* when the excitation density is increased ($0.3 \times 10^{15} \text{ cm}^{-3} < n < 30 \times 10^{15} \text{ cm}^{-3}$ at short times), as borne out by our experiments. However, with a further increase in the excitation density, screening between carriers starts to be an important factor and inhibits the binding of electron-hole pairs into excitons;[149] electron-hole pair recombination is again important and the dynamics accelerate. At the highest densities ($n > 150 \times 10^{15} \text{ cm}^{-3}$) the emission occurs mainly from electron-hole pair recombination.

The preceding discussion shows that the interplay between the exciton recombination and electron-hole pair emission determines the shape of the time evolution of the onset of the PL at the free-exciton energy. At the shortest times the emission comes mainly from electron-hole pair recombination (*fast component*). Its relative contribution to the PL, compared to the excitonic one (*slow component*), increases when T_L is increased and decreases when the excitation density is increased, as long as n is kept below $15 \times 10^{15} \text{ cm}^{-3}$. With a further increase in excitation density (above $150 \times 10^{15} \text{ cm}^{-3}$) the system is populated by electron-hole pairs as exciton formation is hindered by screening.

Figure 5.14 also shows a striking feature in the high T_L temporal evolutions. For T_L above 49 K the *fast component* of the onset of the PL is followed by an initial fast decay, which is more evident as T_L is increased. If we focus on the $T_L = 80$ K case, Fig. 5.13(b) reveals that this fast initial drop is more important at low excitation densities, being completely absent for $n > 50 \times 10^{15} \text{ cm}^{-3}$. The origin of this initial fast decay may be

sought in the warming of the electron-hole plasma. At the lowest excitation densities, the fast sub-picosecond thermalization[225, 5, 148] in conjunction with efficient LO-phonon assisted relaxation, may result in thermalized carrier populations with initial temperatures close but slightly below T_L . Figure 5.15(a) shows the initial carrier temperature $\langle T \rangle$ (averaged over the first 25 ps, i. e., just before the initial fast decay) as a function of excitation density for $T_L = 80$ K. The temperature was extracted from the high energy tail of the PL assuming, for the sake of simplicity, Boltzmann distributions.[219] Indeed, for excitation densities below $50 \times 10^{15} \text{ cm}^{-3}$ the initial carrier temperature is lower than T_L . We interpret the initial fast decay of the PL as a consequence of the warming of the carriers to T_L , which changes the carrier distributions, in particular resulting in a depletion of the states at the energy of the maximum of the PL band (close to E_{gap}), as indicated by the red arrow in the inset of Fig. 5.15(a). Figure 5.15(b) —red dotted line— shows the expected PL time evolution under such conditions of carrier warming [modeled in Fig. 5.15(c)]. This behavior has also been observed for excitons in GaAs QWs.[79] For $n > 50 \times 10^{15} \text{ cm}^{-3}$ this initial drop is absent since the carrier temperature is above T_L and, therefore, the depletion does not occur [see solid lines in Fig. 5.15(b) and (c), and black arrow in the inset of (a)]. Similar effects related to the fast redistribution of carriers in the bands and their influence in the PL dynamics, will be discussed in detail in Chapter 7.

Let us finally comment on the observed monotonic increase of $\langle T \rangle$ with n , for high carrier densities. In a low power, linear regime in which all excitations (carriers, phonons, ...) in the system are in quasi-thermodynamical equilibrium at all times, the initial carrier temperature would only be determined by the excess energy above the gap of the excitation laser. However, at high n the establishment of an initial carrier temperature and the subsequent cooling is strongly affected by (i) the screening of the carrier-carrier and carrier-phonon interaction, (ii) the electron degeneracy which may affect the cooling rates by frustrating the relaxation of electrons to the low energy states, and (iii) the creation of non-thermal phonon distributions.[176, 210, 258, 257, 227] The latter contribution causes the appearance of a phonon bottleneck and arises from the slow diffusion and decay of the carrier-generated phonons. Fast re-absorption of the excited phonons by the electron-hole plasma thus results in higher initial temperatures, as obtained from our experiments, and slower cooling rates.

The main conclusion that we can extract from all the above discussions is that a critical temperature $T_c = 49$ K can be identified, which sets a boundary in the spectral

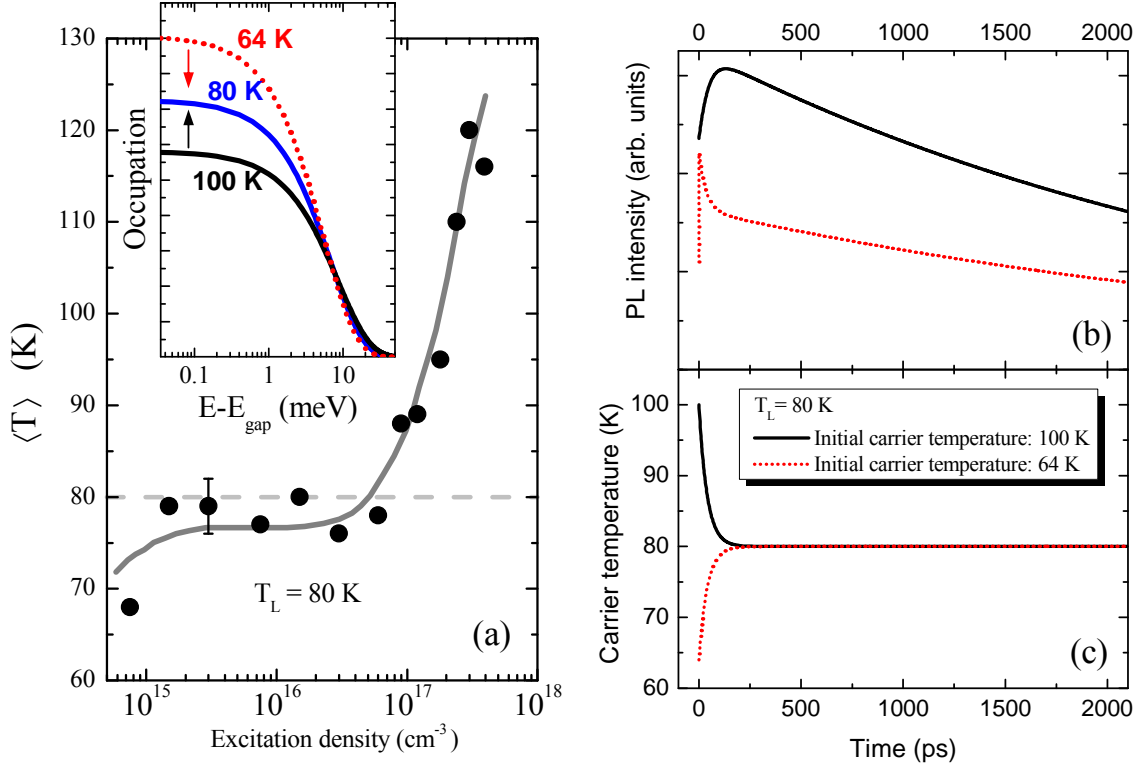


Figure 5.15: (a) Initial carrier temperature $\langle T \rangle$, (averaged over the first 25 ps), as a function of excitation density for $T_L = 80$ K; the solid line is a guide to the eye. (b) Simulated photoluminescence 0.5 meV above the band gap and (c) carrier temperature in the plasma regime. In order to simulate the curves in (b) and (c), Boltzmann distributions of electrons and holes were assumed with a carrier decay time of 3.5 ns. For the large (small) photo-injected n —solid line (red dotted line)— a cooling (warming) time of 40 ps and an initial temperature of 100 K (64 K) were employed. The inset of (a) depicts the electron occupation in the conduction band for carrier temperatures of 100 K (black line), 80 K (blue line) and 64 K (red dotted line).

(Fig. 5.10) and dynamic (Figs. 5.13 and 5.14) behavior of the carriers in the system. In the case of the dynamics, the interplay between the excitonic (*slow component*) and electron-hole pair (*fast component*) recombination is summarized in Figs. 5.16 and 5.17 for different T_L and excitation densities. Figure 5.16 depicts t_{max} as a function of excitation density, n , for different lattice temperatures. The curves can be classified in two groups, corresponding to $T_L < T_c$ (solid symbols) and $T_L > T_c$ (open symbols), plus the curve at 49 K. The t_{max} dependence on n of these groups shows certain symmetry with respect to the $T_L = T_c$ curve, with negative curvature for $T_L < T_c$ and positive for $T_L > T_c$. This symmetric behavior is characteristic of a metal-to-insulator transition,[276, 154] with T_L as the order parameter having a critical value of 49 K (in resistivity measurements in doped semiconductors the order parameter in the metal-to-insulator transition is the electron density). The lattice temperature that sets the boundary between the insulator and metal behavior in t_{max} ($T_c = 49$ K) coincides with the exciton binding energy (i. e., $k_B \cdot T_c = 4.2$ meV). This fact evidences that ionization is dominated by exciton-phonon interaction rather than by exciton-exciton scattering.

The first group of curves in Fig. 5.16, $T_L < 49$ K (solid symbols), corresponds to the excitonic insulating phase in which the onset of the PL is dominated by the *slow component* and t_{max} is governed by the exciton relaxation, as was discussed in Sec. 5.3. As discussed in that section, a detailed analysis reveals that for $n < 3 \times 10^{15} \text{ cm}^{-3}$ and T_L up to 30 K, the monotonic increase of t_{max} with density is related to the trapping of free excitons in bound states. For higher excitation densities, the steady decrease of t_{max} with increasing density arises from the fast exciton formation time and from the rapid relaxation of excitons induced by exciton-exciton scattering (see section 5.3).

The second group, $T_L > 49$ K (open symbols), corresponds to the metallic phase, with the onset of the PL dominated by the *fast component* (electron-hole pair recombination). The rise time, which increases monotonically with increasing n , is determined by the thermalization and cooling of carriers. This increase can be qualitatively explained, taking into account the initial carrier temperature, as follows. For densities above $\sim 50 \times 10^{15} \text{ cm}^{-3}$, the temperature of the initial electron-hole plasma is higher than T_L (see Fig. 5.15); carriers cool down to T_L through carrier-phonon interaction and it takes some time to reach the highest occupation of the lowest energy states, resulting in a delay for the PL to reach its maximum.[79, 270] As the excitation density is raised, the initial carrier temperature is higher and the cooling takes longer, leading to an increase of t_{max} . [176, 170, 69]

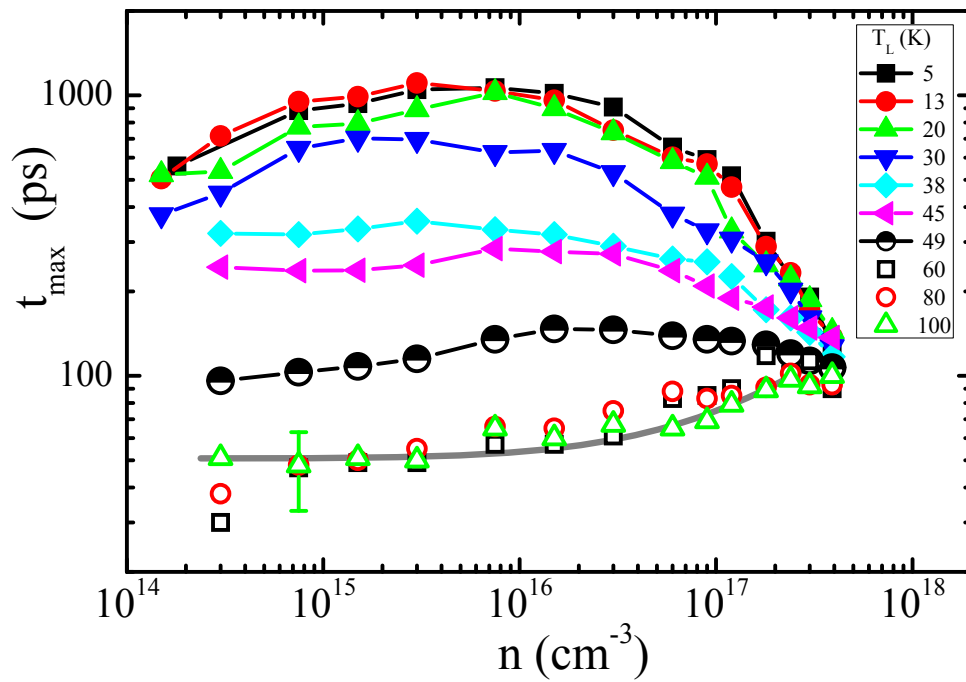


Figure 5.16: t_{\max} as a function of excitation density for different lattice temperatures. Solid symbols correspond to the excitonic/insulating phase; open symbols correspond to the electron-hole/metallic phase. The solid grey line is a guide to the eye.

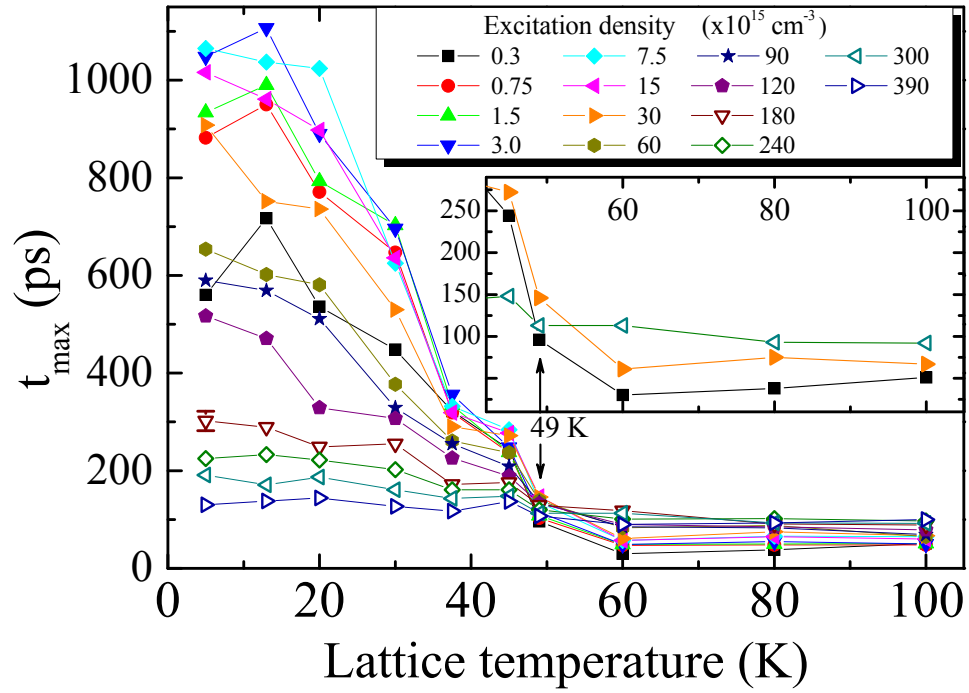


Figure 5.17: t_{\max} versus lattice temperature for each set of excitation densities (note that excitation densities are in units of 10^{15} cm^{-3}). The inset shows the temperature range 42 K-105 K in greater detail for excitation densities $0.3 \times 10^{15} \text{ cm}^{-3}$ (squares), $30 \times 10^{15} \text{ cm}^{-3}$ (solid triangles) and $300 \times 10^{15} \text{ cm}^{-3}$ (open triangles).

Only at the highest excitation densities, in the region where all the curves tend to approach a common value of $t_{max} \approx 100$ ps, the rise time is essentially characterized by electron-hole recombination for any lattice temperature, due to the effective carrier screening, as already discussed above. In order to reinforce this idea we have plotted, in Fig. 5.17, the dependence of t_{max} on T_L for several excitation densities. There is a temperature (49 K, the critical temperature) for which t_{max} is nearly independent of the excitation density. Moreover, the curves reverse their order when crossing this temperature (see inset of Fig. 5.17; only 3 curves are shown for clarity). These two facts are qualitatively identical to what is found in resistivity studies around the metal-to-insulator transition in two dimensional high mobility semiconductors.[154, 124]

Figure 5.17, shows again two groups of curves, separated by an excitation density of $\sim 150 \times 10^{15} \text{ cm}^{-3}$. For $n \leq 120 \times 10^{15} \text{ cm}^{-3}$ (solid points) and $T_L \leq 49$ K, the dependence of the rise time on lattice temperature reflects the aforementioned interplay between exciton and electron-hole pair recombination. For $n \geq 180 \times 10^{15} \text{ cm}^{-3}$ (open points) the rise-time dependence on T_L shows a behavior much less dependent on excitation density, as in this regime the carriers in the system form an electron-hole plasma (metallic state). Thus, the excitation density range $120 - 180 \times 10^{15} \text{ cm}^{-3}$ establishes a phase boundary in the characteristics of the onset of the PL, similar to the $T_L = 49$ K boundary discussed above. The metal-to-insulator transition in the system, set by this density range (densities varying by a factor 1.5), is much more abrupt than the observed Mott transition in recent experiments in QWs,[131] which takes place over an order of magnitude in excitation densities. The transition densities we find are about five times greater than the theoretical calculations for the Mott transition by Haug and Schmitt-Rink.[105] Their calculations, making use of Hartree-Fock and self-screening corrections to the exciton energy, yield a Mott density for GaAs of $28.1 \times 10^{15} \text{ cm}^{-3}$ at $T_L = 0$.

5.4.4 Phase diagram for t_{max}

The existence of a critical T_L and n in the phase space that describes the rise-time characteristics of the system enables us to compose a phase diagram for the transition from the excitonic dominated to the electron-hole pair recombination dominated luminescence. Figure 5.18 shows T_L data already depicted in Figs. 5.16 and 5.17 as a function of these two coordinates (T_L and n) in which the boundaries between the two phases are marked

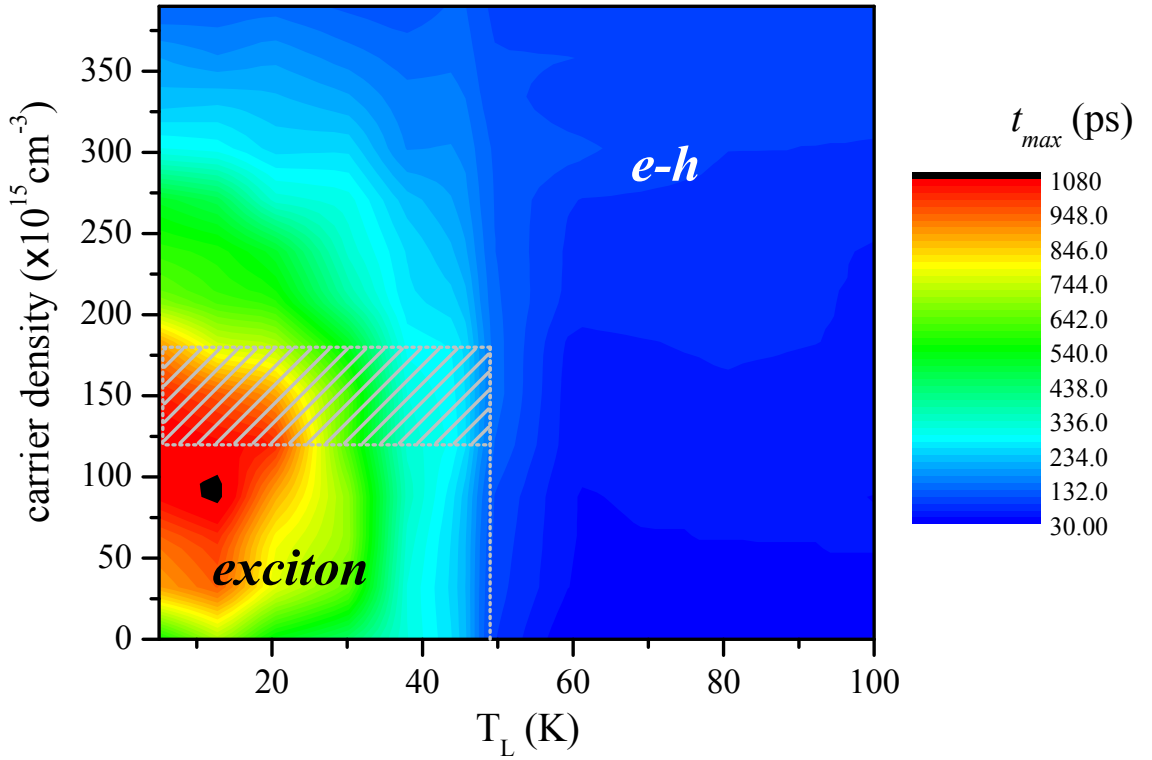


Figure 5.18: Color map of the t_{max} as a function of temperature and carrier density (in units of 10^{15} cm^{-3}). The z-scale in picoseconds is indicated on the right-hand side bar.

by dotted lines. The dashed area correspond to the carrier density range over which the transition takes place.

Finally, let us further comment on the relation between the exciton binding energy and the density and temperatures at which the Mott transition takes place. This can be readily investigated in QWs, where the binding energy can be controlled by varying the well width. One could argue that higher binding energies would lead to higher critical lattice temperatures for the metal-to-insulator transition. Theoretical calculations[206] show that for GaAs/AlGaAs QWs and a fixed lattice temperature, both the binding energy and the critical transition density increase when the well width is reduced, confirming that a stronger exciton is harder to dissociate. However, when it comes to the critical temperature the scenario is rather complex. Calculations of Ben-Tabou de-Leon and coworkers[28] show that even for a given well width (fixed E_b) the transition temperature varies from 40 K to 80 K when the carrier density is increased in a given GaAs/AlGaAs QW.

5.4.5 Summary

As a summary of this chapter, let us mention that a systematic study of the exciton/electron-hole plasma PL dynamics in bulk GaAs in a wide range of lattice temperatures and excitation densities after a pulsed non-resonant excitation has been presented. We concentrated on the onset of the luminescence and on the effect of the coexistence of free carriers and excitons on the temporal evolution of the PL. The *excitation density dependence of the rise time* for different lattice temperatures presents a behavior typical of a metal-to-insulator transition, qualitatively similar to those observed in resistivity measurements in doped bulk semiconductors,[276, 224] in high mobility two-dimensional electron systems,[153, 154, 124] or in superconducting thin films.[106, 139, 278] This transition, which is continuous but abrupt, takes place at a critical lattice temperature T_c . In a similar way, the *lattice-temperature dependence of the rise time* as the excitation density is increased, also undergoes a relatively abrupt change at a critical density n_c . Thus, monitoring the PL rise time, we have observed a transition that takes place at a density that is about five times greater than the theoretically predicted Mott transition density in photoexcited semiconductors.[105]

Chapter 6

Electron spin dynamics in the plasma regime

In the preceding chapters we have presented experimental results on the PL dynamics of carriers in bulk GaAs under very different regimes of excitation density and lattice temperatures. In this chapter we will study an additional degree of freedom that so far has not been considered, namely, the spin of the carriers in the system. In particular, we will present experimental results on the momentum dependence of the spin-flip dynamics of the electrons in bulk GaAs. We will make use of the knowledge of the phase diagram of the dynamics introduced in the preceding section in order to prepare the system in the conditions of excitation density and lattice temperature that ensure that the dominant excited population is conformed by free electrons and holes. Let us first present a brief phenomenological introduction on the state of the field of electron spin-flip in bulk semiconductors.

6.1 Phenomenological introduction

As introduced in Secs. 2.1 and 2.2, excitons, electrons and holes in semiconductors possess a spin degree of freedom. The spin degree of freedom of these particles can be accessed through optical spectroscopy given the specific polarization selection-rules that govern the light coupling to these excitations, in what has been called “optical orientation”.[187]

From the three mentioned species, the electron spin-relaxation processes have attracted the most attention in the solid-state physics community for the past three decades. This interest has been renewed recently due to the feasibility of spin-based devices for the

storage, transport and processing of information.[309] In fact, optical-orientation related techniques have proved to be extremely powerful tools for the manipulation and study of the electron-spin degree of freedom in direct gap semiconductors. An extensive review of some of the most significant experiments in this field both in bulk and lower dimensional systems can be found in Ref. [309].

Although the theoretical basis underlying the physics of the electron spin-flip processes were established in the late 1970's (a review can be found in Ref. [187]), its understanding is still a very active field of research.[179, 265, 173, 303] Theoretical studies have been performed mainly considering doped systems. They have composed a very detailed map of the electron spin-flip relaxation mechanisms under very different conditions of material composition, temperature, and doping density,[265, 78, 205, 142] and have successfully explained and predicted many of the experimental observations in this field. In the last decade, on the quest for the use of the electron spin as a fundamental constituent in spintronic devices, many experimental studies have concentrated on the design and development of GaAs-based structures with long electron spin-relaxation times,[78, 140, 286, 230, 142] which can reach the microsecond scale.[56]

However, despite all the thorough investigations, some fundamental aspects of the physics of electron spin relaxation in semiconductors have historically been neglected. One of these issues is the electron-momentum (k) dependence of the spin-flip processes. This k -dependence is of great importance not only from a fundamental point of view, but also for the design of applications that rely on the transport and injection of electrons with a preserved spin state. In these applications electrons travel some distance in the system with a non-zero momentum, and a precise knowledge of the k -dependence of the spin relaxation time may help to improve the designs.[229, 125, 88, 141] Generally, this is carefully accounted for in the theoretical derivations of the spin-flip times (τ_{sf}) under different mechanisms,[179, 265, 205] but has remained largely unexplored in experimental works. For example, in the related topic of the electron g-factor, only recently direct data has been obtained on the energy dependence of the electron g-factor in bulk GaAs.[162]

Bulk n -doped GaAs, in which the conduction band is filled up to the Fermi level with electrons coming from dopants, is not very suitable for such experimental studies since photoinjected electrons may only keep a spin imbalance at the Fermi edge.[78, 140] Then, in these systems the spin-flip times can only be investigated for electrons with momentum corresponding to the Fermi energy. In the case of p -doped and undoped GaAs samples, the

measurement of the k -dependence of τ_{sf} by optical means should be feasible, but it has simply not been performed.¹ In any case, the use of doped samples should be avoided in such studies as doping introduces (i) extrinsic scattering centers whose strength may vary depending on the dopant and even depending on the sample (compare τ_{sf} values, for the same doping concentration, in Refs. [55] and [78]); and (ii) localization centers that are critical in the determination of the spin-relaxation mechanism.[78, 230, 56]

Another fundamental issue that has not been explored until very recently, is the physics of spin-dependent electron many-body processes[211, 193, 303] and phase-space filling effects.[130, 209] Due to the difficulties in the theoretical modeling and in the analysis of the experimental results, the spin relaxation mechanisms in the regime where these effects are important are not well known.

As already anticipated, in this chapter we present experimental results on some aspects of the two aforementioned issues, i.e., the k -dependence of the electron τ_{sf} , and the spin-dependent many-body and phase-space filling effects on the electron spin-flip processes. The optical-orientation technique used to access the spin degree of electrons with different k will be introduced in subsection 6.2, while the experimental results and Monte-Carlo simulations that model the physical processes evidenced in the experimental results will be presented in Secs. 6.3 and 6.4 respectively. As a brief preview of the results contained in this section, let us mention that the experiments presented here yield the largest observed τ_{sf} in undoped GaAs.

6.2 Optical orientation

The main experimental results of this section make use of optical orientation to obtain the electron spin-flip times. In an intrinsic bulk semiconductor, the probability for the excitation of electrons from the valence to the conduction band after a circularly σ^+ polarized non-resonant pump pulse with photon energy E is given by Eq. 6.1:

$$\alpha^+(E) \propto \left[|\langle e | P_{dip} | hh \rangle|^2 \cdot \mu_{e-hh}^{3/2} + |\langle e | P_{dip} | lh \rangle|^2 \cdot \mu_{e-lh}^{3/2} \right] (E - E_g)^{1/2}, \quad (6.1)$$

where $\langle e | P_{dip} | hh \rangle$ ($\langle e | P_{dip} | lh \rangle$) is the electric dipole matrix element for the absorption of a σ^+ photon and creation of a spin-down (spin-up) electron and a $J_z = +3/2$ heavy-hole

¹In the experiments available in the literature, only a single electron energy has been studied in each investigated sample.[302, 254, 89]

($J_z = +1/2$ light-hole), E_g is the band gap, μ_{e-hh} (μ_{e-lh}) is the reduced electron and heavy-hole (light-hole) mass, and J_z is the third component of the total angular momentum. Thus, a σ^+ incident pulse excites both spin-down and spin-up electrons. Taking into account that $|\langle e | P_{dip} | hh \rangle|^2$ is 3 times greater than $|\langle e | P_{dip} | lh \rangle|^2$ if valence band mixing effects are neglected,[186] and that the reduced masses μ_{e-hh} and μ_{e-lh} are nearly the same when they are averaged in all directions of space, the maximum injected total electron spin imbalance amounts to $\sim 50\%$. Even though this is an old, well established theoretical result,[187] only recently, by means of two photon absorption techniques, Bhat and coworkers[30] have presented detailed experimental results that corroborate this theoretical prediction.

The photogenerated holes are also spin polarized but, due to the angular momentum mixing in the valence bands, they loose their spin memory in a time scale of ~ 100 fs,[111] much shorter than any other spin-flip time considered here. Therefore, for the rest of this section, we will assume that holes are not polarized.

After thermalization and energy relaxation of the carriers in the bands, the electrons recombine with the unpolarized holes, and the σ^+ polarized light emitted at energy E is given by Eq. 6.2:

$$I(E, \sigma^+) \propto \left[|\langle e | P_{dip} | hh \rangle|^2 \cdot f_{e\downarrow} f_{hh\uparrow} \cdot \mu_{e-hh}^{3/2} + |\langle e | P_{dip} | lh \rangle|^2 \cdot f_{e\uparrow} f_{lh\uparrow} \cdot \mu_{e-lh}^{3/2} \right] (E - E_{gap}^*)^{1/2}, \quad (6.2)$$

where E_{gap}^* is the renormalized band gap, $f_{e\downarrow(\uparrow)}$ are the Fermi-Dirac occupations of spin-down (-up) electrons and $f_{hh\uparrow(lh\uparrow)}$ those of $J_z = +3/2$ heavy- ($J_z = +1/2$ light-) holes. The same selection rules apply to the excitation and emission processes. σ^+ luminescence will originate from the recombination of spin-down electrons with heavy-holes, and spin-up electrons with light holes in a ~ 3 to 1 ratio. The σ^- emission [i. e., $I(E, \sigma^-)$] is given by an expression analogous to Eq. 6.2 with the arrows in the distribution functions in the opposite direction, meaning a change of sign in the spin or J_z . Then, due to the just mentioned 3 to 1 ratio in the optical selection rules, electrons mainly recombine with heavy-holes. The degree of circular polarization of the emitted light, at energy E , after excitation with a σ^+ pulse, is given by Eq. 6.3:

$$\wp(E) = \frac{I(E, \sigma^+) - I(E, \sigma^-)}{I(E, \sigma^+) + I(E, \sigma^-)}. \quad (6.3)$$

\wp provides a direct measurement of the imbalance of the two electronic spin populations.

After the pulsed injection of spin-polarized carriers, they thermalize, slowly cool down (see Sec. 5.4) and progressively flip their spin towards a spin balanced situation of electrons in the conduction band. The maximum value of $\wp(E)$ is obtained at zero delay after the excitation. The spin-flip rate of the electrons $\tau_{sf}(E)$ at a given energy can be monitored through the time evolution of $\wp(E)$. The decay time of the polarization $\tau_{\wp}(E)$ is directly connected to $\tau_{sf}(E)$ through:[274] $\tau_{sf}(E) = 2 \cdot \tau_{\wp}(E)$.

Let us mention that the use of polarization- and time-resolved PL procedures, as that described in the previous paragraphs, provide a direct quantification of τ_{sf} without the possible spurious effects and complications associated to the use of external magnetic fields and/or post-experimental theoretical fittings which are inherent to other techniques, such as those based on the Hanle or Kerr effects.[78] It also avoids other limitations present in techniques like time-resolved photoemission, which just probes the surface of the sample where the localization of carriers destroys any possibility of accessing the information on the electron momentum.[240]

6.3 Experimental results

We have used the same experimental configuration as in the experiments of Secs. 5.3 and 5.4, with the additional use of polarization optics in the excitation beam and in the PL collection path (see Sec. 4.2.1). Combinations of linear polarizers and $\lambda/4$ plates enabled the preparation of the excitation pulses in a σ^+ polarized state and the analysis of the collected luminescence into its σ^+ and σ^- components. All experiments were performed in the bulk GaAs sample at a lattice temperature of 5 K.

Figure 6.1(a) shows the GaAs PL spectrum 300 ps after the arrival of the laser pulse (energy: 1.630 eV) at low excitation density ($1.5 \times 10^{15} \text{ cm}^{-3}$), where the photoexcited electrons and holes mainly form free excitons. As only excitons with $K \approx 0$ couple to light, the spectral characteristics of the free exciton line primarily arise from the homogeneous nature of the resonance and from exciton dephasing processes.[245, 85] Due to the homogeneous origin of the free-exciton line, no spectral dependence of \wp is expected across the resonance,² as observed in Fig. 6.1(a): \wp remains almost constant along the free exciton

²Even if the excitonic lineshape would have shown inhomogeneous broadening (caused for example by alloy fluctuations), no spectral dependence of \wp would be expected. Individual excitons at slightly different energies contributing to the inhomogeneously broadened lineshape would in principle show the same spin dynamics.

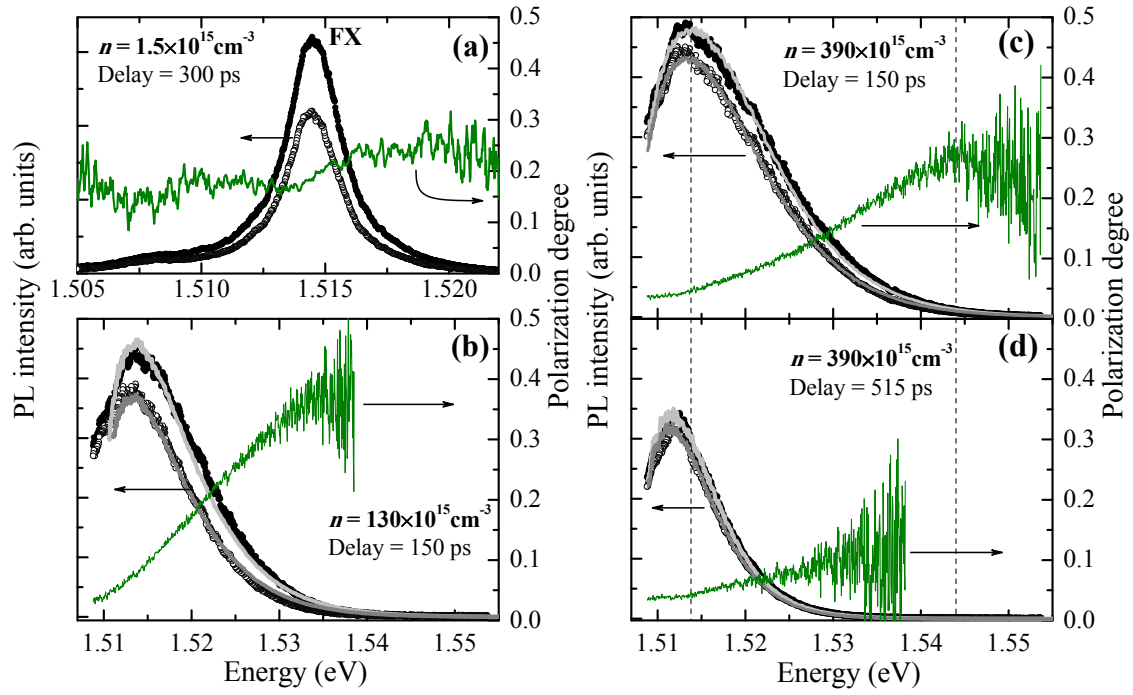


Figure 6.1: GaAs PL spectra (σ^+ —closed points—, σ^- —open points—; left scales) and degree of circular polarization (right scales) for different excitation densities and delays after the σ^+ pulse arrival: (a) very low excitation density, $1.5 \times 10^{15} \text{ cm}^{-3}$ at 300 ps; (b) $130 \times 10^{15} \text{ cm}^{-3}$ at 150 ps; (c) $390 \times 10^{15} \text{ cm}^{-3}$ at 150 ps; (d) $390 \times 10^{15} \text{ cm}^{-3}$ at 515 ps. The thick solid lines are fits to the PL as explained in the text. The dashed vertical lines in (c)-(d) depict the selected energies at which the time evolution of the PL is depicted in Fig. 6.2.

emission, and in particular at its high-energy side with a value of 0.21 ± 0.04 . The slight abrupt jump ($\Delta\phi \leq 0.05$) at the center of the line originates from a splitting between the σ^+ and σ^- components of the PL ($\sim 0.1\text{meV}$), due to inter-excitonic interactions.[281]

As was thoroughly discussed in Sec. 5.4, at high excitation densities (above $n_c \sim 120 \times 10^{17}\text{cm}^{-3}$) screening of the carriers leads to the formation of an electron-hole plasma. In this case, the σ^+ photoexcitation creates two ensembles of electrons with a high excess energy in the conduction band (with down- and up-spin in a ~ 3 to 1 ratio as discussed earlier). Again, due to strong carrier-carrier and carrier-phonon interactions, each population thermalizes within 1 ps conforming broad Fermi-Dirac distributions in the band, with a common temperature well above the lattice temperature.[225, 5] Simultaneously, an analogous process for the depolarized holes leads to the achievement of a thermal distribution also in the valence band. The carrier distributions then slowly cool down towards the lattice temperature through carrier-phonon interaction. For such high carrier densities, where exciton formation is hindered, electrons and holes with any k can radiatively recombine, as long as the total electron-hole pair momentum is close to zero (only vertical transitions between the bands are allowed). Electrons with finite kinetic energy can then recombine at energies above the gap. In this situation the PL lineshape does not originate from the homogeneous character of the resonance (as in the case of excitons) but from the occupation of electrons and holes at different energies in the band.

The kinetic energy E_{k-e} and the momentum k of the electrons that recombine at an emission energy E are related by:

$$E_{k-e} = \frac{\hbar^2 k^2}{2m_e} = \frac{m_h}{m_h + m_e}(E - E_g^*), \quad (6.4)$$

where m_e is the electron effective mass, and m_h is the heavy- or light-hole mass depending on the kind of hole with which the electron recombines.

Figures 6.1(b)-(d) show the PL spectra for two excitation densities in the electron-hole plasma regime, at different delays after the excitation pulse arrival. Very broad emission from the plasma is observed (notice the x -scales). The graphs show the widest spectral window allowed by the setup; the central detection energy was chosen in order to cover the high energy tail, which contains all the information about the electron populations. The large amount of injected carriers produces a renormalization of the band gap, due to exchange and correlation effects.[280] Band-gap renormalizations as large as 25 meV have

been reported in similar systems under analogous conditions.[39]

As clearly seen in Fig. 6.1(b), the degree of circular polarization shows a strong spectral dependence, which results from the spin imbalance of the two spin electron populations. At short delays after excitation, the occupation of electron states with low E_{k-e} (emission energy close to the renormalized band gap, 1.508 eV) is very similar for both electron spin populations, resulting in very low values of \wp . However, for higher E_{k-e} there are progressively more spin-down than spin-up electrons, yielding higher polarization degrees, which approach values of 0.4 for the lowest initial carrier density at high energy. At larger densities [Fig. 6.1(c)] an analogous spectral dependence of \wp can be observed but with smaller values. This decrease of \wp with power can originate from a broader initial distribution of carriers together with a reduction of τ_{sf} with E_{k-e} (see below) with increasing n , and/or from spectral-hole burning effects, which are more important for electrons excited from the heavy-hole than from those from the light-hole band.³ At latter times [Fig. 6.1(d)], the spin-flip processes, which tend to balance both populations, produce an overall decrease of the polarization degree. Nonetheless, the monotonous increase of $\wp(E)$ with emission energy is preserved.

We can now focus on the PL dynamics at different emission energies. Figure 6.2 depicts the time evolution traces of the σ^+ and σ^- luminescence for the highest investigated excitation density at two different emission energies [corresponding to the vertical lines in Figs. 6.1(c) & (d)]. Both rise and decay dynamics are very different in the two cases as a consequence of the relaxation and cooling dynamics of the electron ensembles. At low (high) energies the PL evolution reflects the radiative recombination and the filling (emptying) of electronic states. The cooling process of the electron populations from high- to low energy states results therefore in a slow (fast) dynamics at low (high) energies.[240]

In the lower panels of Fig. 6.2 the time evolution of \wp , extracted from the upper panels traces, is presented. \wp decays with time and τ_\wp can be obtained by fittings to mono-exponential decay functions.

Figure 6.3(a) depicts the electron spin-flip time τ_{sf} obtained from τ_\wp , for different excitation densities as a function of electron kinetic energy in the conduction band. To obtain the kinetic energy we have used Eq. 6.4 assuming that the emission energy comes

³Nemec *et al.* (Ref. [193]) have reported significant non-linear effects in pump-and-probe configurations under strong optical pumping above the bandgap. However, these effects are negligible in PL experiments, as those considered here.

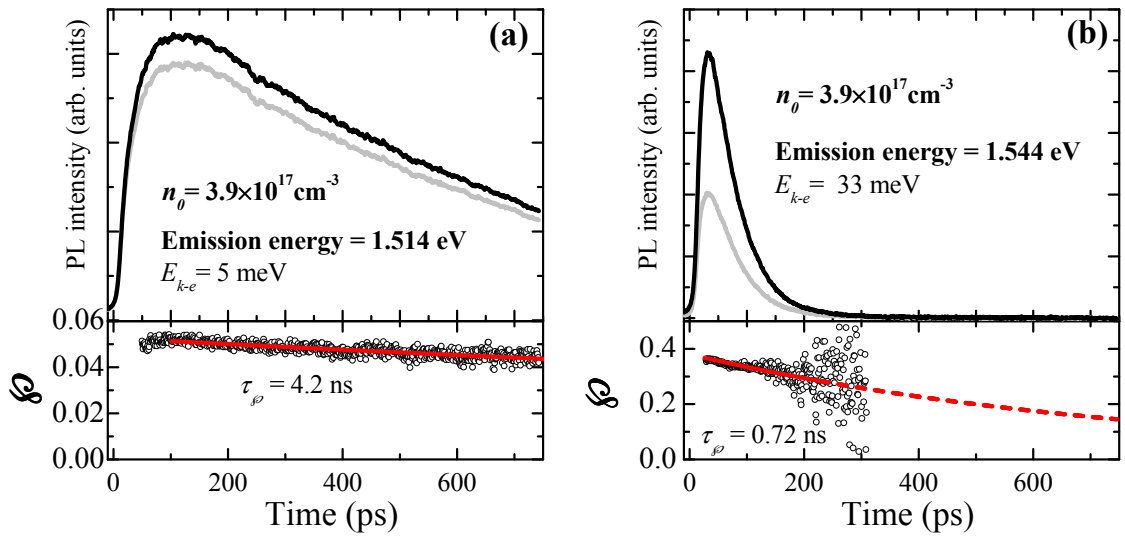


Figure 6.2: PL intensity (upper panels) of the σ^+ (black line) and σ^- (grey line) components, after σ^+ excitation, for the highest excitation density ($390 \times 10^{15} \text{ cm}^{-3}$), at two emission energies [denoted by vertical lines in Figs. 6.1(c) and 6.1(d)]: (a) 1.514 eV ($E_{k-e} = 5 \text{ meV}$); (b) 1.544 eV ($E_{k-e} = 33 \text{ meV}$). The lower panels show the corresponding degree of circular polarization. The lines are fits to an exponential decay function, with polarization decay times of 4.2 ns in (a) and 0.72 ns in (b). Note the different vertical scales in (a) and (b).

from *electron* and *heavy-hole* recombination. The renormalized band-gap energy, E_{gap}^* has been obtained from the fits to the PL that will be discussed in Sec. 6.4 τ_{sf} increases with excitation density and decreases with increasing electron kinetic energy. Values of τ_{sf} up to 26 ns are obtained for low E_{k-e} at the highest density. These are the longest spin-relaxation times reported in a nominally undoped GaAs sample, and of the same order than those reported for lightly doped *n*-type GaAs.[56] As it will be discussed in the following sections, the observation of such long τ_{sf} is related to the Pauli blockade of the spin-flip processes for electron states with occupations close to 1.

6.4 Monte-Carlo simulation and discussion of the experimental results

6.4.1 Spin relaxation mechanisms

The three main electron spin relaxation mechanisms in bulk zinc-blende semiconductors are the Elliot-Yaffet (EY),[82, 299] D'yakonov-Perel (DP) and Bir-Aronov-Pikus (BAP).[32, 33] Let us briefly discuss them.

EY arises from the spin-orbit interactions of conduction band electrons. This coupling mixes opposite spins in the electron wavefunctions due to *bulk inversion asymmetry*⁴-related terms in the electron Hamiltonian, and more importantly, mixes electron wavefunctions with valence band states. In this way, when scattering with carriers, impurities or phonons, electrons have a finite probability of flipping their spin. The spin-flip rate for an electron with kinetic energy E_k following this mechanism is given by:[205]

$$\frac{1}{\tau_{sf}^{EY}} = \frac{16}{27} \Phi \left(\frac{E_k}{E_{gap}} \right)^2 \eta^2 \left(\frac{1 - \frac{1}{2}\eta}{1 - \frac{1}{3}\eta} \right)^2 \frac{1}{\tau_p}, \quad (6.5)$$

where Φ is a cross section related to the dominant scattering mechanism, τ_p is the electron momentum relaxation time, and $\eta = \frac{\delta E_{so}}{\delta E_{so} + E_{gap}}$. The EY mechanism is important in narrow gap semiconductors, where band mixing effects are more important, as indicated by Eq. 6.5, or at very low temperatures.[265]

DP purely originates from the spin splitting caused by *bulk inversion asymmetry* (Sec. 2.1.3), which results in electrons with the same wavevector k but opposite spin having

⁴This effect has been briefly mentioned in Sec. 2.1.3 and arises from the mixing of the spin terms in the electron Hamiltonian.

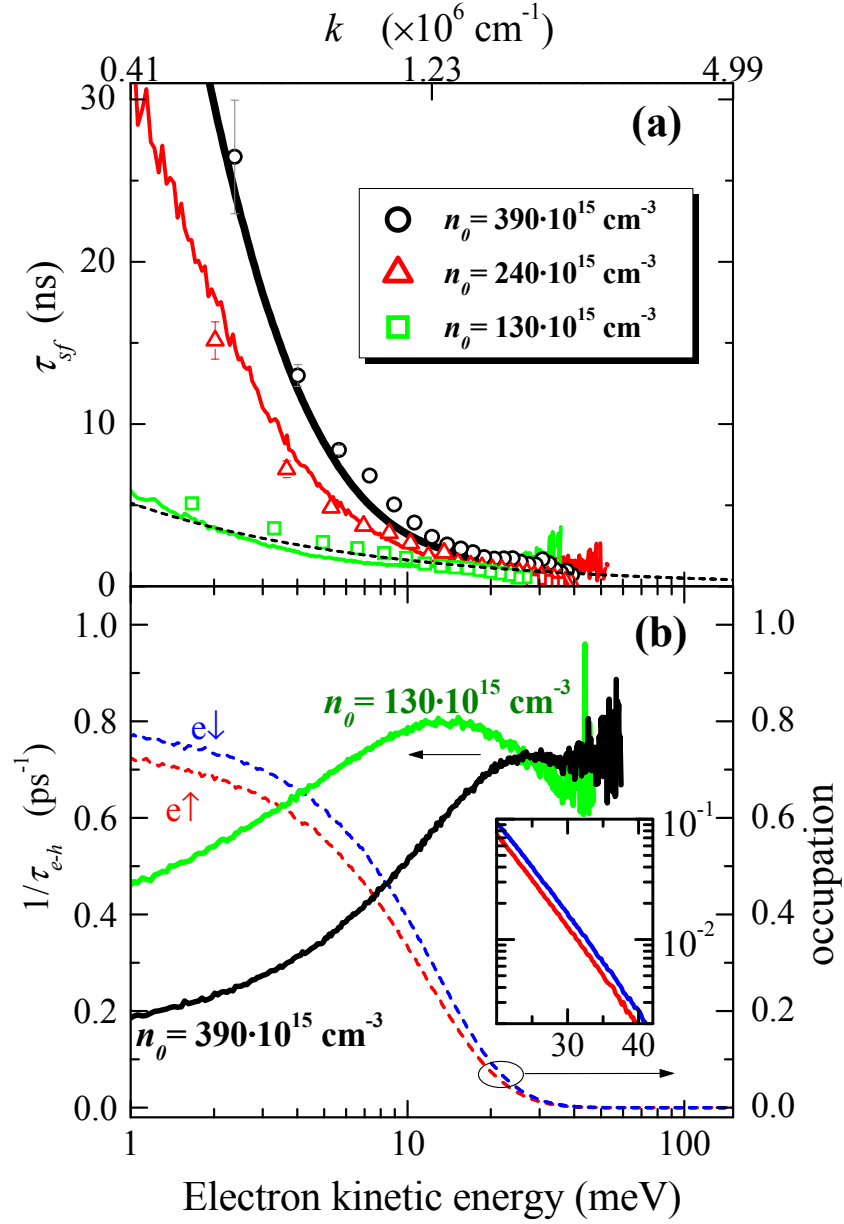


Figure 6.3: (a) Measured spin-flip time as a function of the electron kinetic energy for initial excitation densities of $390 \times 10^{15} \text{ cm}^{-3}$ (circles), $240 \times 10^{15} \text{ cm}^{-3}$ (triangles) and $130 \times 10^{15} \text{ cm}^{-3}$ (squares). Solid lines depict the fitted spin-flip time as discussed in the text. The dashed line corresponds to the non-degenerate case ($\tau_{sf}^{non-deg}$, Eq. 6.9) with a hole density of $143 \times 10^{15} \text{ cm}^{-3}$, which corresponds to the hole density at 150 ps for the highest excitation case ($n = 390 \times 10^{15} \text{ cm}^{-3}$). The black dashed line is then to be compared with the solid black line. (b) Occupation of the electron states with spin-down and -up (dashed lines), as well as the total electron-hole scattering rate (solid dark line) for the excitation and time delay shown in Fig. 6.1(c). The solid light green line depicts the scattering rate for the conditions of Fig. 6.1(b). The inset presents a zoom of the electron occupations in order to clearly show the electron spin imbalance in the 20-42 meV electron kinetic energy range. The non-linear upper scale in (a) corresponds to the momentum of the electrons.

slightly different energies. The splitting can be modeled as originating from an effective, internal magnetic field in the direction of k . Electron collisions randomly change the direction and magnitude of k , giving rise to a τ_{sf} inversely proportional to the electron scattering time τ_p :[205]

$$\frac{1}{\tau_{sf}^{DP}} = \frac{32}{105} \gamma \alpha_c^2 \tau_p \frac{E_k^3}{\hbar^2 E_{gap}}, \quad (6.6)$$

where γ is a parameter that accounts for an average of the angular dependent scattering probability and depends on the dominant scattering mechanism, and $\alpha_c \approx \frac{4\eta}{\sqrt{3} - \eta} \frac{m_e^*}{m_0}$ [265]

BAP relies on the electron-hole exchange interaction. In an scattering process like the one depicted in Fig. 6.4, the involved electron and hole have a finite probability of exchanging their spin. This action in itself is not enough to relax the spin of an electron ensemble, as an electron which just flipped its spin in this exchange process could flip its spin back by scattering with another hole. However, due to the valence band mixing, holes randomize their spin in a time-scale much shorter than the electron-hole scattering time. In this way, a process such as the one described in Fig. 6.4 effectively contributes to the relaxation of the electron spin. In the case of a non-degenerate system τ_{sf} is given by:

$$\frac{1}{\tau_{sf}^{BAP}} = \Gamma_p \frac{\mu_{eh}^{1/2} a_B^4}{\hbar} n_h \sqrt{E_k}, \quad (6.7)$$

where n_h is the hole concentration in the system, and Γ_p is a rate related to the electron-hole exchange and scattering probabilities. The most important feature from Eq. 6.7 is that τ_{sf} is directly proportional to the electron-hole exchange and scattering time.

For temperatures above ~ 4 K and very weak photoexcitation, DP is the dominant mechanism in n -GaAs, and in p -GaAs for doping concentrations below 10^{16} cm^{-3} . At higher acceptor concentrations, the main spin-relaxation mechanism is BAP.[265] Theoretical calculations predict that, in undoped samples under weak photoinjection, the main spin relaxation mechanism is DP.[265] We are interested in a situation of strong optical pumping in an undoped semiconductor, which has not been explored in detail.[254] Under this circumstance, a high electron concentration would favor a spin relaxation mechanism based on DP but, on the same ground, a high hole concentration would result in the enhancement of the BAP mechanism.[265, 78, 140] However, if we extrapolate the results for electron-spin relaxation obtained in doped samples, where the BAP relaxation rate in p -type materials is much stronger than the DP in n -type for the same doping concentrations,[265, 230] we

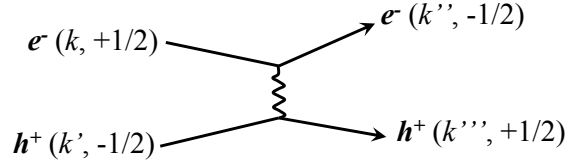


Figure 6.4: Electron-hole scattering event with spin exchange (momentum, J^z). Note that momentum and spin are conserved in the process as $\mathbf{k} + \mathbf{k}' = \mathbf{k}'' + \mathbf{k}'''$

expect the BAP mechanism to dominate the electron-spin relaxation in undoped samples under strong pumping. The BAP mechanism is so efficient in flipping the electron spin, as compared to DP, that even in n -doped samples the presence of photoexcited holes has been proved to shorten the spin lifetime due to the efficient electron-hole exchange scattering (see Ref. [142] and the inset of Fig. 2 in Ref. [78]). Additionally, calculations of Fishman and Lampel[89] and Maialle[179] show that, for hole concentrations similar to the ones photoinjected in our system and electron kinetic energies below 100 meV, the spin relaxation rate associated to the BAP mechanism is up to 3 orders of magnitude greater than that associated to the DP mechanism.

6.4.2 Monte-Carlo simulations: phase-space filling effects

In strongly excited systems, on the top of the intrinsic spin-relaxation mechanisms, phase-space filling effects can be of great importance. Spin-flip rates can be highly influenced by the occupation of the final electron state. In the framework of a *spin relaxation fully dominated by the BAP mechanism*, and in order to explore the influence of the phase-space filling effects, we have performed Monte-Carlo simulations of the carrier populations that evaluate the electron-hole scattering rates ($1/\tau_{e-h}$) under our experimental conditions.

The injected electrons and holes in the Monte-Carlo simulations scatter among themselves and with phonons, conforming thermalized Fermi-Dirac distributions. The carrier-carrier and carrier-phonon scattering processes, which carefully include final-state exclusion effects, are accounted for by using a static multiscreening approach as discussed in Ref. [225]

with the simplification of considering only degenerate Γ conduction bands, and a heavy-hole valence band (no light-hole band), all of them parabolic. The simplification in the use of a heavy-hole valence band only, is justified in our case as the electron—light-hole scattering has a very weak influence on the electron spin-flip time.[179]

Before proceeding to the calculation of τ_{e-h} one needs a precise knowledge of the electron and hole distribution functions, $f_{e\uparrow(\downarrow)}(E)$ and $f_{hh}(E)$, for each considered excitation density and time-delay after excitation (the spin in the hole distribution can be neglected due to the depolarization of the holes). In order to do so, at a given time delay we have simultaneously fitted the σ^+ - and σ^- -PL emission with $I(E, \sigma^+)$ and $I(E, \sigma^-)$ [Eq. 6.2], respectively. We have used the density of each type of carriers, their temperature and the renormalized gap as fitting parameters. In the fits, electrons and holes are forced to stay in thermodynamic equilibrium, i.e., the temperature of spin-up electrons, spin-down electrons and holes is the same, and the total density of holes is equal to the total density of electrons. By performing such fits at different delays, the time-dependent $f_{e\uparrow(\downarrow)}(E)$ and $f_{hh}(E)$ can be obtained. The thick solid lines in Figs. 6.1(b)-(d) depict the results of these fits for different excitation powers and delays. Table 6.4, show the temperature and carrier densities extracted from the fits to the analyzed σ^+ - and σ^- -PL spectra.

Once the distribution of spin-up and spin-down electrons and holes is obtained from the experiments, we can proceed to the calculation of τ_{e-h} . The Monte-Carlo method enables us to calculate the electron-hole scattering rates for each fitted delay. In the simulations, a carrier is randomly chosen from the spin-up/-down electron or hole distributions and made to scatter with electrons, holes or phonons with a probability given by the above mentioned static multiscreening approach.[225]

The Monte-Carlo method here employed can only compute the direct Coulomb carrier scattering. Actually, accounting for the exchange interaction in inter-particle scattering goes beyond the scope and capabilities of the standard Monte-Carlo simulation of the relaxation dynamics of a photoexcited electron-hole distribution. To the best of our knowledge, only very preliminary attempts in such direction have been presented in the literature (see, e.g. Ref. [87]). We have therefore considered explicitly only the direct Coulomb-like carrier-carrier interactions. We will phenomenologically account for the effect of the exchange interaction via a fitting on the results of the results of the direct Coulomb scattering results, as will be explained in detail later.

The electron-hole scattering rates are calculated by integrating during a fixed time

(a)

delay (ps)	$T_{carriers}(K)$	$n_{tot} (\times 10^{15} \text{ cm}^{-3})$	n_{\uparrow} / n_{tot}	n_{\downarrow} / n_{tot}
150	54.0	143	0.539	0.461
265	48.0	102	0.531	0.469
515	36.6	60	0.524	0.476

(b)

delay (ps)	$T_{carriers}(K)$	$n_{tot} (\times 10^{15} \text{ cm}^{-3})$	n_{\uparrow} / n_{tot}	n_{\downarrow} / n_{tot}
150	54.2	112	0.542	0.458
265	43.8	83	0.531	0.469
515	37.6	50	0.523	0.477

(c)

delay (ps)	$T_{carriers}(K)$	$n_{tot} (\times 10^{15} \text{ cm}^{-3})$	n_{\uparrow} / n_{tot}	n_{\downarrow} / n_{tot}
150	47.4	52	0.567	0.433
265	41.9	44	0.553	0.447
515	35.2	30	0.538	0.462

Table 6.4: Parameters obtained from the fits of Eq. 6.2 to the measured σ^+ - and σ^- -PL at different delays for a nominal excitation density of (a) $390 \times 10^{15} \text{ cm}^{-3}$, (b) $240 \times 10^{15} \text{ cm}^{-3}$, (c) $130 \times 10^{15} \text{ cm}^{-3}$. n_{tot} indicates the total density of electron hole-pairs, while $n_{\uparrow(\downarrow)}$ shows the density of spin-up (-down) electrons.

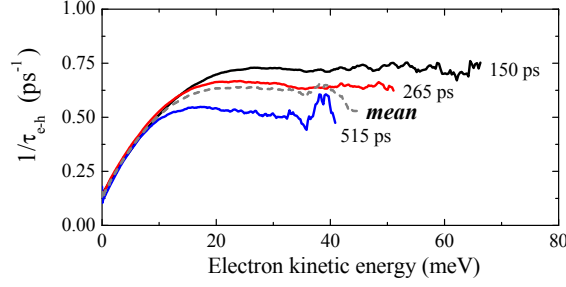


Figure 6.5: Computed electron-hole scattering rate for an injected carrier density of $390 \times 10^{15} \text{ cm}^{-3}$ at different delays after the arrival of the pulse (solid lines). Black: 150 ps, red: 265 ps, blue: 515 ps. The dashed line depicts the averaged scattering rate.

interval (5 ps), the number of total scattering events between holes and electrons of either spin that are not frustrated by the final state occupation of the scattering partners.

Let us discuss the results of the simulations for a fixed delay of 150 ps and two different excitation densities. Figure 6.3(b) depicts $1/\tau_{e-h}$ (thick solid lines) for the scattering of electrons with heavy holes, in the conditions of Fig. 6.1(b) — $n = 130 \times 10^{15} \text{ cm}^{-3}$, green line—, and Fig. 6.1(c) — $n = 390 \times 10^{15} \text{ cm}^{-3}$, black line—. For the latter case, also the Fermi-Dirac distributions of both electron populations are shown (dashed lines). The scattering rates of the low kinetic energy electrons are considerably smaller than those of high-energy ones, due to the higher occupation of the low E_{k-e} states. Figure 6.3(b) shows that for the case of $n = 390 \times 10^{15} \text{ cm}^{-3}$, the electron-hole scattering rates are 4 times smaller for electrons with $E_{k-e} = 1$ than for electrons with $E_{k-e} = 25$. The effect of the electron occupation on $1/\tau_{e-h}$ is also evidenced when comparing the electron-hole scattering rates for different excitation densities: at low E_{k-e} , $1/\tau_{e-h}$ is more than twice larger for low carrier density [green line in the figure, $n = 130 \times 10^{15} \text{ cm}^{-3}$] than for high carrier density [black line in the figure, $n = 390 \times 10^{15} \text{ cm}^{-3}$], where the higher occupation of electronic states inhibits the electron-hole scattering.

So far we have discussed the simulations for a time delay of 150 ps. As time evolves, the carrier distributions slowly change due to the radiative recombination and to the cooling of the ensembles. Figure 6.5 depicts the computed scattering rate at different delays for an injected carrier density of $390 \times 10^{15} \text{ cm}^{-3}$. τ_{e-h} changes only slightly during the PL lifetime. To account for these small changes, in the simulations we have averaged τ_{e-h} during the time needed for the PL to decay to $1/e$ of its maximum value (dashed line in Fig. 6.5).

6.4.3 Scaling relation

As we have discussed above, the employed Monte-Carlo approach can only account for the direct Coulomb scattering. In order to compare results of the simulation for the direct electron-hole scattering rate with the experimental results on the spin-flip rate (which is equivalent to the electron-hole exchange scattering rate in the BAP mechanism), we have made use of a scaling relation of the type:

$$\frac{1}{\tau_{sf}(k)} = C \left(\frac{1}{\tau_{e-h}(k)} \right)^\beta, \quad (6.8)$$

where C and β are the scaling coefficient and scaling exponent respectively showing no dependence on k . Analogous scaling relations can be inferred from calculations on the electron-electron scattering rates including and excluding exchange[53] (see discussion below), and can also be deduced for the case of the correlation and exchange mean-energies per electron in an electron-hole plasma in the context of a screened potential approximation.[105]

We have fitted the experimental points shown in Fig. 6.3(a) with Eq. 6.8 using the simulated averaged τ_{e-h} for each excitation density. The fit was performed simultaneously for the three considered excitation densities to obtain the fitting parameters C and β . The results of the fit is shown in Fig. 6.3(a) as solid lines, yielding values of $C = 2.05 \times 10^{-3}$ and $\beta = 2.81$. The agreement is excellent for the three investigated densities.

Let us further comment on the justification for the use of the scaling model introduced in Eq. 6.8. Our scaling model of the direct and exchange spin-flip electron-hole scattering rates is based on the idea that the spin flip is dominated by exchange interaction. Both direct and exchange interactions scale with different powers of the density. Therefore, one can scale exchange as a power of the direct term. This general argument has proved to be valid in calculations of carrier-carrier scattering by Collet in undoped GaAs in a static screening approximation.[53] The calculations of Collet focus on the electron-electron scattering rates as a function of density (instead of electron-hole rates) and are here reproduced in Fig. 6.6(a) [Fig. 5 of Ref. [53]]. Triangles depict the calculated rate without exchange (τ_{direct} ; direct terms only), while the diamonds include exchange both exchange and direct terms (τ_{total}). If we focus on the points enclosed by the dashed circle, we can plot the bare exchange scattering rate (τ_{exc}) vs the bare Coulomb scattering rate τ_{direct} . In order to estimate the bare exchange scattering rate from the data of Fig. 6.6(a), we make the following approximation: $\tau_{exc} = \tau_{total} - \tau_{direct}$. The obtained τ_{exc} is plotted vs τ_{direct} in Fig 6.6(b),

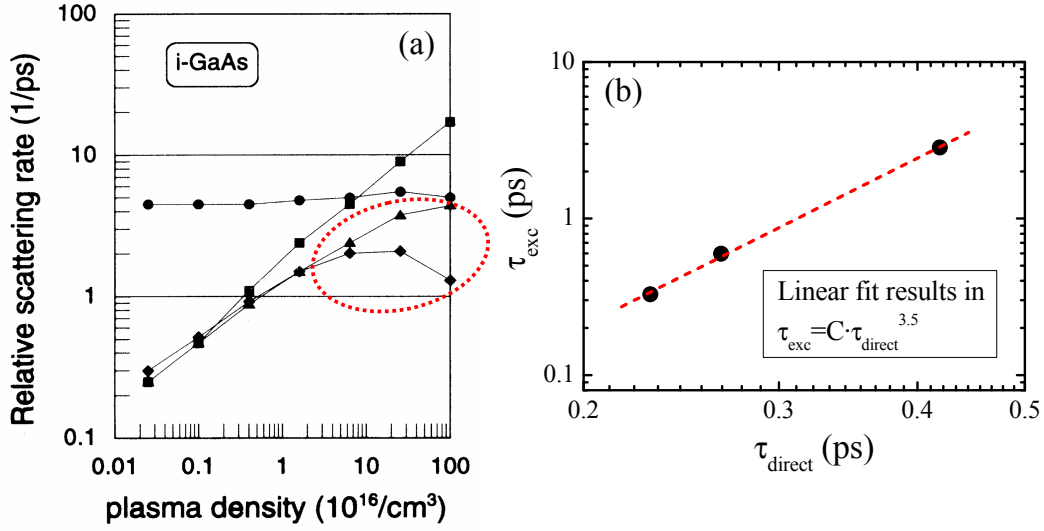


Figure 6.6: (a) Figure 5 of Ref. [53]: calculated electron-electron scattering rate as a function of density for electrons with a distribution 20 meV wide in energy, centered at an excess energy of 60 meV. Triangles: static screening approximation without exchange (τ_{direct}); diamonds: static screening approximation with exchange (τ_{total}); squares: dynamic screening with exchange; circles: electron—LO-phonon scattering. (b) τ_{exc} vs τ_{direct} obtained from the points enclosed in a circle in (a). Note that both scales are logarithmic. The dashed line is a linear fit to the data.

where a scaling relation between direct and exchange scattering rates analogous to Eq. 6.8 can be extracted, as indicated by the dashed linear fit. In this case of electron-electron scattering, which should not differ much from the electron-hole case, a scaling exponent of 3.5 is obtained, not far from our result of $\beta = 2.81$ for electron-hole scattering.

Let us now focus on the effects of phase-space filling on the spin-flip time. In order to do so, we have calculated τ_{sf} for the case of non-degenerate holes and empty conduction band. The dashed line in Fig. 6.3(a) shows τ_{sf} as derived by Bir *et al.*, [32, 33] and reformulated in Ref. [179] as:

$$\frac{1}{\tau_{sf}^{non-deg}} = n_h \sigma_s \left(\frac{2}{\mu_{e-hh}} \right)^{1/2} E_{k-e}^{1/2}, \quad (6.9)$$

where n_h is the hole density and σ_s is the spin-flip cross section. For our evaluation of $\tau_{sf}^{non-deg}$ we have used a hole density corresponding to the highest investigated density in our experiments at a delay of 150 ps ($143 \times 10^{15} \text{ cm}^{-3}$), which is far beyond the assumption of non-degeneracy, but provides a qualitative reference for the effect of phase-space filling on the spin-flip rates.[179] To visualize the effects one has to compare the dashed line with the bold solid black line: for low kinetic energies τ_{sf} is greatly increased with respect to $\tau_{sf}^{non-deg}$ (~ 8 times, from 3.6 ns to 29 ns for $E_{k-e} = 2 \text{ meV}$) due to the frustration of the electron spin-flip in highly occupied states (*Pauli blockade*). At higher electron kinetic energies ($> 20 \text{ meV}$), the occupation is much lower [see Fig. 6.3(b)] and τ_{sf} approaches the non-degenerate values. Thus, the *Pauli blockade* of the spin relaxation does not only modify the overall value of τ_{sf} , but it also affects the energy dependence of the spin-flip processes.[179]

The k -dependence of the electron spin-flip time reported in Fig. 6.3(a) shows τ_{sf} values and follows trends very close to those calculated by Maialle in bulk GaAs, assuming a BAP spin-relaxation mechanism, with p -doping concentrations very similar to the photoinjected electron-hole pair densities of our experiments.[179] Our measurements yield slightly higher values of τ_{sf} caused by a higher Pauli blockade of the electron-hole scattering due to the presence of degenerate electron populations (the calculations of Ref. [179] are performed in the absence of electrons in the conduction band, but account for degenerate valence bands). Despite the differences in the system's conditions between the calculations of Ref. [179] and our experimental results shown in Fig. 6.3(a), the good qualitative agreement between the two supports our model of electron spin relaxation through the BAP

spin flip mechanism	scattering time <i>vs</i> n	spin-flip time <i>vs</i> excitation density
DP	$\tau_e \sim n$	$\tau_{sf} \propto \frac{1}{\tau_e} \Rightarrow \tau_{sf} \downarrow \text{when } n \uparrow$
Our model (BAP)	$\tau_{e-h} \sim n$	$\tau_{sf} \propto (\tau_{e-h})^\beta \Rightarrow \tau_{sf} \uparrow \text{when } n \uparrow$

Table 6.5: Expected qualitative dependence of τ_{sf} for the Dyakonov-Perel (DP) and Bir-Aronov-Pikus (BAP) mechanisms with increasing n assuming that the electron scattering time (τ_e and τ_{e-h}) increases with excitation density as obtained in the Monte-Carlo simulations due to the *Pauli blockade*.

mechanism under strong *Pauli blockade* for our experimental results.

Let us finally note that the DP mechanism, as compared with the BAP one, would result in a very different dependence of τ_{sf} with n . In the DP mechanism, τ_{sf} is inversely proportional to the electron scattering time, while in our model both *times* are proportional to each other [see Eq. 6.8 and Table 6.5]. Our experiments clearly show an increase of τ_{sf} with increasing optically pumped carrier density ($\tau_{sf} \sim n$). The simulations obtain an increase of the electron scattering time with density ($\tau_{e-h} \sim n$), due to *Pauli blockade* [compare green and black solid lines in Fig. 6.3(b)], confirming the validity of our model ($\tau_{sf} \sim \tau_{e-h}$) and discarding the DP mechanism ($\tau_{sf} \sim 1/\tau_{e-h}$).

6.5 Summary

In this chapter, by means of optical orientation techniques, we have shown experimental results on the k -dependence of the electron spin-flip times in a direct-gap bulk semiconductor. In the case of undoped GaAs under strong photoexcitation, where the densities of free electrons and holes are identical, the main spin-flip mechanism is BAP. Furthermore, by means of a Monte-Carlo simulation we have evidenced that in this situation of a highly degenerate system, the large occupation of low energy states frustrates the electron-spin relaxation, yielding an increase of τ_{sf} of up to 8 times as compared with a non-degenerate system. This *Pauli blockade* also affects the energy dependence of τ_{sf} , as the occupation of electrons in the conduction band follows a Fermi-Dirac distribution, with the highest occupation for the lowest energy electrons. These effects result in values of τ_{sf} up to 30 ns at $k \approx 0$, the longest reported spin-relaxation time in undoped GaAs in the absence of a magnetic field. Additionally, we have introduced a simple scaling relation between the direct Coulomb and exchange electron-hole scattering rates, that fully accounts for the measured

dependence of τ_{sf} on n and k .

Chapter 7

Tailoring the carrier distributions in QWs: two pulses experiments:

7.1 Introduction

In the preceding chapters we have presented studies demonstrating that the distribution of excited excitons, electrons and holes in the bands determine many emission properties (rise time dynamics, luminescence spectra, spin-flip dynamics) in bulk direct-gap semiconductors such as GaAs. In particular, in the experiments presented so far, we have seen that there is an intimate relation between the exciton formation time (Secs. 5.3.2 and 5.4.3), the distribution and cooling dynamics of the unbound electrons and holes (Secs. 5.4.3 and 6.4), and the emission dynamics of the system.[270, 44, 128] Under several circumstances, both species (excitons and electron-hole plasma) coexist in the system (see rate equations of Sec. 5.3.2 and Sec. 5.4.3). Moreover, recent studies have demonstrated that at low T_L excitons and plasma do not only coexist but share a thermodynamical quasi-equilibrium.[18, 271, 222] Bearing these facts in mind, it is expected that induced changes in the distributions of free carriers in the bands will affect the excitonic emission dynamics.

The aim of the experiments presented in this chapter is the study and manipulation of the excited carrier distributions in their bands. In these experiments we will concentrate in high quality QWs instead of bulk samples. The reasons for this choice are related to the reduced dimensionality effects. In bulk systems, the small exciton binding-energy and the high ratio in oscillator strength between excitonic and electron-hole pair recombination,

hinders the possibility of simultaneously detecting the exciton and the plasma dynamics with high resolution. The plasma pair-recombination is simply buried in the high energy tail of the inhomogeneous exciton lineshape. However, in the QWs employed here, the high quality of the samples and the confinement effects, which increase the exciton binding-energy, do enable us to measure the emission from both the heavy-hole excitons and from the electron-hole plasma above the band gap. In this way we can study the relationship between the exciton dynamics and the distribution of free carriers in their bands. Additionally, confinement effects also simplify the *DOS* and split the valence bands in QWs (see Sec. 3.1.1), so that the calculation of the carrier temperature from the measured electron-hole pair recombination is straightforward, as we shall see below.

Here we show experimental results on how pre-existing thermalized distributions of carriers in QWs can be modified by the pulsed photoexcitation of hot carriers in the bands, resulting in abrupt, but controlled, changes of the carrier and exciton temperatures. The most striking effect of the induced ultrafast redistribution of carriers is the appearance of sharp dips in the PL dynamics of heavy-hole (*hh*) excitons. We will present a quasi-equilibrium thermodynamical model of the exciton/carrier excitations in the QW that accurately relates the magnitude of the observed dips in the excitons PL with the precise carrier warming induced by the pulse.

7.2 Photoluminescence under two pulses excitation

The studies were carried out on two samples based on GaAs/AlAs: the first one was a heterostructure with a single wide QW (20 nm), the second one contains multiple (50) narrow QWs (7.7 nm). Similar results were also found in a multiple InGaAs/GaAs QW sample (10 nm), showing the generality of the phenomena presented in this section. More details of the samples structure can be found in Sec. 4.1.4.

The samples were kept in a cold finger cryostat at 9 K. We employed the time-resolved PL excitation and detection configurations in a back reflection geometry described in Sec. 4.2.1, with a pulsed non-resonant excitation energy 26 meV above the *hh* exciton. In this case we used two consecutive pulses (P_I and P_{II}), whose power and delay can be independently controlled by means of attenuators and a delay unit. Both pulses arrive at the sample at the same excitation spot ($\sim 20 \mu\text{m}$ in diameter).

Figure 7.1 shows streak camera images of the excitonic emission from the single QW

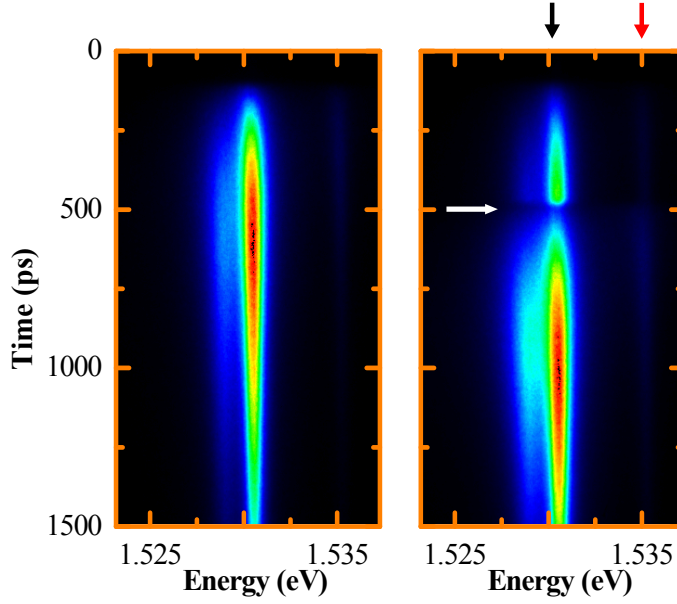


Figure 7.1: Streak camera images of the single QW hh -PL under one pulse excitation (left panel) and under two consecutive pulses excitation with a delay between pulses of 400 ps (right panel). The color scales are normalized in each panel. The white arrow indicates the arrival of P_{II} and the subsequent formation of a dip in the hh -exciton PL emission. The black (red) arrow mark the emission from hh (lh) excitons.

after excitation by one single pulse of $70 \mu\text{W}$ (left panel) and by two identical consecutive pulses delayed by 400 ps (right panel; $70 \mu\text{W}$ each). In the latter case, a clear dip appears in the emission of the hh exciton (black arrow) at the time of arrival of P_{II} (marked with a white arrow).

Figure 7.2(a) shows in detail the time evolution of the hh exciton PL when the two pulses excite the QW independently (dashed lines) and when both excite it jointly (solid line). The abrupt quenching of the PL is limited by our time resolution. The emission from the light-hole (lh) exciton can also be detected 4.7 meV above the hh exciton [red dotted line; red arrow in Fig. 7.1]. In contrast to the hh , the lh dynamics do not show the appearance of a dip in the PL at the time of arrival of P_{II} .

7.3 Origin of the dip: thermodynamical model

The origin of the dip can be explained considering the redistribution of carriers in the bands that takes place after the absorption of P_{II} . To account quantitatively for

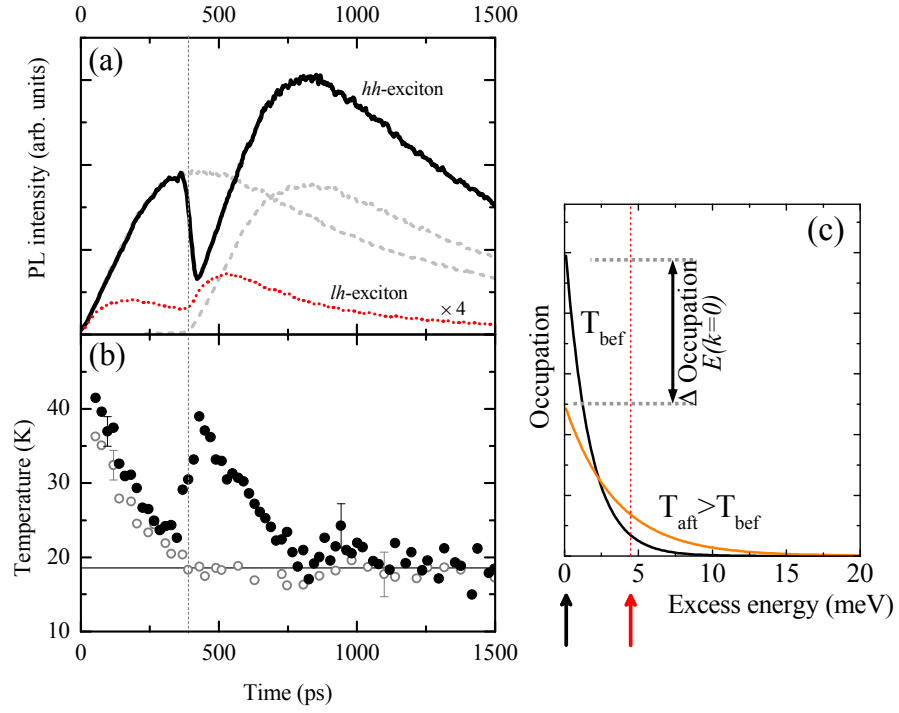


Figure 7.2: (a) Photoluminescence dynamics of the single QW hh -exciton under one pulse excitation (grey dashed lines) and under two consecutive pulses excitation (black solid line; conditions of Fig. 7.1). In red dotted line the emission of the lh excitons (enhanced by a factor of 4) is presented under two pulses excitation. (b) Measured electron-hole temperature for a single (open points) and double (solid points) pulse experiment. (c) Exciton occupation right before (black line) and right after (orange line) the arrival of P_{II} ; the black (red) arrow indicates the energy of the $K = 0$ heavy (light)-hole exciton.

the observed magnitude of the dip depth, we have developed a dynamical quasi-equilibrium thermodynamical model of the carriers in the QW, which is sketched in Fig. 7.3. The absorption of the first non-resonant pulse creates a non-thermal population of electrons and holes at high energies in the conduction and valence bands [Fig. 7.3 panel (a)]. In a time scale of the order of 200 fs the carriers distribute in the bands achieving a well defined temperature, higher than the lattice temperature [panel (b)]. [225, 148] The carrier densities considered in this section are far from the degeneration limit, and the electron population can be well described by a Maxwell-Boltzmann distribution function:

$$f_{MB}(E) = \frac{n}{k_B T} \frac{1}{DOS} \exp(-E/k_B T), \quad (7.1)$$

where E is the energy of the electrons above the bottom of the conduction band, and n is the density of electrons. A similar description can also be made for holes. As time evolves, the carrier distributions cool down due to the interaction with phonons, and the populations decrease due to pair recombination and exciton formation [panel (c)]. [176] When the P_{II} reaches the QW new hot carriers are photoinjected at high energy in the bands [panel (d)]. Due to efficient carrier-carrier scattering, the newly created carriers and the preexisting populations rethermalize in a timescale given by the pulse duration, at a temperature (T_{aft}) higher than the carrier temperature right before the absorption of P_{II} (T_{bef}) [panel (e)]. Thus, the effect of the delayed pulse is to warm-up the carriers and increase their concentration, in a time-scale shorter than a few picoseconds (~ 2 ps).

Concomitantly to the free carrier dynamics that has just been described, electrons and holes bind to form excitons in a time-scale, for the conditions of our experiments, of the order of several hundreds of picoseconds. [18, 270] The exciton population obeys also a Maxwell-Boltzmann distribution law.¹ Recent studies have successfully developed kinetic theories, fitted to experimental data, based on the assumption that excitons and the coexisting electron-hole plasma have the same temperature at all times. [270, 271, 44, 116] Bajoni *et al.* [18] have actually measured independently the temperature of the excitons and that of the electron-hole plasma, in a sample very similar to the single, wide QW structure used here. They observe that both species do show the same temperature for times larger than

¹In Sec. 5.1 it was argued that due to the fact that only optically active excitons are those with $K \approx 0$ results in *non-thermal* character of the exciton distributions. However, the exciton population outside the light-cone, which accounts for the vast majority of the total population, do follow quasi-Maxwell-Boltzmann like distributions, and so we will consider them in the rest of this section. [203]

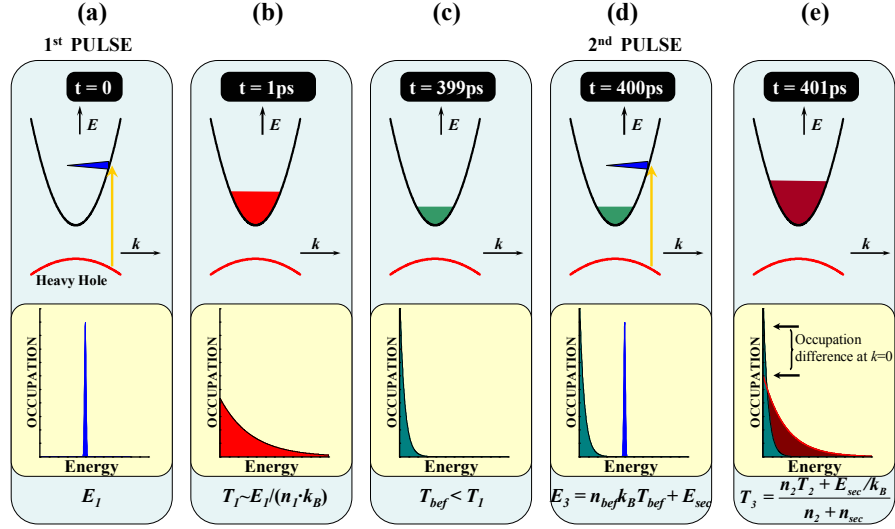


Figure 7.3: Schematic time evolution of the electron distributions in a two pulses experiment (holes are not shown for simplicity). See text for details.

200 ps after a pulse non-resonant excitation. For shorter times, Bajoni and coworkers propose that the exciton populations have not reached a thermal configuration to explain the differences in the measured temperature. This argument agrees with the theoretical predictions of Selbmann *et al.*[250]. They find that the exciton formation is favored for electrons lying with kinetic energies around the LO-phonon, as LO-phonon assisted electron and hole binding is the most favorable excitons formation mechanism according to their calculation. This fact, added to the slow exciton momentum relaxation, results in the non-thermality of the exciton population in the first 200 ps, according to their model. During this initial time excitons form, relax and thermalize simultaneously.

The situation in our two-pulses configuration is slightly different. In our case P_{II} reaches the sample more than 200 ps after the arrival of P_I , and we can expect thermal equilibrium between excitons and plasma at that time. Therefore, P_{II} injects hot electron-hole pairs in a system populated by already thermalized excitons. In the first picoseconds, after the arrival of P_{II} , the rethermalized electron-hole plasma just warms the preexisting excitons. However, in contrast to the plasma population, due to the slow formation dynamics of excitons—two orders of magnitude slower than the excitation pulse—, the exciton density is hardly altered within the pulse duration. Thus, no additional non-thermalized excitons should be considered during the time of arrival of P_{II} .

From these premises, we can conclude that within a reasonable approximation, we can assume that excitons and the electron-hole plasma have the same temperature at the time of arrival of P_{II} , and probably for some time after that. Therefore, an analogous dynamics to that of the free carriers takes place also for the exciton population: during the arrival of P_{II} , the abrupt warming of the carriers results in an ultrafast warming of the exciton population.

With these assumptions and using Eq. 7.1 the appearance of the dip in the hh -exciton PL can be understood. The hh -exciton occupation of the *zero* momentum states ($K = 0$) before/after the arrival of P_{II} is given by:

$$f_{MB}^{bef/aft}(0) = \frac{n'}{k_B T_{bef/aft}} \frac{1}{DOS}, \quad (7.2)$$

where n' is the pre-existing density of excitons at the arrival time of the pulse, and $T_{bef/aft}$ is the exciton (and carrier) temperature before/after the arrival of P_{II} .

The PL intensity of the hh excitons is directly proportional to the occupation of states with K close to *zero*, as these are the excitonic states that can couple to light. Therefore, modifications in the occupation of these states at the arrival of the delayed pulse [see Fig. 7.2(c)] induce changes in the PL. In particular, the abrupt warming of the carriers produced by the arrival of P_{II} ($T_{aft} > T_{bef}$) results in an abrupt drop of the $K = 0$ populations ($f_{MB}^{aft}(0) < f_{MB}^{bef}(0)$) and consequently in an ultrafast quenching of the hh -PL, as born out by our experiments (see Fig. 7.2).

The details of the exciton redistributions after the arrival of P_{II} also accounts for the absence of a dip in the lh emission. The lh -exciton energy is higher than that of the hh exciton and the increase in temperature of the excitons results in a negligible change of the excitonic occupation at the $K = 0$ lh states [as depicted in Fig. 7.2(c) for an energy marked with the red arrow].

In order to gain a deeper insight into the quantitative validity of this quasi-equilibrium thermodynamical model, we have directly measured the carrier temperature in the single, wide QW. Figure 7.4 shows PL spectra detected at different times after the arrival of P_I for the conditions of Fig. 7.2 (P_{II} arrives at 400 ps). The spectra show the hh - and lh -exciton lines as well as the direct free electron-hole pair recombination above the lh exciton energy. A Maxwellian fit can be performed at the high energy tail (indicated by solid lines) to extract the carrier temperature. Figure 7.2(b) shows the temperatures of the electron-hole plasma for the conditions of Fig. 7.2(a). The solid (open) dots corresponds to the double

(single) pulse experiments. In the case of the single pulse excitation, a monotonous cooling of the plasma is observed, with a final equilibrium temperature (~ 19 K) higher than the lattice temperature (~ 9 K).[176, 300] In the two-pulses experiment, an abrupt warming of the plasma, and consequently of the excitons, can be observed at the time of arrival of P_{II} . At longer times (> 1 ns) the same temperature as that obtained in a single pulse experiment is reached.

The measured temperature of the carriers enables us to predict the dip depth following our model. A relative dip depth can be defined as $r \equiv (I_{bef} - I_{aft})/I_{bef}$, where I_{bef} (I_{aft}) is the intensity of the hh -exciton PL right before (after) the arrival of P_{II} . From this definition and Eq. 7.2, the relative dip depth can be related to the excitonic temperature before and after the arrival of P_{II} by:

$$r \equiv \frac{f_{MB}^{bef}(0) - f_{MB}^{aft}(0)}{f_{MB}^{bef}(0)} = 1 - \frac{T_{bef}}{T_{aft}}. \quad (7.3)$$

The inset of Figure 7.5(a) shows in solid dots (\bullet) the values of r directly measured from the hh -exciton PL as a function of the delay between the two pulses for the single QW. The high values of r demonstrate the capability of P_{II} to quench the PL. The open dots (\circ) depict r obtained from the measured carrier temperature ratio T_{bef}/T_{aft} and Eq. 7.3. In a symmetrical manner Figure 7.5(a) depicts in open dots T_{bef}/T_{aft} as directly measured, while the solid points compile the temperature ratio as obtained from Eq. 7.3. Figure 7.5(b) shows T_{bef}/T_{aft} as a function of the power of P_{II} relative to that of P_I . In this case, the signal to noise ratio of the spectra limited the lowest power of P_{II} for which the temperature of the electron-hole plasma could be attained. The good agreements between the temperature ratios obtained from the relative dip depth in the hh PL (\bullet) and those measured directly (\circ) confirms the validity of our model.

This is further demonstrated in Fig. 7.5(c) that depicts T_{bef}/T_{aft} obtained from the hh PL for the GaAs/AlAs narrow multiple QW sample as a function of the power of P_{II} (delay = 300 ps) in the low power regime (solid points). In this case the broader excitonic linewidth hinders the possibility of extracting the carrier temperature from the spectra. Nonetheless, our model reproduces quantitatively the observed experimental dependence without the need of any adjustable parameters, as shown by the red line, which plots T_{bef}/T_{aft} obtained in the following way: the temperature after P_{II} is given by $T_{aft} = (n_{bef}T_{bef} + n_{inj}T^*)/(n_{bef} + n_{inj})$, where n_{bef} is the density of carriers at the time of arrival

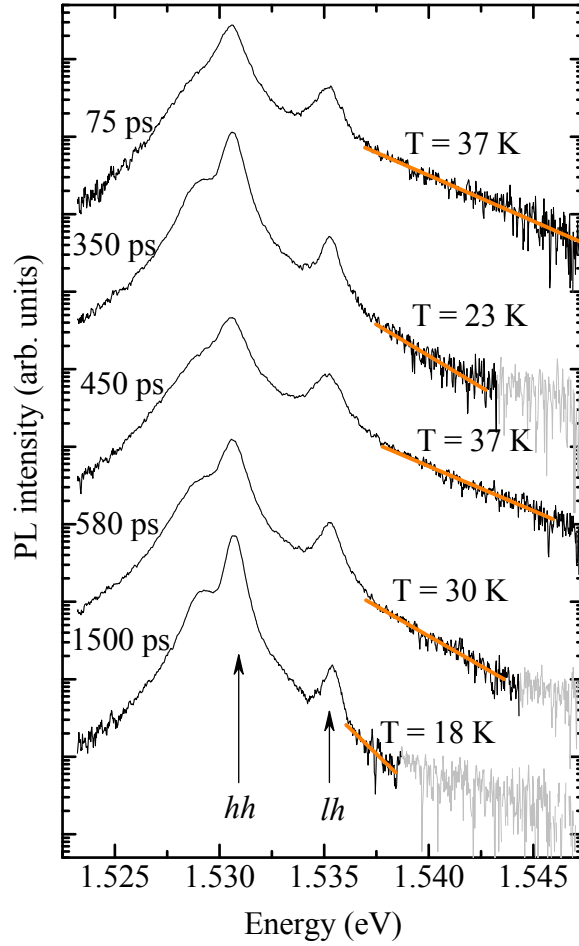


Figure 7.4: Spectra taken at different delays for the conditions of Fig. 7.2 for the single, wide QW. The spectra have been rigidly offset. The thick solid lines are fits to the free electron-hole pair recombination following a Maxwell-Boltzmann distribution, from which the temperature of the carriers can be extracted. Recall that the second pulse reaches the sample at a delay of 400 ps.

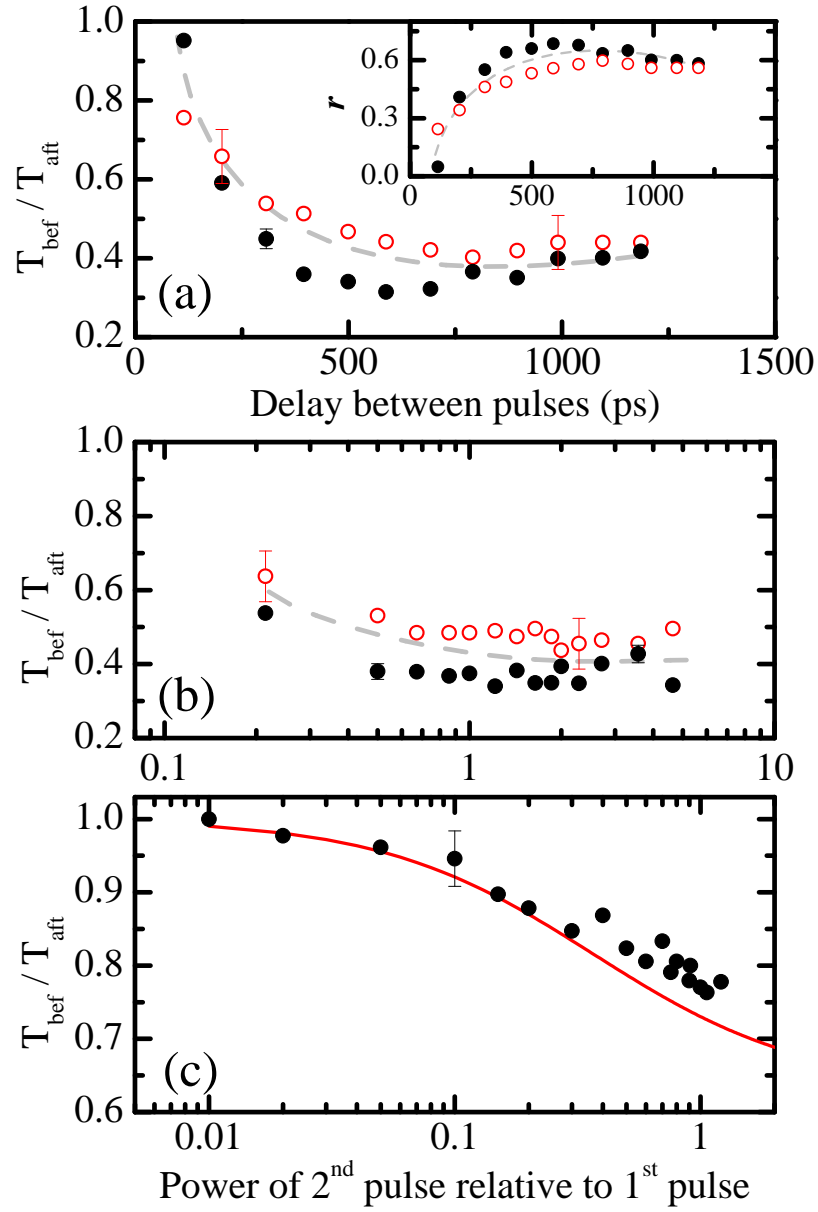


Figure 7.5: Temperature ratio (just before the second pulse/just after the pulse) in the single GaAs/AlAs QW sample as a function of (a) *delay* between pulses for a fixed power for both pulses ($70 \mu\text{W}$), and (b) *power* of P_{II} for a fixed delay between pulses of 400 ps and fixed power of P_I ($70 \mu\text{W}$). The solid (open) dots quantify the temperature ratio as directly measured from the PL (predicted from the model). The dashed lines are guides to the eye. The inset of (a) shows the corresponding relative dip depths (r). (c) Same as (b) for the multiple narrow QW sample with delay between pulses of 300 ps; the solid line computes the model (see text).

of P_{II} , determined from the power of P_I and the PL decay-time; n_{inj} is the density photoinjected by P_{II} ; T^* and T_{bef} , taken as 38 K and 24 K, respectively, are the initial carrier temperature and that measured at a delay of 300 ps in the single QW experiments (see Fig. 7.2), which were performed under very similar conditions to those in the multiple-QW structure.

7.4 Summary

In this chapter, we have presented experimental results demonstrating the capability to optically control in a short time-scale (< 2 ps) the carrier distributions in the bands in QWs. In particular, we have seen that the arrival of a short light pulse results in a sudden warming of a pre-excited electron-hole plasma. The exciton distributions, which are in thermal equilibrium with the electron-hole plasma, are also abruptly warmed-up by the arrival of the pulse, originating an ultrafast dip in the hh -exciton luminescence.

We have introduced a model that quantitatively reproduces the observed luminescence quenching and can be used to obtain the relative increase in carrier/exciton temperature induced by the arrival of the pulse, by measuring the magnitude of the dip in the hh exciton PL [Eq. 7.3]. Let us also mention that although the results presented here concentrate on the light emission from bare QWs, the physics and observed phenomena can be directly extrapolated to more complicated systems such as semiconductor microcavities, VCSELs or structures with active media of higher dimensionality, like the bulk direct-gap semiconductors treated in the preceding chapters. In particular, the relationship between the dip depth and the carrier warming can be exploited to study the carrier-relaxation dynamics in microcavities as we will show in Sec. 9.3. It could also be helpful to investigate phase transitions, such as condensation of indirect excitons [37] or polaritons,[133, 21] in which the carrier temperature plays an important role.

Chapter 8

Introduction to the many-body properties of microcavity polaritons

8.1 Bose-Einstein condensation of polaritons

One of the most interesting properties of microcavity polaritons is their capability to form Bose-Einstein condensates (BEC). This property arises from the bosonic character of polaritons, which is inherited from the bosonic nature of its constituents: photons and excitons. It is easy to see that a set of indistinguishable integer-spin particles in a system of energy levels ϵ_i follows the so called Bose-Einstein distribution function:[163]

$$f_{BE}(\epsilon_i, T, \mu) = \frac{1}{\exp\left(\frac{\epsilon_i - \mu}{k_B T}\right) - 1}, \quad (8.1)$$

where μ is the chemical potential. And the total number of particles in the system is:

$$N(T, \mu) = \sum_i \frac{1}{\exp\left(\frac{\epsilon_i - \mu}{k_B T}\right) - 1} = \sum_i f_{BE}(\epsilon_i, T, \mu). \quad (8.2)$$

The fact that the occupation of a state cannot be negative ($N_i \geq 0$) imposes that $\mu \leq \epsilon_0$, being ϵ_0 the ground state of the system. Note that μ increases with the number of particles.

We can rewrite Eq. 8.2 as:

$$N(T, \mu) = f_{BE}(\epsilon_0, T, \mu) + \sum_{i \neq 0} f_{BE}(\epsilon_i, T, \mu) \equiv N_0(T, \mu) + N_{exc}(T, \mu) \quad (8.3)$$

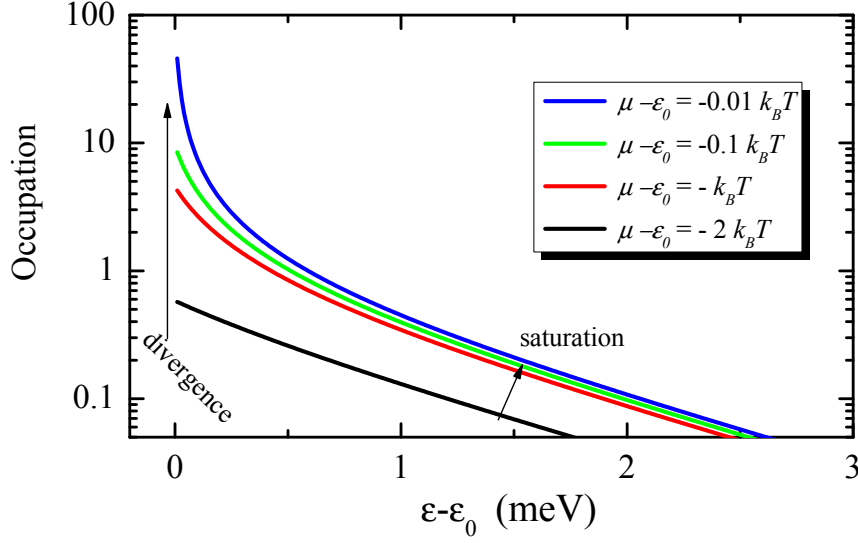


Figure 8.1: Occupation of particles following Bose-Einstein statistics at a temperature of 10 K and increasing density in the system (μ increases with density).

At a finite T , when the chemical potential μ approaches ϵ_0 from lower values something special happens: on one hand $f_{BE}(\epsilon_i > \epsilon_0)$ saturates asymptotically and the number of particles in all the excited states tends to:

$$N^c(T) \equiv N_{exc}(T, \mu = \epsilon_0) \quad (8.4)$$

On the other hand $f_{BE}(\epsilon_0, T, \mu)$ diverges, as can be seen in Fig. 8.1.

If the total number of particles exceeds $N^c(T)$ then the additional particles, $N - N^c$, will populate the ground state. In other words, above $N^c(T)$ if we add a new particle in such a way that this particle does not change the temperature of the system, this particle will occupy the ground state. In this way, the ground state can achieve macroscopic occupations, and Bose-Einstein condensation takes place. In fact, this degenerate situation starts to dominate the physics of the system when the ground state occupations are close to 1, and it is the basis for many properties found in bosonic systems such as polaritons in microcavities. For instance, the tendency to occupy the ground state above the degeneration limit results in final state stimulation phenomena as we will describe later.

Using the above mentioned condition [Eq. 8.4], it is straightforward to calculate the density of particles required for condensation to take. If we take a three dimensional gas of free particles of mass m , with dispersion $\epsilon = \frac{\hbar^2 k^2}{2m}$ ($\epsilon_0 = 0$), and we consider that the

level states are so close together that we can integrate over the energy states with use of the *DOS* [Eq. 2.31], then the critical density is given by:

$$n_c(T) = \frac{N^c(T)}{V} = \frac{N_{exc}(T, 0)}{V} = \left(\frac{mk_B T}{2\pi\hbar^2} \right)^{\frac{3}{2}} \left(\frac{2}{\sqrt{\pi}} \int_0^\infty \frac{1}{e^x - 1} x^{1/2} dx \right), \quad (8.5)$$

where V is the volume of the system. The first parenthesis in the right hand side of Eq. 8.5 is the inverse cube of the so-called de Broglie wavelength $\lambda_T \equiv \left(\frac{2\pi\hbar^2}{mk_B T} \right)^{\frac{1}{2}}$, and it reflects the average quantum size of the particles conforming the gas at temperature T . The second parenthesis in the equation has a value of 2.612 and, therefore:

$$n_c(T) \lambda_T^3 = 2.612 \quad (8.6)$$

Equation 8.6 tells us that in order for a Bose gas to condensate in a BEC, the average distance between particles must be on the order of their quantum size. When this occurs, the wavefunctions that describe the individual bosonic particles start to overlap and the particles start to occupy the same quantum state. The macroscopic ensemble of condensed particles can then be well defined by a single wavefunction:[207]

$$\Psi(\mathbf{r}) = \sqrt{n_0} |\psi_0(\mathbf{r})| e^{i\phi_0(\mathbf{r})} + \sum_{j \neq 0} \sqrt{n_j} |\psi_j(\mathbf{r})| e^{i\phi_j(\mathbf{r})} = \Psi_0(\mathbf{r}) + \Psi_{exc}(\mathbf{r}), \quad (8.7)$$

where $\psi_j(\mathbf{r})$ and $\phi_j(\mathbf{r})$ are the amplitude and phase of the individual quantum states of the system. The wavefunction describing the macroscopically occupied ground state $\Psi_0(\mathbf{r})$ has a well defined phase $\phi_0(\mathbf{r})$. [61, 174] The density matrix of the system is given by:

$$\rho_1(\mathbf{r}, \mathbf{r}') = \langle \Psi^\dagger(\mathbf{r}) \Psi(\mathbf{r}') \rangle = \langle \Psi_0^\dagger(\mathbf{r}) \Psi_0(\mathbf{r}') \rangle + \langle \Psi_{exc}^\dagger(\mathbf{r}) \Psi_{exc}(\mathbf{r}') \rangle \quad (8.8)$$

and describes the first-order correlation between particles at different positions \mathbf{r} and \mathbf{r}' in the system. The second term in the right hand side of Eq. 8.8 goes to zero when $|\mathbf{r} - \mathbf{r}'|$ goes to ∞ , while the first term has a finite and constant value due to the well defined phase of the macroscopically occupied ground state.[61] This property is called off diagonal long-range order, and along with superfluidity, which will be treated in Sec. 8.5, is one of the most important and characteristic properties of Bose gases, and has been thoroughly studied in dilute atomic systems since they were obtained for the first time in 1995.[65, 6]

species	atomic gases	polaritons
mass m^*/m_0	10^4	10^{-5}
Bohr radius	10^{-1}\AA	10^2\AA
λ_T at T_c	10^3\AA	10^4\AA
T_c	$< 1\mu\text{K}$	$10 - 300\text{K}$

Table 8.1: Comparison between different parameters in atomic and polaritonic BECs. m_0 indicates the free electron mass.

Due to the heavy mass of the atomic bosons employed in BEC studies, and the low density required to keep the bosonic character of those particle, condition 8.6 implies working at sub- μK temperatures. Alternative BECs can be studied in the microcavity polariton system, as polaritons themselves are bosons. Polaritons have a very small effective mass due to its photonic component, of the order of 10^9 times smaller than those of atoms. For this reason, the transition to a Bose-condensed phase can take place at much higher temperatures, as compiles in Table 8.1.

So far we have considered an ideal non-interacting Bose gas. It is not straightforward to see why the non-interacting particles should all condense into a single quantum state instead of in a series of quasi degenerate states if, their energy separation is small enough, as could be inferred from Fig. 8.1. However, BEC in a single quantum state does occur, and the reason is that particles in real Bose gases interact repulsively. The repulsion interaction prevents the gas from collapsing and also accounts for condensation taking place in a single quantum state, as this is the energetically favored situation when considering Hartree and exchange interactions in the system.[194]

Atomic condensates are regularly studied in three dimensional configurations, where the above mentioned properties of BEC can be directly applied. However, polaritons in microcavities live in a two dimensional environment. Considering the constant density of states characteristic of two-dimensional systems (see Sec. 3.1.1) the critical density for the Bose phase transition described by Eq. 8.5 diverges and the transition can only take place at $T = 0$. Equivalently, the impossibility of formation of a BEC in 2D can be seen as caused by the destruction of the phase correlations by long wavelength thermal fluctuations.[112] This is actually caused by the divergence at low energy of the Bose-Einstein distribution itself when $\mu \rightarrow \epsilon_0$ [see Fig. 8.1]. A BEC phase transition can be recovered in 2D in the presence of potential traps.[15, 202, 61] Nevertheless, if interactions are present long-range order and superfluidity can still develop below a critical temperature. This critical temperature char-

acterizes a phase transition known as Berezinski-Kosterlitz-Thouless (BKT).[29, 152] The critical density and temperature are related by a linear relation:

$$n_c = \frac{2mk_BT_{BKT}}{\pi\hbar^2}, \quad (8.9)$$

where, in this case, n_c is the density of the condensed fraction of the gas. Equation 8.9 can also be expressed in terms of the de Broglie length:

$$n_c(T) \lambda_T^2 = 4, \quad (8.10)$$

and the same interpretation about the overlapping of the Bose particle wavefunctions can be applied as in 3D. Note that even though the BKT transition requires interactions between particles, Eq. 8.9 does not show any particular interaction-energy term. The BKT transition actually relies on two particles interactions. Above the critical temperature unconnected local quasi-condensed droplets can form, but also free vortices do spontaneously appear, destroying the superfluidity and the long-range order. Below the critical temperature phase fluctuations also induce the formation of vortices, but in this case they tend to bind in pairs of opposite circulations due to the energy relief of such configuration caused by interactions. The pairs and clusters of vortices with total *zero* circulation have little influence on the superfluid properties. In this way the condensate ends up conforming percolation paths that connect the phases of spatially separated points, and quasi-long range order is recovered. Two different fluids coexist: a normal fluid and a percolated condensed phase. In this situation the first term of the correlation function [Eq. 8.8] is not constant, and decreases as a function of distance $|\mathbf{r} - \mathbf{r}'|$. Then true long range order is not achieved and the system does not conform a true BEC.

Recent calculations specifically performed on the two-dimensional polariton system and starting from the internal structure of polaritons without considering BKT effects, find that the problem can actually be treated in a mean-field approach.[138] When phase fluctuations are introduced in the calculation, at low densities n_c follows a linear dependence on T , similar to that given by Eq. 8.9.

Although the above mentioned differences between the two and three dimensional cases must be kept in mind, the theoretical treatment of the polariton condensate in two dimensions can be carried on within the standard Gross-Pitaevskii and Bogoliubov theories as in the three dimensional case. In Sec. 8.5 we will briefly introduce the Bogoliubov theory

to describe the most important features of superfluidity in these systems, in the framework of Bose-condensed phases. In any case, even though it may not be the most rigorous terminology, from now on we will refer to the two-dimensional polariton condensate as a BEC.

8.2 Microcavity polaritons phase diagram

It is important to remark that excitons, and consequently polaritons, are composite bosons, formed from two spin-paired fermions. This sets up an important limit to the bosonic treatment of microcavity polaritons. If the density of polaritons is too high, the bosonic picture of polaritons does not hold, as the electron and hole wavefunctions that conform the excitons from different polaritons start to overlap, evidencing their fermionic nature. Also, interparticle screening changes the exciton oscillator strength and the coupling to the photon modes, eventually destroying the strongly-coupled polariton. In this case the microcavity enters into the regime of weak-coupling, in which the system is well described by the bare exciton and cavity modes. In GaAs based microcavities at low temperature and non-resonant excitation, the carrier density threshold for the onset of laser operation, in the uncoupled exciton-photon system, is usually lower than the threshold for the weak-coupling regime, and lasing usually takes place right at the density point of polariton destruction.[38] In the photon-lasing regime (VCSEL) the quantum wells inside the cavity act as a gain medium, and the cavity itself as a laser resonator.

Thermal ionization of the exciton can also take place at high enough temperatures, driving the system into LED operation. Figure 8.2 shows the different phases in excited microcavities of different materials as a function of particle density and temperature. Only at temperatures and densities lower than those characterizing the onset of LED and VCSEL operation, strongly coupled polaritons conform the excitations and light-emission properties of the system, in the region enclosed by the dashed vertical and horizontal lines in Fig. 8.2. Within this region, an incoherent polariton phase (polariton diode) or a BEC of polaritons can be found. The solid line shows the BKT transition with its linear dependence on T described by Eq. 8.9 at low densities.

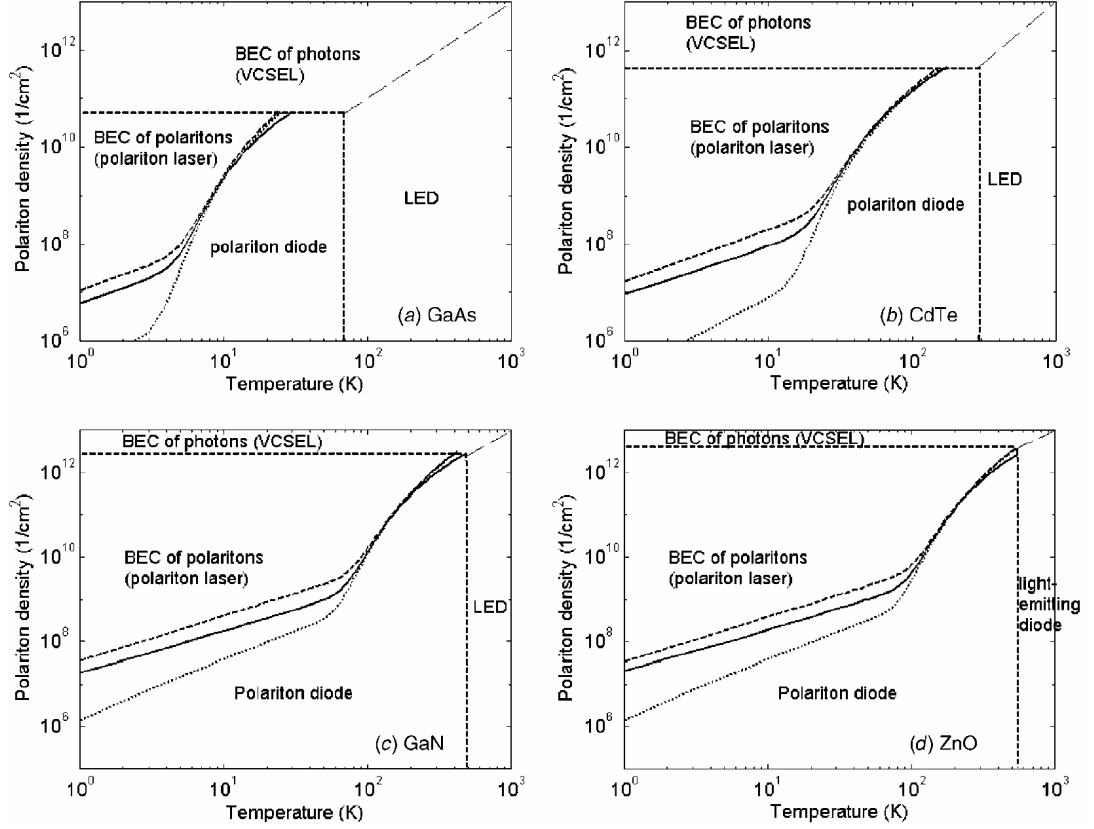


Figure 8.2: Phase diagrams for microcavities based on (a) GaAs, (b) CdTe, (c) GaN and (d) ZnO. The vertical and horizontal dashed lines show the limits of the strong coupling regime imposed by the exciton thermal broadening and screening, respectively. The solid lines show n_c vs temperature relation at the BKT phase transition. The dotted and dashed lines show the n_c for the case of quasi-condensation in finite size systems (lateral dimension of $100\ \mu\text{m}$ and $1\ \text{m}$, respectively). Taken from Ref. [181].

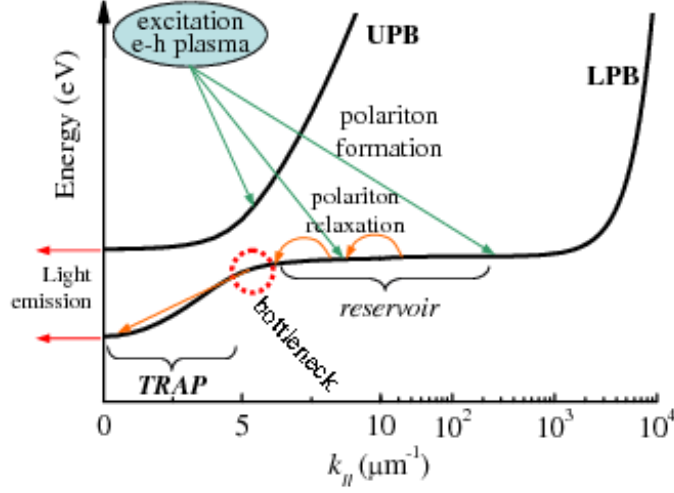


Figure 8.3: Microcavity dispersion in the strong coupling showing the trap in momentum space and the polariton formation and relaxation channels.

8.3 Spontaneous BEC of polaritons

Many properties associated to the formation of BEC of polaritons in microcavities have been observed in many different experiments in the past decade.[64, 239, 267, 220, 221, 133, 147, 132, 161] The most extended configuration employed to explore this phenomenon is the use of the energy trap in momentum space found in the lower polariton branch around $k = 0$. If a sufficient amount of polaritons accumulate in the quantum states at the bottom of the trap, condensation may take place.

This momentum trap configuration is sketched in Fig. 8.3. In order to unambiguously observe a true phase transition, the externally injected polariton population in the system must be incoherent. In this way, if any long range order coherence arises in the system it will be solely due to the spontaneous condensation, and not inherited from the coherence of the excitation source (which is usually a laser). For this reason, in experiments that attempt to demonstrate the condensation of polaritons, the polaritons injected in the system are created non-resonantly, with energies far above the bottom of the trap, expecting that relaxation in the carrier bands will destroy any trace of the coherence of the injected carriers. As depicted in Fig. 8.3 the non-resonantly created polaritons relax energy and momentum until they reach the momentum-bottleneck region.

Relaxation from the bottleneck region to the bottom of the polariton trap is a slow

process at low excitation densities, as it requires the simultaneous relaxation of significant amounts of energy and momentum. LO-phonon assisted scattering processes cannot participate due to energy conservation constraints, and only polariton-polariton and acoustic phonon-polariton interaction can mediate in the polariton relaxation.[180] Apart from the relaxation bottleneck, another important constraint for the accumulation of polaritons at the bottom of the trap is their reduced lifetime. As discussed in Sec. 3.2.2, due to the photonic content of the lower branch polaritons, which is close to 50% in the considered experiments ($\delta = 0$), the polariton lifetime in those states is of the order of 1-10 ps in standard GaAs and CdTe based systems. Faster relaxation times are required to achieve occupations at $k_{\parallel} = 0$ above 1 to trigger the condensation. The usual strategy has been to increase the excitation density until the occupation of the ground state is high enough, as long as the strong-coupling regime is not destroyed by the high carrier density.

The relaxation bottleneck has been the major obstacle for the observation of the BEC phase transition in GaAs based microcavities until very recently.[161] In these systems due to the reduced electron-hole binding energy ($\lesssim 10$ meV) the exciton can be ionized (and the polariton destroyed) at not very high carrier densities. This is the situation depicted in Fig. 8.2(a) with an horizontal dashed line. When the excitation density is increased it is found that the system loses strong coupling due to screening and exciton ionization in the high-dense polariton gas. Actually, when non-resonant excitation is above the QW bandgap (as in Fig. 8.3) the critical carrier density for the strong coupling to break down is even smaller than that indicated in Fig. 8.2(a). In this situation polaritons coexist with free carriers (injected by the excitation source), which contribute to the screening in the system and eventually destroy the strong coupling at densities lower than those required for condensation. In such conditions, the system is driven into the VCSEL regime, where photon lasing takes place under weak coupling.[38, 251, 35, 17]

Several configurations have been attempted in order to reduce the bottleneck effect and to enhance the polariton relaxation in the lower branch in GaAs based microcavities: (*i*) the increase of the lattice temperature to relax the energy-momentum conservation constrictions,[275, 157, 200] and (*ii*) the introduction of free carriers in the system to enhance the polariton relaxation scattering.[157, 200, 16] Despite the fact that these approaches have demonstrated that the bottleneck effect can be substantially reduced, none of them result in $k = 0$ occupations high enough to trigger the condensation. In Chapter 9 we will present some studies on the thermodynamics of the polariton states above the bottleneck.

Recently, spontaneous Bose-Einstein condensation of microcavity polaritons has been demonstrated in a CdTe based microcavity.[133] In these systems the exciton binding energy is much larger than in GaAs and the density threshold for the ionization of the polariton is much higher [see Fig. 8.2(b)]. For this reason, the non-resonant excitation density can be increased above the limit over which the occupation of the ground state becomes macroscopic and condensation can take place. Let us note that once this occupation is above 1, in a thermalized bosonic distribution newly injected particles will tend to occupy the ground state just by following the Bose-Einstein distribution, and the condensed state is reinforced. Figure 8.4 depicts the momentum distribution below (a) and above (b)-(c) the condensation threshold for the condensed state realized by Kasprzak and coworkers.[133] In the last two cases the macroscopic occupation of a single momentum state ($k = 0$) can be easily appreciated. Other predicted properties associated to the polariton BEC condensation are accessible through the photons that scape out of the cavity. These photons retain information of the polariton state from which they were originated. For instance, the condensed ground state is expected to show the build-up of spontaneous linear polarization,[261] narrowing of the emission linewidth,[208] superlinear excitation density dependence,[208] and spatial long-range coherence.[182] All these properties have been demonstrated in the aforementioned CdTe based microcavity experiments.[64, 220, 221, 133, 147, 132]

In very recent experiments, the group of Yamamoto has also been able to demonstrate BEC of polaritons in a GaAs based microcavity. In order to overcome the bottleneck and excitons ionization problem, in their experiments the excitation is resonant with the lower polariton branch with very large in plane momentum (i.e., very large incidence angle, $\sim 60^\circ$), where polaritons have a very large excitonic character. With this configuration, only polaritons are created in the system and no free carrier bath, which would screen the excitations. In this way, a sufficiently high polariton density of the ground state is achieved and condensation takes place. The most important feature demonstrated in these experiments is the appearance of long-range order,[71, 161] in particular when an array of weak spatial polariton traps is built.[161]

Nevertheless, some aspects of the observations of BEC of polaritons are still not clear. One of them is, for instance, the importance of achieving a thermalized distribution of polaritons. By measuring the light intensity emitted from the microcavity as a function of angle (i.e., polariton momentum) it is possible to obtain the polariton occupation distribution as a function of polariton momentum.[133, 70, 201, 17] However, in many occasions,

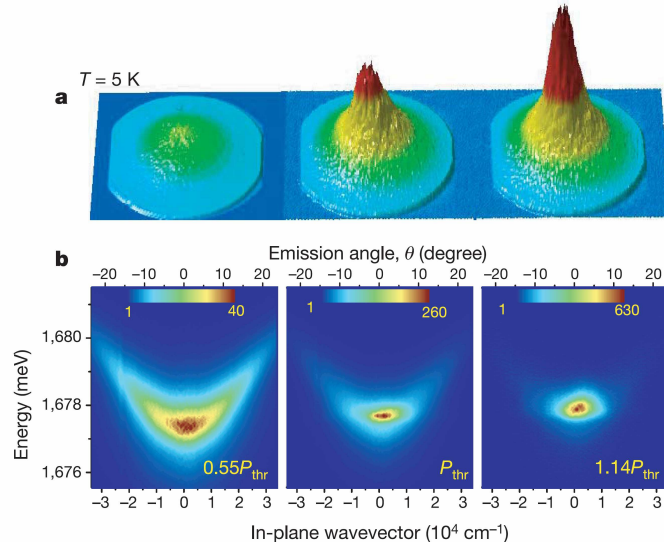


Figure 8.4: (a) Far field emission (k_x and k_y momentum space) from the LPB of a CdTe based microcavity under non-resonant excitation at 5 K at different polariton densities, in the experiment of Kasprzak *et al.* where a BEC of polaritons was observed. (b) Same as (a) for $k_y = 0$ and energy resolution. Extracted from Ref. [133].

under the conditions of condensation (where spectral narrowing of the ground state, onset of non-linear power dependence, etc. take place) polaritons do not always follow a proper Bose-Einstein distribution.[133] In order for the system to be thermal, the ground and excited states lifetimes should be longer than the thermalization time. It has been shown that this might only be achieved under particular exciton-photon detunings. In particular, large enough positive detunings are more favorable, as the excitonic content of the polariton extends its lifetime and increases the polariton-polariton and polariton-phonon interactions so that thermalization is accelerated.[70] On top of these difficulties, a recent work by Bajoni *et al.* shows that a microcavity in the weak coupling regime, above the onset of photon lasing, may show an angle-dependent emission pattern resembling very much that of a Bose-Einstein distribution.[17]

Let us finally mention that a different strategy has recently been proposed for the formation of a BEC of polaritons in microcavities by making use of spatial traps.[21] These traps in real space are created by the local reduction of the photonic potential when localized pressure is applied to the microcavity sample. The traps act as the magnetic quadrupole traps in atomic condensates and should be able to lower the temperature of the polariton

ensemble by evaporative cooling. However, in these experiments the optical excitation is performed resonantly with the lower polariton branch at an angle of about 17° , which is very close to the so called *magic angle* at which polariton pair scattering to $k = 0$ states in the OPO regime has its lowest intensity threshold.[239] It is therefore not clear in these experiments whether the observed phenomena (narrowing of the linewidth, nonlinear power dependence, build up of linear polarization, spatial coherence) are spontaneously formed from an incoherent ensemble, or inherited from the driven coherence of the pump state in an OPO process, as in the experiments described in Sec. 8.4.

In summary, as described above, BEC of polaritons in microcavities has recently been demonstrated. However, several properties related to BECs, which are well known in atomic physics, are yet to be found in the polariton system. Some of these phenomena are the creation of vortices,[2] observation of Josephson oscillations between two interacting condensates, appearance of Čerenkov-like shockwaves,[43] or superfluidity. The experimental observation of the last of these two phenomena in GaAs based microcavities will be the subject of Chapter 10.

8.4 The polariton system under resonant excitation of the LPB

When polaritons are resonantly injected into the lower polariton branch, the polariton relaxation mechanisms giving rise to the LPB luminescence are very different to those described in the previous section. In this case, the excitation laser introduces large populations of polaritons in a particular state, which is easily macroscopically occupied. The configuration we are considering is depicted in Fig. 8.5, where the laser energy and incidence angle is set to excite the LPB close to its inflexion point. At low powers, polaritons relax incoherently via phonon scattering, populating (pretty much evenly) all the LPB states below the pump energy. If the pump intensity is high enough, polaritons created in this state strongly interact with each other and there is a high probability for pair scattering events to take place.[51, 293, 164, 165] The pair (parametric) scattering events are characterized by the following conservation rules:

$$2E_P = E_S + E_I, \tag{8.11}$$

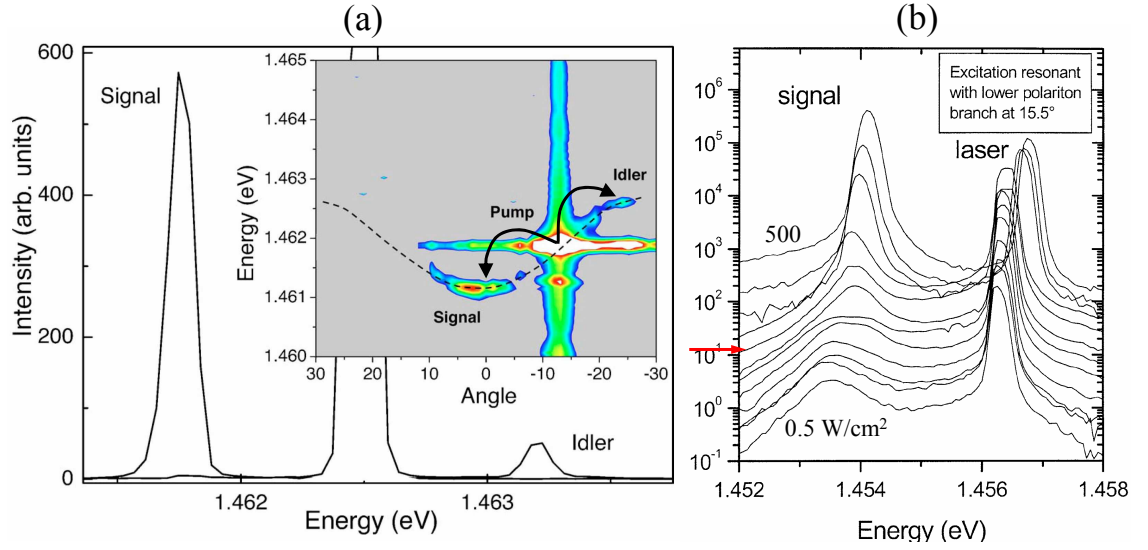


Figure 8.5: (a) PL spectra of a resonantly excited GaAs-based microcavity at the magic angle and at a CW power above the threshold for stimulated OPO operation. The inset shows the dispersion, where the pair scattering process is indicated by arrows. From Ref. [231]. (b) Power dependence of the PL spectra under similar conditions of excitation as (a), in the range 0.5 – 500 W/cm². The laser intensity saturates the detector. The onset of the stimulated OPO regime occurs at 150 W/cm² (marked with an arrow). From Ref. [263].

$$2k_P = k_S + k_I, \quad (8.12)$$

P , S , and I , indicating the pump, signal and idler modes, respectively. The so-called phase matching conditions 8.11 and 8.12 are only satisfied when pumping is performed at very specific points of the dispersion curve. The configuration shown in Fig. 8.5 is in fact the most suitable for this process as pump is resonant with the inflexion point of the LPB, at the so called *magic angle*. Around the *magic angle* it is easy to find pairs of points that satisfy Eq. 8.11 and 8.12.[155] If the polariton linewidth is taken into account, pair scattering is also possible when pumping at different angles. The efficiency of the process diminishes the further apart the pump is from the magic angle, as energy and momentum conservation rules are less likely satisfied.[25] Let us note that the quantum nature of the pair scattering process can be evidenced through the observation of intensity correlations between the signal and idler states.[234, 14, 223]

In addition to the activation of the pair scattering processes, if the pump power is further increased, it is possible to populate the ground state of the system with occupancies

above unity. In this case, stimulated scattering to the ground state is triggered as a result of the boson distribution properties described in Sec. 8.1, and as depicted in Fig. 8.5(b). Therefore, above a given threshold, polariton pair scattering is strongly favored towards the ground state¹, and simultaneously an idler state is formed, such that conditions 8.11-8.12 are satisfied. The idler state is visible in Fig. 8.5(a), and the regime under which this takes place is called Optical Parametric Oscillator (OPO). From now on we will refer to the low-energy parametric state of the OPO as signal.

The OPO regime is accompanied by the abrupt decrease of the signal emission linewidth, and the non-linear increase of the signal intensity with pump power.[267, 239] These two facts appear as a consequence of the macroscopic occupation of the signal state. On the other hand, the emission from the idler state is significantly smaller than that of the signal. The number of particles in both states should be identical, if pure parametric processes were responsible for their occupation. However, the idler state lies at an energy and momentum very close to the polariton states above the bottleneck, with a large excitonic component. The states above the bottleneck region [at about 30° in Fig. 8.5(a)] are usually referred to as the *reservoir*, and they strongly interact with the idler leading to its very fast dephasing and spread in k . It is this fast dephasing of the idler what ultimately limits the coherence of the OPO. If the idler state is not well defined (large energy indetermination caused by dephasing), the parametric process is not well set.

The non-linearities associated with the onset of OPO regime are also responsible for the appearance of bi-stability.[49, 294] This effect has recently been observed as a hysteresis loop in the variations of the signal intensity versus the pump intensity around the onset of the threshold density.[13, 95]

One of the most spectacular properties of the polariton OPO, and final state stimulation, is the observation of very high gains when a weak probe is shone on the signal state at $k = 0$. [239] Under OPO conditions, the weak probe increases the occupation of the signal $k = 0$ state and stimulates the scattering from the pump state to the signal state. The probe transmitted light through the sample shows ultrafast gains of up to 70.[239] Additionally, the process is very much dependent on the polarization configurations of the interplaying beams, evidencing the important effects of spin on the pair stimulated scattering mechanisms.[160, 134] Final state stimulation and high gains (up to 20) have also

¹The parametric process could be spontaneously initiated towards signal states different to $k = 0$. However, the OPO with signal state at $k = 0$ has the lowest density threshold.[294]

been observed in atomic BEC in four-wave-mixing experiments,[283, 72] demonstrating the universality of the phenomenon, purely associated to the bosonic statistics.

Let us point out that in this configuration the system as a whole does not follow a true Bose-Einstein distribution, as there is a very high occupation of polaritons in a well defined state different from the ground state (the pump state). Nevertheless the signal state does show characteristics associated to the condensed ground state of a BEC. Recent theoretical studies by Wouters and Carusotto[298] support this idea, as they predict that the ground state in an OPO configuration should show the appearance of Goldstone modes, associated to the spontaneous breaking of the symmetry characteristic of a transition into a BEC phase. These authors consider the spontaneous parametric processes associated to an OPO as the one depicted in Fig. 8.5(a), where the aforementioned momentum and energy phase matching conditions are satisfied between pump, signal and idler modes. The amplitude and phase of the pump mode is fully determined by the pump incident laser. However, the phase of the signal and idler remain free as they are invariant under a simultaneous complementary rotation:

$$S \rightarrow S e^{i\Delta\phi} \quad I \rightarrow I e^{-i\Delta\phi}, \quad (8.13)$$

where S and I are the complex amplitudes of the signal and idler modes, respectively. In other words, the total phase of the trimodal system should be conserved:

$$\phi_P + \phi_S + \phi_I = \text{constant}. \quad (8.14)$$

ϕ_P is fixed by the pump laser, and ϕ_S and ϕ_I are in principle free as long as condition 8.14 is satisfied. Above the threshold for the onset of the OPO, a random value of the phase of the signal and, thus, of the idler, is spontaneously set, and a U(1) phase-rotation symmetry [Eq. 8.13] is spontaneously broken. This is the kind of spontaneous symmetry breaking associated to many properties of Bose-Einstein condensates, like the onset of superfluidity. Wouters and Carusotto show that the spectrum of excitations [$\omega_G(k)$, Goldstone modes] around the signal state has a linear shape $\text{Re}[\omega_G(k)] = c_G(k - k_S)$. This linear dispersion of the excitations is indeed a manifestation of the Bogoliubov modes characteristic of systems with superfluidic properties. A detailed analysis shows that given that $\text{Re}[\omega_G(k)] = 0$ at $k = k_S$, and the absence of a singularity at that point, the Goldstone modes physically correspond to spatially slowly varying twist excitations of the signal and idler phases. Moreover, a

localized phase perturbation will not propagate, but simply relax back down. This confers a diffusive character to these modes in non-equilibrium situations, such as that encountered in a microcavity OPO, where polaritons are constantly feeding and exiting the system.

The situation is different in an equilibrium system such as that conformed by a BEC of atoms, where the corresponding Goldstone modes dispersion goes as $\text{Re}[\omega_G(k)] = c_G |k - k_S|$ around the considered state k_S , and presents a singularity at $k = k_S$. In this case an excitation (Goldstone mode) physically correspond to a weakly-damped sound wave propagating at the speed of sound c_G . [298] In any case, the Bogoliubov-like excitation spectrum indicates that the polariton system, under resonant excitation of the LPB, may show superfluid properties such as movement through an obstacle without dissipation, appearance of vortices, or Josephson oscillations between two weakly-interacting polariton fluids.

Let us point out that recently, Szymanska and coworkers [272] have found a similar diffusive nature of the modes belonging to the spectrum of excitations of a polariton condensed phase under non-resonant incoherent pumping (this is the situation in the experiments of Kasprzak *et al.* [133] where a BEC of polaritons has been reported). Therefore, very similar physics may rule the excitation spectrum of polariton coherent states in microcavities when they are either created resonantly or non-resonantly. [298, 297]

8.5 Superfluidity of polaritons

The theoretical treatment of the collective excitations of the microcavity polariton system under resonant excitation of the lower polariton branch has been the subject of intense study by the groups of Cuiti, Carusotto [42, 49] and Whittaker. [293, 294] Here we will follow the treatment of Ciuti and Carusotto developed in detail in Refs. [42] and [49]. We will just reproduce and point out the results of their theory that will be useful for the interpretation of the results shown in Chapter 10. For further details, the reader is directed to the just mentioned references.

Let us consider the exciton and photon field operators $\hat{\Psi}_x(\mathbf{r})$, and $\hat{\Psi}_c(\mathbf{r})$, respectively, in a situation of coherent pumping with a laser of energy $\hbar\omega_P$ and momentum k_P . Within a mean field approximation, the time evolution of the exciton and cavity mean fields $\Psi_{x,c}(\mathbf{r}) = \langle \hat{\Psi}_{x,c}(\mathbf{r}) \rangle$ is given by the solution to the Schrödinger equation:

$$i\hbar \frac{d}{dt} \begin{pmatrix} \Psi_x(\mathbf{r}) \\ \Psi_c(\mathbf{r}) \end{pmatrix} = \begin{pmatrix} 0 \\ \hbar F_P e^{i(\mathbf{k}_P \mathbf{x} - i\omega_P t)} \end{pmatrix} + \left[h^0 + \begin{pmatrix} V_x(\mathbf{x}) + \hbar g |\Psi_x(\mathbf{r})|^2 - \frac{i}{2} \hbar \gamma_x & 0 \\ 0 & V_c(\mathbf{x}) - \frac{i}{2} \hbar \gamma_c \end{pmatrix} \right] \begin{pmatrix} \Psi_x(\mathbf{r}) \\ \Psi_c(\mathbf{r}) \end{pmatrix}, \quad (8.15)$$

where h^0 is the usual exciton-photon interaction Hamiltonian:

$$h^0(\mathbf{k}) = \hbar \begin{pmatrix} \omega_x(\mathbf{k}) & \Omega_R \\ \Omega_R & \omega_c(\mathbf{k}) \end{pmatrix}. \quad (8.16)$$

$\hbar\omega_{x(c)}(\mathbf{k})$ is the in-plane energy dispersion of the excitons (cavity photons), Ω_R is the Rabi frequency associated to the exciton-photon coupling (see Sec. 3.2.2), F_P is the amplitude of the driving pump laser, $\gamma_{x(c)}$ is the homogeneous broadening of the exciton (cavity photon) mode, $V_x(\mathbf{x})$ and $V_c(\mathbf{x})$ are excitonic and photonic spatial fluctuations produced by interface and alloy imperfections in the QWs and cavity length of Bragg mirrors, respectively. Finally, g , which is greater than *zero*, is a repulsive exciton-exciton contact potential, and the term that contains it is the source of many of the non-linearities of the system. For instance, this term results in the renormalization of the polariton branches (blueshift) when many polaritons are introduced in the system, even under incoherent non-resonant excitation.

Following the Bogoliubov theory of a weakly interacting Bose gas,[174] the spectrum of the excitations of the system can be obtained from the eigenvalues of Eq. 8.15 when linearized. In order to do so it is convenient to define slowly varying fields (perturbations) with respect to the pump state:

$$\delta\phi_i(\mathbf{r}, t) = \delta\Psi_i(\mathbf{r}, t) \exp(i\omega_P t), \quad (8.17)$$

and a four component displacement vector:

$$\delta\phi(\mathbf{r}, t) = (\delta\phi_x(\mathbf{r}, t), \delta\phi_c(\mathbf{r}, t), \delta\phi_x^*(\mathbf{r}, t), \delta\phi_c^*(\mathbf{r}, t)). \quad (8.18)$$

Then the equation of motion of $\delta\phi(\mathbf{r}, t)$, according to the linearization of Hamiltonian 8.15 when a weak perturbation \mathbf{f}_d is applied to the system, is:

$$i\frac{d}{dt}\delta\phi(\mathbf{r}, t) = \mathcal{L} \cdot \delta\phi(\mathbf{r}, t) + \mathbf{f}_d, \quad (8.19)$$

where:

$$\mathcal{L} = \begin{pmatrix} \omega_x + 2g|\Psi_x^{ss}|^2 - \omega_P - \frac{i}{2}\gamma_x & \Omega_R & g\Psi_x^{ss2}e^{2ik_Px} & 0 \\ \Omega_R & \omega_c(-i\nabla) - \omega_P - \frac{i}{2}\gamma_c & 0 & 0 \\ -g\Psi_x^{ss2}e^{2ik_Px} & 0 & (\omega_x + 2g|\Psi_x^{ss}|^2) - \omega_P - \frac{i}{2}\gamma_x & -\Omega_R \\ 0 & 0 & -\Omega_R & -\omega_c(-i\nabla) + \omega_P - \frac{i}{2}\gamma_c \end{pmatrix}. \quad (8.20)$$

Ψ_x^{ss} are the stationary state solutions to Eq. 8.15 with $V_x(\mathbf{x}) = V_c(\mathbf{x}) = 0$. When $V_x(\mathbf{x}) = V_c(\mathbf{x}) = 0$ the perturbation term $\mathbf{f_d}$ is *zero* and the solutions to Eq. 8.19 depict the spectrum of collective excitations of the system (Bogoliubov modes). In this case the nature of the excitations is characterized by the coupling induced by the pump between a generic signal k_S mode and an idler mode, whose wavevector and energy satisfy conditions 8.12 and 8.11.

The introduction of a photonic or excitonic defect in the system via $\mathbf{f_d}$ in Eq. 8.19 results in the appearance of the well known Rayleigh related scattering in the photon fields. In the paper we are following,[49] Ciuti and Carusotto have calculated the dispersion of excitations, and the momentum (far field) and real space (near field) Rayleigh scattering images when a defect is encountered in a resonantly excited microcavity near the bottom of the LPB. The magnitude $|\delta\phi_c(\mathbf{k})|^2$ is proportional to the intensity of the Rayleigh scattering emission. Figures 8.6 and 8.7 show those magnitudes for two different situations of incident momentum and photon energy of the pump. Let us note that the potentials $V_{c,x}(\mathbf{r})$ break the spatial invariance of the system and can excite Bogoliubov modes with momentum different to $\mathbf{k_P}$. However they are static perturbations, and can only excite states with energy equal to $\hbar\omega_P$ (elastic processes).

In the excitation spectra depicted in panel (a) of Figs. 8.6 and 8.7 it is remarkable that a portion of the dispersion shows a linear shape. This is reminiscent of the linear Bogoliubov dispersion of excitations of a superfluid given, at small momentum, by² $\omega(k) = v_s k$, with:

$$v_s = \sqrt{\hbar g |\Psi_{LP}^{ss}|^2 / m_{LP}}, \quad (8.21)$$

where $\Psi_{LP}^{ss}(\mathbf{r})$ is the density of lower branch polaritons injected by the pump, and m_{LP} is their mass (obtained in the low-density linear regime). If a photonic or excitonic defect in the microcavity moves against the polariton fluid at a relative velocity v lower than v_s , no excitations will be produced in the system and the polariton fluid will remain unperturbed

²See also the discussion of the dispersion of the Goldstone modes in Sec. 8.4

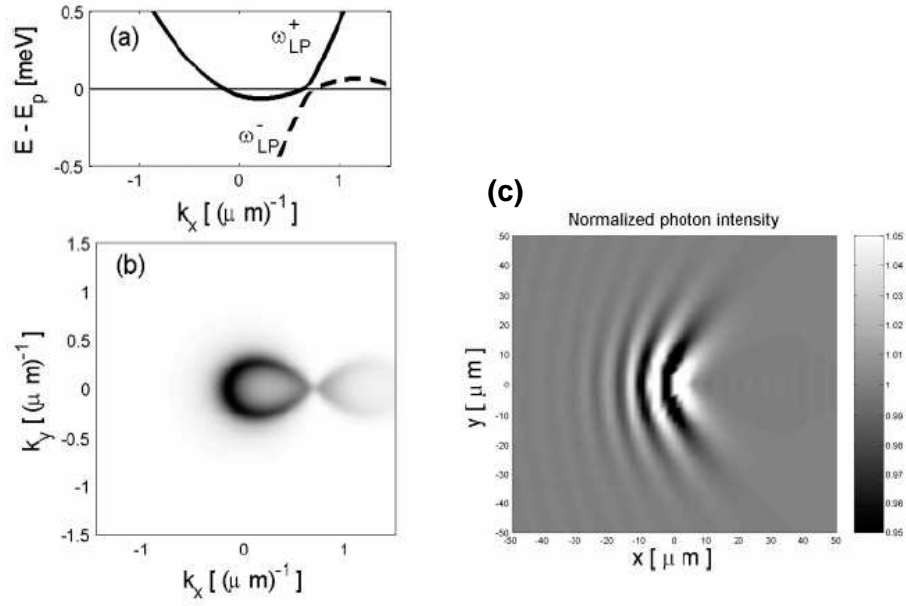


Figure 8.6: (a) Spectrum of excitations of the pump polariton state, i.e., the eigenenergies of Eq. 8.19, (b) intensity (arb. units) of the photonic resonant Rayleigh scattering signal $|\delta\phi_c(\mathbf{k})|^2$, and (c) near field image of the photonic scattered signal (Fourier transform of $|\delta\phi_c(\mathbf{k})|^2$), for $k_P = 0.7 \mu\text{m}^{-1}$, $\hbar\omega_P = \hbar\omega_{LP}(k_P) + 0.599 \text{ meV}$, and $\hbar g |\Psi_x^{ss}|^2 = 1 \text{ meV}$. Note that $\hbar\omega_{LP}(k_P)$ is that of the lower polariton state with k_P in the low density linear regime (no exciton-exciton interaction). This situation corresponds to the Čerenkov regime, in which a Bogoliubov linear excitations dispersion is present near the pump state but the relative velocity of the defect [placed in the center of (c)] is higher than v_s , producing scattering in a Čerenkov pattern.

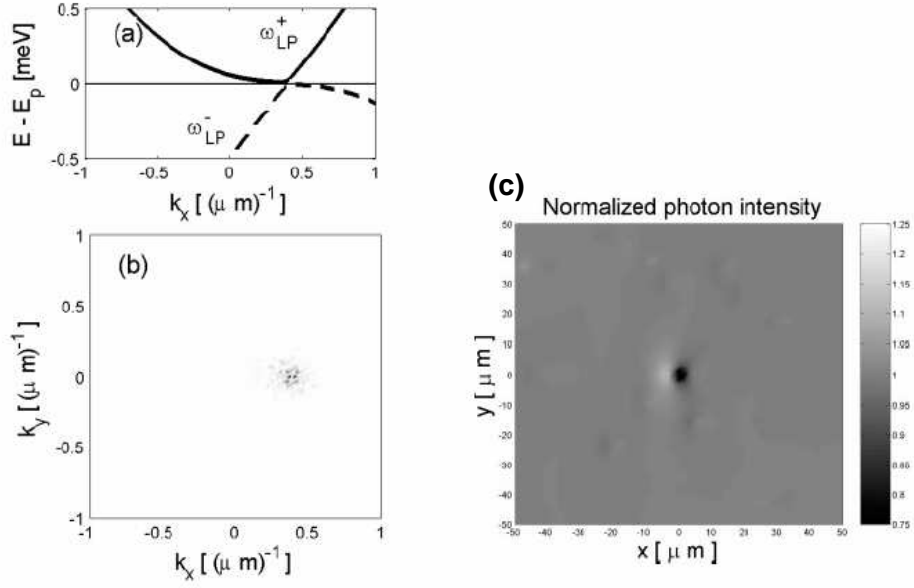


Figure 8.7: Same as Fig. 8.6, for $k_P = 0.4 \mu\text{m}^{-1}$, $\hbar\omega_P = \hbar\omega_{LP}(k_P) + 0.467$ meV, and $\hbar g |\Psi_x^{ss}|^2 = 1$ meV. This situation corresponds to the superfluid regime, in which a Bogoliubov linear dispersion of the excitations is present with a singularity at the pump state, which additionally lies at the bottom of the excitations branch. In this situation the polariton state cannot scatter to any other state as long as the relative velocity of the defect is below v_s , and the Rayleigh signal has collapsed.

after passing through the defect. Otherwise, excitations in the fluid are possible and scattering between polaritons causes dissipation. This, condition $v < v_s$ plus the requisite that $\omega_{LP}(k) > \omega_P$ for every $\mathbf{k} \neq \mathbf{k}_P$, conform the Landau criteria for superfluidity in a polariton system.

In Chapter 10 we will show experimental results on polariton fluids showing behaviors very similar to that depicted in Figs. 8.6 and 8.7.

8.6 Final remarks

The next two chapters will show experimental results in GaAs based microcavities in the strong-coupling regime. In Chapter 9 we will show experiments under non-resonant excitation, paying particular attention to the dynamics of relaxation of polaritons and the bottleneck effect introduced in Sec. 8.3. In these experiments, polariton condensation effects can not be observed due to the presence of an excited plasma of electrons and holes (created by the laser excitation) that ionizes excitons, driving the system into the weak-coupling regime, before the critical density for condensation is attained.

Finally, in Chapter 10 we will probe some properties associated to the condensation and formation of polariton quantum fluids by resonant excitation of the LPB close to the bottom of the polariton trap.

Chapter 9

Dynamics of microcavity polaritons under non-resonant excitation

9.1 Introduction: CW characterization

The samples used for the studies presented in this chapter are the InGaAs/GaAs/AlGaAs microcavities grown at the University of Sheffield and described in Sec. 4.1.2. The samples were grown with a cavity wedge so that different exciton cavity detunings can be studied by changing the position of the excitation spot on the sample. A basic characterization of the samples was performed in order to determine the Rabi splitting and emission energies. Figure 9.1(a) shows the $k = 0$ emission spectra as a function of position along a straight line on the sample, under low-power, CW non-resonant excitation. The emission from the LPB and UPB is clearly observed, with the characteristic polariton anticrossing between the exciton and cavity modes [Fig. 9.1(b)]. Several factors cause the luminescence from the LPB to be much more intense than that from the UPB. The most important one is the very fast incoherent relaxation of upper branch polaritons to the lower lying states of the lower polariton branch. Additionally, at positive detuning [$\hbar\omega_c(0) > \hbar\omega_x(0)$] the lifetime of the UPB states is much shorter than that of the LPB, due to the high excitonic component of the latter. On the other hand, at negative detuning the $k = 0$ states of the UPB are very close in energy to the *reservoir* states of the LPB, and interaction with polaritons from these states quickly depletes the UPB.

The value of the detuning exciton-cavity at different points along the sample is

plotted in Fig. 9.1(c). The $\delta = 0$ position can be easily identified as the point of least energy difference between the UPB and LPB, yielding a Rabi splitting $2\hbar\Omega_R = 6.6$ meV. δ can be obtained from the difference between the UPB and LPB energies at $k_{\parallel} = 0$ (E_{UPB} , E_{LPB} respectively) and is given by the equation:¹

$$|\delta| = \sqrt{(E_{UPB} - E_{LPB})^2 - (\hbar\Omega_R)^2} \quad (9.1)$$

In the remaining of this chapter we will present studies of the emission dynamics under pulsed excitation for several exciton-cavity detunings. The samples were kept at 5 K, and the photoluminescence time-resolved set-up employed is the one described in Sec. 4.2.2, in which a pinhole selected the emission of polaritons at $k = 0$ (normal to the cavity surface). Excitation was performed above the first reflectivity minimum of the stop band, in the continuum of electron-hole states of the GaAs cavity spacer, except in Sec. 9.3, where, in some of the presented experiments, the excitation is resonant with the UPB close to its minimum.

9.2 Power dependent dynamics

Figure 9.2(a) shows a streak-camera image of the $k = 0$ emission of the microcavity at $\delta = +7$ meV after non-resonant excitation for low laser power (4 mW). Under these conditions the LPB and UPB modes can be observed. In Fig. 9.2(b) the time evolution traces of the upper and lower polaritons are shown. The lower polariton branch presents slow dynamics, characterized by a long rise and decay. In the case of the upper polaritons, the dynamics are much faster.

The time evolution characteristics can be qualitatively understood considering the phenomenological model described in Fig. 9.3. Free electron-hole pairs are created by the non-resonant pulses in the QWs. Analogously to the process described in Sec. 7.3, in less than a picosecond the electrons and holes achieve thermalized distributions in the QWs. Simultaneously, polaritons start their formation process $\{[A]$ in Fig. 9.3(a) $\}$, populating both the UPB and the LPB. The cavity lifetime in the samples under study is of the order of 2 ps. Attending to the Hopfield coefficients (Sec. 3.2.2), at detunings close to *zero* the short photon escaping time implies that the polariton lifetimes are also very short (~ 4 ps)

¹Equation 9.1 can be derived from Eqs. 3.27-3.28 after some straightforward algebra.

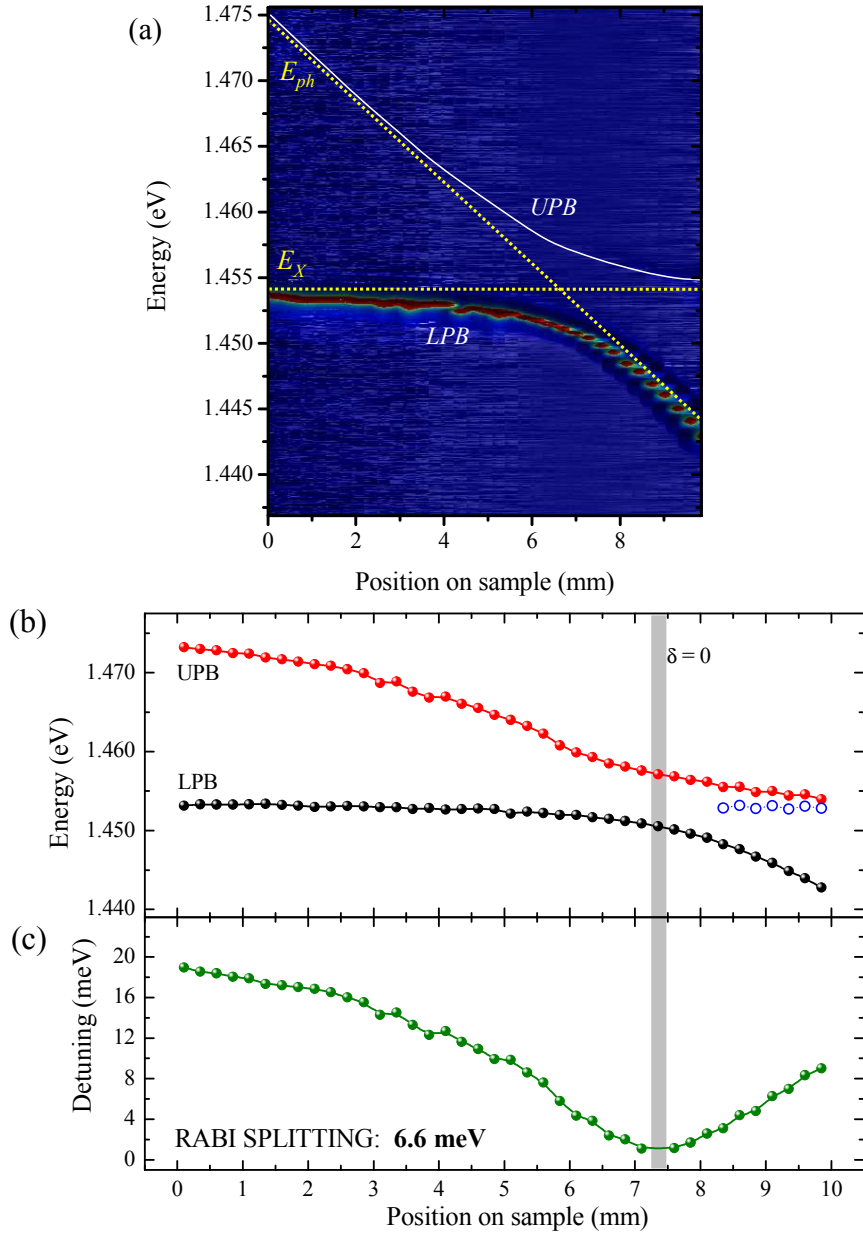


Figure 9.1: (a) Color map of the $k = 0$ emission from the InGaAs/GaAs/AlAs microcavity under non-resonant CW excitation at 5 K. The horizontal axis indicates the position in millimeters along a straight line parallel to the cavity wedge on the sample. The UPB peaks are indicated by a white solid line; its position in the map is evidenced in a z -logarithmic scale. The dashed lines depict the energy of the exciton and cavity modes. (b) Energy of the UPB and LPB peaks extracted from (a); the open points depict the emission from uncoupled excitons, visible at slightly negative detunings. (c) Detuning as a function of position on the sample calculated from Eq. 9.1. The minimum energy difference takes place at the position of $\delta = 0$.

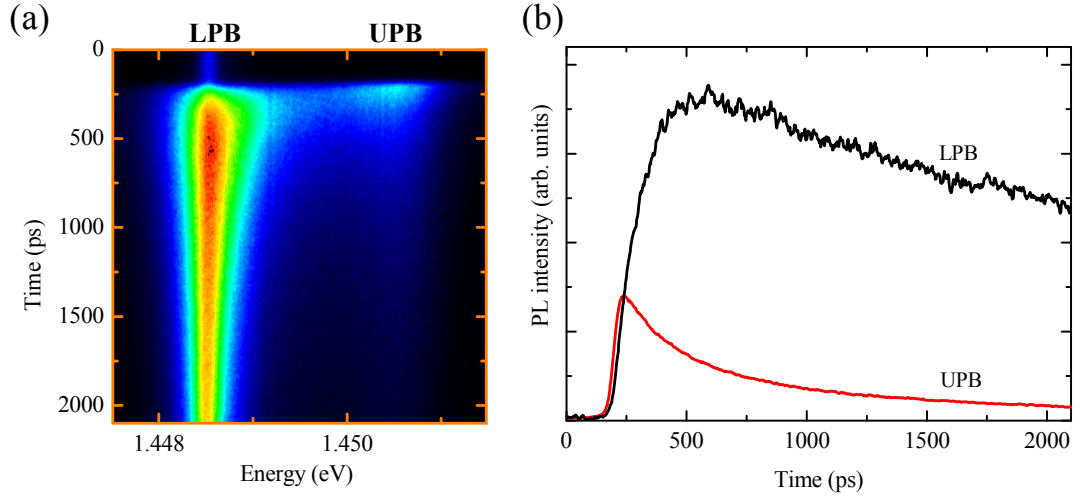


Figure 9.2: (a) Streak camera image of the $k = 0$ microcavity emission for a detuning of +7 meV. (b) Time evolution traces of the upper and lower polariton branches, extracted from (a).

for states close to $k = 0$, where polaritons have a large excitonic component ($\sim 50\%$). For this reason, any polariton falling inside the dispersion energy trap escapes very fast from the system. On the other hand, polaritons above the bottleneck, outside the trap, possess a very high excitonic component ($> 90\%$) and a weak coupling to light. Additionally, above a certain momentum, polaritons lie outside the light cone [indicated by a grey line in Fig. 9.3(a)] and do not couple to light at all.² Thus, the polariton lifetime is very different depending strongly on the polariton momentum. Inside the trap the polariton modes are strongly depleted, while above the bottleneck polaritons have long lifetimes and dynamics similar to that of excitons, due to their high excitonic component. Moreover, the bottleneck effect results in very slow relaxations from the *reservoir*³ to the bottom of the trap {[C] in Fig. 9.3(a)}. Given the very different lifetimes of polaritons inside and outside the trap, and the bottleneck effect, it is straightforward to see that any polariton relaxing from the *reservoir* to the trap immediately escapes from the system, and the emission dynamics at

²Let us note that the trap region in momentum space, and even the light cone region, are very small compared to the region of momenta over which thermalized polaritons extend above the bottleneck at the typical carrier temperatures of the photoluminescence experiments in these systems. An idea of the ratio between the number of carriers in each region can be obtained from the analysis of Fig. 5.3, where exciton depletion within the light cone can be compared to the extension of the distribution of excitons in momentum space at temperatures similar to those in microcavity systems.

³Given that the *reservoir* polaritons have a very strong excitonic character, and their energy-momentum dispersion is almost that of excitons, we will refer to them indistinctly as polaritons or as excitons. This is a nomenclature convention widely used in the literature.

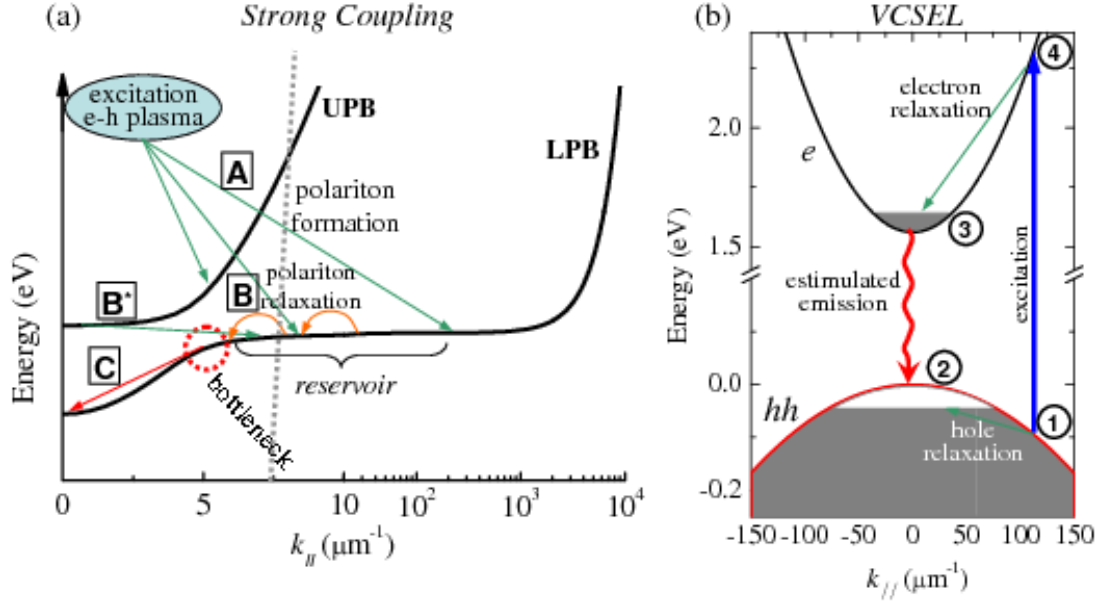


Figure 9.3: (a) Carrier relaxation in a microcavity in the strong-coupling regime: [A] polariton formation from the photocreated plasma of electrons and holes, [B] polariton relaxation and thermalization within the *reservoir* states, [B*] polariton relaxation from the bottom of the UPB to the *reservoir* states, [C] polariton relaxation from the bottleneck to the bottom of the LPB. The grey line indicates the light cone: polaritons with k_{\parallel} greater than that of the line cannot escape from the cavity due to total internal reflection. (b) Carrier relaxation and light emission in the weak-coupling regime above the threshold for photon lasing (VCSEL regime). The numbers indicate the leveling of the 4-level lasing system.

$k = 0$, for non-resonant excitation, is mainly determined by the polariton dynamics of the *reservoir* states close to the bottleneck, as these require the least amount of phonon or carrier scattering events to relax their energy and momentum.

The situation we have just described about the population distribution in the LPB can be extended to any detuning, the only difference being that at very positive detunings the LPB lifetime in the trap is increased, and the bottleneck effect is reduced. Eventually, at very positive detuning, the bare exciton dynamics are recovered, but still states close to $k = 0$ are significantly depleted as compared to the states outside the light cone [see Sec. 5.1.2 and Fig. 5.3].

According to the arguments presented in the previous paragraphs, the LPB $k = 0$ polariton dynamics under non-resonant excitation reflects the exciton dynamics at the *reservoir* states. In this sense, the long rise time depicted in Fig. 9.2(b) is caused by the

slow exciton formation, while the decay is mainly characterized by the long exciton lifetime. This interpretation is consistent with calculations of the polariton dynamics at different temperatures and detunings.[237]

The UPB dynamics can also be explained attending to the sketch of Fig. 9.3(a). As discussed in the preceding section, the upper branch polaritons are very fast depleted due to either their high photonic component (positive δ) or to their strong interaction with and fast relaxation to *reservoir* lower branch polaritons $\{[B^*]$ in Fig. 9.3(a)}.[34, 252] The large upper polariton linewidth is a manifestation of these interactions.

The very fast rise time of the UPB dynamics depicted in Fig. 9.2(b), at a considerable positive detuning ($\delta = +7$ meV), is a manifestation of the above mentioned fast depletion channels. The rise and decay UPB-dynamics depicted in Fig. 9.2(b), at a considerable positive detuning ($\delta = +7$ meV), are determined by two factors: (i) at this positive detuning, the UPB is of highly photonic character, with a very short state lifetime; (ii) the relaxation channel $[B^*]$ in Fig. 9.3(a) communicates the *reservoir* states with the UPB. In this way, the fast rise and slow long time decay of the $k = 0$ upper branch polaritons observed in Fig. 9.2(b) are a consequence of the quasi-thermal equilibrium between the *reservoir* states and the UPB: the fast rise is a consequence of the achievement of a polariton distribution in the *reservoir*, while the decay reflects the cooling of that distribution and the decay of the *reservoir* population.

In Sec. 8.2 and 8.3 of the preceding chapter, the calculated phase diagram of the microcavity system was presented. We mentioned that in the case of GaAs-based microcavities at low temperature, when increasing the carrier density the strong coupling is lost before reaching the critical density for the BEC of polaritons. This situation is explored in Fig. 9.4, where the emission dynamics of $k = 0$ polaritons are shown as a function of excitation power for a spot (~ 100 μm in diameter) on the sample with a detuning very close to *zero* ($\delta = +0.8$ meV). At very low power [Fig. 9.4(a)], a narrow emission (~ 500 μeV) is observed at the energy of the LPB. Also emission from the UPB can be observed with the appropriate setting of the z -scale, but it is not shown in this figure. As the carrier density is increased, the polariton linewidth increases due to the enhancement of the polariton-polariton and polariton-carrier interactions.[50, 12, 119] These interactions are also responsible for the shortening of the rise time as they also reduce the exciton formation time and ease the relaxation to the bottom of the trap. In Figs. 9.4(d)-(f) the transition from the strong to the weak coupling is evidenced. At short times, at these powers (and above), the high

density of free carriers injected by the non-resonant excitation pulse screens the electrons and holes that form the excitons leading to their ionization and the system evolves into the weak-coupling regime, characterized by emission at the energy of the cavity mode. At longer times, the number of carriers in the system decreases due to recombination. In this way the screening also decreases and the system goes back to the strong-coupling regime, characterized by emission at the energy of the LPB and UPB, as evidenced in Figs. 9.4(d)-(g) at long times.

Once the strong coupling is lost, the dispersion relations of the energy states of the system are given by those of the first electron and heavy-hole subbands, as depicted in Fig. 9.3(b). A four level system can be considered, as indicated in the figure, and population inversion between levels 3 and 2 is easily achieved as the electron and hole relaxation to the bottom/top of their bands is very efficient due to carrier-carrier interaction.[225] In this case the Bragg mirrors act as very efficient resonators with a photonic mode very close to the bandgap, and photon lasing is triggered, with a very low power threshold.[199, 38, 159]

Figures 9.4(f)-(i) show how, as soon as the system reaches the weak-coupling regime, photon stimulated emission takes place and the microcavity is driven into VCSEL operation. Due to the stimulated character of the recombination, the light emission is very fast in this regime. Most available electron-hole pairs at the cavity energy recombine in the first ~ 50 ps.

This situation of photon lasing is very different to that of a polariton laser (*plaser*).[121] Optical emission in a plaser would come from the leakage out of the microcavity of a BEC of polaritons at the bottom of the momentum trap. As was discussed in Sec. 8.1, due to the bosonic nature of the condensate, the stimulation process takes place during the relaxation of *reservoir* polaritons with large k to $k = 0$ states at the bottom of the LPB. The condensed polaritons are in a well defined quantum state, and when they leak out of the cavity present very similar characteristics to those of a conventional photon laser, i.e. monochromaticity, well defined phase, directionality. The fact that the stimulation and emission processes are decoupled can lead, in principle, to *plasing* devices without excitation threshold.[121]

Note that in the GaAs based systems we are discussing here, due to the small exciton binding-energy, and to the aforementioned screening of the excitons, the weak coupling threshold is reached at densities much smaller than those for BEC to take place. In systems with “stronger” excitons (i.e., with larger binding energy) the weak-coupling excitation threshold under non-resonant excitation is much higher,[133] even allowing for *plasing*

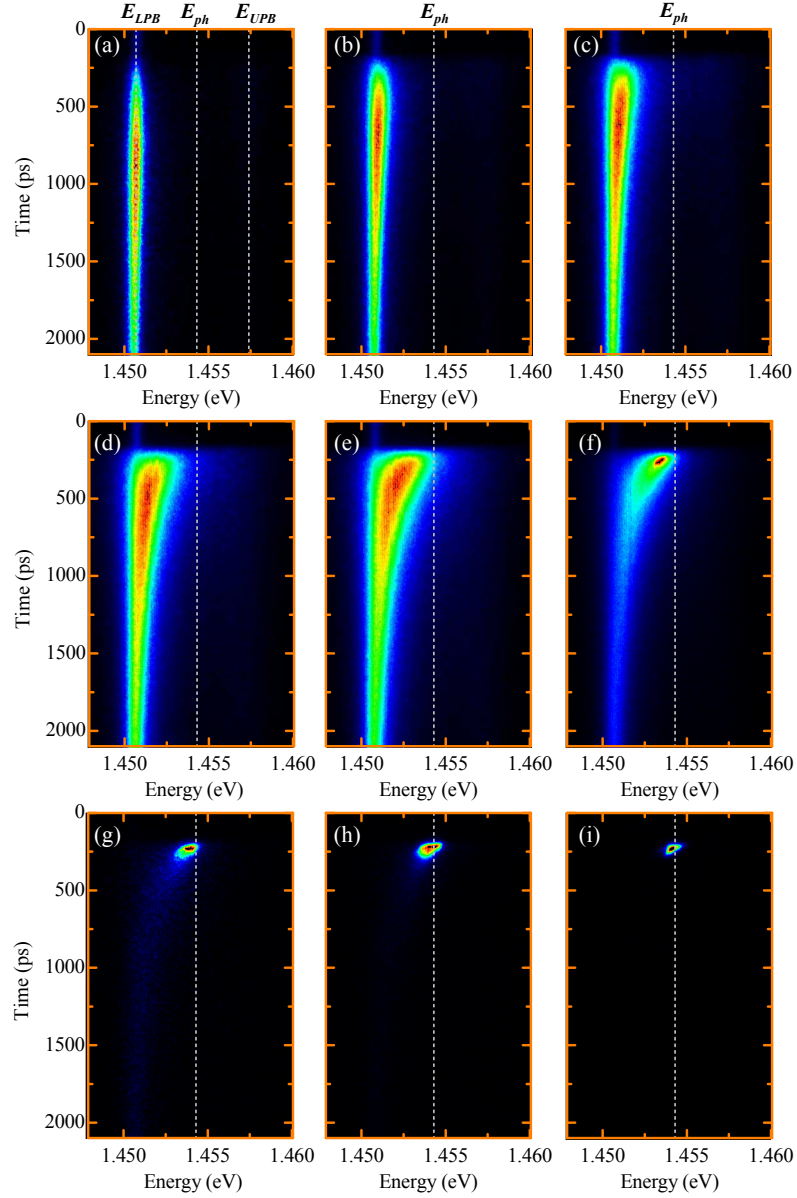


Figure 9.4: Microcavity luminescence at $k = 0$ at 5 K after pulsed non-resonant excitation above the first minimum of the stop band at different powers: (a) 1 mW, (b) 6 mW, (c) 10 mW, (d) 15 mW, (e) 20 mW, (f) 25 mW, (g) 30 mW, (h) 35 mW, (i) 45 mW. The dotted lines in (a) depict the energy of the $k = 0$ states of the LPB (1.4507 eV), cavity mode (1.4542 eV) and UPB (1.4574 eV).

to take place at room temperature, as evidenced in a recent observation in a GaN based microcavity[46].

Figure 9.4(f) shows that, at short times after excitation, emission from weakly (at the photon mode) and strongly (at the LPB) coupled modes coexist. This phenomenon can be observed in experiments at very different detunings. Figure 9.5 shows the emission energy (green and blue dots) as well as the intensity (red dots) dependence on pulsed-excitation power at several detunings in the sample. At low excitation density, the microcavity is in the strong-coupling regime with emission occurring at the LPB and UPB energies, with a linear dependence of the photoluminescence intensity on excitation density. The light blue areas depict the transition from the strong to the weak coupling at high densities. Analogously to the analysis carried on Fig. 9.4, the transition threshold can be identified by the shift of the emission to the cavity mode states (blue triangles). The appearance of emission at the cavity mode is accompanied by the onset of a superlinear dependence of the photoluminescence intensity on excitation power. Such a superlinear behavior is characteristic of lasing systems right at the threshold density.[75, 233] At higher excitation intensities the linear behavior is recovered, as hinted in Fig. 9.5(a).

The width of the light blue areas in Fig. 9.5 indicates the excitation power range over which strongly and weakly coupled modes can be observed. At detunings close to *zero*, where the strongly and weakly coupled modes are furthest apart in energy the coexistence is clearly observed. In this case the coexistence region could probably be extended to higher densities if a larger dynamic range would have been available in these experiments, as the photon lasing mode increases non-linearly while the coupled modes increase linearly with density. Let us also mention that studies in the same system evidence that the coexistence of strong and weak coupling takes place on emission areas smaller than $\sim 10 \mu\text{m}$. [22]

9.3 Polariton relaxation from the UPB in the strong coupling regime

The $k = 0$ lower-branch polariton dynamics is mostly determined by the dynamics of the reservoir polaritons, as it was pointed out in the discussion of the polariton relaxation channels [Fig. 9.3(a)] and evidenced by the slow dynamics shown in Fig. 9.4(a). In this section we will gain insight into this relationship through the results of a two pulses exper-

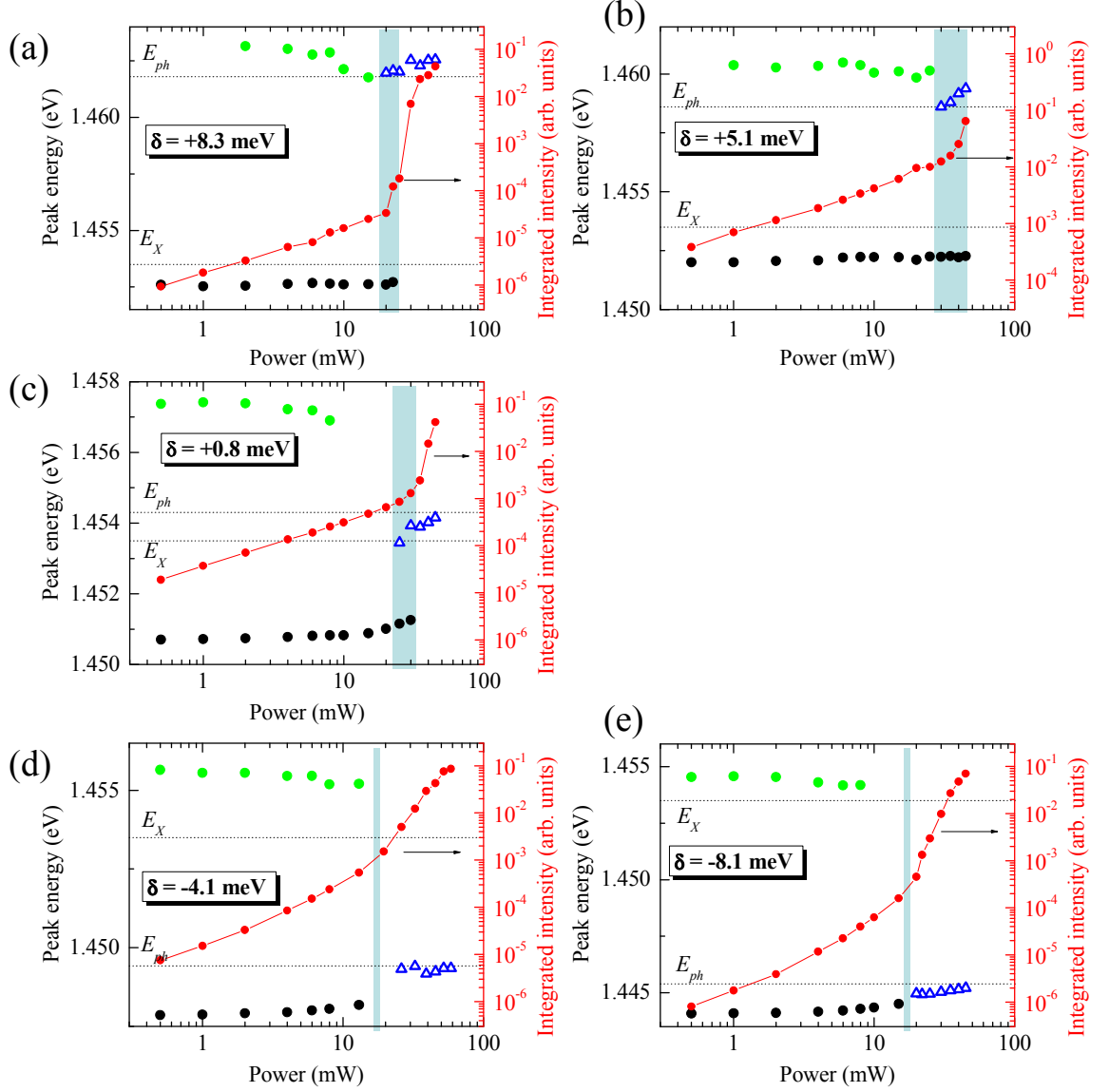


Figure 9.5: Energy of the $k = 0$ emission of the UPB (green dots), LPB (black dots) and cavity mode (blue open triangles) —left scales—, and total integrated emission (red dots) —right scales— as a function of non-resonant pulse power for several values of δ : (a) $+8.3$ meV, (b) $+5.1$ meV, (c) $+0.8$ meV, (d) -4.1 meV, (e) -8.1 meV. The blue area shows the transition from the strong to the weak coupling regimes. The dotted lines indicate the energy of the bare cavity and exciton modes.

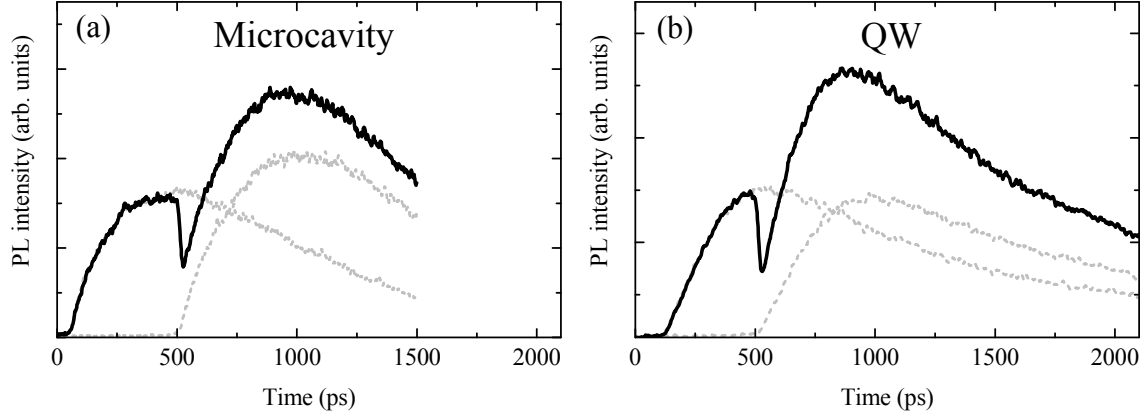


Figure 9.6: (a) PL dynamics of the $k = 0$ lower branch polaritons in the microcavity under one pulse excitation (grey dashed lines) and under two consecutive pulses excitation (black solid line; delay between pulses: 450 ps; power of both pulses: 0.1 mW). (b) Same as (a) for the PL dynamics of the bare QW excitons in an identical microcavity without top mirror. In this case the delay between pulses is 400 ps and the power of each pulse is 0.3 mW.

iment analogous to that described in the experiments of Chapter 7. In those experiments, two delayed excitation pulses P_I and P_{II} reach the sample on the same excitation spot, P_{II} inducing an ultrafast warming of the exciton population created by P_I . Figure 9.6(a) shows the LPB $k = 0$ emission under such a configuration for a spot on the sample at $\delta = 0$. In this case both pulses excite the sample non-resonantly (above the QW electron-hole continuum) with the same power (0.1 mW) and a delay between them of 450 ps. Analogously to the results presented in Chapter 7, a quench of the photoluminescence is observed at the arrival of the second pulse. P_I creates an electron-hole pair population that decays into *reservoir* excitons, which eventually relax to the bottom of the polariton dispersion trap giving rise to the emission shown in Fig. 9.6(a). The arrival of P_{II} induces an ultrafast warming of the exciton distribution in the reservoir producing an abrupt decrease of the exciton populations at the bottleneck and a subsequent quench of the $k = 0$ luminescence.

In order to stress that the physics behind the dip are fully determined by the redistribution of excitons in the reservoir, we have also performed a similar two pulses experiment in an identical microcavity sample that has been processed (chemical etching) in order to remove the top DBR mirror. In this way, the luminescence from the bare QWs can be accessed. Figure 9.6(b) shows the QW emission under the same non-resonant two pulses experiment (in this case with a delay between pulses of 400 ps). The dynamics of

the PL under a single pulse excitation (grey dashed lines) are alike in the microcavity and the QW, evidencing that they have the same origin. For a similar delay between pulses and ratio of the powers of P_I and P_{II} , the magnitude of the dip is also very similar in both cases, which is what would be expected from the model described in Sec. 7.3 if the dip is caused by the redistribution of excitons.

Taking advantage of the model described in Sec. 7.3 and the relation between dip depth and relative temperature change of the excitonic distribution [Eq. 7.3], we are going to study the relaxation of resonantly created upper-branch polaritons. In this case the excitation will no longer be non-resonant above the first minimum of the stop band. Here we will describe two pulses experiments in which polaritons are resonantly injected in an UPB state close to $k = 0$. Figure 9.7 shows the $k = 0$ LPB emission under excitation with two independent (black lines) and two consecutive (red lines) pulses resonant with the aforementioned UPB state, at different detunings. The first pulse is linearly polarized, the second one is σ^+ -polarized, and the σ^- -emission is detected. We use this configuration for reasons that will be explained below. Control of the polarization of the excitation and detection paths is performed by use of appropriate combinations of linear polarizers and quarter waveplates.

In these experiments P_I , linearly polarized, resonantly injects polaritons at the bottom of the UPB (see Fig. 9.7 upper panels). The direct relaxation via phonon emission to the $k \approx 0$ LPB states results in the very fast rise of the PL observed right after the arrival of P_I (black lines in the lower panels of Fig. 9.7).[252] Nonetheless, a significant portion of polaritons scatter to the *reservoir* states in the LPB, conforming a thermalized distribution. Some of these polaritons relax towards $k = 0$ states where they escape from the cavity giving rise to the decay observed at later times after the arrival of P_I . [34, 252] When a second delayed pulse reaches the sample, at the same energy and momentum as P_I , the photocreated upper polaritons relax again to the *reservoir* states with an excess energy given by the difference between the upper polariton energy and the *reservoir* energy (bare excitonic energy), which is indicated by Δ in Fig. 9.7. The second pulse is σ^+ circularly polarized (injecting spin-up polaritons), while only the σ^- circularly polarized emission is detected (from the escape of spin-down polaritons). In this way the direct relaxation of the polaritons injected by P_{II} from the UPB to the $k = 0$ LPB states is disregarded, as this phonon mediated process does not change the polariton spin. In contrast, the *reservoir* polaritons do flip their spin via usual exciton spin flip mechanisms,[63] and any change in

their distribution is reflected in the σ^- PL emission at $k = 0$. The slow rise observed in the lower panels of Fig. 9.7 after the arrival of P_{II} reflects the time required for reservoir polariton to flip their spin.

The red line in Fig. 9.7 shows the LPB $k = 0$ emission when the two consecutive pulses reach the sample. In Fig. 9.7(d) a dip in the PL can be observed indicating that the upper polaritons generated by P_{II} very efficiently relax towards the *reservoir* states [red arrows in (c)] changing significantly their distribution. By measuring the relative magnitude of the dip depth, and making use of Eq. 7.3 we can calculate the temperature increase of the reservoir polaritons induced by the injection of upper branch polaritons by P_{II} . In the case of $\delta = 0$ [Fig. 9.7(c)-(d)], the temperature increase is given by $T_{aft} = 1.2 \times T_{bef}$. For a larger detuning, as that depicted in Fig. 9.7(e)-(f), Δ is significantly increased, and the carriers injected by P_{II} more efficiently warm the exciton reservoir ($T_{aft} = 2.1 \times T_{bef}$), inducing a larger dip. In this case the UPB lies within the electron-hole continuum, and P_{II} injects electron-hole pairs in the system, which warm the reservoir excitons even more efficiently than upper-branch polaritons. Figure 9.7(a)-(b) depicts the case of very negative detuning. In this case Δ is very small, and the negligible excess energy of the polaritons injected by P_{II} results in a negligible warming of the *reservoir*.

9.4 Polarization dynamics in the weak coupling regime

A subject, within the field of microcavity polaritons, that has attracted the attention of both theoretical and experimental research groups is the issue of the spin dynamics of polaritons, which can be accessed through the study of the polarization of the light leaking out of these systems. Let us recall (see Sec. 3.2) that polaritons have the same spin states as light, with its $+1$ or -1 helicity oriented along the growth direction of the microcavity. Linear superpositions of these states give rise to elliptical or linear polarization, and polariton emission can in principle show any polarization.

The spin-dependent dynamics under resonant excitation of the LPB close to the magic angle show very complex behavior.[160, 134, 156, 218, 137] Several mechanisms participate in the polarization dynamics in this regime: (*i*) In the linear regime the polariton states are split into linearly-polarized modes (TE and TM) that act as an effective Voigt magnetic field for the circularly polarized polariton states. Let us note that this splitting is *zero* for polariton states at $k = 0$, but it may be important for polariton states at the

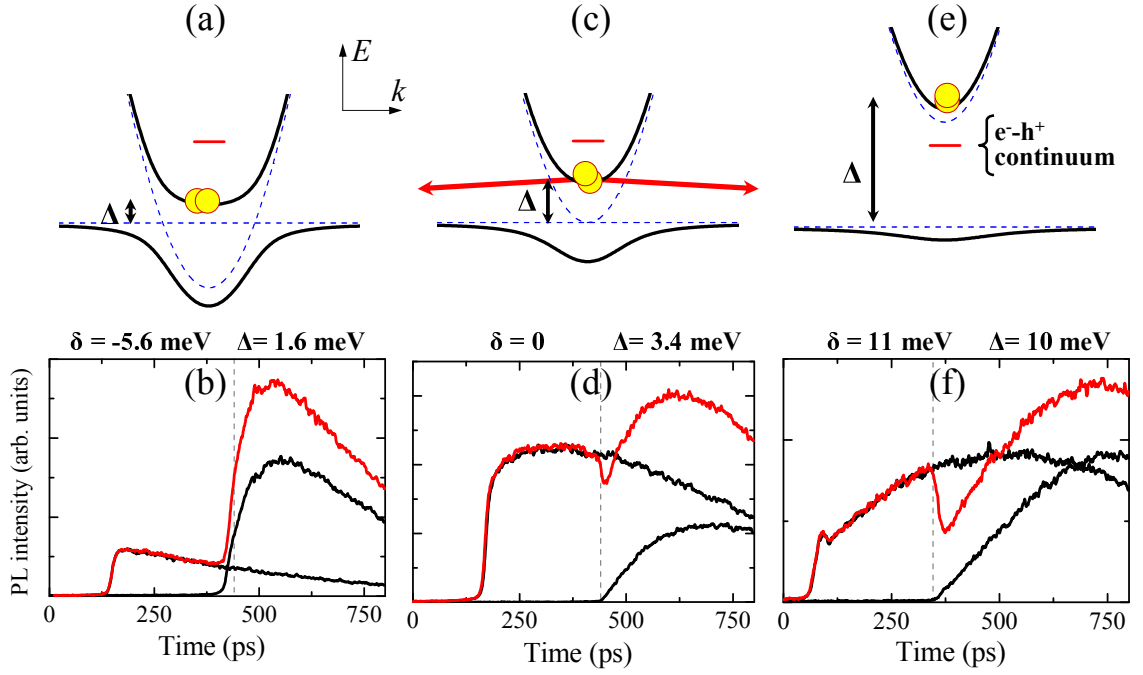


Figure 9.7: Upper panels: polariton dispersion (solid lines) at $\delta = -5.6$ meV (a), $\delta = 0$ (b), $\delta = +11$ meV (c). The blue dashed lines depict the dispersion of the uncoupled excitons and cavity photons. The short red line indicates the energy of the electron-hole continuum in the QWs. The yellow circles indicate the excitation energy and momentum. The red arrows in (c) indicate the upper polariton scattering into *reservoir* states. Lower panels: PL emission at $k = 0$ in the LPB under one pulse excitation (black lines) and under two consecutive pulses excitation (red lines) at the detunings indicated in the upper panels. In each case the power of both pulses is equal. The first pulse is linearly polarized, while the second one is σ^+ circularly polarized; only the σ^- component of the emission is detected (see text for details).

bottleneck.[196] (ii) Due to in plane asymmetries of the QWs or Bragg mirrors, a splitting may arise between the linearly polarized polaritons along the directions of asymmetry, usually oriented along the crystallographic directions of the heterostructure.[156, 231] (iii) In the non-linear regime, the renormalization associated to the high occupation of polariton states of a given polarization, induces a splitting between circularly polarized polariton states equivalent to an effective magnetic field in the Faraday geometry. Under the effect of this field the polarization of an elliptical polariton state would precess about the growth direction.[260, 218, 259] (iv) Polariton-polariton scattering shows a strong spin dependence due to the repulsion between polaritons of the same spin, resulting in the rotation of the polariton polarization in this type of events.[160, 134]

Under non-resonant excitation the polariton emission also shows non-trivial polarization dynamics,[185, 146] particularly in the regime of BEC. It has been predicted that the spontaneously condensed polariton state at $k = 0$ must show linear polarization, and several experimental evidences of this behavior have been provided.[132, 21] However, non-negligible degrees of linear polarization have been observed at $k = 0$ below the condensation threshold,[147] due to crystallographic anisotropies of the sample.

In this section we will briefly show experimental results on the polarization dynamics in a different situation in a microcavity: the high-power weak-coupling regime. We will see that this regime also shows peculiar polarization characteristics, most probably related to sample asymmetries along the crystal directions of the sample.

In order to access the polarization properties of the system we have employed a similar experimental configuration to that used in the previous section, with polarization optics (quarter-waveplates and linear polarizers) in the excitation and detection arms. In this way, excitation with linearly or circularly polarized light pulses can be performed, while the emission can be analyzed into its polarization components.

In the case of linear polarization experiments it is convenient to define the TE and TM polarization directions. In the TE mode, or transverse electric, the light is polarized *perpendicular* to the direction of propagation of polaritons in the plane of the microcavity. In the TM mode, or transverse magnetic, light is linearly polarized *parallel* to the to the propagation direction inside the cavity,

As shown in Fig. 9.8, TE modes can be excited with light linearly *perpendicular* to the plane of incidence (green arrow), while TM modes will be excited by light linearly polarized parallel to that plane (red arrow, orange component parallel to the direction of

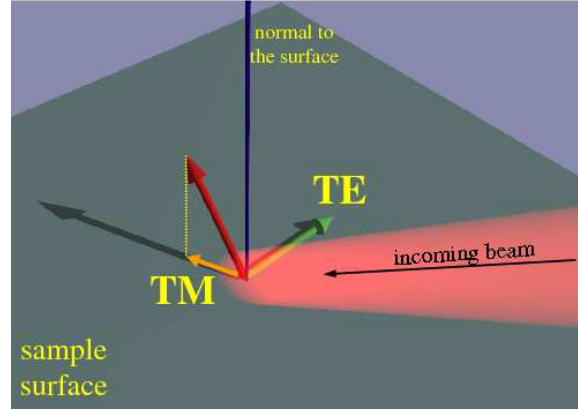


Figure 9.8: Excitation of TE and TM polarization modes. The sample surface is parallel to the quantum well and cavity spacer, and the plane of incidence is that defined by the incoming beam and the normal to the surface. The green arrow indicates the direction of linear polarization *perpendicular* to the plane of incidence. The red arrow represents the linear polarization *parallel* to the plane of incidence. In this case there is always a component of the electric field *parallel* to the propagation direction in the cavity (orange arrow).

propagation inside the cavity).

The orientation of the polarized light and the angle of excitation will set a well defined TE or TM configurations. In the experiments shown in this section, the excitation beam arrives on the sample with an angle of 2.5° . A degree of linear polarization (\wp_{LIN}) of the emission can be defined as:

$$\wp_{LIN} = \frac{I^{TM} - I^{TE}}{I^{TM} + I^{TE}}, \quad (9.2)$$

where I^{TM} (I^{TE}) indicates the emission intensity linearly polarized parallel to the TM (TE) direction.

Figure 9.9(a)-(b) depicts the PL intensity of the $k = 0$ σ^+ (σ^-) emission [black (red) line] and the corresponding circular polarization (\wp_{CIR} , blue lines), at low [(a); 2 mW] and high [(b); 45.5 mW] excitation power after the arrival of a σ^+ pulse for a detuning of -4.1 meV. \wp_{CIR} is defined by Eq. 6.3. In the low power case (a) the emission arises from the LPB of the strongly coupled modes, showing no polarization, while at high densities the system operates in the VCSEL regime and a low value of \wp_{CIR} , constant in time, can be observed. The situation in a linearly polarization geometry is very different. Figure 9.9(c)-(d) shows the PL emission at $k = 0$ decomposed into its TM and TE components⁴ for

⁴At $k = 0$ the TM and TE components are defined with respect to the plane of incidence of the excitation

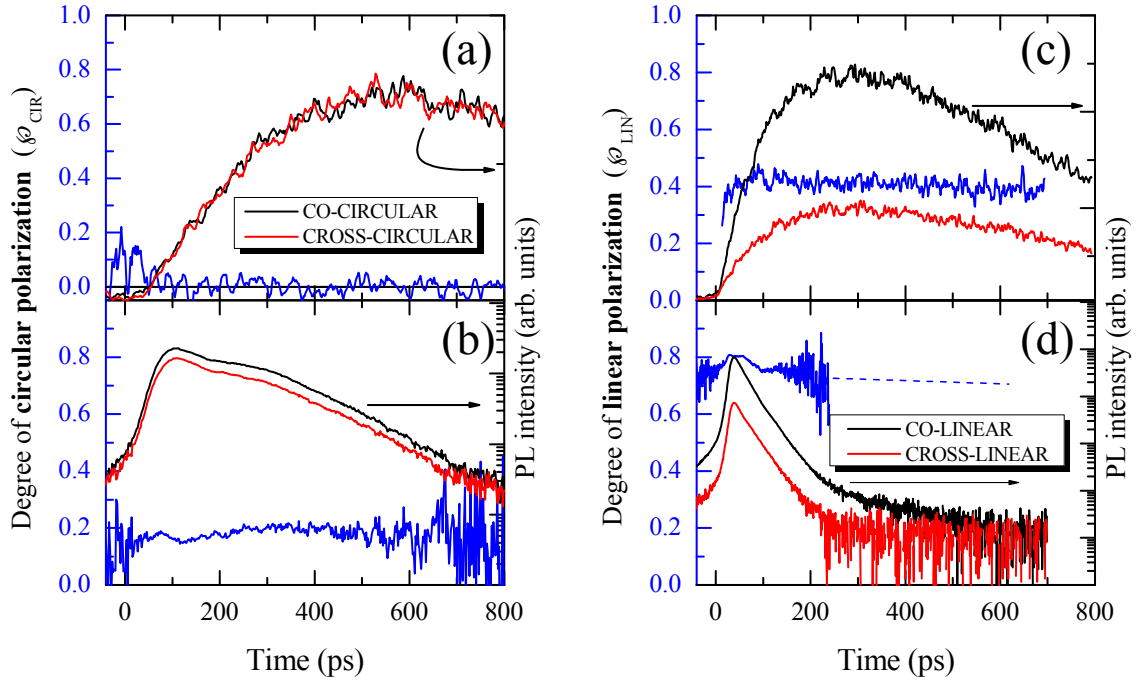


Figure 9.9: Degree of circular polarization (left scales, blue lines) and PL intensity for each circularly polarized component at $k = 0$ (right scales) under σ^+ excitation in the low power (a) —2 mW, strong coupling, LPB— and high power (b) —45.5 mW, photon lasing— regimes. (c) and (d), same as (a) and (b) for linearly polarized (TM) excitation. The black (red) lines denote emission co-(cross-)polarized to the excitation. Note the logarithmic scale for the PL intensity in the lower panels. The position on the sample corresponds to a detuning of -4.1 meV

TM-polarized excitation. Much larger values of linear polarization \wp_{LIN} of the emission are found, even at low power, and the decay time of the polarization is very long (> 4 ns).

The results at different excitation powers are summarized in Fig. 9.10, where the power dependence of the time and energy-integrated \wp_{CIR} (a) and \wp_{LIN} (b) as well as the total PL-intensity are depicted under σ^+ and TM excitation, respectively. Under σ^+ excitation [Fig. 9.10(a)], only in the regime above the threshold for VCSEL operation (~ 20 mW, characterized by a non-linear increase in the emission intensity, dotted line) a non-zero value of \wp_{CIR} can be observed, always lower than 0.2. On the other hand, \wp_{LIN} [Fig. 9.10(b)] always shows a high degree, approaching 1 above the VCSEL threshold.

In the experiment shown in Fig. 9.10(b), excitation was kept in a TM configuration. However, the plane of linear polarization of the emission is in fact unrelated to the polarization of excitation. The plane of polarization is found to be pinned to a particular crystallographic direction of the sample. The polarization plane of the emission remains the same under TE-, TM- and circularly- polarized excitations, and it rotates when the sample is rotated. This behavior is very different to that found in optically excited VCSELs at room temperature. In such conditions, under non-resonant circularly polarized excitation the VCSEL emission is found to be highly co-polarized with the excitation.[7, 120] Even under elliptical excitation the emission partially “remembers” the axis orientation of the polarization ellipsis of the excitation.[109] These effects can be well described with the spin-flip model developed by San Miguel, Feng and Moloney.[228] According to this model, a circularly polarized absorbed beam excites three times more electrons of a given spin than the opposite in the QW (see Fig. 3.3). The spin imbalance is partially retained during the carrier relaxation and amplified by stimulated emission in the circularly optical transition associated to the majority spin population. On top of this, the fact that one of the spin sublevels in the active medium (the QW) is more populated (even reaching saturation limits) than the other, results in nonlinear optical anisotropy effects.[92, 77]

In contrast, electrically pumped VCSELs tend to emit in linearly polarized light along one of two crystallographic directions ($\langle 011 \rangle$ and $\langle 01\bar{1} \rangle$ in GaAs based systems) with no change in the emission spectra between the two polarizations (same fundamental cavity mode). Polarization bi-stability has been found when changing the injection current within a given current range,[195, 45] while polarization instabilities correlated with changes in the

beam.

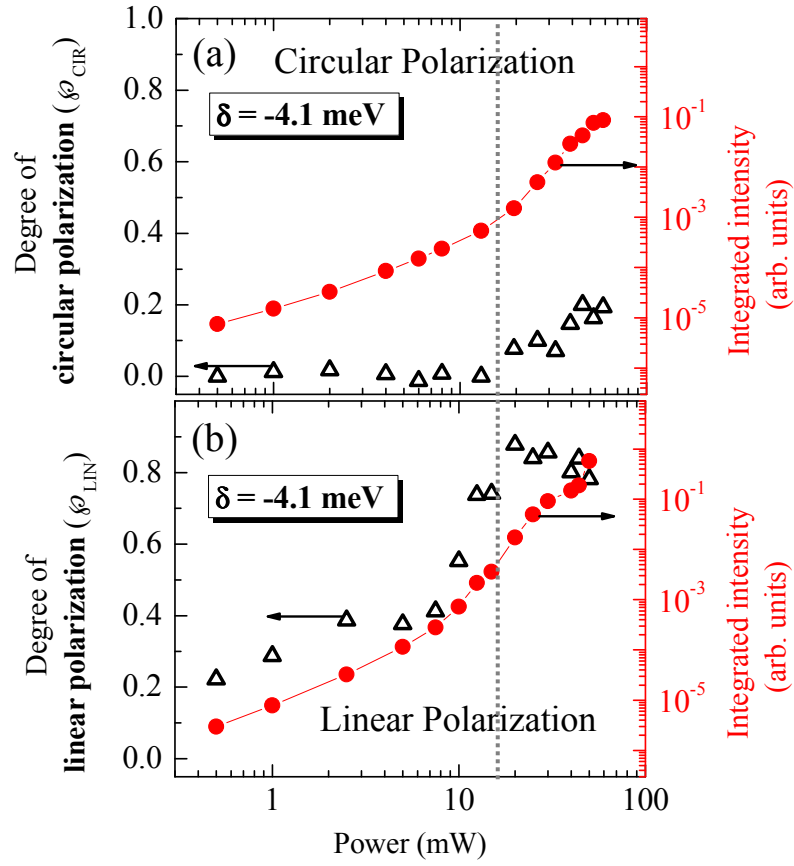


Figure 9.10: (a) Time- and energy- integrated degree of circular polarization (open triangles) and total PL intensity (red dots) as a function of the photoexcitation power of σ^+ pulses. (b) Same as (a) for the degree of linear polarization under TM-polarized excitation. The dotted line depicts the onset of non-linear emission.

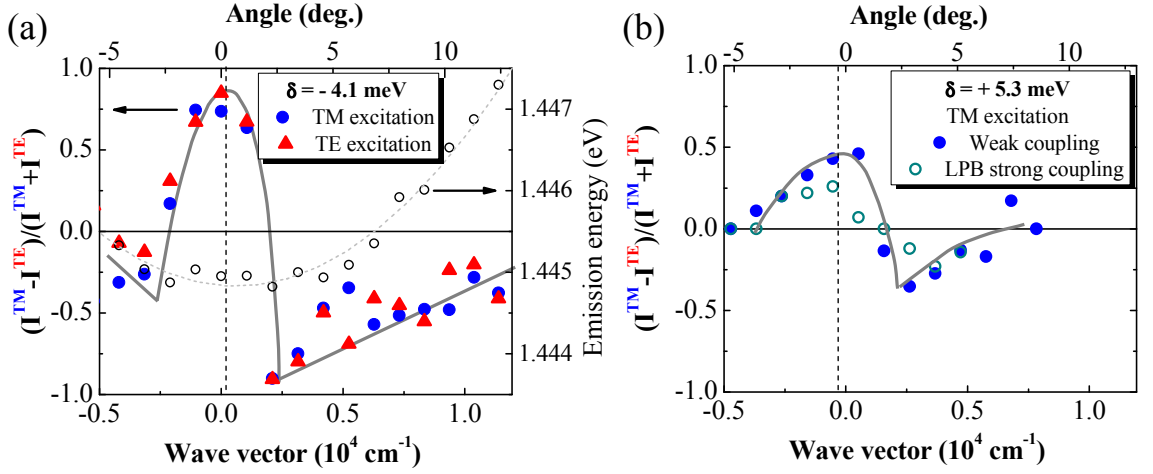


Figure 9.11: (a) Angle dependence of the energy- and time-integrated linear polarization of the cavity mode emission at high power (42 mW, weak-coupling regime) for TM (blue solid dots) and TE (red triangles) polarized excitation at $\delta = -4.1 \text{ meV}$. The open dots depict the emission energy. (b) Same as (a) for $\delta = +5.3 \text{ meV}$ at high power (43 mW, solid blue dots; weak coupling, cavity mode emission) and low power (14 mW, open dots; strong coupling, LPB emission).

spectral profile of the emission have been observed.[84]

The results shown in Figs. 9.9 and 9.10 indicate that in the microcavity under study, pinning to one of the crystallographic axis dominates the polarization properties both in the strong and in the weak coupling regimes. Additionally, the long decay times of φ_{LIN} depicted in Fig. 9.9(b) indicate that linearly polarized states might be the eigenstates of the system. Let us mention that in many microcavity systems parametric processes[74, 231, 223] or spontaneous polarization[147, 132, 21] are also pinned to particular crystallographic orientation.

In order to understand whether the polarization pinning originates from anisotropies in the QW or in the cavity DBRs, angle-resolved experiments have been performed at different detunings. Figure 9.11 shows the degree of linear polarization with respect to the TM emission at different emission angles. In this case, the TM and TE emission is defined from the plane of observation [TM (TE): linear polarization perpendicular (parallel) to the plane of observation]. In the particular experimental realization of the experiments shown in Fig. 9.11, the TM and TE directions coincide with the relevant crystallographic axis of the sample.

Figure 9.11(a) shows that at high excitation power (42 mW, weak-coupling regime)

and negative detuning ($\delta = -4.1$ meV) the degree of linear polarization is independent from the polarization of excitation, and presents very strong angular oscillations. The polarization remains approximately constant for angles of ± 2 around $k = 0$. However, a increasing the detection angle above that value results in an abrupt switching in the degree of linear polarization from $+0.8$ to -0.9 . A further increase of the detection angle leads to a monotonic reduction of the degree of polarization. Thus, the polarization plane of the emission changes from TM to TE in a narrow cone around $k = 0$.

The case of positive detuning ($\delta = +5.3$ meV) is depicted in Fig. 9.11(b). The polarization emission pattern at high excitation (43 mW, weak-coupling regime; solid dots) is similar to that of $\delta = -4.1$ meV, with a lower absolute magnitude of the polarization. At low power (14 mW, strong coupling), the emission from the LPB still shows the pattern, with an even lower value of the polarization. This seems to indicate that the higher the photonic component of the emitting quasiparticle from the microcavity, the higher polarization in the emission can be found. Then, the pinning effect of the linear polarization should be attributed to the axial anisotropies in the DBRs. Although the DBRs are made of layers of quasi lattice-matched materials (GaAs/AlGaAs), it has been shown that in heterostructures with so many layers (each DBR is composed of about 40 epilayers), strain may develop along particular crystal directions.[168] The fact that higher values of the linear polarization are found at negative detuning may be also linked to the fact that at $\delta = +5.3$ meV, the cavity mode lies well above the continuum of free electrons and holes of the QW. High carrier scattering is present at the energy level from which luminescence is originated [see Fig. 6.3(b)], somewhat affecting the degree of linear polarization imposed by the photonic anisotropy. At negative detuning, the weak-coupling emission originates from the recombination of the low energy tail of the electron-hole distribution in the QW, which shows low scattering rates due to degeneration effects [Fig. 6.3(b)].

The physical origin of the unconventional angular polarization distributions depicted in Fig. 9.11 is not clear and has not been reported in VCSELs, where PL studies are limited to the emission parallel to the growth direction. The angular effects reported here might be originated from TE/TM birefringence associated to the photonic anisotropy in the system.

9.5 Summary

In this chapter we have presented experimental results on the time-resolved PL in semiconductor microcavities under non-resonant excitation. At low excitation density the system remains in the strong-coupling regime and the polariton emission at $k = 0$ is dominated by the exciton formation and polariton relaxation from the bottleneck states. The relaxation from upper-branch polaritons to reservoir states has been investigated in a two pulses experiment. In this experiment, the controlled warming of the *reservoir* polariton distribution has been demonstrated.

Going back to the non-resonant excitation configuration, we have shown how the microcavity is driven into the weak-coupling regime as the power is increased, where photon lasing dominates the emission. In this case we have shown that the emission is linearly polarized along a direction pinned to one of the crystallographic axis of the system. The pinning arises from anisotropies in the photonic confinement and might also be responsible for the abrupt switching between perpendicularly-polarized modes at different emission angles.

Chapter 10

Polariton quantum hydrodynamics

10.1 Introduction

In the previous chapter we presented experiments under non-resonant excitation in an InGaAs/GaAs/AlGaAs based microcavity. The emission dynamics in the strong-coupling regime are well explained by free carriers and polariton relaxation mechanisms, giving rise to polariton incoherent populations. Even though only the emission from the $k = 0$ states has been so far considered, in this incoherent regime polaritons distribute along the polariton dispersion giving rise to incoherent luminescence from all states within the light cone.

As discussed in detail in Sec. 8.3 and shown in the experimental results of Sec. 9.2, under highly non-resonant excitation (via photocreation of free electrons and holes) in GaAs based microcavities it is not possible to reach a quantum condensed phase of polaritons. In CdTe based microcavities a Bose-Einstein condensed state has been observed by Kasprzak and coworkers under such excitation conditions,[133] and also in GaAs based microcavities, by the group of Yamamoto, under direct injection of *reservoir* polaritons.[71, 161] The importance of those experiments is that a phase transition from an incoherent state (injected free electrons and holes in the experiment of Kasprzak, *reservoir* excitons in the Yamamoto experiments) to a coherent condensed state of polaritons is observed. Due to the Bose-Einstein character of the transition, polaritons spontaneously condense in a state that lies at the bottom of the polariton dispersion, in a macroscopically occupied state with *zero* linear momentum.

Very interesting properties distinctive of a condensed phase have been observed from this *zero* momentum state, as detailed in Sec. 8.3. In fact, experimental observations

of spectral and momentum narrowing, spatial coherence and long-range order have been used as proof for the polariton Bose-Einstein phase transition, However, despite these observations being clear evidence that polariton BECs can be formed in microcavities, they do not differ significantly from what can be found in a pure photonic laser.[17]

A differential landmark between a Bose-Einstein condensate of interacting polaritons and a condensate of non-interacting photons (a laser), would be the observation of superfluid properties in the polariton condensate. The observation of these properties would confirm the quantum nature of the condensed phase.

As demonstrated in many experiments in atomic condensates, superfluidity may be evidenced in different ways. Two of the most intuitive are the formation of vortices with quantized angular momentum,[2] and the interaction with moving point-like potential barriers (“obstacles”).[43] In the latter case, a quantum condensate interacting with an obstacle traversing it presents very specific scattering properties. Some of them were detailed in Sec. 8.5. If the quantum condensate is in the superfluid regime, the obstacle will traverse the quantum fluid without causing any scattering [Fig. 8.7]. If the speed of sound of the quantum fluid is smaller than the velocity of the moving obstacle, scattering takes place giving rise to a Čerenkov like pattern [Fig. 8.6].[43]

A polariton condensed state with *zero* momentum, as those created by Kasprzak *et al.* and by the group of Yamamoto, is not suitable to study these phenomena. A polariton quantum state with well defined non-zero momentum must be employed so that it can interact with static obstacles in the sample.¹ In this chapter we will experimentally explore this situation. We will show a novel technique for the creation and observation of polariton quantum states with a well defined and controlled non-*zero* momentum (Secs. 10.2 and 10.3). Then we will discuss experimental results on the interaction of these quantum fluids with obstacles of different sizes found in the sample (Sec. 10.4). Some of the phenomena introduced in the previous paragraph and in Sec. 8.5 will be evidenced in these experiments.

10.2 Making polaritons flow

The most straightforward way to make polaritons flow would be by the resonant, pulsed² photocreation of polaritons in a state of well defined momentum in the LPB. However

¹Just by making a Galilean transformation this situation is equivalent to that of a static condensed state interacting with a moving object.

²A pulsed source is essential if the dynamics of the polariton fluid is to be studied.

this configuration presents many difficulties when it comes to the detection of the polariton movement. First of all, polaritons only live a few picoseconds before escaping the cavity (the polariton lifetime is on the order of 1-4 ps in most of the available microcavities). The temporal dynamics of polaritons after a resonant pulsed laser excitation can be resolved detecting photon arrival times from the sample. However, even the best detectors do not allow for resolution better than 1-2 ps,³ when the polariton population of the excited state has almost completely disappeared. Additionally, stray light from the resonant laser excitation is much stronger than the light emitted by the polaritons, hindering the detection of their movement in the cavity, even a few picoseconds after the arrival of the pulse.

Very few experiments in the literature address the issue of polariton movement. Freixanet, Sermage and coworkers[90, 253] presented an experimental configuration in which polaritons with a well defined momentum state were created by resonant pulsed excitation of the LPB at a given angle of incidence. In order to avoid the aforementioned difficulties, they made use of a pinhole to block the stray light from the laser. In this way they restricted the observation to polariton states with different momentum and energy to those resonantly addressed by the laser. The observed states do not conform polariton fluids with macroscopic occupations, as they are populated by the incoherent scattering from other polariton states (mainly from the state excited by the laser).

Another experiment on this issue is that recently presented by Langbein *et al.*[169] In this case a well defined polariton state is not excited, as the pulsed source simultaneously populates a plethora of states with all possible in-plane momenta at a given energy in the LPB. The stray light from the laser is eliminated by use of a confocal setup with a mask of the excitation spot. In any case, incoherent propagation of the polaritons in a ring departing from the excitation spot can be observed, with a very fast decay (~ 4 ps).

In the experiments of Freixanet, Sermage, Langbein and coworkers, besides the difficulties related to the very fast decay of the polariton populations, the addressed polariton states present an incoherent nature. Thus, they do not conform a condensed quantum phase and they are not subject to the superfluidic description of bosonic quantum states.

Here we present a experimental configuration that allows us to create a polariton fluid in a well defined energy and momentum quantum state while being able to observe its

³An experimental set-up based on the up-conversion technique would provide a resolution below 1 ps. However, we are interested in the real- and momentum-space time-resolved imaging of the system in order to observe the polariton flow, and this can hardly be realized with the up-conversion technique due to its particular characteristics.

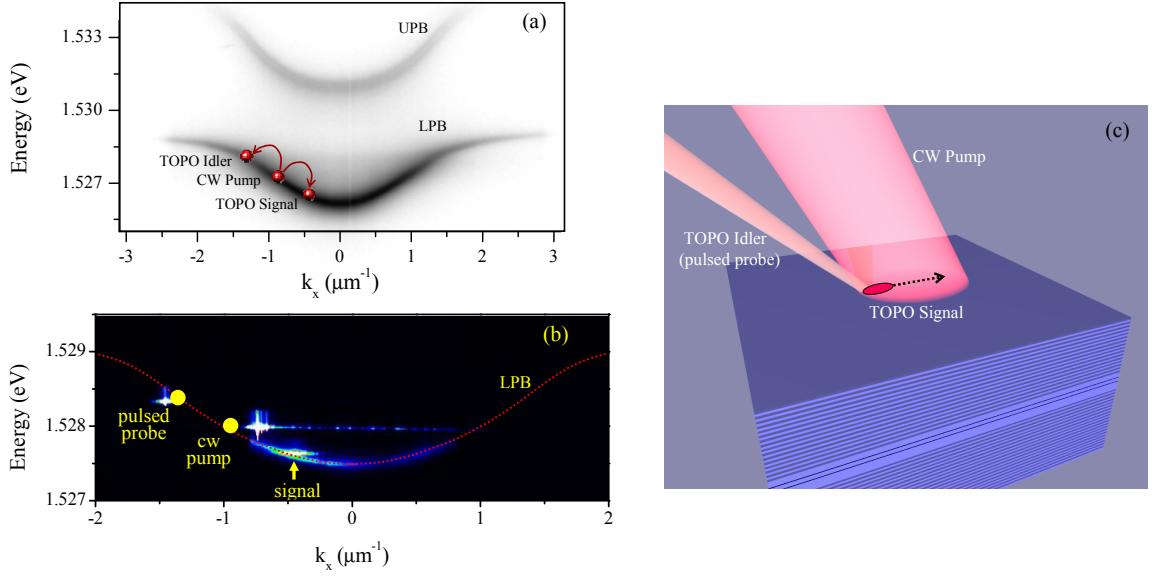


Figure 10.1: (a) Far field PL emission from the investigated microcavity under non-resonant excitation at $\delta = 0$. In the LPB, a sketch of the TOPO configuration is presented. The CW pump and pulsed idler arrive at the sample with angles of 10° and 16° respectively, giving rise to a signal state expected at 4° from the growth direction (normal to the surface). (b) Far field PL emission under resonant pump and idler excitation in the OPA configuration (same configuration as the TOPO with both pump and idler beams being CW). The laser scattered-light from the CW pump and idler (indicated by the yellow dots) has been blocked in order to avoid the bleaching of the detection CCD. The signal state is visible at $k_x = 0.5 \mu\text{m}^{-1}$. (c) Sketch of the pump and idler laser spots on the sample.

spatial evolution without any of the difficulties related to the decay of the populations and of the stray light from the laser.

Our experimental configuration is based on a continuous replenishing of the polariton fluid from a higher-lying state driven coherently by an external CW-laser in a configuration of a triggered optical-parametric-oscillator (TOPO) in the lower polariton branch. Figure 10.1(a) shows a sketch of the excitation conditions in this configuration. The sample employed for the experiments described in this section is a $\lambda/2$ -GaAs/AlGaAs microcavity with a single wide QW in the antinode of the electromagnetic field in the center of the cavity. The sample was grown at the *Laboratoire de Photonique et de Nanostructures* (CNRS, France). More details about this sample can be found in Sec. 4.1.3. The sketch of the excitation conditions in Fig. 10.1(a), is plotted on top of the PL dispersion under low power, non-resonant excitation, at 10 K (temperature at which all experiments in this chapter have

been done). We will restrict all the experiments shown here to the case of $\delta = 0$ (where light-matter coupling is strongest).

The way the TOPO works is the following. Under CW pumping, a large polariton population is created at a LPB state (the “pump” state, P) with energy E_P and in-plane momentum k_P . E_P can be selected by tuning the laser energy, while the in-plane momentum k_P is established by the angle of incidence of the CW-pump beam on the sample [k_P and incidence angle are related by Eq. 3.15]. Polariton pair-scattering processes are possible to the signal (S) and the idler states (I), as long as the phase matching conditions 8.11 and 8.12 between pump, signal and idler states are fulfilled:

$$2E_P = E_S + E_I,$$

$$2\mathbf{k}_P = \mathbf{k}_S + \mathbf{k}_I.$$

If the pump population is large enough, pair scattering is spontaneously stimulated to the signal at $k_S = 0$ (i.e., $\mathbf{k}_I = 2 \times \mathbf{k}_P$), which becomes macroscopically occupied in a well defined quantum state⁴. [267, 239, 293, 51] However, if a polariton population at an idler state (E_I , $\mathbf{k}_I \neq 2 \times \mathbf{k}_P$) is created by a CW probe while CW exciting the pump state, pair scattering processes will be stimulated to a signal state predetermined by Eqs. 8.11-8.12. Thus, the momentum and energy of a signal-polariton population can be arbitrarily prepared with the proper selection of pump and idler energies and incidence angles. This configuration is called Optical Parametric Amplifier (OPA), [232] and can be easily achieved for a range of pump, signal and idler states due to the peculiar dispersion found in semiconductor microcavities and the strong non-linearities associated to the polariton interaction.

In our experiment, the pump is a CW beam but the probe is a short (2 ps) pulse at the idler state, which just initializes the system, inducing a population at the signal state. After the probe pulse has disappeared, the signal state is left macroscopically occupied, and final state stimulation of the pump polaritons to the signal polaritons carries on for nanoseconds. This novel experimental configuration, only initialized by the probe pulse, corresponds to a triggered OPO (TOPO), where the final-state stimulation of the pair-scattering process is provided by the self-sustained high occupancy of the signal and idler

⁴In this configuration, known as OPO, scattering to the signal quantum state is stimulated by the high occupation of the final state (signal) and its bosonic character (see Sec. 8.4)

states and it is fueled by the continuously replenished polariton population in the pump state (Fig. 10.1).

With the experimental configuration just described, we can create polariton states with a well defined non-vanishing momentum at an energy different from that of the excitation lasers. By making use of a spectrometer in the detection setup, we can select the emission from the signal states and filter out the stray light from the excitation sources. Additionally, the high occupancy of the signal state (which is an essential precondition for the TOPO process to be activated) assures that signal polaritons are indeed in a quantum macroscopically occupied state. Figure 10.1(b) shows an actual time integrated CCD image of the far field PL in the regime of OPA, with CW pump and idler excitations.

In the time resolved experiments, the CW pump is focused on the sample on a spot of $110\mu\text{m}$ in diameter, while the pulsed idler is focused with a size of $16\mu\text{m}$ inside the pump spot, as depicted in Fig. 10.1(c). Once the TOPO is initialized on the spot of the sample illuminated by the pulsed laser, the signal polaritons start to move at a velocity given by their center of mass momentum. In a time given by the polariton lifetime in the cavity (2-4 ps), polaritons move to a nearby different point in the sample and then leak out of the cavity. However, the CW pump continues to feed the signal state by the TOPO mechanism, as long as the signal polaritons move within the pump spot. Once the fluid reaches the pump-spot edge, the signal dies away. The position of the signal-polariton fluid is evidenced by the light emitted at the energy of the signal state, which arises from the photons escaping from that state. In all the experiments presented here (except stated otherwise), the CW pump will be injected at an angle of 10° (corresponding to an in-plane momentum of $\sim 1.15\mu\text{m}^{-1}$).⁵

Let us note that polariton-polariton interactions result in appreciable renormalizations (blueshifts) of the LPB when large populations are injected in the system. These interactions arise from the exciton content of the polaritons and are described by the g dependent terms in Eq. 8.15. When preparing the pump and idler states in the TOPO, the band blueshift must be taken into account by fine adjusting the energy of the CW pump and pulsed idler so that the phase matching conditions are satisfied.

⁵This angle is slightly below the magic angle (12° , inflexion point of the LPB). In this way, the threshold for the spontaneous OPO of the pump is increased and the emission of the OPO signal at $k = 0$, which could contaminate the emission from the nearby TOPO signal state, is minimized. However, this pump angle is close enough to the inflexion point so that the phase matching conditions 8.11-8.12 for the TOPO are still easily achieved.

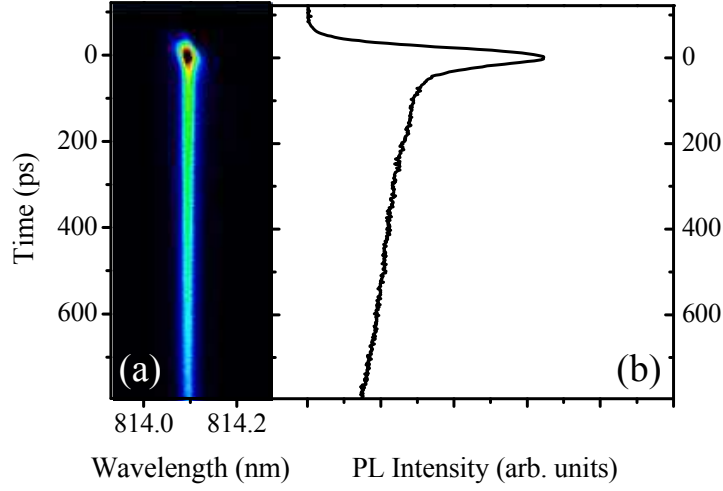


Figure 10.2: Time evolution of the TOPO signal at $k = 0$ after the arrival of the pulsed idler for pump and idler energies and momenta such that the phase matching conditions result in a signal at $k = 0$ (pump incidence angle: 12°). (a) Streak-camera image. (b) Time profile, showing a signal decay-time of 1.1 ns.

The setup used for the detection of the polariton fluids moving across the sample is shown and explained in detail in Sec. 4.2.3. The employed configuration allows us to alternatively form the 2D images of the near-field (real space) or far-field (momentum space) emissions on a CCD or on the input slit of a streak camera at a given energy. Therefore, movies of the real- and momentum-space movement of the polaritons in the sample can be recorded at a given emission energy with a time resolution of about 8 ps. The total spectral and spatial resolutions are on the order of 0.2 meV and $4 \mu\text{m}$, respectively.

The sustainability in time of the TOPO process can be investigated if the pump and idler beams are set, following the phase matching conditions 8.11-8.12, to in-plane momenta and energies such that the signal state appears at $k_S = 0^6$ (bottom of the LPB). In this case the signal polaritons state does not move in space and its lifetime can be measured. Figure 10.2(a) shows a streak-camera image in its usual configuration (wavelength *vs* time) of the signal PL at $k = 0$. The signal emission is triggered at the arrival of the idler pulse. The very fast initial decay is caused the disappearance of the idler pulse, whose photon density sets the initial occupation of the signal states. After the pulsed has disappeared the signal is fed by the pump polaritons, showing a decay of 1.1 ns [Fig. 10.2(b)]. The factors

⁶ $\mathbf{k}_I = 2 \times \mathbf{k}_P$ and $E_I = 2 \times E_P - E(k = 0)$.

determining this decay are currently under investigation.

10.3 Polariton flow in the absence of defects

10.3.1 Polariton flow

Figure 10.3(a) shows several frames of the real-space emission at the energy of the signal polaritons, in the TOPO configuration described in the caption of Fig. 10.1(a), after the arrival of the pulsed idler. Far field images at the same emission energy are also displayed at the same time delays [Fig. 10.3(b)]. In Fig. 10.3, as well as in the rest of the movies presented in this chapter, the images are obtained by recording the emission with pump and idler beams impinging upon the sample and subtracting the emission from just the pump excitation. In this way only the polaritons populated by parametric processes triggered by the pulsed idler are recorded. It is readily seen that signal polaritons freely move across the sample without expanding or interacting with the surrounding medium until polaritons reach the edge of the area excited by the CW pump. In k -space the motion is unperturbed and the total polariton momentum is conserved, with a value of $k_p = -0.75 \mu\text{m}^{-1}$, without any appreciable spreading.

A detailed analysis of real-space films shows that the polariton fluid moves at a constant speed. Its group velocity is $v_g = (1.7 \pm 0.4) \mu\text{m}/\text{ps}$. We can compare this value with the velocity associated to the observed momentum in the k -space images. The group velocity and the momentum of the center of mass of the fluid is given by:

$$v_g = \frac{\hbar k_p}{m_p}, \quad (10.1)$$

where m_p is the polariton mass. The polariton mass can be obtained from the measured dispersion relation of the LPB under non-resonant excitation shown in Fig. 10.1(a): the bottom of the LPB can be fitted to a parabolic function and the effective mass of the polaritons can be obtained ($m_p = \frac{1}{\hbar^2} \frac{\partial^2 E}{\partial k_p^2}$). For the conditions of $\delta = 0$ considered here a LPB polariton mass of $1.89 \times 10^{-4} m_0$ is obtained.

In this case, with the value of k_p measured in Fig. 10.3(b), a polariton group velocity of $v_g = (0.5 \pm 0.3) \mu\text{m}/\text{ps}$ is obtained. This value is lower, but close to, that directly measured from the movement in real space. The reason for this discrepancy might be in the uncertainties associated to the calibration of the momentum space in the CCD images

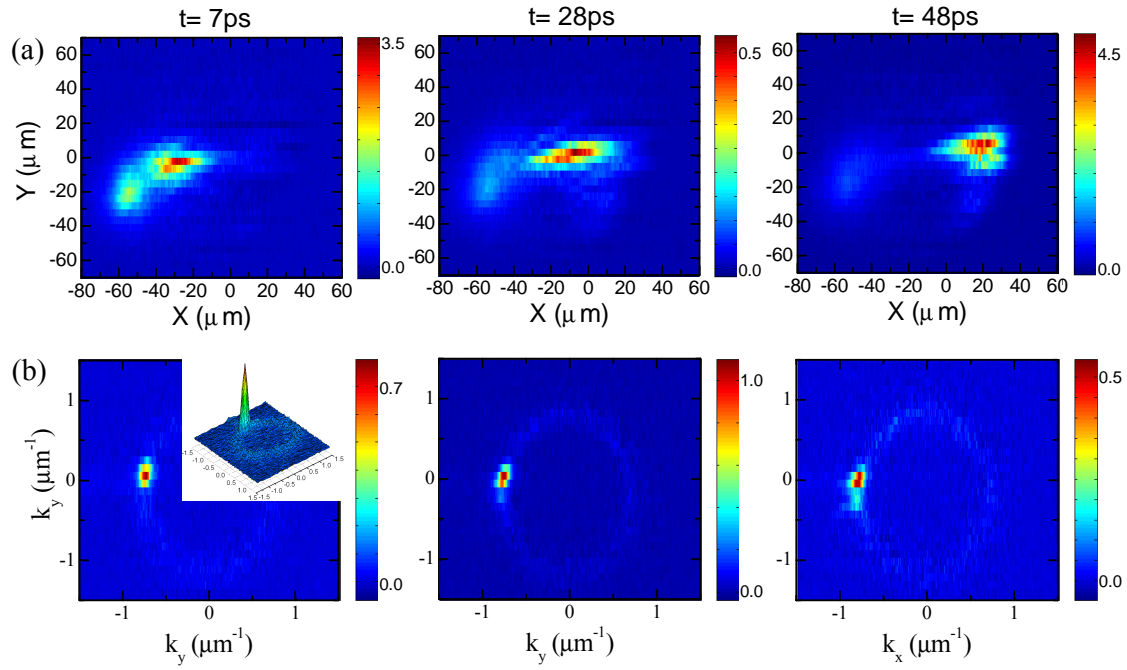


Figure 10.3: Spectrally selected observation at the TOPO signal energy of a coherent polariton gas moving at $v_g = 1.7 \mu\text{m}/\text{ps}$. The images are real space shots taken at different times after the probe pulse arrival ($t = 0$). (b) Reciprocal (momentum) space frames recorded at the same time delays and energy as (a). The inset displays a 3D view which evidence the narrowness of the k distribution. The diffusion-less motion and the invariance of the k -vector are a clear signature that polaritons are in a regime showing quantum coherence. The CW pump power is 20 mW (10°), while the pulsed probe power is 110 μW (16°).

from which the polariton mass is obtained [Fig. 10.1(a)]. Nonetheless, other important considerations should be taken into account. In order to calculate v_g from the measured center of mass momentum of the fluid, we employed the polariton mass from the non-resonant, low power polariton dispersion. However, the polariton dispersion is subject to important changes when it is resonantly excited in the LPB. Figure 10.4(a) shows the LPB dispersion around $k_x = 0$ (k_y is kept 0), as obtained in the TOPO regime at short times after the arrival of the idler pulse, for a spot on the sample and exciton condition similar but not identical to those used to obtain the dynamics displayed in Fig. 10.3. The emission is spatially integrated over all the excitation spot, but as shown in Fig. 10.3, the emission characteristics do not significantly change along the trajectory of the fluid.

To obtain the image shown in Fig. 10.4(a), the detection path in the experiment was setup in order to form an image of the far-field emission on the entrance slit of the streak camera (which in such configuration produces k_x -momentum space images resolved in time at a given detection energy). In this case, $k_y = 0$ was selected, and the detection energy was scanned obtaining a k_x vs energy plot at a short time (12 ps) after the arrival of the pulsed idler. Note that the image is obtained by recording the emission of the TOPO (CW pump plus pulsed idler) and subtracting the emission caused by the CW pump only. Only the polaritons populated by parametric processes triggered by the pulsed idler are recorded.

The signal states in Fig. 10.4(a) can be easily identified as a PL peak at negative values of k_x . Due to the finite energy width of the idler pulse (~ 2.5 meV), the phase matching conditions give rise to several signal states, that conform the observed peak in Fig. 10.4(a). Each of them presents a macroscopic occupation (as this is the condition for stimulated scattering to those states in the TOPO configuration), and can be treated as a polariton fluid in itself. Let us recall that in the real- and momentum-space images shown here, we select one of these states by energy filtering.

Figure 10.4(b) shows in black dots the PL peak positions extracted from (a), under resonant CW-pump (orange arrow) and pulsed-idler excitations. The red dots depict the LPB dispersion from the same spot on the sample after non-resonant, low-power excitation. Marked differences can be appreciated between the two situations. First of all, the resonantly excited dispersion presents a blueshift in the emission of about 0.75 meV. This renormalization of the band arises from the strong polariton-polariton interaction in the system (terms containing g in Eq. 8.15), due to the high density of polaritons injected by the pump beam. Additionally, the polariton band shows a linearized section close to the

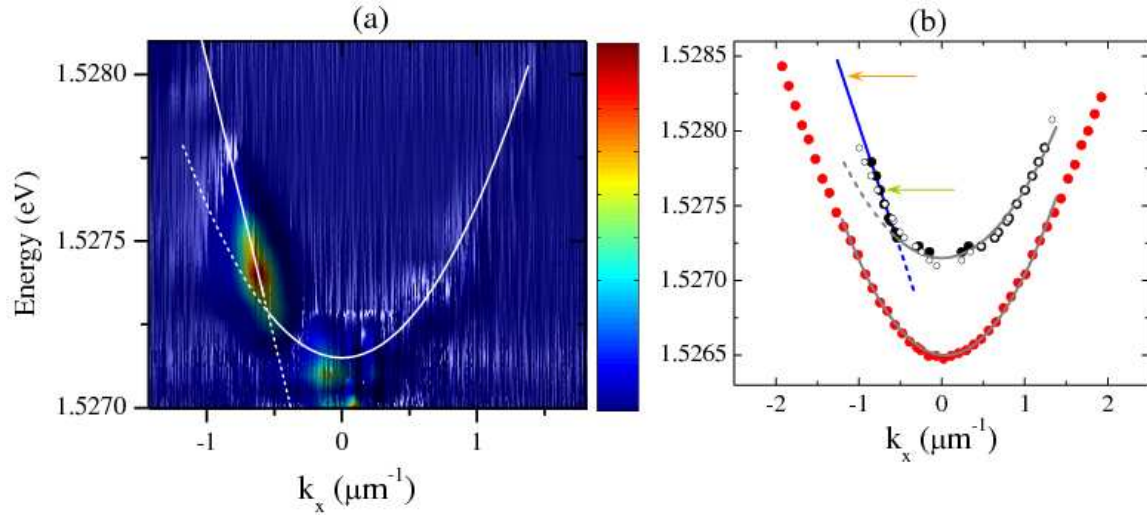


Figure 10.4: (a) PL intensity as a function of energy and momentum of the emission for $k_y = 0$, at short time (12 ps) after the arrival of the pulsed laser in the TOPO configuration. Note that the image is obtained by recording the emission of the TOPO (CW-pump plus pulsed-idler) and subtracting the emission caused by the CW pump only. In this way only the polaritons populated by parametric processes triggered by the pulsed idler are recorded. The white lines are a linear and parabolic fit as in (b). (b) Black dots: PL-peak positions extracted from (a). Open points: dispersion under just CW-pump excitation (no idler pulse). Red dots: LPB dispersion obtained under low-power, non-resonant excitation in the same spot as that depicted by the black dots. The orange arrow indicates the energy of the CW-pump, while the green arrow depicts the position of the signal state. The blue line is a linear fit to the black dots with $k_x < -0.45 \mu\text{m}^{-1}$, while the grey line is a parabolic fit to the emission at $k_x > -0.45 \mu\text{m}^{-1}$.

states where the pump is being injected. In the same graph, the open points depict the measured dispersion in the absence of the idler pulse. In this case the emission does not show an intensity peak at the energy of the signal states (not shown here), as no TOPO has been initialized, but the dispersion relation is very similar to that depicted in black solid dots. This fact indicates that both the overall blueshift and the linearization of the polariton band, observable through the PL emission, arise from the renormalization induced by the high density of injected polaritons in the pump state. In fact, considering the pump spot size, the size of the traveling signal and the power of the emitted PL intensity we estimate that the density of signal polaritons is at maximum one tenth of that of the pump polaritons.

The dispersion relation shown in Fig. 10.4(b) is very similar to that calculated by Ciuti and Carusotto[49] and displayed as a solid line in Fig. 8.6(a). This calculated dispersion actually depicts the spectrum of excitations ($\delta\phi$, Eq. 8.18) of a polariton fluid coherently injected by a laser at the pump state, with no pulsed idler. The most important type of excitations considered by Ciuti and Carusotto when calculating such a spectrum are pair-polariton scattering events from the pump fluid.[49] This is precisely the kind of excitations that give rise to the occupation of LPB states in the conditions of Fig. 10.4. In fact, the signal state in the TOPO regime can be considered a pair-polariton scattering excitation of the pump state, as depicted in Fig. 10.1(a). For this reason the dispersion obtained from the PL (Fig. 10.4) and that calculated and shown in Fig. 8.6(a) correspond to the same physical situation. However, Ciuti and Carusotto treat the pair-polariton excitations as a first-order perturbation to the polariton system, while the signal state triggered by the pulsed idler may require a full non-perturbative treatment in order to fully understand its properties.[41] Thus, comparisons between the theory developed by Ciuti and Carusotto and the experimental results presented here must be done with caution.

With these premises, we can consider the signal state as a polariton fluid moving in a dispersion mainly renormalized by the large pump population. This situation may explain the aforementioned discrepancy in the calculation of the velocity of the fluid depicted in Fig. 10.3. In order to calculate the velocity associated to the signal wavevector shown in Fig. 10.3(b) we used Eq. 10.1 and the polariton mass obtained from the LPB parabolic approximation under non-resonant excitation. We have just seen that the signal polariton fluid “lives” on top of the renormalized dispersion. The signal polariton velocity can then be directly calculated from the dispersion shown in Fig. 10.4(b):

$$v_g = \frac{1}{\hbar} \frac{\partial E}{\partial k_p} \quad (10.2)$$

For $k_p = -0.75 \mu\text{m}^{-1}$ (where the dispersion is linear) we obtain a velocity of $v_g = (2.6 \pm 0.3) \mu\text{m}/\text{ps}$, very close to the value of $(1.7 \pm 0.4) \mu\text{m}/\text{ps}$ directly obtained from the real space film in Fig. 10.3(b) under similar (but not identical) conditions to those of Fig. 10.4.

10.3.2 Polariton diffusion

A direct consequence of the signal polaritons moving on top of a linearized section of the dispersion as that shown in Fig. 10.4 is that the signal polariton wavepacket does not spread. A wavepacket of non-interacting particles on a parabolic dispersion is subject to real- and momentum-space expansion due to the effects of the uncertainty principle (non-commutability of space and momentum operators).[52] Under such circumstances, if the considered wavepacket has a size (FWHM) of Δ_0 at $t = 0$, the time evolution of its Gaussian width Δ is given by:[171, 52]

$$\Delta = \sqrt{\Delta_0^2 + \left(\frac{2\hbar t}{m_p \Delta_0} \right)^2} \quad (10.3)$$

However if the wavepacket lives on a linear dispersion, as is the case of the signal polariton fluid, no expansion at all is expected,⁷ neither in real or momentum space.[80] Figure 10.5 depicts in solid dots the Gaussian width, in the y direction, of the signal polariton fluid shown in Fig. 10.3(a) as it traverses the excitation spot. No apparent diffusion of the polariton packet is observed. The red solid line displays the time evolution of the width of the wavepacket, if the polariton fluid would be characterized by a parabolic dispersion (Eq. 10.3).

A similar behavior is expected in reciprocal (momentum) space. Indeed, Fig. 10.3(b) shows no apparent diffusion of the well defined momentum of the polariton wavepacket.

It is interesting to compare the behavior of a characteristic polariton quantum fluid as that depicted in Figs. 10.3-10.5, with a polariton packet in the incoherent regime.

⁷If we take into account the polariton-polariton repulsive interactions, even in a linearized dispersion the polariton wavepacket should spread in time. However, these interactions are not expected to be apparent in the time scales considered here. In atomic condensates on the other hand, atoms move in a parabolic dispersion but present a very large mass. In this case the broadening of the wavepacket given by Eq. 10.3 is negligible, and the observed expansion of the atomic clouds in millisecond timescales is caused by repulsive inter-atomic interaction.[103, 97]

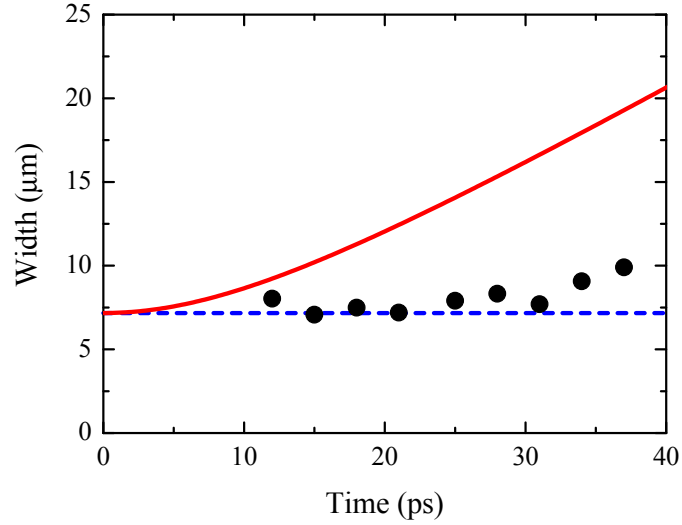


Figure 10.5: Solid dots: Gaussian width of the polariton packet in the y -direction extracted from the real space images of Fig. 10.3(a). Solid red line: calculated wavepacket diffusion for a parabolic dispersion [Eq. 10.3]. Blue dashed line: expected wavepacket diffusion in a linear dispersion.

Figure 10.6 shows the time evolution in real (a) and momentum (b) space at the energy of the signal polaritons for a low (7 mW) CW pump excitation. The emission from the signal polaritons is still triggered by the arrival of the pulsed idler. In this case, the PL arises from the phonon assisted relaxation of the idler polaritons and from lightly induced pair scattering from the pump to the signal state. However, in this case no occupation greater than 1 is achieved in the signal state and a quantum fluid is not formed.

In this particular case, if the pump is increased above certain threshold (10 mW) the TOPO is initiated and a quantum fluid is formed at the signal state.

The real space dynamics are very different to the case of Fig. 10.3. In Fig. 10.6(a) the polariton packet very slowly moves from the spot where it is created to a nearby site where it gets localized in a shallow photonic well. In momentum space we can see that a ring very rapidly forms after the arrival of the pulsed idler due to the inelastic-scattering origin of the PL at the signal state and also to elastic polariton-polariton scattering within the signal states. The appearance of the ring is a direct evidence of the signal state not being in a well defined quantum state, but conforming a plethora of incoherent states at different momentum. Still, for the first ~ 45 ps the fluid has a favored momentum, which reflects the slow movement of the ensemble at those early times. When the packet becomes

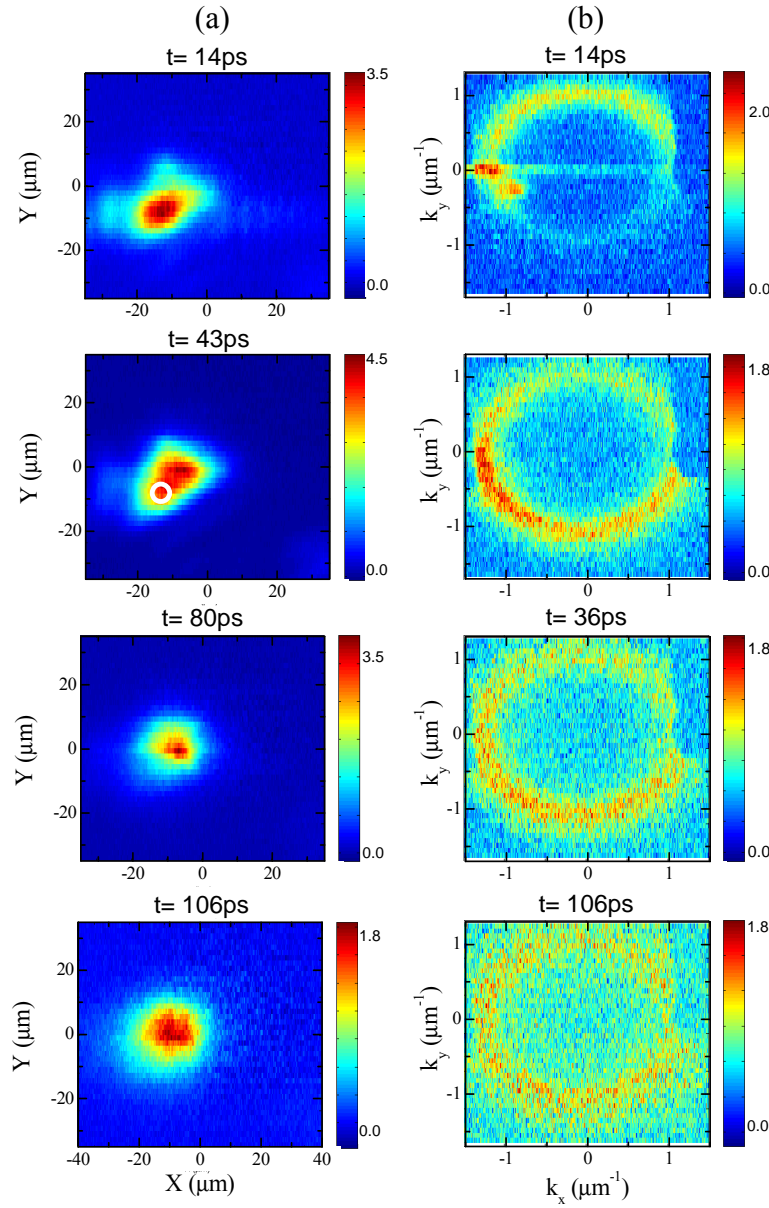


Figure 10.6: Real-space (a) and momentum-space (b) images, of an incoherent polariton fluid, at a detection energy above the bottom of the LPB at different times. The color scales vary from panel to panel. The images are obtained at low pump power (7 mW, 10°). The idler is set at 16° at $130\text{ }\mu\text{W}$. In real space the fluid slowly moves diagonally to the right and upwards. The white circle at 43 ps depicts the position of the fluid at $t = 14\text{ ps}$. A $t \gtrsim 45\text{ ps}$ the fluid gets localized in a shallow potential.

localized, the momentum fully randomizes resulting in the observed homogeneous ring.

10.3.3 The pump and signal polariton quantum fluids

From the discussion in the previous paragraphs it is important to emphasize that in the TOPO experimental configuration we must consider that at least two polariton quantum fluids coexist in the system. The most largely populated is the polariton fluid in the pump state. This fluid is coherently driven by the CW laser and, therefore, the phase of its wavefunction, is externally imposed. Additionally, the large population of this state results in the renormalization of the of the whole lower polariton band.

The second coexisting quantum polariton fluid is that at the signal state that results from the TOPO process described above, and lives on the renormalized polariton dispersion established by the large pump population. One of the most important characteristics of the signal state is that its phase is not necessarily set by the coherently driven pump state. As discussed in Sec. 8.4 [Eq. 8.14], once the signal emission is initialized by the pulsed idler and the OPO regime sets on, the phase of the signal state is unrelated to that of the pump. This implies that the spectrum of excitations of the signal polariton fluid may be of a Goldstone-mode nature, and it may show superfluid behavior.[298]

Finally, a polariton fluid at the idler state should also be present as a consequence of the parametric process associated with the OPO. However, this fluid is subject to very fast dephasing as it is very close in energy to the *reservoir* (see Sec. 8.4). Therefore, it will not be considered here.

In order to explore in detail the nature of the signal (and pump) polariton fluids, in the next sections we will present results on the interaction of these fluids with potential barriers of different sizes and shapes. Localized potential barriers are present in the micro-cavity in the form of photonic or excitonic defects. In the sample under study, which is of a very high crystalline quality, scattering centers are present with an approximate density of $0.01 \mu\text{m}^{-2}$. In the calculations of Ciuti and Carusotto reported in Refs. [42, 49] (also introduced in Sec. 8.5) it's shown that the interaction of a polariton fluid with such defects on the sample may reveal its quantum nature and superfluidic properties, if any. For instance, Figs. 8.6(b)-(c) and 8.7(b)-(c) show calculations of the near- and far-field emissions of a polariton quantum fluid at the pump state interacting with a defect in two different pump configurations.[49]

10.4 Interaction of the polariton fluids with localized defects

This section shows a menagerie of interaction effects between polariton fluids and potential barriers of different shape and size. Even though the three cases treated here reflect quite different situations, the understanding of the behavior of the fluids in each case provides insights into its quantum nature and properties.

10.4.1 Scattering with a small point-like defect

Figure 10.7(a) shows images obtained in the near field of a TOPO polariton-fluid colliding against a defect positioned in the middle of its trajectory. It is important to realize that the images reflect the addition of two different contributions: a) the pump polaritons (extended in an area of $\sim 8 \times 10^3 \mu\text{m}^2$) which constantly feed the signal polariton, and b) the motion of the signal polaritons by themselves, which pass through the defect. Figure 10.8 illustrates how these two contributions are detected at the signal polariton energy. The fringes observed around the defect appear due to the local change in density of the pump polaritons, which is reflected in the structure of the signal.

The pump polaritons are injected in a coherent state, at high energies, high density and with high k -vector. In the conditions of Fig. 10.7 the pump polariton state, whose phase is determined by the CW pump, is well described by the situation depicted in Fig. 8.6, which shows the calculations of Ciuti and Carusotto for a polariton fluid in the so called Čerenkov regime.[49] In the conditions of Fig. 10.7 the pump polaritons *must* have a group velocity higher than the velocity of sound (v_s) (i. e., a Mach number > 1), giving rise, in the presence of a defect, to very characteristic quantum interferences resembling Čerenkov waves, observable through the emission of the signal polaritons as depicted in Fig. 10.8.⁸ The velocity of sound is given by Eq. 8.21, and its value can be estimated from the blueshift of the polariton dispersion, which is equal to $\hbar g |\Psi_{LP}^{ss}|^2$, and from the measured mass of the unperturbed polaritons. In this case we find $v_s = 3 \mu\text{m}/\text{ps}$. Similar shockwaves have been reported recently for an atomic BEC flowing against a potential barrier at Mach numbers greater than one,[43]

It is important to note that the visibility of these waves does not imply that the signal polaritons are also in the Čerenkov regime. On the contrary, the signal polaritons

⁸The observation of the Čerenkov shockwaves in the pump state does actually reveal the position of the defect on the sample.

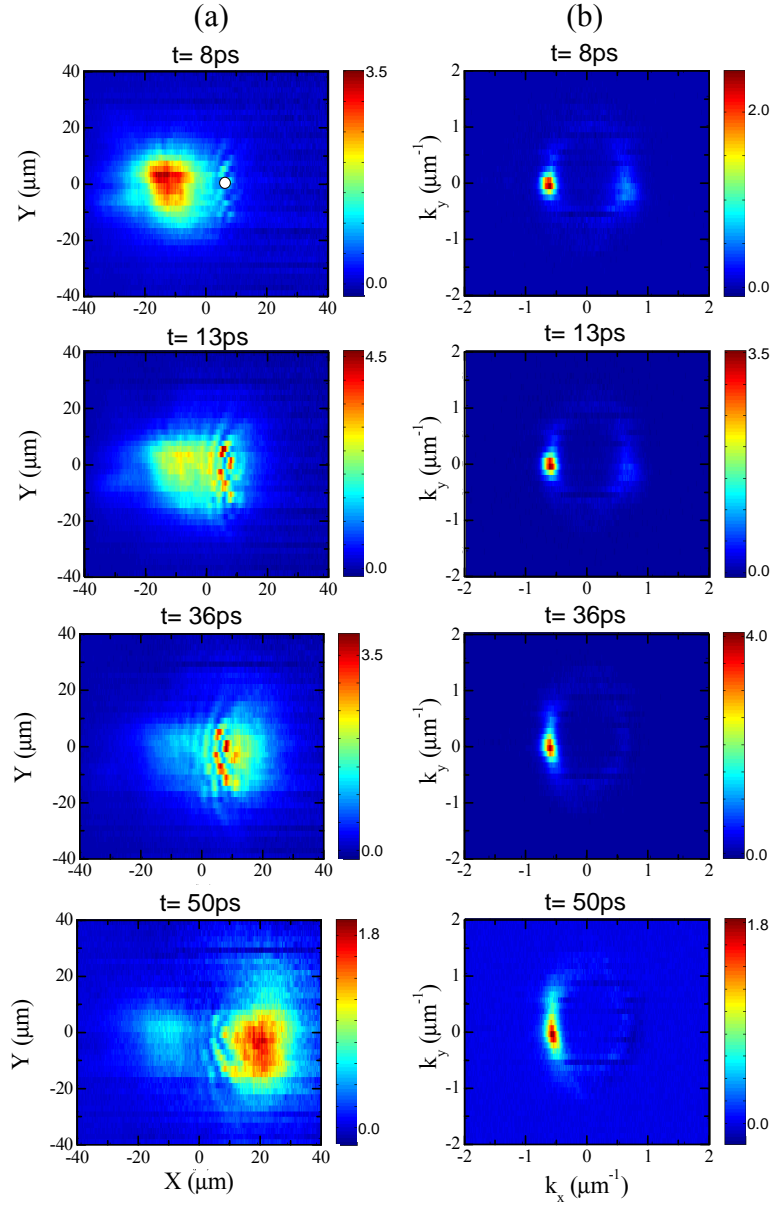


Figure 10.7: (a) Signal polariton movement in real space at different times in the presence of a small defect (marked with a white dot in the first panel). The observed Čerenkov waves reflect the local change in density of the pump polaritons, which are traveling at a supersonic velocity (see text and Fig. 10.8). (b) Corresponding momentum space images. The color scales vary from panel to panel. The pump (idler) power is 54 mW (315 μW) and the angle of incidence is 10° (16°).

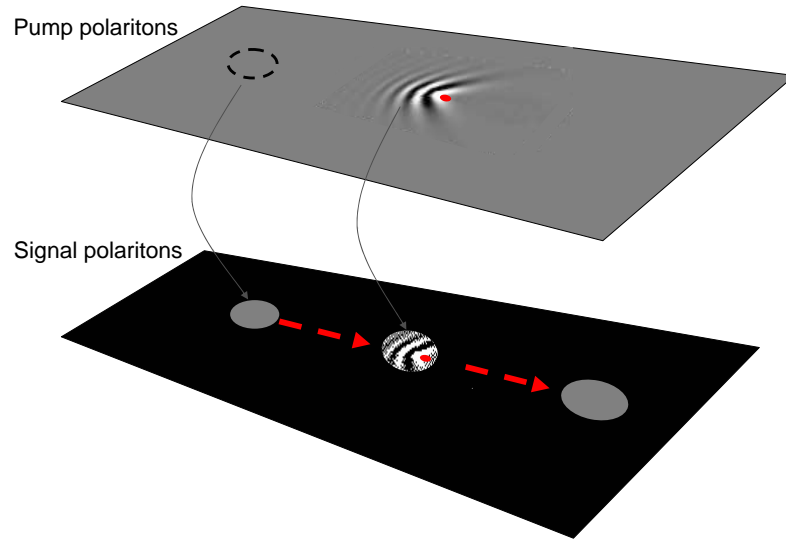


Figure 10.8: Sketch of the TOPO in real space. The observation of the signal polariton-fluid is represented by the circles running from left to right on the black background. We are able to detect this motion thanks to the continuous feeding from the pump polaritons which are represented by the gray plane. The supersonic regime of the pump polaritons is evidenced by the presence of Čerenkov waves around the defect. The change in density of the pump polaritons is projected into the signal polaritons which, instead, move through the defect. The red point shows the position of the defect.

(which are at lower energy and wavevector) seem to flow unperturbed when passing through the defect. In fact, Fig. 10.7(b) shows that the signal polaritons present a very narrow and well defined momentum (evidencing its quantum-state nature) that hardly changes when passing through the defect (note that the color scale changes for the different images).

The group velocity of the *signal* polaritons extracted from the film depicted in Fig. 10.7(a) is $v_g = 0.9 \mu\text{m}/\text{ps}$.⁹ This value is lower than the sound velocity calculated above, $v_s = 3 \mu\text{m}/\text{ps}$ (i. e. $\text{Mach} < 1$). This is actually one of the Landau criteria for superfluidity defined in Sec. 8.5. Additionally, the fact that both the momentum- and the real-space shape of the signal polariton fluid do not change significantly when passing through the defect indicates that the polariton wavepacket does not scatter with the defect (while the pump polaritons do, as evidenced by the Čerenkov waves). All this evidence could indicate that the signal state is in fact in the superfluid regime expected for a macroscopically occupied bosonic state under particular conditions (Fig. 8.7).[42, 49]

The demonstration of the superfluid character of the signal polaritons is not an easy task. For instance, in the system we are studying, the sound velocity is not clearly defined. In Sec. 8.5 and in Refs. [42, 49] the system is only occupied by pump polaritons. In this case v_s is given by Eq. 8.21 and the first Landau criterion for superfluidity is clearly established (see end of Sec. 8.5) In our case at least two polariton fluids coexist in the system, with different density, energy and momentum. Moreover, it seems that, to a first approximation, the signal polaritons live on top of a LPB dispersion renormalized by the pump polaritons. It is not clear then if v_s for the signal polaritons would also be given by Eq. 8.21. Additionally, a careful measurement of the LPB dispersion is required in order to check if the signal polaritons satisfy the second Landau criterion [$\omega_{LP}(k) > \omega_S$ for every $\mathbf{k} \neq \mathbf{k}_S$, as depicted in Fig. 8.7(a)]. The direct measurement of the excitation spectrum of the signal state would reveal important information on the collective behavior associated to superfluidity. Wouters and Carusotto[298] predict for a non-triggered OPO,

the appearance of diffusive Goldstone modes in the spectrum of excitation of the signal state that spontaneously forms close to $k = 0$. The appearance of Goldstone modes with a non-zero sound velocity are clear indications of the superfluidity of the signal state. In order to measure the spectrum of excitation of the signal fluid, an absorption measurement should be performed in the states close to the signal, as proposed in Ref. [298]. This

⁹The group velocity of the *pump* polaritons cannot be directly measured due to the presence of the strong scattered light from the pump beam, and its CW character, at the energy of those states.

requires an intricate experimental set up, in particular considering that in our case the signal polaritons have a non-*zero* momentum and are constantly moving across the sample.

Apart from these important considerations, the absence of scattering of the signal polariton quantum fluid when traversing the defect, as observed in Fig. 10.7, and the measured $v_g < v_s$, constitute evidence compatible with the superfluid character of the signal polaritons.

10.4.2 Scattering with a large defect

In Fig. 10.9(a), a more striking collision is observed as the size of the defect is now comparable with the dimension of the polariton fluid. The finite-size traveling polariton-fluid scatters coherently and elastically on the potential and it is split into two after the collision. Fig. 10.9(b) shows that before the collision the polariton fluid presents a well defined narrow momentum distribution. The collision splits the momentum distribution into two narrow and well defined states, corresponding to each of the the observed polariton fluids in real space.

In this case, the splitting of the signal polariton quantum fluid into two, when encountering the defect, can be interpreted as consequence of the fact that not enough particles can compensate for the local reduction of the fluid momentum and allow an unperturbed motion. Note that the process is dissipationless. This behavior is again compatible with the superfluid character of the signal state. A normal polariton fluid[90, 169] would diffuse both in real and reciprocal space in this configuration due to polariton-polariton and polariton-defect incoherent scattering.

10.4.3 Reflexion on a line defect

Figure 10.10 depicts the real space image of the interaction of a polariton fluid with a line defect on the sample. The line defect [sketched with a white line in (a)] is located along one of the crystallographic axis of the sample. In this case the fluid is created with a higher in-plane momentum (TOPO signal at 5°), pointing in at $t = 0$ in a $(x, y) = (1, 1)$ direction on the plane of the sample.

When the fluid reaches the potential barrier it is partially reflected and partially transmitted [frame (d)]. The trajectory of each component is sketched with purple arrows in frame (a). Let us stress that the observation of a partial reflection is a direct manifestation

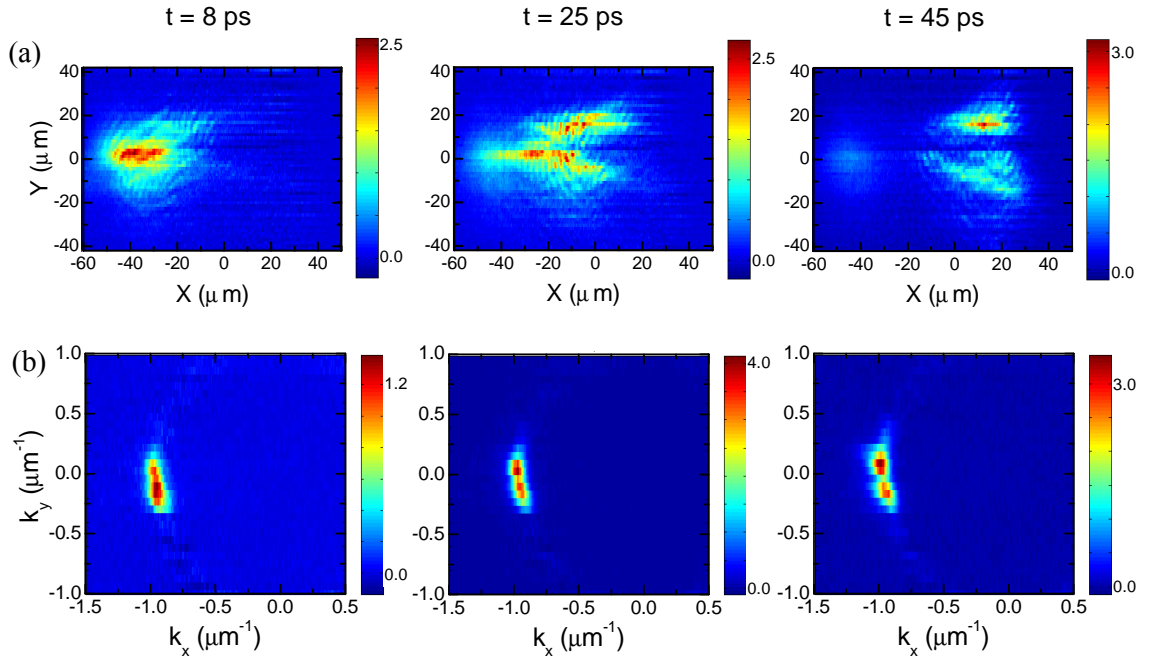


Figure 10.9: Images of a signal polariton quantum-fluid at different times facing a defect of size comparable with its own dimension. Under these conditions the polariton fluid is forced to “feel” the defect which is now breaking the polariton trajectory in real space (a) and showing the appearance of two independent polariton states with different k -vectors (b). The pump (idler) power is 39 mW (70 μW) and the angle of incidence is 10° (16°).

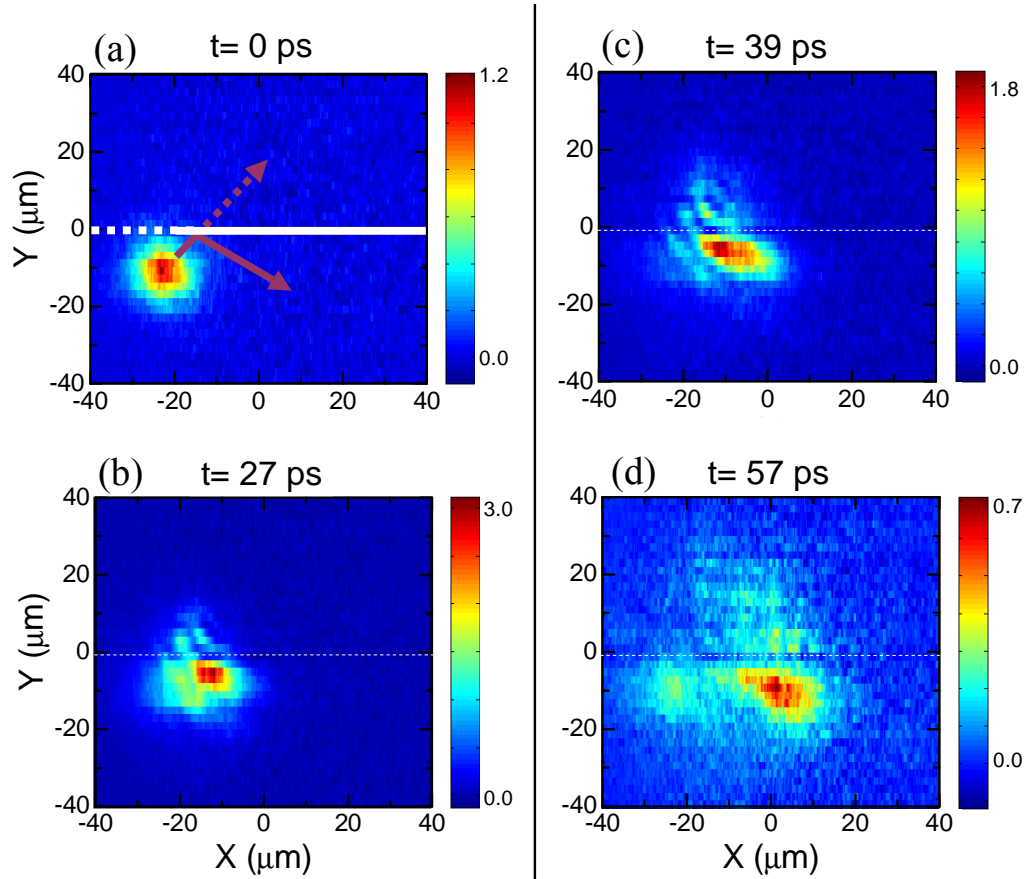


Figure 10.10: Real-space images at the energy of the signal polaritons at different times. The polariton fluid encounters a line defect in its path, sketched in (a) as a white line. The initial momentum points in the $(x, y) = (1, 1)$ direction. When the polariton fluid encounters the line defect it is partially reflected and partially transmitted as indicated by the purple arrows in (a). In this case TOPO is configured with a pulsed idler angle of incidence of 15° ($80 \mu\text{W}$), a pump angle of 10° (100 mW), giving rise to a signal at 10° . The white lines depict the line defect.

of the quantum nature of the signal polariton fluid. A classical object with a well defined velocity facing a potential barrier will either overcome it or not, depending on the kinetic energy of the object and the height of the barrier. However, a quantum object will always have a finite tunnel probability of passing through and a finite probability of being reflected. In our experiment in which millions of pulsed events are recorded, this partial probabilities are manifested in the observation of both a transmission and a reflection.

The reflected beam is stronger than the transmitted one, and it does not seem to show any internal structure. However the transmitted fluid does show standing density waves similar to those observed in Fig. 10.7. In this case, the waves do not present a round shape, but have a straight appearance perpendicular to the direction of motion of the signal fluid. The waves are standing, that is, the maxima remain at the same point at all times, as long as they are visible.

The origin of the waves observed in the direction of the transmitted fluid is not clear. They could still be a manifestation of the pump state which is probably in the conditions of Čerenkov behavior. Additionally, frames (b) and (c) show that the waves are present already before the fluid has completely reached the defect, appearing both above and below the line defect (located at $y = 0$).

Standing waves are in fact expected in the region of space below the line defect. Figure 10.11 shows several snapshots of the calculation of Martin, Scott and Fromhold for the dynamics of a BEC of Na atoms accelerated against a tunnel barrier.[184] In their calculation the tunnel barrier has a Gaussian profile and is formed by a focused laser beam along a plane (y direction, dashed vertical lines), and the condensate is incident normal to the barrier at a velocity of 6.3 mm/s^{-1} . For the particular width and height of the barrier shown in Fig. 10.11, a strong reflection and a partial transmission of the condensate is observed. Standing waves form on the fluid in the incoming side (to the left of the barrier) due to the self interference of the condensate wavefunction. This situation resembles very much the standing waves observed below the defect line in Fig. 10.10(b)-(c). On the other hand no standing waves are observed in the calculated transmitted fluid, while they seem to be present in the polariton case. More experimental work is needed to further clarify the physics behind this partially transmitted situations, in particular for scattering angles close to the normal of the defect line where clear self interference of the coherent polariton fluids should be observed.

Let us finally point out that partial reflections of atomic BECs against surfaces

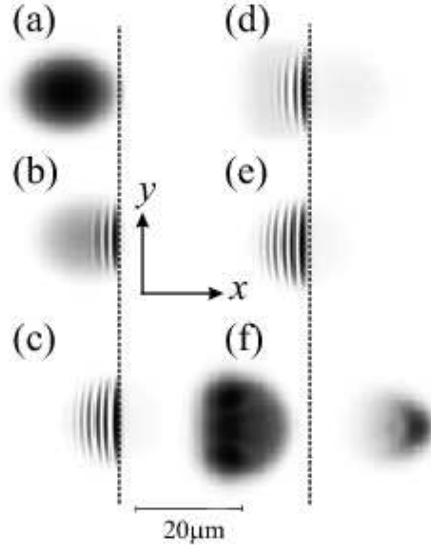


Figure 10.11: Simulation of the time evolution of an atomic Na BEC with a lentil shape colliding against a tunnel barrier at a velocity of 6.3 mm/s^{-1} in the x direction. The figure shows real space snapshots at $t = 3 \text{ ms}$ (a), 4 ms (c), 5 ms (d), 6 ms (e), 7 ms (f). The tunnel barrier is created by the optical field of a laser. From Ref. [184].

have already been observed. The group of Ketterle at the MIT have reported such kind of quantum reflections on Si surfaces under different conditions.[198, 197] The physics behind the quantum reflections of atoms on surfaces lies on the Casimir-Polder potential formed close to the surface. This potential drags the atoms so violently towards the surface that the result is the reflection of the atoms away from it.

A deeper understanding of the microscopic shape and origin of the polariton potential barriers found in the microcavities would be required to further extend the analogy between the atomic and polaritonic case. Nonetheless, very exotic behavior is expected during such reflections, at least in the atomic case. Various fluid excitations, such as solitons and vortices, are predicted to form depending on the particular conditions of the phase, shape and velocity of the incoming fluid.[249, 184, 248, 247]

10.5 Summary and future perspectives

In this chapter we have presented an experimental configuration that allows for the creation and detection of polariton quantum fluids with a non-*zero* momentum. The high pump-polariton density renormalizes the LPB and changes its shape, due to the strong

polariton interactions in such a coherently driven state. The selection of the phase matching conditions that rule the TOPO allow for the control of the initial momentum of the flowing signal polaritons.

In the absence of defects, the signal polaritons move with an unperturbed flow across the sample, with a well defined and fixed momentum. When defects are present, different phenomena can be observed. The pump polariton quantum-fluid scatters with the defect giving rise to Čerenkov-like waves, as the velocity of sound of the pump state is lower than its group velocity. The observation of these interference waves is a direct indication of the quantum nature of the polariton fluid. On the other hand, the group velocity of the signal polaritons might in general be smaller than the sound velocity. If the defect is small in size, the signal polaritons traverse it without scattering. These observations are compatible with the description of the signal fluid as a superfluid.

With larger defect sizes, a splitting of the signal quantum fluid, or hints of quantum reflections can be observed.

The phenomenology associated to bosonic quantum fluids has just been recently uncovered in atomic condensates. For instance, in the regime of quantum reflections, very rich effects have been recently observed[198, 197] and theoretically characterized[184, 249, 246] in atomic BEC interacting with surfaces. There is plenty of room for the exploration of these effects in semiconductor microcavities, with the advantage of the simple implementation of barriers and defects of on-demand shapes and sizes by use of lithographic techniques. For instance, the group of Yamamoto has recently demonstrated that the deposition of thin metallic strips on top of the upper Bragg mirror creates shallow photonic traps of up to about 100 μeV in a micrometer scale.[144, 161] However, other high precision lithographic techniques, like electron beam lithography, might prove to be useful in the manufacture of deeper barriers. Such experiments, as well as those presented here, probe the quantum nature of the polariton fluids inside the cavity. All the observed and expected interference phenomena, like the Čerenkov waves of Fig. 10.7, take place inside the cavity, and are directly related to the quantum nature of the polariton fluids.

Other phenomena predicted to appear in atomic condensates, such as the exotic reflection of a bosonic vortex with a potential barrier,[184] have not yet been observed but could be implemented in a semiconductor microcavity. In fact, the creation of vortices in polariton condensates is not far from realization and should offer some advantages over the atomic system. The dynamic (rather than thermal) equilibrium in a semiconductor

microcavity caused by the constant introduction and escape of polaritons in the system, lifts the particle-number conservation constriction characteristic of atomic BECs. In this way, phase-squeezed states (high spatial coherence), or vortices of controlled and well defined phase could be created. Moreover, due to the strong polariton-photon coupling, the phase and position of the vortices could be controlled by the position on the sample of a light vortex.

Faraday waves[83] and Josephson oscillations[4, 177, 212] already observed in atomic condensates are some of the phenomena directly implementable in semiconductor microcavities, for instance by use of surface acoustic waves[66, 68, 67] or by creating two nearby-connected polariton condensates. Nonetheless, the field of polariton quantum hydrodynamics should not restrict itself to follow the achievements of atomic condensates. The experiments presented here, and the recent publication of landmark experiments on BEC of polaritons, show that the gap between the two realizations is narrowing. The great advantage of the polariton system is that it does not require the very sophisticated methods that include ultrahigh vacuum, very well controlled magnetic traps, and optical tweezers technology just to create the condensate (at microkelvin temperatures).[172, 103] In semiconductor microcavities, condensates and fluids are easily manipulated with the excitation laser-beams, and are currently created with standard liquid-He cryogenic techniques, at 5-20 K. Furthermore, wide bandgap systems, such as those based on GaN have already shown very promising results[46] on the prospective creation of Bose-Einstein polariton condensates at room temperature.

Chapter 11

General conclusions

We have presented a cross-study, through different material and optical confinements, of the carrier dynamics and many-body physics in bulk and two-dimensional semiconductor systems by means of time-resolved spectroscopy. We will now summarize the main results.

Bulk AlGaAs carrier dynamics

- At low excitation density, the dynamics of the free excitons in AlGaAs epilayers is strongly dependent on the density of localization centers. A non-monotonous dependence of the rise time on excitation density has been clarified.
- A detailed phase diagram of the origin of the PL (exciton *vs* electron-hole pair recombination), in bulk GaAs has been determined. The Mott transition between the insulating (excitonic) and conducting (plasma) phases is very abrupt, with a well defined critical temperature (49 K) and excitation density (in the range $120\text{--}180 \times 10^{15} \text{ cm}^{-3}$).

Bulk GaAs spin dynamics

- The electron-momentum dependence of the spin flip-time has been experimentally determined in a direct-gap semiconductor for the first time.
- Under high-density optical pumping, the electron spin-flip in GaAs is governed by the Bir-Aronov-Pikus mechanism, and the spin dynamics are strongly affected by Pauli blockade effects: the high occupancy of the final states frustrates the spin-flip

scattering events, resulting in very long spin-flip times. In fact, for the best of our knowledge, we have found the longest reported spin flip times in undoped GaAs.

Tailoring of the carrier distributions in QWs

- In QWs, we have presented an experimental configuration that allows for the ultrafast and controlled tailoring of the carrier distributions in a two, delayed pulses experiment. A first pulse excites carriers in the system, while a second pulse induces an ultrafast warming of the electrons, holes and excitons. The direct consequence of the warming is the observation of an abrupt quench of the excitonic PL at the arrival of the second pulse.
- We have presented a model that quantitatively accounts for the measured dip depths in the two pulses experiment. The magnitude of the dip, is determined by the temperature change of the carriers induced by the second pulse, and can be controlled by varying its power and delay.

Semiconductor microcavities under non-resonant excitation

- In semiconductor GaAs based microcavities, under non-resonant excitation and low temperature, the light-emission properties are greatly determined by the excitation density. At low excitation density, the system is characterized by the polariton resonances (strong coupling). However, the PL dynamics are mainly determined by the slow formation and recombination times of the excitons populating the *reservoir*. When the excitation density is increased above a certain threshold, carrier screening destroys the polaritons driving the system into VCSEL operation (weak coupling). In this regime the PL dynamics is very fast due to the photon-stimulated recombination. A detailed map of the strong- to weak-coupling transition density at different exciton-cavity detunings has been presented.
- Under non-resonant excitation of the microcavity, the polarization dynamics are determined by the crystalline anisotropies of the sample. While the degree of circular polarization is almost negligible at all investigated excitation densities, a strong linear polarization dominates the emission even at low power. At high power, when the system enters into the photon-lasing regime, the stimulation process drives the emission

into almost 100% linear polarization.

- The direction of linear polarization is pinned to one of the crystallographic axis of the sample, and it is independent of the polarization characteristics of the excitation. The degree of linear polarization of the luminescence has been investigated at different emission angles and sample detunings. When the emission is angular resolved, the polarization shows strong oscillations, going from positive to negative values within a few degrees from the sample normal. The angle-dependent effects and the polarization pinning arise from the crystallographic induced anisotropies of the cavity modes.

Quantum polariton hydrodynamics

- We have presented a novel experimental configuration that allows for the creation and detection of quantum polariton fluids with a non-vanishing momentum, under resonant excitation of the lower polariton branch.. The excitation is performed in a triggered optical parametric oscillator configuration, in which a CW pump fuels the signal polariton state after a pulsed idler has induced the occupation of the signal.
- The quantum fluids move on top of a linearized dispersion showing no diffusion and at constant velocity. The linearization is caused by the strong polariton-polariton interaction at the pump state, and resembles the spectrum of excitations of a quantum bosonic fluid.
- We have presented data on the interaction of polariton fluids with different types of defects on the sample. The pump polaritons show Čerenkov waves, characteristics of a bosonic fluid whose group velocity is higher than the velocity of sound. The signal polaritons present different phenomenology depending on the size and shape of the defect: splitting into two daughter condensates, partial quantum reflections or unperturbed flow through the defect. All of these observations are compatible with superfluid behavior.

Conclusiones generales

Se ha presentado un estudio transversal, a través de diferentes materiales y confinamientos ópticos, de la dinámica de portadores y de la física de muchos cuerpos en sistemas semiconductores volúmicos y dos-dimensionales, mediante espectroscopia resuelta en tiempo. Aquí se resumen las conclusiones principales.

Dinámica de portadores en AlGaAs volúmico

- A densidad de excitación baja, la dinámica de los excitones libres en láminas de AlGaAs depende fuertemente de la densidad de centros de localización. Se han clarificado los mecanismos que dan lugar a la observada dependencia no monotónica del tiempo de subida de los excitones libres con la densidad de excitación.
- Se ha obtenido un detallado diagrama de fases del origen de la fotoluminiscencia (recombinación de excitones frente a la originada en pares electrón-hueco) en GaAs volúmico. La transición de Mott entre las fases aislante (excitónica) y conductora (plasma) es muy abrupta, con una temperatura (49 K) y densidad de excitación (en el rango $120 - 180 \times 10^{15} \text{ cm}^{-3}$) críticas bien definidas.

Dinámica de espín en GaAs volúmico

- La relación entre el tiempo de volteo de espín y el momento del electrón ha sido determinada experimentalmente por primera vez en un semiconductor de gap directo.
- A alta densidad de bombeo óptico, el mecanismo de volteo de espín en GaAs es el Bir-Aronov-Pikus, y la dinámica de espín se ve determinada fuertemente por efectos de bloqueo de Pauli: la alta ocupación de los estados finales frustra los eventos de volteo de espín, dando lugar a tiempos de volteo muy grandes. De hecho, se ha encontrado el tiempo de volteo de espín en GaAs no dopado más largo publicado hasta la fecha.

Manipulación de las distribuciones de portadores en pozos cuánticos

- En pozos cuánticos se ha mostrado una configuración experimental basada en dos pulsos láser retrasados, que permite el control ultrarrápido de las distribuciones de portadores. En esta configuración un primer pulso excita portadores en el sistema,

mientras que un segundo pulso retrasado induce un calentamiento ultrarrápido de los electrones, huecos y excitones. La consecuencia directa del calentamiento es la observación de un abrupto descenso de la intensidad de luz emitida por los excitones cuando llega el segundo pulso.

- Hemos mostrado un modelo que explica cuantitativamente las caídas de luminiscencia en el experimento de dos pulsos. La magnitud de la caída está determinada por el cambio de temperatura de los portadores inducido por el segundo pulso, y puede ser controlado variando la potencia y retraso de dicho pulso.

Microcavidades semiconductoras bajo excitación no resonante

- En microcavidades semiconductoras basadas en GaAs, bajo excitación no resonante y a baja temperatura, las propiedades de emisión de luz están fuertemente determinadas por la densidad de excitación. A densidad de excitación baja, el sistema está caracterizado por las resonancias polaritónicas (acoplamiento fuerte). Sin embargo, la dinámica de fotoluminiscencia está principalmente determinada por los lentos tiempos de formación y recombinación de los excitones que pueblan el *reservorio*. Cuando la densidad de excitación es incrementada por encima de cierto umbral, el apantallamiento producido por los portadores destruye los polaritones, llevando el sistema al régimen de operación VCSEL (acoplamiento débil). En este régimen la dinámica de fotoluminiscencia es muy rápida debido a la recombinación fotoestimulada. Se ha presentado un mapa detallado de la densidad de excitación para la transición desde la situación de acoplamiento fuerte a débil, para diferentes energías relativas de exciton y cavidad (*detunings*).
- Bajo excitación no resonante de la microcavidad, la dinámica de polarización está determinada por las anisotropías cristalinas de la muestra. Mientras que el grado de polarización circular de la emisión es prácticamente inapreciable en todas las densidades de excitación estudiadas, una fuerte polarización lineal domina la emisión incluso a potencia baja. A potencia alta, cuando el sistema entra en el régimen de láser de fotones, el proceso de estimulación induce polarizaciones lineales en la emisión de casi el 100%.
- La dirección de la polarización lineal está fijada por uno de los ejes cristalográficos de

la muestra, y es independiente de las características de la polarización de excitación. El grado de polarización lineal de la luminiscencia ha sido investigado para diferentes *detunings*. La polarización muestra fuertes oscilaciones en su valor, pasando de valores positivos a negativos cuando la dirección de emisión es analizada en un rango de unos pocos grados respecto a la normal a la superficie. Los efectos dependientes del ángulo y el fijado de la dirección de polarización se originan en las anisotropías cristalinas asociadas a los modos de cavidad.

Hidrodinámica cuántica de polaritones

- Se ha presentado una configuración experimental novedosa que permite la creación y detección de fluidos cuánticos polaritónicos con un valor del momento distinto de *cero*, bajo excitación resonante de la rama polaritónica inferior. La excitación se lleva a cabo en una configuración de oscilador paramétrico óptico desencadenado, en el que un bombeo de onda continua alimenta los polaritones de la señal después de que un pulso láser haya inducido la ocupación de los estados de la señal.
- Los fluidos cuánticos se mueven sobre una dispersión linearizada, sin mostrar difusión, y a una velocidad constante. La linearización está causada por la fuerte interacción polaritón-polaritón en el estado del bombeo, y muestra grandes similitudes con el espectro de excitación de un fluido cuántico bosónico.
- Se han presentado datos sobre la interacción de fluidos de polaritones con diferentes tipos de defectos nativos existentes en la muestra. Los polaritones del bombeo muestran ondas de tipo Čerenkov, características de los fluidos bosónicos cuya velocidad de grupo es mayor que la velocidad del sonido. La señal de polaritones muestra diferentes efectos dependiendo del tamaño y forma del defecto: división en dos condensados, reflexiones cuánticas parciales, o movimiento del fluido a través del defecto sin interacción. Todas estas observaciones son compatibles con comportamiento superfluido.

Bibliography

- [1] J. Aaviksoo, I. Reimand, V. V. Rossin, and V. V. Travnikov. Kinetics of free-exciton luminescence in GaAs. *Phys. Rev. B*, 45(3):1473, 1992.
- [2] J. R. Abo-Shaeer, C. Raman, J. M. Vogels, and W. Ketterle. Observation of vortex lattices in Bose-Einstein condensates. *Science*, 292(5516):476–479, 2001.
- [3] F. Adler, M. Geiger, A. Bauknecht, F. Scholz, H. Schweizer, M. H. Pilkuhn, B. Ohnesorge, and A. Forchel. Optical transitions and carrier relaxation in self assembled InAs/GaAs quantum dots. *J. Appl. Phys.*, 80(7):4019–4026, 1996.
- [4] M. Albiez, R. Gati, J. Fölling, S. Hunsmann, M. Cristiani, and M. K. Oberthaler. Direct observation of tunneling and nonlinear self-trapping in a single bosonic Josephson junction. *Phys. Rev. Lett.*, 95(1):010402, 2005.
- [5] A. Alexandrou, V. Berger, and D. Hulin. Direct observation of electron relaxation in intrinsic GaAs using femtosecond pump-probe spectroscopy. *Phys. Rev. B*, 52(7):4654, 1995.
- [6] M. H. Anderson, J. R. Ensher, M. R. Matthews, C. E. Wieman, and E. A. Cornell. Observation of Bose-Einstein condensation in a dilute atomic vapor. *Science*, 269(5221):198–201, 1995.
- [7] H. Ando, T. Sogawa, and H. Gotoh. Photon-spin controlled lasing oscillation in surface-emitting lasers. *Appl. Phys. Lett.*, 73(5):566–568, 1998.
- [8] L. C. Andreani. private communication.
- [9] L. C. Andreani and A. Pasquarello. Accurate theory of excitons in GaAs/Ga_{1-x}Al_x quantum wells. *Phys. Rev. B*, 42(14):8928–8938, 1990.

-
- [10] L. C. Andreani, A. Pasquarello, and F. Bassani. Hole subbands in strained GaAs/Ga_{1-x}Al_xAs quantum wells: Exact solution of the effective-mass equation. *Phys. Rev. B*, 36(11):5887–5894, 1987.
- [11] N. W. Ashcroft and N. D. Mermin. *Solid State Physics*. Harcourt College Publishers, 1976.
- [12] T. Baars, M. Bayer, A. Forchel, F. Schäfer, and J. P. Reithmaier. Polariton-polariton scattering in semiconductor microcavities: Experimental observation of thresholdlike density dependence. *Phys. Rev. B*, 61(4):R2409, 2000.
- [13] A. Baas, J.-P. Karr, M. Romanelli, A. Bramati, and E. Giacobino. Optical bistability in semiconductor microcavities in the nondegenerate parametric oscillation regime: Analogy with the optical parametric oscillator. *Phys. Rev. B*, 70(16):161307, 2004.
- [14] A. Baas, J.-P. Karr, M. Romanelli, A. Bramati, and E. Giacobino. Quantum degeneracy of microcavity polaritons. *Phys. Rev. Lett.*, 96(17):176401, 2006.
- [15] V. Bagnato and D. Kleppner. Bose-Einstein condensation in low-dimensional traps. *Physical Review A*, 44(11):7439–7441, 1991.
- [16] D. Bajoni, M. Perrin, P. Senellart, A. Lemaître, B. Sermage, and J. Bloch. Dynamics of microcavity polaritons in the presence of an electron gas. *Phys. Rev. B*, 73(20):205344, 2006.
- [17] D. Bajoni, P. Senellart, A. Lemaître, and J. Bloch. Photon lasing in GaAs microcavity: Similarities with a polariton condensate. *Phys. Rev. B*, 76:201305(R), 2007.
- [18] D. Bajoni, P. Senellart, M. Perrin, A. Lemaître, and J. Bloch. Control of exciton formation and exciton cooling by use of an electron gas. (*submitted to Phys. Rev. B*).
- [19] A. Baldereschi and N. O. Lipari. Spherical model of shallow acceptor states in semiconductors. *Phys. Rev. B*, 8(6):2697–2709, 1973.
- [20] A. Baldereschi and N. O. Lipari. Cubic contributions to the spherical model of shallow acceptor states. *Phys. Rev. B*, 9(4):1525–1539, 1974.
- [21] R. Balili, V. Hartwell, D. Snoke, L. Pfeiffer, and K. West. Bose-Einstein condensation of microcavity polaritons in a trap. *Science*, 316(5827):1007–1010, 2007.

- [22] D. Ballarini, A. Amo, D. Sanvitto, L. Viña, M. Skolnick, and J. S. Roberts. Coexistence of weak- and strong-coupled modes in semiconductor microcavities. *Physica E*, (in press).
- [23] G. Bastard. *Wave Mechanics Applied to Semiconductor Heterostructures*. Les Editions de Physique, Les Ulis, 1988.
- [24] G. Bastard and J. Brum. Electronic states in semiconductor heterostructures. *Quantum Electronics, IEEE Journal of*, 22(9):1625–1644, 1986.
- [25] J. J. Baumberg, P. G. Savvidis, R. M. Stevenson, A. I. Tartakovskii, M. S. Skolnick, D. M. Whittaker, and J. S. Roberts. Parametric oscillation in a vertical microcavity: A polariton condensate or micro-optical parametric oscillation. *Phys. Rev. B*, 62(24):R16247, 2000.
- [26] J. J. Baumberg and L. Viña, editors. *Special Issue on Microcavities*, volume 18 of *Semiconductor Science and Technology*. Semiconductor Science and Technology, 2003.
- [27] D. Baxter, M. Skolnick, A. Armitage, V. Astratov, D. Whittaker, T. Fisher, J. Roberts, D. Mowbray, and M. Kaliteevski. Polarization-dependent phenomena in the reflectivity spectra of semiconductor quantum microcavities. *Phys. Rev. B*, 56:R10032–10035, 1997.
- [28] S. Ben-Tabou de Leon and B. Laikhtman. Mott transition, biexciton crossover, and spin ordering in the exciton gas in quantum wells. *Phys. Rev. B*, 67:235315, 2003.
- [29] V. L. Berezinsky. Destruction of long-range order in one-dimensional and 2-dimensional systems possessing a continuous symmetry group. 2. quantum systems. *Sov. Phys. JETP*, 34:610, 1972.
- [30] R. D. R. Bhat, P. Nemec, Y. Kerachian, H. M. van Driel, J. E. Sipe, and A. L. Smirl. Two-photon spin injection in semiconductors. *Phys. Rev. B*, 71:035209, 2005.
- [31] D. Bimberg, H. Münzel, A. Steckenborn, and J. Christen. Kinetics of relaxation and recombination of nonequilibrium carriers in GaAs: Carrier capture by impurities. *Phys. Rev. B*, 31(12):7788, 1985.
- [32] G. L. Bir, A. G. Aronov, and G. E. Pikus. Spin relaxation of electrons scattered by holes. *Zh. Éksp. Teor. Fiz.*, 69(4):1382–97, 1975.

-
- [33] G. L. Bir, A. G. Aronov, and G. E. Pikus. Spin relaxation of electrons scattered by holes. *Sov. Phys. JETP*, 42(4):705, 1975.
- [34] J. Bloch and J. Y. Marzin. Photoluminescence dynamics of cavity polaritons under resonant excitation in the picosecond range. *Phys. Rev. B*, 56(4):2103 LP – 2108, 1997.
- [35] J. Bloch, B. Sermage, C. Jacquot, P. Senellart, and V. Thierry-Mieg. Time-resolved measurement of stimulated polariton relaxation. *Phys. Stat. Sol. (a)*, 190(3):827 – 831, 2002.
- [36] M. Born and E. Wolf. *Principles of optics electromagnetic theory of propagation, interference and diffraction of light*. Pergamon, Oxford, 6th edition, 1980.
- [37] L. V. Butov, A. C. Gossard, and D. S. Chemla. Macroscopically ordered state in an exciton system. *Nature*, 418(6899):751, 2002.
- [38] R. Butté, G. Delalleau, A. I. Tartakovskii, M. S. Skolnick, V. N. Astratov, J. J. Baumberg, G. Malpuech, A. Di Carlo, A. V. Kavokin, and J. S. Roberts. Transition from strong to weak coupling and the onset of lasing in semiconductor microcavities. *Phys. Rev. B*, 65(20):205310, 2002.
- [39] M. Capizzi, S. Modesti, A. Frova, J. L. Staehli, M. Guzzi, and R. A. Logan. Electron-hole plasma in direct-gap GaInAs and k -selection rule. *Phys. Rev. B*, 29(4):2028, 1984.
- [40] M. Cardona, N. E. Christensen, and G. Fasol. Relativistic band structure and spin-orbit splitting of zinc-blende-type semiconductors. *Phys. Rev. B*, 38(3):1806–1827, 1988.
- [41] I. Carusotto. private communication.
- [42] I. Carusotto and C. Ciuti. Probing microcavity polariton superfluidity through resonant rayleigh scattering. *Physical Review Letters*, 93(16):166401, 2004.
- [43] I. Carusotto, S. X. Hu, L. A. Collins, and A. Smerzi. Bogoliubov-cerenkov radiation in a Bose-Einstein condensate flowing against an obstacle. *Phys. Rev. Lett.*, 97:260403, 2006.

- [44] S. Chatterjee, C. Ell, S. Mosor, G. Khitrova, H. M. Gibbs, W. Hoyer, M. Kira, S. W. Koch, J. P. Prineas, and H. Stolz. Excitonic photoluminescence in semiconductor quantum wells: Plasma versus excitons. *Phys. Rev. Lett.*, 92(6):067402, 2004.
- [45] K. D. Choquette, K. L. Lear, R. E. Leibenguth, and M. T. Asom. Polarization modulation of cruciform vertical-cavity laser diodes. *Appl. Phys. Lett.*, 64(21):2767–2769, 1994.
- [46] S. Christopoulos, G. Baldassarri Hoyer von Hogersthall, A. J. D. Grundy, P. G. Lagoudakis, A. V. Kavokin, J. J. Baumberg, G. Christmann, R. Butte, E. Feltin, J.-F. Carlin, and N. Grandjean. Room-temperature polariton lasing in semiconductor microcavities. *Phys. Rev. Lett.*, 98(12):126405, 2007.
- [47] D. Citrin. A note on the photoluminescence decay of thermalized excitons in quantum structures: Many-band model. *Solid State Commun.*, 92:851, 1994.
- [48] D. S. Citrin. Time-domain theory of resonant rayleigh scattering by quantum wells: Early-time evolution. *Phys. Rev. B*, 54(20):14572 LP – 14579, 1996.
- [49] C. Ciuti and I. Carusotto. Quantum fluid effects and parametric instabilities in microcavities. *Phys. Stat. Sol. (b)*, 242(11):2224–2245, 2005.
- [50] C. Ciuti, V. Savona, C. Piermarocchi, A. Quattropani, and P. Schwendimann. Threshold behavior in the collision broadening of microcavity polaritons. *Phys. Rev. B*, 58(16):R10123, 1998.
- [51] C. Ciuti, P. Schwendimann, and A. Quattropani. Parametric luminescence of microcavity polaritons. *Phys. Rev. B*, 63(4):041303, 2001.
- [52] C. Cohen-Tannoudji, B. Diu, and F. Laloë. *Quantum Mechanics, vols. I and II*. Hermann, Paris, France, 1977.
- [53] J. H. Collet. Screening and exchange in the theory of the femtosecond kinetics of the electron-hole plasma. *Phys. Rev. B*, 47(16):10279, 1993.
- [54] J. H. Collet, W. W. Rühle, M. Pugnet, K. Leo, and A. Million. Electron-hole plasma dynamics in CdTe in the picosecond regime. *Phys. Rev. B*, 40(18):12296, 1989.

-
- [55] J. S. Colton, T. A. Kennedy, A. S. Bracker, and D. Gammon. Spin lifetime measurements in mbe-grown GaAs epilayers. *Phys. Stat. Sol. (b)*, 233(3):445, 2002.
- [56] J. S. Colton, T. A. Kennedy, A. S. Bracker, and D. Gammon. Microsecond spin-flip times in n-GaAs measured by time-resolved polarization of photoluminescence. *Phys. Rev. B*, 69:121307(R), 2004.
- [57] M. Combescot. Estimation of the critical temperature of electron-hole droplets in ge and si. *Phys. Rev. Lett.*, 32(1):15–17, 1974.
- [58] M. Combescot and O. Betbeder-Matibet. Coherent effects in the physics of composite excitons. *Phys. Rev. B*, 74(4):045110, 2006.
- [59] M. Combescot, O. Betbeder-Matibet, and R. Combescot. Exciton-exciton scattering: Composite boson versus elementary boson. *Phys. Rev. B*, 75(17):174305, 2007.
- [60] M. Combescot, O. Betbeder-Matibet, and F. Dubin. Mixture of composite-boson molecules and the pauli exclusion principle. *Phys. Rev. A*, 76(3):033601, 2007.
- [61] F. Dalfovo, S. Giorgini, L. P. Pitaevskii, and S. Stringari. Theory of Bose-Einstein condensation in trapped gases. *Rev. Mod. Phys.*, 71(3):463–512, 1999.
- [62] T. C. Damen, J. Shah, D. Y. Oberli, D. S. Chemla, J. E. Cunningham, and J. M. Kuo. Dynamics of exciton formation and relaxation in GaAs quantum wells. *Phys. Rev. B*, 42(12):7434, 1990.
- [63] T. C. Damen, L. Viña, J. E. Cunningham, J. Shah, and L. J. Sham. Subpicosecond spin relaxation dynamics of excitons and free carriers in GaAs quantum wells. *Phys. Rev. Lett.*, 67(24):3432, 1991.
- [64] L. S. Dang, D. Heger, R. André, F. Boeuf, and R. Romestain. Stimulation of polariton photoluminescence in semiconductor microcavity. *Phys. Rev. Lett.*, 81(18):3920–3923, 1998.
- [65] K. B. Davis, M. O. Mewes, M. R. Andrews, N. J. van Druten, D. S. Durfee, D. M. Kurn, and W. Ketterle. Bose-Einstein condensation in a gas of sodium atoms. *Phys. Rev. Lett.*, 75(22):3969–3973, 1995.

-
- [66] M. M. de Lima Jr., R. Hey, J. A. H. Stotz, and P. V. Santos. Acoustic manipulation of electron–hole pairs in GaAs at room temperature. *Appl. Phys. Lett.*, 84(14):2569–2571, 2004.
- [67] M. M. de Lima Jr., M. v. d. Poel, P. V. Santos, and J. M. Hvam. Phonon-induced polariton superlattices. *Phys. Rev. Lett.*, 97(4):045501, 2006.
- [68] M. M. de Lima Jr. and P. V. Santos. Modulation of photonic structures by surface acoustic waves. *Rep. Prog. Phys.*, 68(7):1639, 2005.
- [69] N. Del Fatti, P. Langot, R. Tommasi, and F. Vallée. Temperature-dependent electron-lattice thermalization in GaAs. *Phys. Rev. B*, 59(7):4576, 1999.
- [70] H. Deng, D. Press, S. Gotzinger, G. S. Solomon, R. Hey, K. H. Ploog, and Y. Yamamoto. Quantum degenerate exciton-polaritons in thermal equilibrium. *Phys. Rev. Lett.*, 97(14):146402, 2006.
- [71] H. Deng, G. S. Solomon, R. Hey, K. H. Ploog, and Y. Yamamoto. Spatial coherence of a polariton condensate. *Phys. Rev. Lett.*, 99(12):126403, 2007.
- [72] P. Deuar and P. D. Drummond. Correlations in a bec collision: First-principles quantum dynamics with 150 000 atoms. *Phys. Rev. Lett.*, 98(12):120402, 2007.
- [73] B. Deveaud, editor. *The Physics of Semiconductor Microcavities*. WILEY-VCH Verlag, Weinheim, 2007.
- [74] C. Diederichs, J. Tignon, G. Dasbach, C. Ciuti, A. Lemaître, J. Bloch, P. Roussignol, and C. Delalande. Parametric oscillation in vertical triple microcavities. *Nature*, 440(7086):904, 2006.
- [75] T. D. Doan, H. T. Cao, D. B. T. Thoai, and H. Haug. Condensation kinetics of microcavity polaritons with scattering by phonons and polaritons. *Phys. Rev. B*, 72(8):085301, 2005.
- [76] M. I. Dyakonov and V. I. Perel. Theory of optical spin orientation of electrons and nuclei in semiconductors. In F. Meier and B. P. Zakharchenya, editors, *Optical Orientation*, volume 8 of *Modern Problems in Condensed Matter Sciences*, page Chapter 2. North-Holland, Amsterdam, 1984.

-
- [77] A. Dyson and M. J. Adams. Spin-polarized properties of optically pumped vertical cavity surface emitting lasers. *J. Opt. B: Quantum Semiclass. Opt.*, 5:222, 2003.
- [78] R. I. Dzhioev, K. V. Kavokin, V. L. Korenev, M. V. Lazarev, B. Y. Meltser, M. N. Stepanova, B. P. Zakharchenya, D. Gammon, and D. S. Katzer. Low-temperature spin relaxation in n-type GaAs. *Phys. Rev. B*, 66:245204, 2002.
- [79] R. Eccleston, R. Strobel, W. W. Rühle, J. Kuhl, B. F. Feuerbacher, and K. Ploog. Exciton dynamics in a GaAs quantum well. *Phys. Rev. B*, 44(3):R1395, 1991.
- [80] B. Eiermann, P. Treutlein, T. Anker, M. Albiez, M. Taglieber, K.-P. Marzlin, and M. K. Oberthaler. Dispersion management for atomic matter waves. *Phys. Rev. Lett.*, 91(6):060402, 2003.
- [81] M. El Allali, C. B. Sørensen, E. Veje, and P. Tidemand-Petersson. Experimental determination of the GaAs and $\text{Ga}_{1-x}\text{Al}_x$ band-gap energy dependence on temperature and aluminum mole fraction in the direct band-gap region. *Phys. Rev. B*, 48(7):4398, 1993.
- [82] R. J. Elliott. Theory of the effect of spin-orbit coupling on magnetic resonance in some semiconductors. *Phys. Rev.*, 96(2):266, 1954.
- [83] P. Engels, C. Atherton, and M. A. Hoefer. Observation of faraday waves in a Bose-Einstein condensate. *Phys. Rev. Lett.*, 98(9):095301, 2007.
- [84] J. E. Epler, S. Gehrsitz, K. H. Gulden, M. Moser, H. C. Sigg, and H. W. Lehmann. Mode behavior and high resolution spectra of circularly-symmetric GaAs/alGaAs air-post vertical cavity surface emitting lasers. *Appl. Phys. Lett.*, 69(6):722–724, 1996.
- [85] J. Feldmann, G. Peter, E. O. Göbel, P. Dawson, K. Moore, C. Foxon, and R. J. Elliott. Linewidth dependence of radiative exciton lifetime in quantum wells. *Phys. Rev. Lett.*, 59:2337, 1987.
- [86] R. Ferreira and G. Bastard. Tunnelling and relaxation in semiconductor double quantum wells. *Rep. Prog. Phys.*, 60:345–387, 1997.
- [87] D. K. Ferry, A. M. Krivan, M. J. Kann, and R. P. Joshi. Molecular dynamics extensions of monte carlo simulation in semiconductor device modeling. *Comp. Phys. Comm.*, 67(1):119, 1991.

- [88] R. Fiederling, M. Keim, G. Reuscher, W. Ossau, G. Schmidt, A. Waag, and L. W. Molenkamp. Injection and detection of a spin-polarized current in a light-emitting diode. *Nature (London)*, 402:787, 1999.
- [89] G. Fishman and G. Lampel. Spin relaxation of photoelectrons in p-type gallium arsenide. *Phys. Rev. B*, 16(2):820, 1977.
- [90] T. Freixanet, B. Sermage, A. Tiberj, and R. Planel. In-plane propagation of excitonic cavity polaritons. *Phys. Rev. B*, 61(11):7233, 2000.
- [91] A. Frova, G. A. Thomas, R. E. Miller, and E. O. Kane. Mass reversal effect in the split indirect exciton of ge. *Phys. Rev. Lett.*, 34(25):1572–1575, 1975.
- [92] A. Gahl, S. Balle, and M. S. Miguel. Polarization dynamics of optically pumped vcsel's. *IEEE J. Quantum Electron.*, 35(3):342, 1999.
- [93] E. O. Göbel, P. H. Liang, and D. von der Linde. Picosecond luminescence spectroscopy of highly excited GaAs. *Solid State Commun.*, 37(8):609, 1981.
- [94] A. M. Gilinsky and K. S. Zhuravlev. Millisecond phosphorescence of free electrons in pure GaAs. *Appl. Phys. Lett.*, 79(21):3455, 2001.
- [95] N. A. Gippius, S. G. Tikhodeev, V. D. Kulakovskii, D. N. Krizhanovskii, and A. I. Tartakovskii. Nonlinear dynamics of polariton scattering in semiconductor microcavity: Bistability vs. stimulated scattering. *Europhys. Lett.*, 67:997, 2004.
- [96] R. L. Greene, K. K. Bajaj, and D. E. Phelps. Energy levels of wannier excitons in GaAs/Ga_{1-x}Al_xAs quantum-well structures. *Phys. Rev. B*, 29(4):1807–1812, 1984.
- [97] A. Griesmaier, J. Werner, S. Hensler, J. Stuhler, and T. Pfau. Bose-Einstein condensation of chromium. *Phys. Rev. Lett.*, 94(16):160401, 2005.
- [98] E. Grilli, M. Guzzi, R. Zamboni, and L. Pavesi. High-precision determination of the temperature dependence of the fundamental energy gap in gallium arsenide. *Phys. Rev. B*, 45(4):1638, 1992.
- [99] M. Gulia, F. Rossi, E. Molinari, P. E. Selbmann, and P. Lugli. Phonon-assisted exciton formation and relaxation in GaAs/Al_xGa_{1-x}As quantum wells. *Phys. Rev. B*, 55(24):R16049, 1997.

-
- [100] M. Gurioli, P. Borri, M. Colocci, M. Gulia, F. Rossi, E. Molinari, P. E. Selbmann, and P. Lugli. Exciton formation and relaxation in GaAs epilayers. *Phys. Rev. B*, 58(20):R13403, 1998.
- [101] S. Haacke, R. A. Taylor, R. Zimmermann, I. Bar-Joseph, and B. Deveaud. Resonant femtosecond emission from quantum well excitons: The role of rayleigh scattering and luminescence. *Phys. Rev. Lett.*, 78(11):2228, 1997.
- [102] J. Hader, N. Linder, and G. H. Döhler. k-p theory of the franz-keldysh effect. *Phys. Rev. B*, 55(11):6960–6974, 1997.
- [103] W. Hansel, P. Hommelhoff, T. W. Hansch, and J. Reichel. Bose-Einstein condensation on a microelectronic chip. *Nature*, 413(6855):498–501, 2001.
- [104] W. A. Harrison. *Electronic Structure and the Properties of Solids*. W. H. Freeman and Company, San Francisco, 1980.
- [105] H. Haug and S. Schmitt-Rink. Electron theory of the optical properties of laser-excited semiconductors. *Prog. Quant. Electr.*, 9(1):3, 1984.
- [106] D. B. Haviland, Y. Liu, and A. M. Goldman. Onset of superconductivity in the two-dimensional limit. *Phys. Rev. Lett.*, 62(18):2180, 1989.
- [107] G. R. Hayes, B. Deveaud, V. Savona, and S. Haacke. Speckle-averaged resonant rayleigh scattering from quantum-well excitons. *Phys. Rev. B*, 62(11):6952, 2000.
- [108] U. Heim and P. Hiesinger. Luminescence and excitation spectra of GaAs. *Phys. Stat. Sol. (b)*, 66:461, 1974.
- [109] R. F. M. Hendriks, M. P. van Exter, J. P. Woerdman, K. H. Gulden, and M. Moser. Memory effect for polarization of pump light in optically pumped vertical-cavity semiconductor lasers. *IEEE J. Quantum Electron.*, 34(8):1455, 1998.
- [110] R. Höger, E. Göbel, J. Kuhl, K. Ploog, and H. Quiesser. Kinetics of free and bound excitons in GaAs/alGaAs double heterostructures. *J. Phys. C*, 17(34):L905, 1984.
- [111] D. J. Hilton and C. L. Tang. Optical orientation and femtosecond relaxation of spin-polarized holes in GaAs. *Phys. Rev. Lett.*, 89(14):146601, 2002.

-
- [112] P. C. Hohenberg. Existence of long-range order in one and two dimensions. *Phys. Rev.*, 158(2):383–386, 1967.
- [113] J. J. Hopfield. Theory of the contribution of excitons to the complex dielectric constant of crystals. *Phys. Rev.*, 112(5):1555–1567, 1958.
- [114] R. Houdré, R. P. Stanley, U. Oesterle, M. Ilegems, and C. Weisbuch. Room-temperature cavity polaritons in a semiconductor microcavity. *Phys. Rev. B*, 49(23):16761–4, 1994. Artículo de Lola.
- [115] R. Houdré, C. Weisbuch, R. P. Stanley, U. Oesterle, P. Pellandini, and M. Ilegems. Measurement of cavity-polariton dispersion curve from angle-resolved photoluminescence experiments. *Phys. Rev. Lett.*, 73(15):2043, 1994.
- [116] W. Hoyer, C. Ell, M. Kira, S. W. Koch, S. Chatterjee, S. Mosor, G. Khitrova, H. M. Gibbs, and H. Stolz. Many-body dynamics and exciton formation studied by time-resolved photoluminescence. *Phys. Rev. B*, 72:075324, 2005.
- [117] W. Hoyer, M. Kira, and S. W. Koch. Influence of coulomb and phonon interaction on the exciton formation dynamics in semiconductor heterostructures. *Phys. Rev. B*, 67(15):155113, 2003.
- [118] R. Huber, R. A. Kaindl, B. A. Schmid, and D. S. Chemla. Broadband terahertz study of excitonic resonances in the high-density regime in GaAs/Al_xGa_{1-x}As quantum wells. *Phys. Rev. B*, 72(16):161314, 2005.
- [119] A. Huynh, J. Tignon, G. Keller, P. Roussignol, C. Delalande, R. André, R. Romestain, and L. S. Dang. Collision broadening in II-VI semiconductor microcavities. *Phys. Rev. B*, 68(16):165340, 2003.
- [120] S. Hövel, N. Gerhardt, M. Hofmann, J. Yang, D. Reuter, and A. Wieck. Spin controlled optically pumped vertical cavity surface emitting laser. *Electronics Letters*, 41(5):251, 2005.
- [121] A. Imamoglu, R. J. Ram, S. Pau, and Y. Yamamoto. Nonequilibrium condensates and lasers without inversion: Exciton-polariton lasers. *Physical Review A*, 53(6):4250, 1996.

-
- [122] I. Institute. New semiconductor materials. characteristics and properties, <http://www.ioffe.rssi.ru/SVA/NSM/>.
- [123] M. Jaros, K. B. Wong, and M. A. Gell. Electronic structure of GaAs-Ga_{1-x}Al_xAs quantum well and sawtooth superlattices. *Phys. Rev. B*, 31(2):1205–1207, 1985.
- [124] H. W. Jiang, C. E. Johnson, K. L. Wang, and S. T. Hannahs. Observation of magnetic-field-induced delocalization: Transition from anderson insulator to quantum hall conductor. *Phys. Rev. Lett.*, 71(9):1439–1442, 1993.
- [125] B. T. Jonker, Y. D. Park, B. R. Bennett, H. D. Cheong, G. Kioseoglou, and A. Petrou. Robust electrical spin injection into a semiconductor heterostructure. *Phys. Rev. B*, 62(12):8180–8183, 2000.
- [126] S. Jorda. Theory of rabi splitting in cavity-embedded quantum wells. *Phys. Rev. B*, 50(24):18690, 1994.
- [127] S. Jorda. Dispersion of exciton polaritons in cavity-embedded quantum wells. *Phys. Rev. B*, 51(15):10185, 1995.
- [128] R. A. Kaindl, M. A. Carnahan, D. Hägele, R. Lövenich, and D. S. Chemla. Ultrafast terahertz probes of transient conducting and insulating phases in an electron-hole gas. *Nature*, 423:734 – 738, 2003.
- [129] Y. Kajikawa, M. Hata, N. Sugiyama, and Y. Katayama. Photocurrent spectroscopy of a (001)- and a (111)-oriented GaAs/Al_{0.33}Ga_{0.67}As quantum-well structure. *Phys. Rev. B*, 42(15):9540–9545, 1990.
- [130] V. K. Kalevich, M. Paillard, K. V. Kavokin, X. Marie, E. Vanelle, T. Amand, V. M. Ustinov, and B. P. Zakharchenya. Electron spin redistribution due to pauli blocking in quantum dots and quantum wells. *Phys. Stat. Sol. (a)*, 190(1):229–233, 2002.
- [131] L. Kappei, J. Szczytko, F. Morier-Genoud, and B. Deveaud. Direct observation of the mott transition in an optically excited semiconductor quantum well. *Phys. Rev. Lett.*, 94:147403, 2005.
- [132] J. Kasprzak, R. Andre, L. S. Dang, I. A. Shelykh, A. V. Kavokin, Y. G. Rubo, K. V. Kavokin, and G. Malpuech. Build up and pinning of linear polarization in the Bose condensates of exciton polaritons. *Phys. Rev. B*, 75(4):045326, 2007.

-
- [133] J. Kasprzak, M. Richard, S. Kundermann, A. Baas, P. Jeambrun, J. M. J. Keeling, F. M. Marchetti, M. H. Szymanska, R. Andre, J. L. Staehli, V. Savona, P. B. Littlewood, B. Deveaud, and L. S. Dang. Bose-Einstein condensation of exciton polaritons. *Nature*, 443(7110):409–414, 2006.
- [134] A. Kavokin, P. G. Lagoudakis, G. Malpuech, and J. J. Baumberg. Polarization rotation in parametric scattering of polaritons in semiconductor microcavities. *Phys. Rev. B*, 67(19):195321, 2003.
- [135] A. Kavokin and G. Malpuech. *Cavity Polaritons*. Films and Nanostructures. Academic Press, 2003.
- [136] A. V. Kavokin. Exciton oscillator strength in quantum wells: From localized to free resonant states. *Phys. Rev. B*, 50(11):8000–8003, 1994.
- [137] K. Kavokin, P. Renucci, T. Amand, X. Marie, P. Senellart, J. Bloch, and B. Sermage. Linear polarisation inversion: A signature of coulomb scattering of cavity polaritons with opposite spins. *Phys. Stat. Sol. (c)*, 2(2):763 – 767, 2005.
- [138] J. Keeling, P. R. Eastham, M. H. Szymanska, and P. B. Littlewood. Polariton condensation with localized excitons and propagating photons. *Phys. Rev. Lett.*, 93(22):226403, 2004.
- [139] S. R. Khan, E. M. Pedersen, B. Kain, A. J. Jordan, and R. P. Barber. Superconductor-insulator transition in granular pb films near a superconducting ground plane. *Phys. Rev. B*, 61(9):5909–5912, 2000.
- [140] J. M. Kikkawa and D. D. Awschalom. Resonant spin amplification in n-type GaAs. *Phys. Rev. Lett.*, 80(19):4313–4316, 1998.
- [141] J. M. Kikkawa and D. D. Awschalom. Lateral drag of spin coherence in gallium arsenide. *Nature*, 397:139 – 141, 1999.
- [142] J. M. Kikkawa, I. P. Smorchkova, N. Samarth, and D. D. Awschalom. Room-temperature spin memory in two-dimensional electron gases. *Science*, 277:1284, 1997.
- [143] D.-S. Kim, J. Shah, J. E. Cunningham, T. C. Damen, W. Schäfer, M. Hartmann, and S. Schmitt-Rink. Giant excitonic resonance in time-resolved four-wave mixing in quantum wells. *Physical Review Letters*, 68(7):1006–1009, 1992.

-
- [144] N. Y. Kim, C.-W. Lai, S. Utsunomiya, G. Roumpos, H. Deng, T. Byrnes, P. Recher, N. Kumada, T. Fujisawa, and Y. Yamamoto. GaAs microcavity exciton-polaritons in a trap. In *9th International conference on the Optics of Excitons in Confined Systems*, Patti, Italy, 2007.
- [145] M. Kira, F. Jahnke, and S. W. Koch. Microscopic theory of excitonic signatures in semiconductor photoluminescence. *Phys. Rev. Lett.*, 81(15):3263–3266, 1998.
- [146] L. Klotowski, A. Amo, M. D. Martín, L. Viña, and R. André. Polarization dynamics of microcavity polaritons: Three excitation regimes. *Phys. Stat. Sol. (a)*, 202(3):357–361, 2005.
- [147] L. Klotowski, M. Martin, A. Amo, L. Vina, I. Shelykh, M. Glazov, G. Malpuech, A. Kavokin, and R. Andre. Optical anisotropy and pinning of the linear polarization of light in semiconductor microcavities. *Solid State Commun.*, 139(10):511–515, 2006.
- [148] W. H. Knox. Optical studies of femtosecond carrier thermalization in GaAs. In J. Shah, editor, *Hot Carriers in Semiconductor Nanostructures: Physics and Applications*. Academic Press, Inc., Boston, San Diego, New York, London, Sydney, Tokio, Toronto, 1992.
- [149] S. W. Koch, W. Hoyer, M. Kira, and V. S. Filinov. Exciton ionization in semiconductors. *Phys. Stat. Sol. (b)*, 238(3):404–410, 2003.
- [150] S. W. Koch, M. Kira, G. Khitrova, and H. M. Gibbs. Semiconductor excitons in new light. *Nature Materials*, 5:523–531, 2006.
- [151] G. Kocherscheidt, W. Langbein, U. Woggon, V. Savona, R. Zimmermann, D. Reuter, and A. D. Wieck. Resonant rayleigh scattering dynamics of excitons in single quantum wells. *Phys. Rev. B*, 68(8):085207, 2003.
- [152] J. M. Kosterlitz and D. J. Thouless. Ordering, metastability and phase transitions in two-dimensional systems. *J. Phys. C*, 6:1181, 1973.
- [153] S. V. Kravchenko, G. V. Kravchenko, J. E. Furneaux, V. M. Pudalov, and M. D’Iorio. Possible metal-insulator transition at $b=0$ in two dimensions. *Phys. Rev. B*, 50(11):8039–8042, 1994.

-
- [154] S. V. Kravchenko, W. E. Mason, G. E. Bowker, J. E. Furneaux, V. M. Pudalov, and M. D'Iorio. Scaling of an anomalous metal-insulator transition in a two-dimensional system in silicon at $b=0$. *Phys. Rev. B*, 51(11):7038–7045, 1995.
- [155] D. N. Krizhanovskii, S. S. Gavrilov, A. P. D. Love, D. Sanvitto, N. A. Gippius, S. G. Tikhodeev, V. D. Kulakovskii, D. M. Whittaker, M. S. Skolnick, and J. S. Roberts. Spontaneous self-organisation of multiple polariton-polariton scattering in semiconductor microcavities. submitted.
- [156] D. N. Krizhanovskii, D. Sanvitto, I. A. Shelykh, M. M. Glazov, G. Malpuech, D. D. Solnyshkov, A. Kavokin, S. Ceccarelli, M. S. Skolnick, and J. S. Roberts. Rotation of the plane of polarization of light in a semiconductor microcavity. *Phys. Rev. B*, 73(7):073303–4, 2006.
- [157] D. N. Krizhanovskii, A. I. Tartakovskii, M. N. Makhonin, A. N. Dremin, and V. D. Kulakovskii. Influence of nonstimulated polariton relaxation on parametric scattering of microcavity polaritons. *Phys. Rev. B*, 70(19):195303–6, 2004.
- [158] R. Kumar, A. S. Vengurlekar, S. S. Prabhu, J. Shah, and L. N. Pfeiffer. Picosecond time evolution of free electron-hole pairs into excitons in GaAs quantum wells. *Phys. Rev. B*, 54(7):4891–4897, 1996.
- [159] P. G. Lagoudakis, M. D. Martin, J. J. Baumberg, G. Malpuech, and A. Kavokin. Coexistence of low threshold lasing and strong coupling in microcavities. *J. Appl. Phys.*, 95(5):2487–2489, 2004.
- [160] P. G. Lagoudakis, P. G. Savvidis, J. J. Baumberg, D. M. Whittaker, P. R. Eastham, M. S. Skolnick, and J. S. Roberts. Stimulated spin dynamics of polaritons in semiconductor microcavities. *Phys. Rev. B*, 65:161310, 2002.
- [161] C. W. Lai, N. Y. Kim, S. Utsunomiya, G. Roumpos, H. Deng, M. D. Fraser, T. Byrnes, P. Recher, N. Kumada, T. Fujisawa, and Y. Yamamoto. Coherent zero-state and π -state in an exciton-polariton condensate array. *Nature*, 450:529, 2007.
- [162] T. Lai, L. Teng, Z. Jiao, H. Xu, L. Lei, J. Wen, and W. Lin. Evolution of spin coherence dynamics and g factor with electron excess energy in bulk intrinsic GaAs. *Appl. Phys. Lett.*, 91(6):062110, 2007.

-
- [163] E. Landau and L. Lifshitz. *Statistical Physics, Parts I and II*, volume 5 of *Course of Theoretical Physics*. Pergamon Press, 1986.
- [164] W. Langbein. Spontaneous parametric scattering of microcavity polaritons in momentum space. *Phys. Rev. B*, 70(20):205301, 2004.
- [165] W. Langbein. Polariton correlation in microcavities produced by parametric scattering. *Phys. Stat. Sol. (b)*, 242(11):2260–2270, 2005.
- [166] W. Langbein, J. M. Hvam, and R. Zimmermann. Time-resolved speckle analysis: A new approach to coherence and dephasing of optical excitations in solids. *Phys. Rev. Lett.*, 82(5):1040 – 1043, 1999.
- [167] W. Langbein, K. Leosson, J. R. Jensen, J. M. Hvam, and R. Zimmermann. Instantaneous rayleigh scattering from excitons localized in monolayer islands. *Phys. Rev. B*, 61(16):R10555, 2000.
- [168] W. Langbein, V. Savona, D. Reuter, and A. D. Wieck. Polariton dynamics in planar microcavities: the effect of cross-hatch disorder. In *9th International conference on the Optics of Excitons in Confined Systems*, Patti, Italy, 2007.
- [169] W. Langbein, I. Shelykh, D. Solnyshkov, G. Malpuech, Y. Rubo, and A. Kavokin. Polarization beats in ballistic propagation of exciton-polaritons in microcavities. *Phys. Rev. B*, 75(7):075323, 2007.
- [170] P. Langot, R. Tommasi, and F. Vallée. Cold-phonon effect on electron heating in GaAs. *Solid State Commun.*, 98(2):171–174, 1996.
- [171] F. Laussy. private communication.
- [172] A. E. Leanhardt, T. A. Pasquini, M. Saba, A. Schirotzek, Y. Shin, D. Kielpinski, D. E. Pritchard, and W. Ketterle. Cooling Bose-Einstein condensates below 500 picokelvin. *Science*, 301(5639):1513–1515, 2003.
- [173] C. Lechner and U. Rössler. Spin-dependent semiconductor bloch equations: Microscopic theory of bir-aronov-pikus spin relaxation. *Phys. Rev. B*, 72:153317, 2005.
- [174] A. J. Leggett. Bose-Einstein condensation in the alkali gases: Some fundamental concepts. *Rev. Mod. Phys.*, 73(2):307–356, 2001.

-
- [175] K. Leo, W. W. Rühle, and K. Ploog. Hot-carrier energy-loss rates in GaAs/Al_xGa_{1-x}As quantum wells. *Phys. Rev. B*, 38(3):1947–1957, 1988.
- [176] K. Leo, W. W. Rühle, H. J. Queisser, and K. Ploog. Reduced dimensionality of hot-carrier relaxation in GaAs quantum wells. *Phys. Rev. B*, 37(12):7121–7124, 1988.
- [177] S. Levy, E. Lahoud, I. Shomroni, and J. Steinhauer. The a.c. and d.c. josephson effects in a Bose-Einstein condensate. *Nature*, 449(7162):579–583, 2007.
- [178] R. Loudon. *The quantum theory of light*. Oxford science publications. Oxford University Press, Oxford, 2000.
- [179] M. Z. Maialle. Spin relaxation of electrons in p-doped quantum wells via the electron-hole exchange interaction. *Phys. Rev. B*, 54(3):1967–1974, 1996.
- [180] G. Malpuech, A. D. Carlo, A. V. Kavokin, J. J. Baumberg, M. Zamfirescu, and P. Lugli. Room-temperature polariton lasers based on gan microcavities. *Appl. Phys. Lett.*, 81(3):412, 2002.
- [181] G. Malpuech, Y. G. Rubo, F. P. Laussy, P. Bigenwald, and A. V. Kavokin. Polariton laser: thermodynamics and quantum kinetic theory. *Semic. Science and Technol.*, 18:S395, 2003.
- [182] G. Malpuech, D. D. Solnyshkov, H. Ouerdane, M. M. Glazov, and I. Shelykh. Bose glass and superfluid phase of cavity polaritons. *Phys. Rev. Lett.*, 98:206402, 2007.
- [183] G. Mannarini, F. Grosse, R. Zimmermann, S. Kassbohm, and W. Langbein. Moving speckles in the rayleigh scattering of excitons in potential gradients. *Physical Review B (Condensed Matter and Materials Physics)*, 69(8):085326–8, 2004.
- [184] A. M. Martin, R. G. Scott, and T. M. Fromhold. Transmission and reflection of Bose-Einstein condensates incident on a gaussian tunnel barrier. *Phys. Rev. A*, 75(6):065602, 2007.
- [185] M. D. Martín, G. Aichmayr, L. Viña, and R. André. Polarization control of the nonlinear emission of semiconductor microcavities. *Phys. Rev. Lett.*, 89(7):077402, 2002.

-
- [186] F. Meier and D. Pescia. Spin-polarized photoemission by optical orientation. In F. Meier and B. P. Zakharchenya, editors, *Optical Orientation*, volume 8 of *Modern Problems in Condensed Matter Sciences*, page Chapter 7. North-Holland, Amsterdam, 1984.
- [187] F. Meier and B. P. Zakharchenya. *Optical Orientation*, volume 8 of *Modern Problems in Condensed Matter Sciences*. North-Holland, Amsterdam, 1984.
- [188] B. Mieck, H. Haug, W. A. Hügel, M. F. Heinrich, and M. Wegener. Quantum-kinetic dephasing in resonantly excited semiconductor quantum wells. *Phys. Rev. B*, 62(4):2686–2695, 2000.
- [189] N. F. Mott. The basis of the electron theory of metals, with special reference to the transition metals. *Proc. Phys. Soc. A*, 62(7):416–422, 1949.
- [190] N. F. Mott. The transition to the metallic state. *Philos. Mag.*, 6(62):287, 1961.
- [191] N. F. Mott. Metal-insulator transition. *Rev. Mod. Phys.*, 40(4):677–683, 1968.
- [192] L. Muñoz, E. Pérez, L. Viña, and K. Ploog. Spin relaxation in intrinsic GaAs quantum wells: Influence of excitonic localization. *Phys. Rev. B*, 51(7):4247–4257, 1995.
- [193] P. Nemec, Y. Kerachian, H. M. van Driel, and A. L. Smirl. Spin-dependent electron many-body effects in GaAs. *Phys. Rev. B*, 72:245202, 2005.
- [194] P. Nozières. Some comments on Bose-einstein condensation. In A. Griffin, D. W. Snoke, and S. Stringari, editors, *Bose-Einstein Condensation*. Cambridge University Press, Cambridge, 1995.
- [195] Z. G. Pan, S. Jiang, M. Dagenais, R. A. Morgan, K. Kojima, M. T. Asom, R. E. Leibenguth, G. D. Guth, and M. W. Focht. Optical injection induced polarization bistability in vertical-cavity surface-emitting lasers. *Appl. Phys. Lett.*, 63(22):2999–3001, 1993.
- [196] G. Panzarini, L. C. Andreani, A. Armitage, D. Baxter, M. S. Skolnick, V. N. Astratov, J. S. Roberts, A. V. Kavokin, M. R. Vladimirova, and M. A. Kaliteevski. Cavity-polariton dispersion and polarization splitting in single and coupled semiconductor microcavities. *Physics of the Solid State*, V41(8):1223–1238, 1999.

-
- [197] T. A. Pasquini, M. Saba, G.-B. Jo, Y. Shin, W. Ketterle, D. E. Pritchard, T. A. Savas, and N. Mulders. Low velocity quantum reflection of Bose-Einstein condensates. *Phys. Rev. Lett.*, 97(9):093201, 2006.
- [198] T. A. Pasquini, Y. Shin, C. Sanner, M. Saba, A. Schirotzek, D. E. Pritchard, and W. Ketterle. Quantum reflection from a solid surface at normal incidence. *Phys. Rev. Lett.*, 93(22):223201, 2004.
- [199] S. Pau, H. Cao, J. Jacobson, G. Björk, Y. Yamamoto, and A. Imamoglu. Observation of a laserlike transition in a microcavity exciton polariton system. *Phys. Rev. A*, 54(3):R1789, 1996.
- [200] M. Perrin, J. Bloch, A. Lemaitre, and P. Senellart. Enhanced polariton relaxation by electron-polariton scattering. *Phys. Stat. Sol. (c)*, 2(2):759–762, 2005.
- [201] M. Perrin, P. Senellart, A. Lemaitre, and J. Bloch. Polariton relaxation in semiconductor microcavities: Efficiency of electron-polariton scattering. *Phys. Rev. B*, 72(7):075340–5, 2005.
- [202] D. S. Petrov, M. Holzmann, and G. V. Shlyapnikov. Bose-Einstein condensation in quasi-2d trapped gases. *Phys. Rev. Lett.*, 84(12):2551–2555, 2000.
- [203] C. Piermarocchi, F. Tassone, V. Savona, A. Quattropani, and P. Schwendimann. Nonequilibrium dynamics of free quantum-well excitons in time-resolved photoluminescence. *Physical Review B*, 53(23):15834–15841, 1996.
- [204] C. Piermarocchi, F. Tassone, V. Savona, A. Quattropani, and P. Schwendimann. Exciton formation rates in GaAs/Al_xGa_{1-x}As quantum wells. *Phys. Rev. B*, 55(3):1333–1336, 1997.
- [205] G. E. Pikus and A. N. Titkov. Spin relaxation under optical orientation in semiconductors. In F. Meier and B. P. Zakharchenya, editors, *Optical Orientation*, volume 8 of *Modern Problems in Condensed Matter Sciences*, page Chapter 3. North-Holland, Amsterdam, 1984.
- [206] E. X. Ping and H. X. Jiang. Effect of charge-carrier screening on the exciton binding energy in GaAs/Al_xGa_{1-x}As quantum wells. *Phys. Rev. B*, 47(4):2101–2106, 1993.

-
- [207] L. Pitaevskii and S. Strindgari. *Bose-Einstein Condensation*. Clarendon Press, Oxford, 1st edition, 2003.
- [208] D. Porras, C. Ciuti, J. Baumberg, and C. Tejedor. Polariton dynamics and Bose-Einstein condensation in semiconductor microcavities. *Phys. Rev. B*, 66:085304, 2002.
- [209] M. Potemski, E. Perez, D. Martin, L. Vina, L. Gravier, A. Fisher, and K. Ploog. Spin polarization of an optically pumped electron gas. *Solid State Commun.*, 110(3):163–8, 1999.
- [210] W. Pötz and P. Kocevar. Electronic power transfer in pulsed laser excitation of polar semiconductors. *Phys. Rev. B*, 28(12):7040–7047, 1983.
- [211] Y. Qi, Z.-G. Yu, and M. E. Flatté. Spin gunn effect. *Phys. Rev. Lett.*, 96:026602, 2006.
- [212] S. Raghavan, A. Smerzi, S. Fantoni, and S. R. Shenoy. Coherent oscillations between two weakly coupled Bose-Einstein condensates: Josephson effects, π oscillations, and macroscopic quantum self-trapping. *Phys. Rev. A*, 59(1):620–633, 1999.
- [213] M. G. Raizen, R. J. Thompson, R. J. Brecha, H. J. Kimble, and H. J. Carmichael. Normal-mode splitting and linewidth averaging for two-state atoms in an optical cavity. *Phys. Rev. Lett.*, 63(3):240, 1989.
- [214] J. Rarity and C. Weisbuch, editors. *Microcavities and Photonic Bandgaps: Physics and Applications*. NATO ASI Series. Kluwer Academic Publishers, 1996.
- [215] I. Reimand and J. Aaviksoo. Exciton interaction with hot electrons in GaAs. *Phys. Rev. B*, 61(24):16653–16658, 1999.
- [216] T. L. Reinecke and S. C. Ying. Droplet model of electron-hole liquid condensation in semiconductors. *Phys. Rev. Lett.*, 35(5):311–315, 1975.
- [217] J. T. Remillard, H. Wang, D. G. Steel, J. Oh, J. Pamulapati, and P. K. Bhattacharya. High-resolution nonlinear laser spectroscopy of heavy-hole excitons in GaAs/alGaAs quantum-well structures: A direct measure of the exciton line shape. *Phys. Rev. Lett.*, 62(24):2861–2864, 1989.
- [218] P. Renucci, T. Amand, X. Marie, P. Senellart, J. Bloch, B. Sermage, and K. V. Kavokin. Microcavity polariton spin quantum beats without a magnetic field: A

- manifestation of coulomb exchange in dense and polarized polariton systems. *Phys. Rev. B*, 72(7):075317–11, 2005.
- [219] W. W. Rühle and H. J. Pollard. Heating of cold electrons by a warm GaAs lattice: A novel probe of the carrier-phonon interaction. *Phys. Rev. B*, 36(3):1683–1685, 1987.
- [220] M. Richard, J. Kasprzak, R. André, R. Romestain, L. S. Dang, G. Malpuech, and A. Kavokin. Experimental evidence for nonequilibrium Bose condensation of exciton polaritons. *Phys. Rev. B*, 72:201301(R), 2005.
- [221] M. Richard, J. Kasprzak, R. Romestain, R. Andre, and L. S. Dang. Spontaneous coherent phase transition of polaritons in CdTe microcavities. *Phys. Rev. Lett.*, 94(18):187401, 2005.
- [222] D. Robart, X. Marie, B. Baylac, T. Amand, M. Brousseau, G. Bacquet, G. Debart, R. Planel, and J. M. Gerard. Dynamical equilibrium between excitons and free carriers in quantum wells. *Solid State Commun.*, 95(5):287–293, 1995.
- [223] M. Romanelli, C. Leyder, J. P. Karr, E. Giacobino, and A. Bramati. Four wave mixing oscillation in a semiconductor microcavity: Generation of two correlated polariton populations. *Phys. Rev. Lett.*, 98(10):106401, 2007.
- [224] T. F. Rosenbaum, R. F. Milligan, M. A. Paalanen, G. A. Thomas, R. N. Bhatt, and W. Lin. Metal-insulator transition in a doped semiconductor. *Phys. Rev. B*, 27(12):7509–7523, 1983.
- [225] L. Rota, P. Lugli, T. Elsaesser, and J. Shah. Ultrafast thermalization of photoexcited carriers in polar semiconductors. *Phys. Rev. B*, 47(8):4226–4237, 1993.
- [226] P. Roussignol, C. Delalande, A. Vinattieri, L. Carraresi, and M. Colocci. Dynamics of exciton relaxation in GaAs/Al_xGa_{1-x}As quantum wells. *Phys. Rev. B*, 45(12):6965, 1992.
- [227] J. F. Ryan, R. A. Taylor, A. J. Turberfield, A. Maciel, J. M. Worlock, A. C. Gossard, and W. Wiegmann. Time-resolved photoluminescence of two-dimensional hot carriers in GaAs-alGaAs heterostructures. *Phys. Rev. Lett.*, 53(19):1841–1844, 1984.
- [228] M. San Miguel, Q. Feng, and J. V. Moloney. Light-polarization dynamics in surface-emitting semiconductor lasers. *Phys. Rev. A*, 52(2):1728, 1995.

-
- [229] H. Sanada, I. Arata, Y. Ohno, Z. Chen, K. Kayanuma, Y. Oka, F. Matsukura, and H. Ohno. Relaxation of photoinjected spins during drift transport in GaAs. *Appl. Phys. Lett.*, 81(15):2788–2790, 2002.
- [230] J. S. Sandhu, A. P. Heberle, J. J. Baumberg, and J. R. A. Cleaver. Gateable suppression of spin relaxation in semiconductors. *Phys. Rev. Lett.*, 86(10):2150–2153, 2001.
- [231] D. Sanvitto, D. N. Krizhanovskii, D. M. Whittaker, S. Ceccarelli, M. S. Skolnick, and J. S. Roberts. Spatial structure and stability of the macroscopically occupied polariton state in the microcavity optical parametric oscillator. *Phys. Rev. B*, 73:241308(R), 2006.
- [232] D. Sanvitto, D. M. Whittaker, M. S. Skolnick, and J. S. Roberts. Continuous wave pump-probe experiment on a planar microcavity. *Phys. Stat. Sol. (a)*, 202(3):353–356, 2005.
- [233] M. Sargent, M. O. Scully, and W. E. Lamb. *Laser Physics*. Addison-Wesley, Reading, MA, 1987.
- [234] S. Savasta, O. D. Stefano, V. Savona, and W. Langbein. Quantum complementarity of microcavity polaritons. *Phys. Rev. Lett.*, 94(24):246401, 2005.
- [235] V. Savona, Z. Hradil, A. Quattropani, and P. Schwendimann. Quantum theory of quantum-well polaritons in semiconductor microcavities. *Phys. Rev. B*, 49(13):8774, 1994.
- [236] V. Savona and W. Langbein. Realistic heterointerface model for excitonic states in growth-interrupted GaAs quantum wells. *Phys. Rev. B*, 74(7):075311–18, 2006.
- [237] V. Savona, C. Piermarocchi, A. Quattropani, P. Schwendimann, and F. Tassone. Optical properties of microcavity polaritons. *Phase Transitions*, 68(1):169 – 279, 1999.
- [238] V. Savona, F. Tassone, C. Piermarocchi, A. Quattropani, and P. Schwendimann. Theory of polariton photoluminescence in arbitrary semiconductor microcavity structures. *Phys. Rev. B*, 53(19):13051, 1996.

-
- [239] P. G. Savvidis, J. J. Baumberg, R. M. Stevenson, M. S. Skolnick, D. M. Whittaker, and J. S. Roberts. Angle-resonant stimulated polariton amplifier. *Phys. Rev. Lett.*, 84(7):1547, 2000.
- [240] H. C. Schneider, J.-P. Wüstenberg, O. Andreyev, K. Hiebbner, L. Guo, J. Lange, L. Schreiber, B. Beschoten, M. Bauer, and M. Aeschlimann. Energy-resolved electron spin dynamics at surfaces of p-doped GaAs. *Phys. Rev. B*, 73:081302(R), 2006.
- [241] J. N. Schulman and Y.-C. Chang. New method for calculating electronic properties of superlattices using complex band structures. *Phys. Rev. B*, 24(8):4445–4448, 1981.
- [242] J. N. Schulman and Y.-C. Chang. Band mixing in semiconductor superlattices. *Phys. Rev. B*, 31(4):2056–2068, 1985.
- [243] L. Schultheis, J. Kuhl, A. Honold, and C. W. Tu. Picosecond phase coherence and orientational relaxation of excitons in GaAs. *Phys. Rev. Lett.*, 57(14):1797–1800, 1986.
- [244] L. Schultheis, J. Kuhl, A. Honold, and C. W. Tu. Ultrafast phase relaxation of excitons via exciton-exciton and exciton-electron collisions. *Phys. Rev. Lett.*, 57(13):1635–1638, 1986.
- [245] L. Schultheis, J. Kuhl, A. Honold, and C. W. Tu. Optical dephasing of wannier excitons in GaAs. In R. del Sole, A. D’Andrea, and A. Lapicciarella, editors, *Excitons in confined systems*, Springer Proceedings in physics, pages 50–58. Springer-Verlag, Heidelberg, 1988.
- [246] R. G. Scott, C. W. Gardiner, and D. A. W. Hutchinson. Nonequilibrium dynamics: Studies of the reflection of Bose-Einstein condensates. *Laser Physics*, 17(4):527, 2007.
- [247] R. G. Scott, D. A. W. Hutchinson, and C. W. Gardiner. Disruption of reflecting Bose-Einstein condensates due to interatomic interactions and quantum noise. *Phys. Rev. A*, 74(5):053605, 2006.
- [248] R. G. Scott, A. M. Martin, T. M. Fromhold, S. Bujkiewicz, F. W. Sheard, and M. Leadbeater. Creation of solitons and vortices by bragg reflection of Bose-Einstein condensates in an optical lattice. *Phys. Rev. Lett.*, 90(11):110404, 2003.

-
- [249] R. G. Scott, A. M. Martin, T. M. Fromhold, and F. W. Sheard. Anomalous quantum reflection of Bose-Einstein condensates from a silicon surface: The role of dynamical excitations. *Phys. Rev. Lett.*, 95(7):073201, 2005.
- [250] P. E. Selbmann, M. Gulia, F. Rossi, E. Molinari, and P. Lugli. Coupled free-carrier and exciton relaxation in optically excited semiconductors. *Phys. Rev. B*, 54(7):4660–4673, 1996.
- [251] P. Senellart, J. Bloch, B. Sermage, and J. Y. Marzin. Microcavity polariton depopulation as evidence for stimulated scattering. *Physical Review B*, 62(24):R16263, 2000.
- [252] B. Sermage, S. Long, I. Abram, J. Y. Marzin, J. Bloch, R. Planel, and V. Thierry-Mieg. Time-resolved spontaneous emission of excitons in a microcavity: Behavior of the individual exciton-photon mixed states. *Phys. Rev. B*, 53(24):16516, 1996.
- [253] B. Sermage, G. Malpuech, A. V. Kavokin, and V. Thierry-Mieg. Polariton acceleration in a microcavity wedge. *Phys. Rev. B*, 64(8):081303, 2001.
- [254] R. J. Seymour, M. R. Junnarkar, and R. R. Alfano. Spin relaxation of photogenerated degenerate electron distributions in GaAs. *Phys. Rev. B*, 24(6):3623–3625, 1981.
- [255] J. Shah. *Ultrafast spectroscopy of semiconductors and semiconductor nanostructures*. Springer-Verlag, Berlin, Germany, 1996.
- [256] J. Shah, M. Combescot, and A. H. Dayem. Investigation of exciton-plasma mott transition in si. *Phys. Rev. Lett.*, 38(25):1497–1500, 1977.
- [257] J. Shah, A. Pinczuk, A. C. Gossard, and W. Wiegmann. Energy-loss rates for hot electrons and holes in GaAs quantum wells. *Phys. Rev. Lett.*, 54(18):2045–2048, 1985.
- [258] C. V. Shank, R. L. Fork, R. Yen, J. Shah, B. I. Greene, A. C. Gossard, and C. Weisbuch. Picosecond dynamics of hot carrier relaxation in highly excited multi-quantum well structures. *Solid State Communications*, 47(12):981–983, 1983.
- [259] I. Shelykh, K. V. Kavokin, A. V. Kavokin, G. Malpuech, P. Bigenwald, H. Deng, G. Weihs, and Y. Yamamoto. Semiconductor microcavity as a spin-dependent optoelectronic device. *Phys. Rev. B*, 70:035320, 2004.

-
- [260] I. Shelykh, G. Malpuech, K. V. Kavokin, A. V. Kavokin, and P. Bigenwald. Spin dynamics of interacting exciton polaritons in microcavities. *Phys. Rev. B*, 70(11):115301, 2004.
- [261] I. A. Shelykh, Y. G. Rubo, G. Malpuech, D. D. Solnyshkov, and A. Kavokin. Polarization and propagation of polariton condensates. *Phys. Rev. Lett.*, 97(6):066402, 2006.
- [262] J. X. Shen, R. Pittini, Y. Oka, and E. Kurtz. Exciton dynamics in GaAs/Ga_{1-x}Al_xAs heterojunctions and GaAs epilayers. *Phys. Rev. B*, 61(4):2765–2772, 2000.
- [263] M. Skolnick, A. Tartakovskii, R. Butté, D. M. Whittaker, and R. M. Stevenson. High-occupancy effects and stimulation phenomena in semiconductor microcavities. *IEEE Journal of Selected Topics in Quantum Electronics*, 8(5):1060–1071, 2002.
- [264] D. L. Smith and C. Mailhot. Theory of semiconductor superlattice electronic structure. *Rev. Mod. Phys.*, 62(1):173–234, 1990.
- [265] P. H. Song and K. W. Kim. Spin relaxation of conduction electrons in bulk III-V semiconductors. *Phys. Rev. B*, 66:035207, 2002.
- [266] M. Stern, V. Garmider, V. Umansky, and I. Bar-Joseph. Mott transition of excitons in coupled quantum wells. In *10th International Conference on the Optics of Excitons in Confined Systems*, Patti, Italy, 2007.
- [267] R. M. Stevenson, V. N. Astratov, M. S. Skolnick, D. M. Whittaker, M. Emam-Ismail, A. I. Tartakovskii, P. G. Savvidis, J. J. Baumberg, and J. S. Roberts. Continuous wave observation of massive polariton redistribution by stimulated scattering in semiconductor microcavities. *Phys. Rev. Lett.*, 85(17):3680, 2000.
- [268] H. Stolz, D. Schwarze, W. von der Osten, and G. Weimann. Transient resonance rayleigh scattering from electronic states in disordered systems: Excitons in GaAs/Al_xGa_{1-x}As multiple-quantum-well structures. *Phys. Rev. B*, 47(15):9669, 1993.
- [269] R. Strobel, R. Eccleston, J. Kuhl, and K. Köhler. Measurement of the exciton-formation time and the electron- and hole-tunneling times in a double-quantum-well structure. *Physical Review B*, 43(15):12564–12570, 1991.

-
- [270] J. Szczytko, L. Kappei, J. Berney, F. Morier-Genoud, M. Portella-Oberli, and B. Deveaud. Determination of the exciton formation in quantum wells from time-resolved interband luminescence. *Phys. Rev. Lett.*, 93:137401, 2004.
- [271] J. Szczytko, L. Kappei, J. Berney, F. Morier-Genoud, M. Portella-Oberli, and B. Deveaud. Origin of excitonic luminescence in quantum wells: Direct comparison of the exciton population and coulomb correlated plasma models. *Phys. Rev. B*, 71(19):195313, 2005.
- [272] M. H. Szymanska, J. Keeling, and P. B. Littlewood. Nonequilibrium quantum condensation in an incoherently pumped dissipative system. *Phys. Rev. Lett.*, 96(23):230602, 2006.
- [273] G. W. 't Hooft, W. A. J. A. van der Poel, L. W. Molenkamp, and C. T. Foxon. Giant oscillator strength of free excitons in GaAs. *Phys. Rev. B*, 35(15):8281–8284, 1987.
- [274] A. Tackeuchi, S. Muto, T. Inata, and T. Fujii. Direct observation of picosecond spin relaxation of excitons in GaAs/alGaAs quantum wells using spin-dependent optical nonlinearity. *Appl. Phys. Lett.*, 56(22):2213–2215, 1990.
- [275] A. I. Tartakovskii, M. Emam-Ismael, R. M. Stevenson, M. S. Skolnick, V. N. Astratov, D. M. Whittaker, J. J. Baumberg, and J. S. Roberts. Relaxation bottleneck and its suppression in semiconductor microcavities. *Phys. Rev. B*, 62(4):R2283, 2000.
- [276] G. A. Thomas, M. Paalanen, and T. F. Rosenbaum. Measurements of conductivity near the metal-insulator critical point. *Phys. Rev. B*, 27(6):R3897–3900, 1983.
- [277] A. Thränhardt, S. Kuckenburg, A. Knorr, T. Meier, and S. W. Koch. Quantum theory of phonon-assisted exciton formation and luminescence in semiconductor quantum wells. *Phys. Rev. B*, 62(4):2706–2720, 2000.
- [278] J. Valles, J. M., S.-Y. Hsu, R. C. Dynes, and J. P. Garno. Electron tunneling studies of ultrathin films near the superconductor-to-insulator transition. *Physica B*, 197(1-4):522–529, 1994.
- [279] P. Vashishta, S. G. Das, and K. S. Singwi. Thermodynamics of the electron-hole liquid in ge, si, and GaAs. *Phys. Rev. Lett.*, 33(15):911–914, 1974.

-
- [280] P. Vashishta and R. K. Kalia. Universal behavior of exchange-correlation energy in electron-hole liquid. *Phys. Rev. B*, 25(10):6492–6495, 1982.
- [281] L. Viña, L. Muñoz, E. Pérez, J. Fernández-Rossier, C. Tejedor, and K. Ploog. Spin splitting in a polarized quasi-two-dimensional exciton gas. *Phys. Rev. B*, 54(12):R8317, 1996.
- [282] A. Vinattieri, J. Shah, T. C. Damen, D. S. Kim, L. N. Pfeiffer, M. Z. Maialle, and L. J. Sham. Exciton dynamics in GaAs quantum wells under resonant excitation. *Phys. Rev. B*, 50(15):10868–10879, 1994.
- [283] J. M. Vogels, K. Xu, and W. Ketterle. Generation of macroscopic pair-correlated atomic beams by four-wave mixing in Bose-Einstein condensates. *Phys. Rev. Lett.*, 89(2):020401, 2002.
- [284] P. Voisin, G. Bastard, and M. Voos. Optical selection rules in superlattices in the envelope-function approximation. *Phys. Rev. B*, 29(2):935–941, 1984.
- [285] D. von der Linde and R. Lambrich. Direct measurement of hot-electron relaxation by picosecond spectroscopy. *Phys. Rev. Lett.*, 42(16):1090–1093, 1979.
- [286] J. Wagner, H. Schneider, D. Richards, A. Fischer, and K. Ploog. Observation of extremely long electron-spin-relaxation times in p-type d-doped GaAs/alxga1-xas double heterostructures. *Phys. Rev. B*, 47(8):4786–4789, 1993.
- [287] H. Wang, K. Ferrio, D. G. Steel, Y. Z. Hu, R. Binder, and S. W. Koch. Transient nonlinear optical response from excitation induced dephasing in GaAs. *Phys. Rev. Lett.*, 71(8):1261, 1993.
- [288] H. Wang, J. Shah, T. C. Damen, and L. N. Pfeiffer. Spontaneous emission of excitons in GaAs quantum wells: The role of momentum scattering. *Phys. Rev. Lett.*, 74(15):3065–3068, 1995.
- [289] M. D. Webb, S. T. Cundiff, and D. G. Steel. Observation of time-resolved picosecond stimulated photon echoes and free polarization decay in GaAs/alGaAs multiple quantum wells. *Phys. Rev. Lett.*, 66(7):934–937, 1991.

-
- [290] C. Weisbuch, H. Benisty, and R. Houdré. Overview of fundamentals and applications of electrons, excitons and photons in confined structures. *J. Luminescence*, 85(4):271–293, 2000.
- [291] C. Weisbuch, M. Nishioka, A. Ishikawa, and Y. Arakawa. Observation of the coupled exciton-photon mode splitting in a semiconductor quantum microcavity. *Phys. Rev. Lett.*, 69(23):3314–3317, 1992.
- [292] S. Weiser, T. Meier, J. Möbius, A. Euteneuer, E. J. Mayer, W. Stolz, M. Hofmann, W. W. Rühle, P. Thomas, and S. W. Koch. Disorder-induced dephasing in semiconductors. *Phys. Rev. B*, 61(19):13088–13098, 2000.
- [293] D. M. Whittaker. Classical treatment of parametric processes in a strong-coupling planar microcavity. *Physical Review B*, 63(19):193305, 2001.
- [294] D. M. Whittaker. Effects of polariton-energy renormalization in the microcavity optical parametric oscillator. *Phys. Rev. B*, 71(11):115301, 2005.
- [295] M. Willatzen, M. Cardona, and N. E. Christensen. Spin-orbit coupling parameters and electron g factor of II-VI zinc-blende materials. *Phys. Rev. B*, 51(24):17992, 1995.
- [296] R. Winkler. private communication.
- [297] M. Wouters and I. Carusotto. Excitations in a nonequilibrium Bose-Einstein condensate of exciton polaritons. *Phys. Rev. Lett.*, 99(14):140402, 2007.
- [298] M. Wouters and I. Carusotto. Goldstone mode of optical parametric oscillators in planar semiconductor microcavities in the strong-coupling regime. *Phys. Rev. A*, 76(4):043807, 2007.
- [299] Y. Yafet. g-factor and spin-lattice relaxation of conduction electrons. In F. Seitz and D. Turnbull, editors, *Solid State Physics*, volume 14, page 1. Academic Press, New York, 1963.
- [300] H. W. Yoon, D. R. Wake, and J. P. Wolfe. Effect of exciton-carrier thermodynamics on the GaAs quantum well photoluminescence. *Phys. Rev. B*, 54(4):2763–2774, 1996.
- [301] P. Y. Yu and M. Cardona. *Fundamentals of Semiconductors*. Springer-Verlag, Berlin, Heidelberg, New York, 3rd edition, 2001.

-
- [302] K. Zerrouati, F. Fabre, G. Bacquet, J. Bandet, J. Frandon, G. Lampel, and D. Paget. Spin-lattice relaxation in p-type gallium arsenide single crystals. *Phys. Rev. B*, 37(3):1334–1341, 1988.
- [303] Y. Zhang and S. Das Sarma. Spin polarization dependence of carrier effective mass in semiconductor structures: Spintronic effective mass. *Phys. Rev. Lett.*, 95:256603, 2005.
- [304] Y. Zhu, D. J. Gauthier, S. E. Morin, Q. Wu, H. J. Carmichael, and T. W. Mossberg. Vacuum rabi splitting as a feature of linear-disperssion theory: Analysis and experimental observations. *Phys. Rev. Lett.*, 64(21):2499–2502, 1990.
- [305] K. S. Zhuravlev, A. I. Toropov, T. S. Shamirzaev, and A. K. Bakarov. Photoluminescence of high-quality alGaAs layers grown by molecular-beam epitaxy. *Appl. Phys. Lett.*, 76(9):1131–1133, 2000.
- [306] R. Zimmermann. Theory of dephasing in semiconductor optics. *physica status solidi (b)*, 173(1):129–137, 1992.
- [307] R. Zimmermann. Theory of resonant rayleigh scattering of excitons in semiconductor quantum wells. *Nuovo Cimento D*, 17D(11):1801, 1995.
- [308] R. Zimmermann, K. Kilimann, W. D. Kraeft, D. Kremp, and G. Ropke. Dynamical screening and self-energy of excitons in the electron-hole plasma. *Phys. Stat. Sol. (b)*, 90(1):175–187, 1978.
- [309] I. Zutic, J. Fabian, and S. Das Sarma. Spintronics: Fundamentals and applications. *Rev. Mod. Phys.*, 76(2):323, 2004.